DCU

Ollscoil Chathair
Bhaile Átha Cliath
Dublin City University

Dublin City University

School of Physical Sciences

Atomic Layer Deposition of Thin Films for Silicon

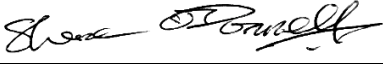# Photoelectrode Protection During Solar Water Splitting

Shane O'Donnell B.Sc.

Thesis Submitted for the award of Doctor of Philosophy (Ph.D)

August 2023

Supervised by Dr. Robert O'Connor

Declaration

I hereby certify that this material, which I now submit for assessment on the programme of study leading to the award of Ph.D. is entirely my own work, and that I have exercised reasonable care to ensure that the work is original, and does not to the best of my knowledge breach any law of copyright, and has not been taken from work of others save and to the extent that such work has been cited and acknowledged within the text of my work.

Signed: _____ (Shane O'Donnell, Candidate)

ID No.:15360946

Date: 25/08/2023

Acknowledgements

Firstly, I would like to thank my supervisor Rob O'Connor for his support, encouragement and opportunities he afforded to me over the years. From his tireless efforts in helping to keep lab equipment going to daily check-ins he has been a massive part of this project. To Greg Hughes, for sharing his passion and infectious enthusiasm about all thing's physics (and bikes!) and for the very memorable Brookhaven trips. To Justin Bogan for taking me on as a student in 3rd year and sharing his passion for surface science. To Joe Woicik and Conan Weiland, the beamline scientists at Brookhaven who welcomed us warmly each time and gave round the clock assistance and support to our measurements.

To Pat Wogan whose working knowledge of every piece of equipment within the building and outstanding skillset that very much keeps the place alive. I hugely appreciate the countless times he has gotten me and the group out of a bind even when most of the problems seem to happen on a Friday evening! To Des Lavelle for his no project or problem too big attitude and his exceeding ability to solve any problem brought before him, taking sketches and hair brain ideas and executing them to the absolute highest standard.

I would also like to thank my friends I was so lucky to have worked with over the years in DCU Caitlin, Darragh, Feljin, Kyle, Matthew, and Rhys. Projects like these are a sum of the people around you and I was lucky to have some of the best.

Most importantly, I would like to thank my family Brenda, Donal, Ciara (and Ozzy) O'Donnell for everything they have given me as well as their continued support, encouragement and belief throughout my time at DCU.

Table of Contents

Table of Figures

List of Abbreviations

AFM	: Atomic Force Microscopy
ALD	: Atomic Layer Deposition
AM	: Air Mass
atm	: Atmosphere
ATR	: Attenuated Total Reflection
AP-XPS	: Ambient Pressure X-Ray Photoelectron Spectroscopy
AR-XPS	: Angularly Resolved X-Ray Photoelectron Spectroscopy
BE	: Binding Energy
BNL	: Brookhaven National Laboratory
CA	: Chronoamperometry
CAE	: Constant Analyser Energy
CB	: Conduction Band
CE	: Counter Electrode
CMOS	: Complementary Metal Oxide Semiconductor
CVD	: Chemical Vapour Deposition
CRR	: Constant Retard Ratio
DCU	: Dublin City University
EAL	: Effective Attenuation Length
ESCA	: Electron Spectroscopy for Chemical Analysis
FE	: Faradaic Efficiency
FF	: Fossil Fuels
FTIR	: Fourier Transform Infrared Spectroscopy
FWHM	: Full Width Half Maximum
GA-ATR-FTIR	: Grazing Angle Attenuated Total Reflection FTIR
GPC	: Growth per Cycle
HAXPES	: Hard X-Ray Photoelectron Spectroscopy
HER	: Hydrogen Evolution Reaction
HV	: High Vacuum
IEA	: International Energy Authority
IMFP	: Inelastic Mean Free Path
IPCE	: Incident-Photon-to-Current-Efficiency
IR	: Infrared
IV	: Current-Voltage Voltammetry Measurement
MPP	: Maximum Power Point
MSE	: Mean Square Error
NHE	: Normal Hydrogen Electrode
NG	: Natural Gas
NIST	: National Institute of Standards and Technology

NSLS-II	:	National Synchrotron Light Source II
OER	:	Oxygen Evolution Reaction
PEALD	:	Plasma Enhanced Atomic Layer Deposition
PEC	:	Photoelectrochemical Cell
PV	:	Photovoltaic
PLD	:	Pulsed Laser Deposition
QE	:	Quantum Efficiency
REF	:	Reference Electrode
RHE	:	Reversible Hydrogen Electrode
RMS	:	Root Mean Square
RSF	:	Relative Sensitivity Factor
SCCM	:	Standard Cubic Centimetre per Minute
SCLJ	:	Semiconductor-liquid Junction
SCR	:	Space Charge Region
SDS	:	Sustainable Development Scenario
SMR	:	Steam Methane Reforming
SNR	:	Signal-to-Noise Ratio
SR	:	Synchrotron Radiation
STH	:	Solar to Hydrogen
TALD	:	Thermal Enhanced Atomic Layer Deposition
TDMAT	:	tetrakis(dimethylaminol) titanium
TTIP	:	titanium isopropoxide
TMN	:	Transition Metal Nitride
UHV	:	Ultra High Vacuum
VB	:	Valence Band
XPS	:	X-Ray Photoelectron Spectroscopy
WE	:	Working Electrode
WF	:	Work Function

Publications Arising from this Work

1. **Thermal and plasma enhanced atomic layer deposition of ultrathin TiO2 on silicon from amide and alkoxide precursors: growth chemistry and photoelectrochemical performance.**
   S O'Donnell, F Jose, K Shiel, M Snelgrove, C McFeely, E McGill and R O'Connor.
   J. Phys. D: Appl. Phys. 2022 **55** 085105

2. **Growth chemistry of cobalt nitride by plasma enhanced atomic layer deposition.**
   S O'Donnell, M Snelgrove, K Shiel, C Weiland, G Hughes, J Woicik, D O'Neill, F Jose, C McFeely and R O'Connor. *Mater. Res. Express,* 2022 **9** 106402

3. **Plasma Enhanced Atomic Layer Deposition of Nickel and Nickel Oxide on Silicon for Photoelectrochemical Applications.**
   S.O'Donnell, D.O'Neill, K.Shiel, M.Snelgrove, F.Jose, C.McFeely, R.O'Connor.
   J. Phys. D: Appl. Phys. **56** 415302

4. **Effect of Polymer Thickness and Molecular Weight on its ability to be Infiltrated Via a Vapour Phase Process**
   C. McFeely, M. Snelgrove, D. O'Neill, S. O'Donnell, F. Jose, C. Weiland, G. Hughes, P. Yadav, J.C. Woicik, M.A. Morris, E. McGlynn, R. O'Connor, *In Preparation*

Conference Proceedings

1. **Thermal and plasma enhanced atomic layer deposition of ultrathin TiO2 on silicon from amide and alkoxide precursors: growth chemistry and photoelectrochemical performance.**
   2020 Virtual American Vacuum Society (AVS) Atomic Layer Deposition (ALD) Symposium Oral Presentation
   S O'Donnell*, F Jose, K Shiel, M Snelgrove, C McFeely, E McGill and R O'Connor

2. **Plasma Enhanced Atomic Layer Deposition of NiO from Nickelocene and Oxygen Precursors: Growth Characteristics and Photoelectrochemical Performance.**
   2022 American Vacuum Society (AVS) Atomic Layer Deposition (ALD) Symposium Ghent, Belgium Poster Presentation
   S.O'Donnell*, D.O'Neill, K.Shiel, M.Snelgrove, F.Jose, C.McFeely, R.O'Connor.

*Underscore Denotes Speaker

Atomic Layer Deposition of Thin Films for Silicon Photoelectrode Protection During Solar Water Splitting

Shane O'Donnell

Abstract

Energy security and climate change have brought on an increasing demand and urgency for the transition from fossil fuel dependency to more sustainable sources of renewable energy. Of the available renewable energy sources at our disposal, solar energy is by far the most abundant. However, the inherent variability of solar energy warrants the development of storage techniques for use during periods of low supply and high demand. Hydrogen fuel is a widely adaptable form of chemical fuel storage making it of great interest for the storage of solar energy. Semiconductor-based photoelectrochemical water splitting has the potential to be an elegant and efficient method of renewable hydrogen fuel production through the capture, conversion and storage of solar energy. Candidate materials must exhibit several exacting characteristics with low cost, and specific electronic properties being paramount. Silicon satisfies these requirements, however its susceptibility to photocorrosion and photopassivation in electrolyte solution hinders its performance. Consequently, Si is incapable of extended use for water splitting without the application of a protective layer such as to distance the harsh water splitting chemical reactions and electrolyte environment from the Si in order to enhance its stability.

This work looks to protect the silicon photoelectrode and improve its performance and operational lifetime. Thin films (< 10 nm) of TiO_2, NiO and CoN were deposited onto SiO_2 via atomic layer deposition (ALD). This thesis details the nucleation, growth chemistry and photoelectrochemical performance of these transition metal -based thin films prepared via thermal and plasma enhanced ALD in addition to exploring the effect of post ALD film treatments by plasma and atmospheric annealing. Films were investigated using photoelectrochemical cell testing to evaluate photoelectrochemical performance, and in-situ cycle-by-cycle x-ray photoelectron spectroscopy was used as the primary characterisation techni

1 Introduction

1.1 Global Warming and the Energy Transition

The combustion of fossil fuels results in the emission of a range of greenhouse gases (GHG) into the atmosphere, with carbon dioxide and methane being two of the most prevalent, causing the trend of rising CO_2 emissions in recent times shown in Figure 1.1. The collection of large quantities of GHGs in the Earth's atmosphere results in the trapping of excessive amounts of heat from the sun which would have otherwise been reflected out into space and a natural regulation and balance of incoming and outgoing solar energy and ultimately heat.
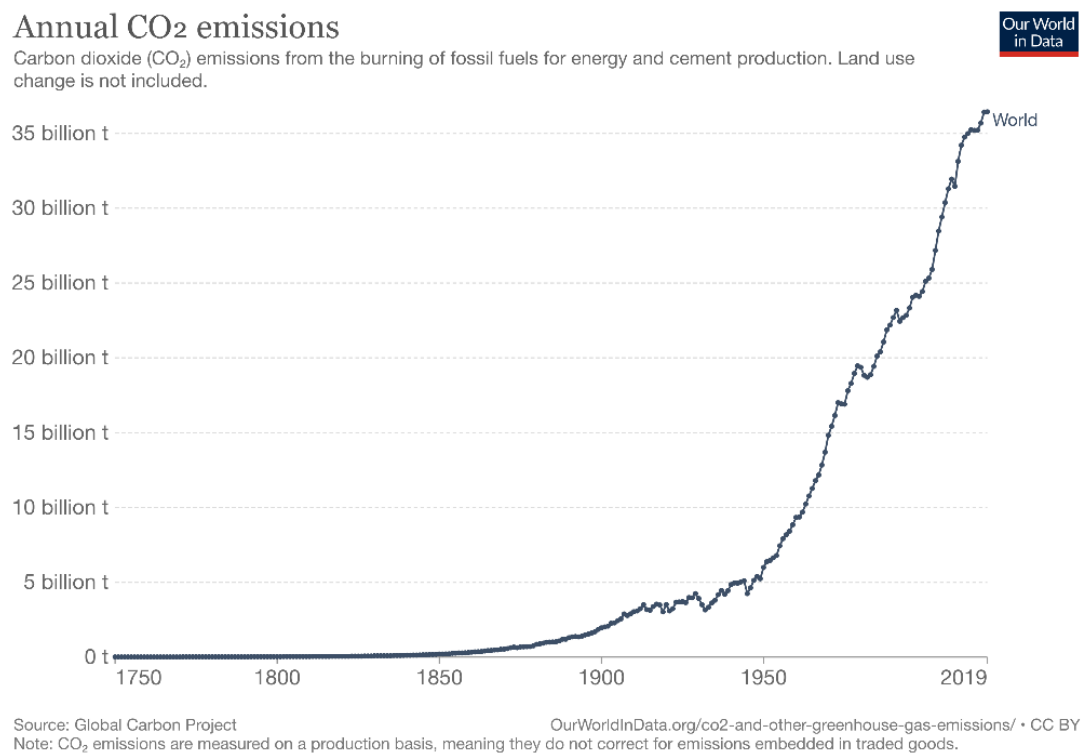
Figure 1.1 Annual global CO2 emissions from fossil fuels and industry [15].

Fossil fuels are also known to have severe impacts on human health [15,16]. The combustion by-products of coal, oil and natural gas release a range of pollutants into the air from particulate matter in the form of soot to polluting gases such as sulphur dioxide and nitrogen oxide [17–19]. Conversely, renewable energies offer a sustainable and comparatively very clean alternative to the polluting future of fossil fuel driven energy production we have been facing down for so long. Solar and wind energy are by far the most popular sources which hold colossal, and in the case of solar energy effectively infinite, energy potential and have become more cost competitive with FFs in recent years. Renewables differ greatly from FFs in that aside from any embodied emissions involved in the construction of infrastructure and technology for the acquisition of the energy in the first place, there are no end use or so-called tailpipe emissions or pollutants resulting from their use. Therefore, no emission of GHGs or any pollutants which can have adverse effects on human health or the environment. The transition from FFs to renewable sources of any form will require significant investment and infrastructure upgrade and development however the potential benefits which may be reaped from this effort will be substantial and profound. Through moving to renewables it is possible to drastically reduce the emission of GHGs which will serve to improve air quality thus protecting human health as well as reducing the global warming effect of these gases in our atmosphere and overall lessening, slowing and potentially halting global warming to below the targeted 2°C rise above pre-industrial global temperature by 2100 set out by the United Nations Climate Change Conference Paris Agreement in 2015 [25]. An additional benefit of renewables is their delocalisation and ability to be produced worldwide rather than being confined to highly contested geographical regions resulting in economic and political

pressures which offers the potential for countries to become energy independent or to provide a portion of their energy demand domestically [26–29].

Although abundant and becoming increasingly popular sources of renewable energy, solar and wind are inherently intermittent on both the shorter scale of day to day variations of weather affecting output as well as longer term wherein seasonal variations of generation will affect supply which culminates in making their integration into the energy mix and grid networks problematic without the addition of energy storage solutions which can be used to bridge these periods of low generation while demand must be met.

One such complication experienced in efforts in attempting to integrate renewable energy into the electricity network stems from this daily and even hourly inconsistency in supply. The variability of supply is a challenge for grid operators as they attempt to balance energy supply and demand in real-time. When the wind blows and the sun shines it is important to make use of renewable energy as it becomes available and bring it onstream, however being that forecasting, and predictions can be unreliable results in the requirement for backup generation to be ready at a moment's notice to ramp up generation if the renewable supply dips or there is an increase in demand. These backups are typically FF sources unless there is some form of traditional hydroelectric or pumped hydroelectric capacity available which can be utilized rapidly.

1.2 Renewable Energy Storage Methods

It is therefore evident that in order to incorporate renewable energy into the energy mix on a large scale, effective means of energy storage are crucial. The two primary forms of storage which have become most popular for the storage of renewables are that of battery technology and hydrogen each with their advantages and disadvantages and particular applications wherein one may be more applicable which will be discussed briefly. A major advantage of hydrogen as a storage medium and ultimately an energy source is its flexibility. Hydrogen is a highly versatile storage medium and can be used for a wide range of energy applications from transportation, heating, and electricity generation. It is possible to use hydrogen in the formation of electricity directly or use it in the formation of synthetic gas or synthetic diesel [33–36].

Particularly when looking to heavy transport, which poses significant challenges to decarbonise effectively, such as shipping where the quantities of energy are massive and refuelling or recharging opportunities are infrequent, hydrogen offers more advantages as a fuel source than via energy stored in batteries. Hydrogen has potential to be developed as an energy source for aviation where it would offer benefits over battery technology for even the most basic of reasons being weight; once expended batteries remain heavy and costly to transport when not generating power and lift whereas once hydrogen is combusted the load is lightened in the more traditional ways of aviation fuel. Furthermore, refuelling with hydrogen could potentially be orders of magnitude faster than charging batteries which is an especially important consideration for aviation and personal vehicle transport where quick turnaround times are important. An additional benefit of hydrogen over battery storage is in long-term storage with hydrogen being suitable to be stored for extended periods while

batteries can in some cases have limited lifetimes which can also be affected by extremes in temperature [37,38]. In terms of electricity generation, the combustion of hydrogen has already undergone a great deal of investigation with early attempts to utilize traditional gas powered electricity generation models combined with adapted gas turbines for the use of a natural gas (NG) and hydrogen mix with Mitsubishi Heavy Industries Group showing in 2018 the possibility of combining the two in a 70:30 (NG:H) ratio resulting in a 10% reduction of CO_2 compared to those using natural gas alone [39].

While there are some key advantages, hydrogen also has its share of disadvantages and limitations associated with its generation, storage, and utilization. One major challenge is its cost as with any new technology the infrastructure is not pre-existing for the most part thus requiring significant investment and development. In order to be practical for use, it must either be compressed to extremely high pressure or liquefied which requires cooling to as low as -250°C which creates massive challenges for its storage and transportation ultimately driving up costs of implementation [40–43]. Safety is of concern particularly in terms of transportation and storage due to hydrogen being a highly flammable and volatile gas igniting easily in the presence of oxygen with a wide flammability range of 4% - 75% which alongside its reduced ignition temperature when compared to petroleum means that a great deal of caution must be observed in its handling [44,45]. Hydrogen is a small molecule making it leak-prone resulting in additional complications in storage and transport. Efficiency of generation is highly relevant to its viability, and with its production via low carbon methods such as electrolysis or photoelectrochemical generation currently being low coupled with the inefficiencies of electrolysers for reconversion back to usable electricity results in the final energy yield being significantly diminished compared to the initial energy input.

1.3 Routes to Hydrogen

While hydrogen is painted as a sustainable and renewable energy source care must be taken in assessing its net carbon emissions and determining the source of energy utilised for its generation as all hydrogen is not created equal.

It is worth discussing the routes to hydrogen available and highlight that hydrogen in and of itself does not signify zero or even low carbon. A colour grading system is widely adopted as the method for differentiating the various methods used for the production or extraction of hydrogen fuel which each have varying levels of impact on the environment. Green hydrogen is the most commonly cited and the best case scenario amongst the 'colours' [58,59]. This involves the production of hydrogen using renewable sources such as solar and wind energy employing the process of water electrolysis to split water into its constituent components [60,61]. This is considered the cleanest route to hydrogen as well as the most sustainable as its production does not result in any carbon emissions aside from those embodied within the manufacture of the technology required [62].

However, currently grey hydrogen is the most commonly used method and involves the extraction of hydrogen from natural gas or methane through a process called steam methane reforming (SMR) which therefore associates this route with significant carbon emissions and is as such not considered a clean form of energy [63]. SMR accounts for the production of approximately 95% of the worlds hydrogen and involves reacting methane (CH_4) with high temperature steam (H_2O) in the presence of a catalyst which forms hydrogen gas (H_2) and carbon monoxide (CO) [64–67]. The SMR process is performed within large reactor vessels under high pressure and temperature which requires a significant amount of energy which due to the current global energy mix being dominated by FFs means that this SMR is directly

powered by FFs. Blue hydrogen follows the same method as grey hydrogen however the carbon emissions are captured and stored or reused in some manner such as to avoid their discharge into the atmosphere [68,69].

Next there is turquoise hydrogen which is a hybrid method combining natural gas with renewable sources wherein renewable energy is used as the energy required to drive the steam methane reforming process which reduces the emissions associated with the process [70,71]. There are a growing number of colours associated with various methods of hydrogen production but the last significant one is yellow hydrogen which is the use of nuclear power to drive the electrolysis process [72–75]. This method is not widely applied and is associated with some safety concerns along with debate about the environmental ethics of this form of energy which will not be detailed within this work [76–80].

1.4 Green Hydrogen from Solar Water Splitting

Of all the renewable energy sources available, many of them are somewhat location dependent which acts to limit their implementation on a wider global scale. This is one of the many advantages of solar energy being that it is not limited to any one or a handful of locations which makes it a highly versatile and extremely valuable renewable energy source. Provided sufficient solar radiation is present, solar energy can be harnessed and used in virtually any part of the world and is therefore a decentralized source [83]. Furthermore, unlike other forms of renewable energy such as hydro and wind, solar energy can be generated in both urban and rural environments allowing it to be used in the generation of power for a variety of applications at the site of demand such as homes, business as well as large scale power plants and even electric vehicle charging stations making solar energy extremely flexible [84–87]. It is clear that the sun is by far our most abundant source or clean energy while also being effectively infinite [83]. Approximately 120,000 TW of solar radiation are incident on the Earth's surface continuously which far exceeds even the most aggressive energy demand scenarios [88]. It is calculated that through covering 0.16% of the Earth's surface with 10% efficient solar conversion panels would provide 20 TW of power which illustrates the magnitude of energy available from the Sun [82]. It is this monumental energy potential which has led to solar energy and its efficient capture and conversion to being termed the 'Holy Grail' of renewable energy sources [83,89,90]. Granted that 0.16% of the Earth's surface is no small area and is equivalent to approximately $900 \times 900 \ km^2$ which is around the size of France and Germany combined, however this serves to illustrate the potential of solar energy to be among, if not the most significant, component in the energy transition [30]. All routes to solar energy follow the steps of capture, conversion and storage [82].

1.5 Principles of Photoelectrochemical (PEC) Water Splitting

It is evident that solar energy emerges head and shoulders above its renewable energy counterparts in term of gross potential for green energy generation and through efficient capture and conversion of solar energy, it is possible to produce green hydrogen. Photoelectrolysis is often used as the term to describe semiconductor-based PEC water splitting with three basic common approaches possible namely photovoltaic cell (PV), semiconductor-liquid junctions (SCLJ) or a combination of the two (PV/SCLJ) [91]. In the PV configuration the electrical potential required for the water splitting process is generated externally before being carried to the electrolyser and/or semiconductor electrodes held in solution [83]. In contrast, the SCLJ arrangement involves the generation of the water splitting potential directly at the semiconductor-liquid interface [91,92].

Both approaches to realise water splitting have their own advantages and disadvantages and the choice of which to employ depends on many factors including cost, efficiency and stability requirements depending on the desired application. While a robust comparison of the two is unwarranted it is worth highlighting one advantage of PV water splitting is its potential to be more efficient than the SCLJ alternative since it directly converts incoming solar energy into electricity. However, the PV approach can in some cases be more complex and therefore costly to manufacture when compared to SCLJ devices through necessity to fabricate separate electrolysers wired to p-n junction solar cells [83,93]. Moreover, SCLJ systems can be more stable allowing them to operate satisfactorily over a range of conditions whereas PV counterparts may require careful control of temperature and illumination [94]. Henceforth all mention of PEC water splitting will refer to the SCLJ configuration as is the method under investigation within this work.

PEC water splitting is a powerful yet complex process for the conversion of solar energy into green hydrogen fuel.

For successful decomposition of water in an efficient and sustainable manner several criteria must be met simultaneously. The semiconductor system and materials in use must be capable of generating a sufficient electropotential upon illumination in order to split water. The bulk band gap must be small enough to absorb a significant portion of the solar spectrum and the band edge potentials at the semiconductor surfaces must straddle the hydrogen and oxygen redox potentials. To be competitive in chemical energy generation the system must exhibit long-term stability against the corrosive effects of the harsh electrolyte environment. Charge transfer from the surface of the semiconductor surface to the electrolyte solution must be free and facile such as to limit energy loss due to kinetic overpotentials which, in electrochemistry, refers to any additional energy required to drive a chemical reaction to completion. Overpotentials will be present as a result of sluggish reaction kinetics, which when referring to electrode interactions involves the transfer of electrons and holes between the electrodes and the electrolyte solution. If the electron transfer reaction kinetics are slow, then a higher potential is necessary to promote the reaction [91]. Charge separation within the semiconductor material of choice is paramount such as to ensure photogenerated electron-hole pairs are separated efficiently to prevent recombination [30,91,92].

Though investigated extensively for several decades now, the original concept of photoelectrochemical water splitting was first demonstrated in 1972 by Fujishima and Honda [95]. Their pioneering research demonstrated that titanium dioxide photoanodes when irradiated could produce oxygen gas through the oxidation of water providing a foundation for the development of photocatalytic systems for hydrogen production through water

splitting [95]. The PEC cell utilised in the original demonstration of water splitting consisted of TiO_2 with a platinum cathode which upon illumination of the TiO_2 electrode led to O_2 evolution on the photoanode and H_2 evolution at the cathode [91,95]. It was later in 1998 when the true potential of the technology was highlighted with Khaselev and Turner demonstrating PEC solar-to-hydrogen efficiencies of 12.4% [96].

The basic principle of solar cells is the photovoltaic effect which is simply the generation of a potential difference at the junction of two semiconductor materials as a result of incident electromagnetic radiation [97]. The photovoltaic effect itself is closely related to that of the photoelectric effect which describes the process whereby electrons are emitted from a material which has absorbed radiation of a frequency above that of the materials in built threshold frequency as illustrated by Einstein in 1905 who explained this effect through the assumption that light consists of well-defined and discrete energy quanta called photons. Photon energy is given in Eq 1.1:

$$E = hv \qquad\qquad (1.1)$$

where h is Planck's constant and v is the frequency of the light. Absorption of a photon in a semiconductor material provides energy to excite an electron from its initial energy level E_i to a higher level denoted E_f as is seen in Figure 1.2 ,with this difference in the initial and final energy level of the electron being equal to that of the incoming photon energy given as $hv = E_f - E_i$. Electrons are permitted to occupy energy levels above the conduction band and below the valence band with the region between these two bands being the band gap E_G = E_C – E_V. Photons striking the semiconductor material with hv less than E_G will not be absorbed by the material but rather traverse without interaction [97].

Therefore, the absorption of light and the ultimate generation of charge carriers in the semiconductor absorber material is dependent on the band gap of the semiconductor material itself. The band gap being the energy difference between the lowest point in the conduction band and the highest point in the valence band with the lowest point in the conduction and valence bands being referred to as the band edges. It is both the electrons excited to the conduction band as well as the holes in the valence band which contribute to electrical conductivity. Intrinsic carrier concentrations and therefore intrinsic conductivity are largely controlled by the ratio of the band gap of a material to its temperature, E_G/k_BT [98]. When this ratio is large the concentration of charge carriers will be low and vice versa. Looking to Figure 1.2 below, at 0 K the conductivity goes to zero as all of the valence band states are filled and all states in the valence band are vacant band thus no available charge carriers. With an increase in energy such as thermal energy or solar energy in the form of photons, electrons become excited from the valence to conduction band thus becoming mobile and available as charge carriers – such carriers are referred to as intrinsic [98]. At room temperature a small quantity of electrons within the valence band gains a sufficient amount of energy to jump to the conduction band. Intrinsic meaning the electrons and holes occur naturally within the material without the addition of external doping or impurities therefore in a pure semiconductor the concentration of electrons and holes is equal.
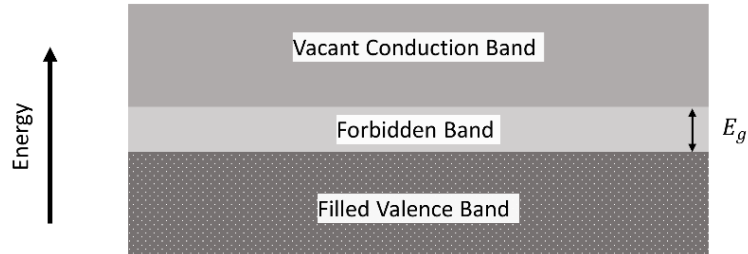
Figure 1.2 Illustration of band scheme of intrinsic conductivity within a semiconductor [98]

Water splitting occurs when a semiconductor device with the right characteristics is immersed in an aqueous electrolyte solution and irradiated with sunlight the incoming solar energy in the form of photons is converted into electrochemical energy through the formation of spatially separated electron-hole pairs which are used in the splitting of water directly into hydrogen and oxygen through interacting electrochemically with ionic species in solution at the semiconductor-liquid interface [30,91,92,99]. These electron-hole pairs are formed when solar energy in the form of photons of sufficient energy strike the photoelectrode and impart their energy on atoms of the electrode material. If the energy of the photon is enough for the electron to be excited from the valence band (VB) to the conduction band (CB) then a hole is left behind in the shell where the excited electron originated from. A 'hole' refers to the absence of an electron in the VB which creates a localised positive charge which can be thought of as a positive charge carrier. The photoexcited holes are used at the photoanode surface where they drive the oxygen evolution reaction (OER) while the photoexcited electrons are swept to the cathode where they are used in the hydrogen evolution reaction (HER) [30,91,100]. The water splitting process involves two half-reactions which are distinct

chemical reactions which occur simultaneously with two variations based on the ph of the electrolyte solution being used [30,91,92,100].

In the case of an alkaline electrolyte the reduction and oxidation reaction equations are as follows:

$$4H_2O + 4e^- \rightleftharpoons 2H_2 + 4OH^- \qquad E^0_{red} = -0.828\ V\ vs. NHE \qquad (1.2)$$

$$4OH^- + 4h^+ \rightleftharpoons 2H_2O + O_2 \qquad E^0_{ox} = -0.401\ V\ vs. NHE \qquad (1.3)$$
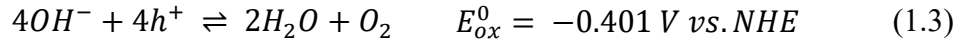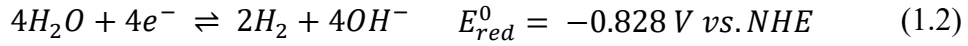
While for an acidic electrolyte the reactions become the following:

$$4H^+ + 4e^- \rightleftharpoons 2H_2 \qquad E^0_{red} = +0.000\ V\ vs. NHE \qquad (1.4)$$

$$2H_2O + 4h^+ \rightleftharpoons 4H + O_2 \qquad E^0_{ox} = -1.229\ V\ vs. NHE \qquad (1.5)$$
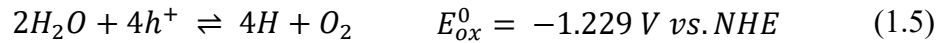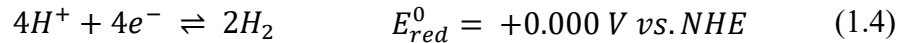
In electrochemistry NHE and RHE are two reference electrodes used to measure and compare the potential of other electrodes or half-cells within the system [101]. NHE stands for the Normal Hydrogen Electrode which is the reference electrode consisting of a platinum electrode immersed in the electrolyte solution [101]. RHE stands for the Reversible Hydrogen Electrode which is a modified version of the NHE which facilitates for reversible electrochemical reactions to take place and the electrode surface [101].

The Gibb's Free energy change for the water splitting reaction is given as.

$$\Delta G = -nF\Delta E \qquad (1.6)$$

Where F is the Faraday constant, representing the charge on one mole of electrons and has units of coulombs per mole. The number of electrons transferred within the reaction is denoted by n. ΔE represents the change in electrochemical potential of the reaction, if this change is positive then the reaction is thermodynamically favourable, while if it is negative, it is unfavourable for electron transfer. The negative sign within the expression indicates that a decrease in Gibbs Free energy corresponds to a positive change in electrochemical potential.

The expression relates the thermodynamics of a reaction to its electrochemical behaviour and is used in order to establish whether a reaction will be spontaneous or will require some external potential to drive the reaction [101]. For the water splitting reaction, at a standard temperature of 298 K and concentration of 1 mol/L at 1 bar the electrochemical cell voltage ΔE of -1.229 V corresponds to a Gibbs free energy change of +237 kJ/mol H_2. This implies that water splitting is thermodynamically uphill [30].

1.6 Water Splitting Photoelectrode Materials and Structure

As discussed, materials used in PEC cells hydrogen fuel generation are required to fulfill several characteristics such as suitable conduction and valence bands, appropriate band gap, stability, efficient charge transport among others. However, no single semiconductor material has yet been identified to meet all of these criteria simultaneously. Various materials and synthesis methods have been investigated toward enhancing the water splitting process with significant efforts in the area of surface coatings, doping, electrocatalyst integration and the effects of nano structuring. It is common for different semiconductor materials to be used in tandem as photoanodes for the OER and photocathodes for the HER such that each material being employed is responsive to different portions of the solar spectrum such as to broaden the overall absorption and utilization of available solar energy. Doping has the advantages of improving the host semiconductor conductivity, participating in band gap engineering, and improving the optical absorption as well as serving to increase the extrinsic charge carrier densities while further augmenting the minority carrier diffusion length. Through depositing electrocatalyst materials on the surface of semiconductors it is possible to reduce the overpotentials present for the HER and OER reactions thus improving the PEC process further. Another focus of investigation within the PEC space is that of nano structing and the implementation of non-planar semiconductor materials which exhibit high aspect ratios in an effort to enhance active surface area and reactive sites at the semiconductor/liquid interface for either the HER or OER reactions while also potentially enhancing the charge transfer kinetics.

1.6.1 Photoanode Materials

As widely discussed within the field, since first being employed by Fujishima and Honda in the 1970's for water splitting under UV irradiation a massive amount of effort has been invested into the deposition and modification of TiO_2 [149–151]. The application of TiO_2 is limited due to its large band gap of approximately 3.2 eV which limits the portion of the solar spectrum which may be used for the PEC process. In an effort to enhance the visible light absorption property of TiO_2 a great many strategies have been explored including doping, the implementation of additional light absorbers, oxygen vacancy addition as well as surface modification. For example, N-doped TiO_2 nanowires were synthesized through calcining TiO_2 using NH_3 which acted to reduce the band gap of TiO_2 to 2.4 eV [151,152]. Heterojunctions have also been introduced in order to narrow the band gap of semiconductors employed in PEC water splitting [151,153]. Reflection is an undesirable loss mechanism in water splitting through reducing the quantity of absorbed photons and so efforts in limiting this effect have been explored through the growth of one-dimensional TiO_2 nanowires and nanotubes. TiO_2 nanotubes have also been treated using a flame and chemical reduction have been shown to exhibit improved catalytic activity for use in the OER [151,154].

Another material which has attracted a great deal of attention within the field is WO_3 due to it being a potentially robust and cost-effective semiconductor for water splitting which although exhibiting high stability within acidic electrolyte solution, the band gap of monoclinic WO_3 is approximately 2.7 eV which remains too large to be efficient as an optimal light absorbing material [151,155,156]. Several studies have shown that through doping and morphological control the photoactivity of WO_3 may be effectively enhanced [155,156]. Furthermore, Choi et al showed that a cobalt phosphate (Co -Pi) OER catalyst layer may be

applied to the base WO_3 substrate to increase photocurrent through reducing electron-hole recombination and shifting the photocurrent onset potential [157].

On the topic of morphological effect on photoelectrode performance, Thind et al report $WO_3/W/WO_3$-Pt bifunctional electrode using W as the substrate material utilizing WO_3 nanoflakes as the photocatalyst and finally WO_3 nanoflakes with Pt nanoparticles acting as the electrocatalyst. Within their report they claim photocurrents of 3.0 mA cm^{-2} at 1.8

1.6.2 Photocathode Materials

A long-studied material for PEC tandem devices has been Si owing to its suitable band gap in this configuration and exhibiting some additional desirable material properties required for the water splitting process [151,158]. Silicon nanowires (SiNWs) were proposed as potentially offering enhanced performance over planar Si, however despite extensive investigation into the development of these nanowires their performance remained low compared to bulk Si or micro scale wires. This was due to intrinsic growth chemistry of the SiNWs rather than the influence of the morphology utilized. In order to increase the PEC performance of Si many cocatalysts and protective layers have been explored such as the earth abundant MoS_2 and MoNi as cocatalysts. Si which had been modified using chemically exfoliated MoS_2 was reported to enhance its performance when compared to bare Si electrodes which is primarily attributed to the protective behavior of the overlying MoS_2 coating acting to alleviate the oxidation of the Si [151,159]. Lewis et al have also recently reported on their investigation into the application of p-Si microwire arrays coupled with a Ni-Mo catalyst film with a TiO_2 light scattering layer also implemented exhibiting -14.3 mA/cm^{-2} which illustrates the potential of these earth abundant co-catalyst materials to enhance the solar driven HER [160].

Cu_2O is another p-Si earth abundant light-absorbing material which exhibits a band gap of approximately 2 eV and as such has the capacity to capture a considerable portion of the solar spectrum and is most often applied as a photocathode material for the HER [161]. The crux with Cu_2O as with Si and many other candidate semiconductor materials is its susceptibility to the oxidating effects of photocorrosion and passivation during the water splitting process. In an effort to overcome this Graetzel et al investigated the application of a 4 nm thick Al_2O_3 coupled with an 11 nm thick TiO_2 layers to act as protective layers shielding the underlying Cu_2O from the harsh oxidative electrolyte environment in combination with Pt as a co-catalyst which yielded -7.6 mA/cm^2 (AM 1.5 G) at 0.0 V vs NHE using a 1.0 M Na_2SO_4 electrolyte solution [162]. This demonstrates the importance of the application of protective layers as well as the effect of utilizing rare earth expensive but very high performing catalyst materials such as Pt as was the case in the study outlined above. Passivation layers having originally been applied such as to distance the OER from the underlying Si substrate for the reduction of the corrosive and oxidative effects of the water splitting process are also used in a secondary capacity to prevent the formation of band gap states which may act to facilitate and promote electron-hole recombination as well as providing catalytic benefits [163].

From a morphological standpoint many reports have looked into non-planar photoelectrodes for PEC purposes with Liu et al reporting on the potential of CoN in overcoming the relatively low HER catalysis efficiencies of planar CoN [164]. These CoN structures were synthesized using hydrothermal and nitridation techniques resulting in the formation of 3D flower-like CoN (CoN-F) architectures along with porous spheres of CoN (CoN-S) and finally polyhedral CoN (CoN-P). This investigation observed the enhanced performance of

the flower like CoN-F derivative owing to the much larger available surface area exposing superior active sites for efficient PEC operation [164]. Moreover, Hu et al reported on the efficacy and tunability of CoN nanowires with these CoN examples among the many investigations exploring various surface modifications with the common goal of introducing increased surface area and therefore superior active water splitting sites. It is uncommon for PEC based studies to detail precisely the deposition characteristics especially with respect to the interfacial region between the substrate material being used and the applied overlayer be that in a catalytic or protective capacity. This interfacial region is of huge importance to gaining key understanding of the overall device performance and as such is among the key focuses within this work as will be developed further in the results chapters.

The list of materials trialled for their photoelectrode potential is lengthy and exhaustive, all with their advantages and disadvantages as they work towards satisfying the exacting material characteristics needed for water splitting. The final material to mention, and the one at the heart of this work, is silicon which has been applied and studied for some time as a result of its suitable light absorption coupled with relatively low-cost owing to its earthly abundance especially when compared to more exotic higher performing materials.

The band gap of Si is 1.11 eV which is lower than the ideal range for suitable water splitting performance however, through band gap engineering and its implementation in a two electrode configuration as shown in Figure 1.3 Si remains a viable photoelectrode candidate material [98].
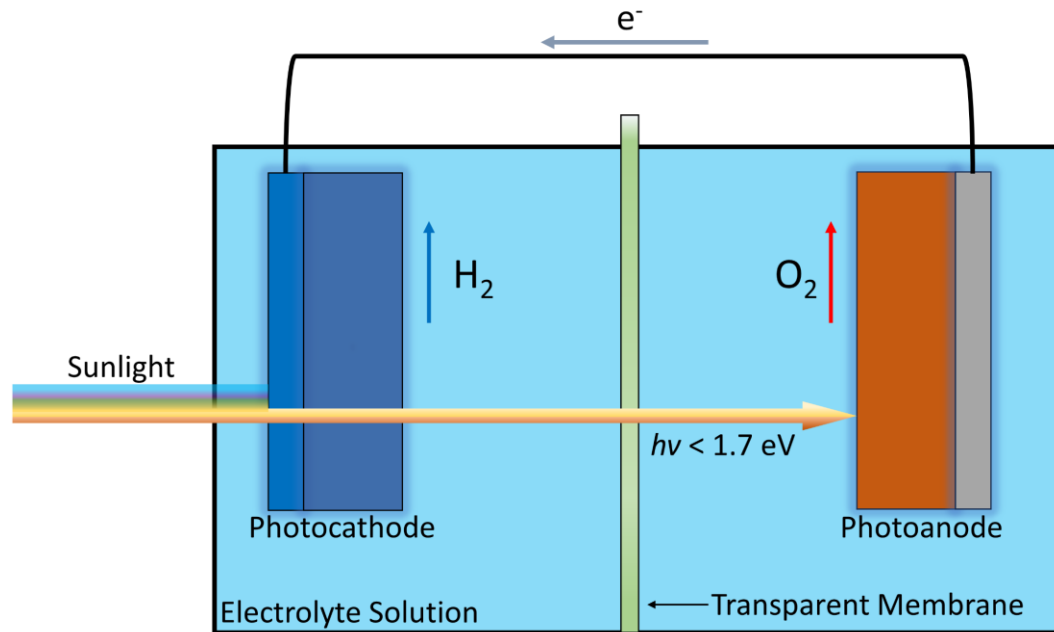
Figure 1.3 Schematic detailing the PEC 2 electrode configuration.

The main limitation of Si is its instability and susceptibility to corrosion in the aqueous environment of the PEC under water splitting conditions. Particularly, when used as a photoanode in the dual-material system shown schematically in Figure 1.3, oxygen evolved at the surface can result in oxidation of the silicon, forming a layer of SiO_2. This material has a bandgap of 8.8 eV, and a large valence band offset with silicon of 4.4 eV which significantly inhibits hole transfer to the surface, and the oxygen evolution reaction as a result. This problem of instability can be circumvented through the application of a protective layer which distances the oxygen evolution reaction and any corrosion from the Si surface. This protective layer must also satisfy the some of the same requirements mentioned earlier as the Si substrate it is to protect such as carrier mobility, stability etc.

1.6.3 Stability

During real world operation of the PEC the photoelectrodes are exposed to harsh alkaline or acidic environments. The acidity or alkalinity of the aqueous environment serves to enhance the water splitting process itself through the introduction of additional ions available to partake in the water splitting half reactions. However, these environments result in undesirable photocorrosion and photopassivation effects on the electrodes. Photocorrosion is the breakdown of the electrode material itself while passivation results from a layer of oxide which forms on the electrode surface which acts to insulate it from further reaction thus reducing or halting the water splitting reaction entirely. Therefore, a material which is immune to these effects is desirable as a candidate protective layer. One such material which has been of significant interest within the field is TiO_2 and has been widely applied as a protective layer as well as for the enhancement of the photoelectrochemical performance of underlying photoelectrodes [102–106].

1.6.4 Light Absorption

Without light, the whole process is void and it is therefore vital that photoelectrode materials absorbs a sufficient amount of light in order to provide the energy to drive the water splitting reactions. The amount of light absorbed by a given material depends on its band gap in addition to its absorption coefficient – the absorption coefficient being a measure of how strongly a material absorbs light of a given frequency and is defined as the fraction of the incident light which is absorbed per unit distance travelled within the material. As it is the energy of the incoming photons which is used to excited electrons from the valence to conduction band within the semiconductor material for the formation of the electron hole pairs necessary for the half reactions, it is vital that the photon energy is equal to or higher

than the band gap of the material. The larger the band gap of a material, the greater the amount of energy which will be available for the reaction, but this reduces the portion of the solar spectrum with energy sufficient to overcome such a band gap.

The energy of a photon is calculated as

$$E_{photon} = \frac{hc}{\lambda} \qquad (1.7)$$

Looking to Figure 1.4 it is clearly evident that solar intensity is at its greatest in the visible portion of the solar spectrum from approximately $450 - 700$ nm, which through calculating using Eq 1.7 corresponds to photon energies of 2.8 to 1.7 eV.
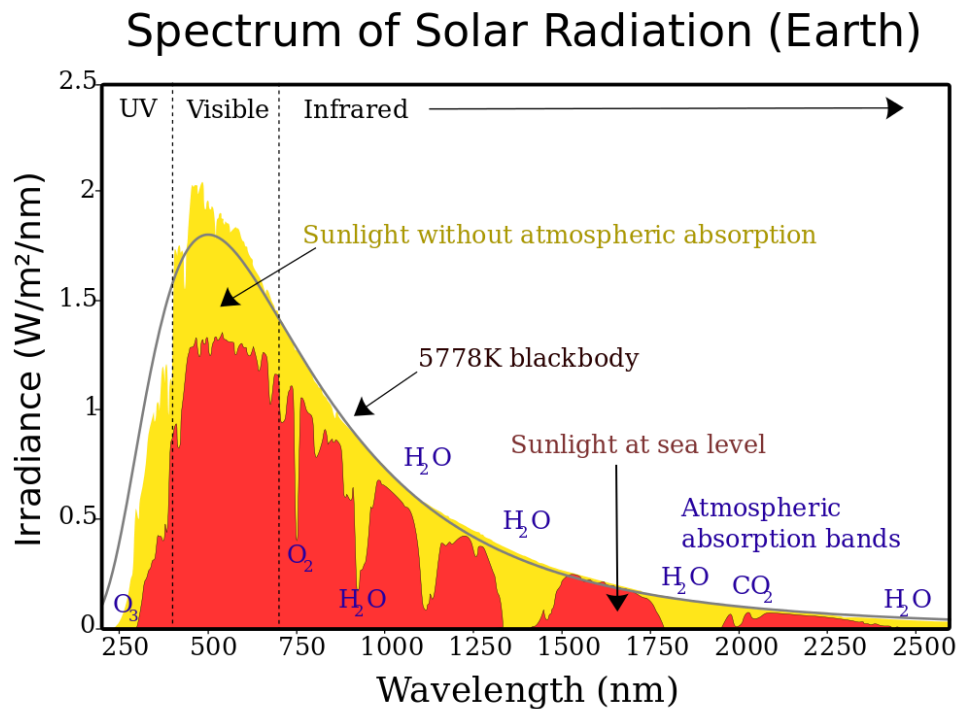
Figure 1.4 Solar spectrum divided into three regions of UV, Visible, IR with the visible region constituting the largest area under the curve [107].

1.6.5 Charge Separation and Mobility

Photogenerated electrons and holes within the semiconductor are prone to recombination within the material bulk as well as at the interfacial region which if not managed can result in low energy efficiency through wasted absorbed photon energy [108]. It is therefore vital to efficiently separate the charge carriers upon generation so as to optimise efficiency. The construction of junctions, for example p-n homojunctions, through doping impurity elements as well as heterojunctions via the fabrication of semiconductor-semiconductor or semiconductor-metal contacts can act to form an electric field which ultimately promotes the migration of the photogenerated charge carriers.

As mentioned, once an electron becomes excited to the conduction band it is prone to recombining with a hole in the valence band. As it is the energy which excited the electron which will be used to power the cell reactions, recombination and the loss of this energy should be avoided. Charges must be separated rapidly to avoid this and directed to the electrode surfaces, which is assisted through the presence of an electric field as a result of band bending which has been discussed already.

The secondary impact of film thickness control is ensuring that the induced electric field within the semiconductor as a result of band bending extends throughout the whole layer and acts on all charge carriers. An additional factor which strongly influences charge separation is carrier mobility, this refers to the magnitude of the drift velocity of a charge carrier per unit electric field and is defined as positive for electrons and holes even though their drift velocities will be opposite within a given electric field as in Eq 1.8.

$$\mu = \frac{|v|}{E} \qquad (1.8)$$

With the drift velocity v calculated for a given charge q as

$$v = \frac{q\tau E}{m} \tag{1.9}$$

Using μ_e and μ_h to denote electron and hole mobility respectively, the electrical conductivity is then the sum of the electron and hole contributions as shown in Eq 1.10 where n and p are the concentrations of electrons and holes:

$$\sigma = (ne\mu_e + pe\mu_h) \tag{1.10}$$

It is vital that carrier mobility is high such as to promote efficient charge transport throughout the material which aids in avoiding recombination.

1.7 Protective Films

One possible route to achieving enhanced performance and stability of silicon photoanodes could potentially come about through the implementation of thin protective films such as to distance the OER reaction from the sensitive anode interface. As discussed throughout Section 1.4, charge transfer characteristics of the semiconductor to water interface is of crucial importance to overall PEC performance and so any material which physically separates the semiconductor and water is itself extremely influential. Thus, the semiconductor-protective layer interface is of major significance and as such forms the foundation of the investigations performed within this thesis.

There is a wide range of deposition techniques which have previously been applied to achieve thin films such as pulsed laser deposition (PLD), spin coating, sputtering and atomic layer deposition (ALD), with spin coating having previously been one of the most common approaches owing to its comparative simplicity in both principle and equipment requirements [115–118]. Despite its basic technique, spin coating falls short in being capable of offering high levels of controllability of film thickness in addition to poor surface coverage and wettability especially in scenarios wherein the base substrate is highly textured which has been noted to introduce interfacial defects [119,120]. Furthermore, although spin coating and other similar solution-based deposition techniques such as hydrothermal, solvothermal and electrodeposition are popular due to their comparable ease of operation, cost effectiveness and scalability films deposited via these means are often seen to fall short. As has become clear in the literature and is developed further throughout this work, detailed analyses of the PEC device materials and properties suggest that performance is highly sensitive to the interfacial region between the substrate and a given overlayer which serves to play a crucial

role in device operation such as impacting charge carrier separation. Therefore, the development and deposition of such highly sensitive interfaces demands a high degree of control over all facets of the deposition from thickness to uniformity to enable stable high performance PEC devices.

Sputtering as well as PLD are prone to the formation of pinholes throughout the deposited film which can lead to undesirable performance for PEC applications [121]. Due to the shortcomings mentioned of alternative deposition techniques, ALD emerges as an attractive option with its superior controllability of film thickness and properties at the atomic level by virtue of its self-limiting deposition technique through the sequential admittance of vapor phase ALD products [122–126]. A further limitation and experimental consideration for the application of these sputtering based techniques stem from their line of sight nature of deposition which make them suboptimal choices for film deposition on high aspect ratio substrates exhibiting complex morphological structures This has led to ALD becoming a popular choice for both planar and non-planar surfaces with its conformality being able to overcome complex morphological features such as 3D arrays of carbon nanotubes and fullerenes among others [127–129].

1.8 ALD Fundamental Theory

Atomic layer deposition (ALD) is a technique used for the growth of thin and ultrathin films for a wide range of applications. ALD is a derivative of chemical vapor deposition (CVD) wherein gaseous reactants called precursors are introduced into the reaction chamber simultaneously where they react to form the desired material for deposition. ALD on the other hand introduces the precursor materials to the chamber alternately, separated by a period of pumping and inert gas purging following each precursor introduction such as to avoid gas phase reactions upon the admission of the following pulse of precursor [130]. It is the sequential saturation and self-limiting growth mechanism of ALD which results in its enhanced conformality, thickness uniformity and control given that layers are deposited in singular atomic layers [124,131]. The ability of ALD to conformally coat a range of morphological structures of high aspect ratio is advantageous over alterative more line of sight techniques which are more suited to depositing on planar substrates.

It is these unique characteristics of ALD which have served to promote ALD in a wide variety of applications particularly in the microelectronics industry enabling the continual downsizing of semiconductor device feature size and increase of aspect-ratio. ALD has also found its place in more developing technological applications of energy-related applications such as photovoltaics and PEC as well as in photonics and biotechnology [124,130,131].

1.8.1 Advantages of ALD

Due to the saturative nature of the sequential admittance of precursor materials the amount of film being deposited is equal across the surface irrespective of the dose received. It is this characteristic of saturating cycles which has the practical effect of conformality and uniformity. With the step-by-step growth comes the deposition of single monolayers or more

often the deposition of a fraction of a monolayer per ALD cycle, thus film thickness can be accurately controlled through establishing a growth per cycle (GPC) rate. Furthermore, switching between film composition can be achieved with relative ease where required with the modification of precursor products being dosed or their quantities which allows for the investigation of multilayer or nanolaminate structures [131]. Alongside thickness control, the very elemental composition of ALD films can be readily altered through the modification of the deposition recipe with the introduction of dopants possible also through interspersing dopant material cycles in between host materials growth cycles adding further versatility to the technique [130].

ALD films are generally continuous, homogeneous, dense and pin-hole free with the exception occurring sometimes with ultrathin films most often caused as a result of issues with nucleation due to a lack of reactive surface sites [130]. Good reproducibility and effective scale-up of the ALD process are also by-products of the self-limiting growth ensuring reliable replication of a given deposition process. Finally, and in some cases most crucially the temperatures required for ALD are considerably lower than those required in CVD with typical ALD processes requiring a temperature in the range of 200 – 350 °C and in some cases lower. This reduced thermal budget is often advantageous when deposition in multilayer architectures wherein other materials being utilised may be thermally unstable beyond the ALD windows.

1.8.2 The ALD Process

The ALD process is divided into steps and proceeds in a cyclic manner and is illustrated in Figure 1.5. The first step involves a pulse of the gaseous precursor reactant of which the film is to be composed into the chamber where is chemisorbed onto the substrate. This is followed

by a period of pumping before inert gas is flowed through the chamber to purge away excess precursor material as well and reaction by-products. Next the second precursor co-reactant is pulsed to the chamber where it undergoes surface reactions with the adsorbate formed by the first pulse and is then followed by additional pumping and gas purging to remove by-products.
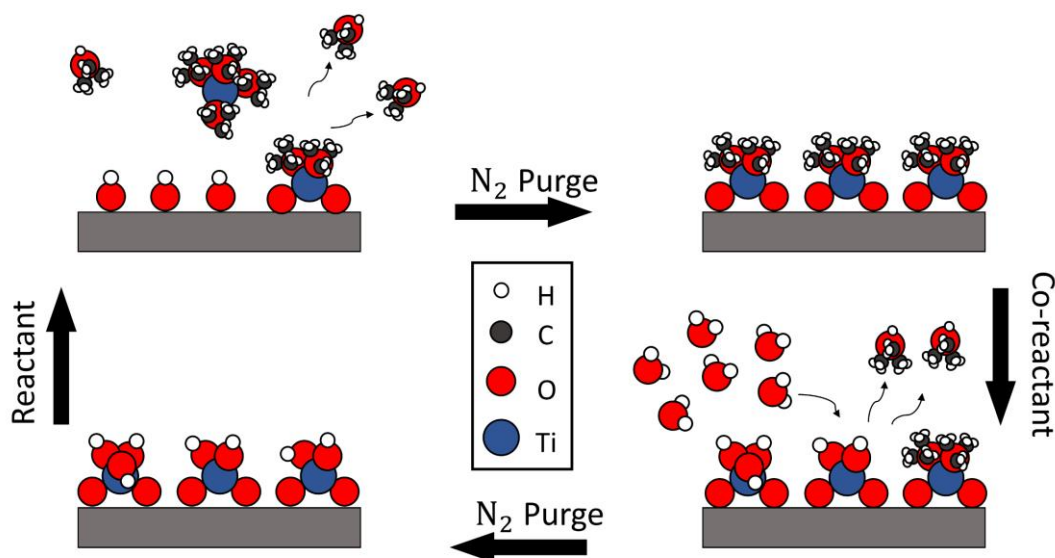
Figure 1.5 Schematic of the ALD process.

To ensure that the ALD process is self-limiting and surface saturative the precursor dose needs to be sufficient to occupy all available surface sites. Precursor dose length beyond the dose required for saturation does not yield to additional film growth. All ALD precursor materials have a certain temperature range where the process will proceed in a self-limiting manner. It is the case during a deposition that some surface sites will react before others due to varying gas fluxes however the precursor will adsorb and then desorb from surface sites where a reaction has already occurred and reached completion [124]. This range of temperature

is referred to as the ALD window and is an important parameter for the successful deposition of high-quality films impacting film growth rates and ideally this range should be large such as to avoid excessive temperature dependence which can result in issues in reproducibility.
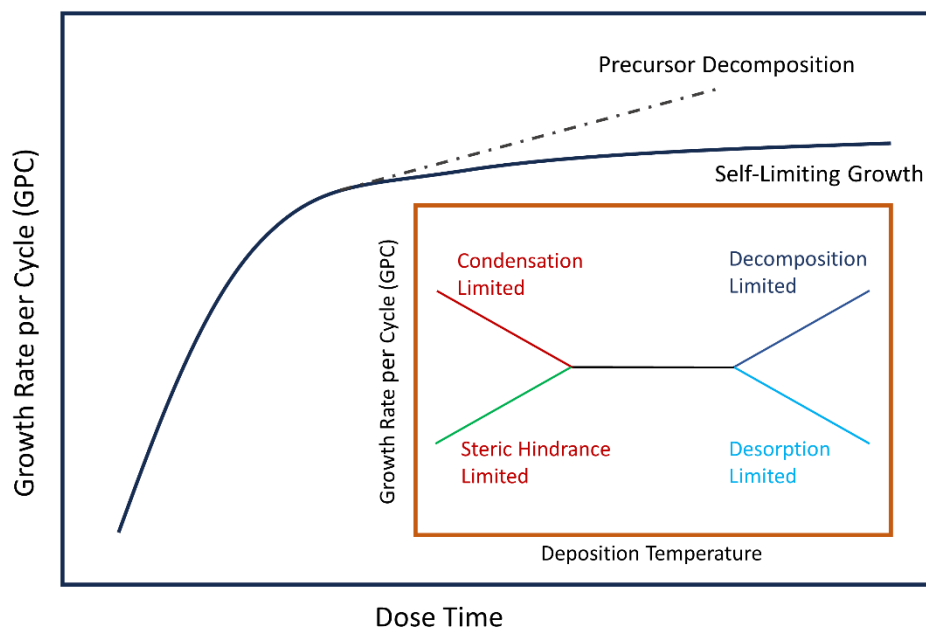
Figure 1.6 Illustration detailing saturating mechanism of ALD dosing.

ALD growth per cycle as a function of both precursor pulse duration and substrate temperature are shown in Figure 1.6 where the saturative nature of the pulse time and the ALD temperature window are shown.

1.8.2.1 Thermal versus Plasma Enhanced ALD

ALD can be carried out in the conventional thermal ALD (TALD) regime or through the implementation of plasma in so called plasma enhanced ALD (PEALD). The difference between these two deposition regimes is the way in which energy is transferred to the process and the resulting impact they can have on the overall film growth.

TALD relies on high temperature to initiate growth and provide energy for the surface reactions between the substrate and precursor materials and employs two vapour phase precursors in the reaction. In TALD the substrate is heated to a specific temperature, typically greater than 150°C, to facilitate the adsorption and reactions within the system. The use of heat acts to enhance the reactivity of precursor and substrate materials introduced to the system acting to promote the formation of high-quality films of satisfactory conformality and uniformity. TALD can however limit the number of ALD precursor materials which can be selected for deposited due to the high temperature requirement for deposition to proceed effectively. TALD most often utilizes water as the co-reactant species.

Conversely, plasma enhanced ALD (PEALD) relies on the use of a plasma for the formation of co-reactant species. A plasma can be defined as an ionised and electrically conductive gas consisting of electrons, ions and neutrals, including reactive species which are gas dependent. Weakly ionised plasmas are typically created by generating an oscillating electric field within a low-pressure gas environment. This can be achieved through various methods including electrical field generation through a capacitively coupled plasma (CCP) or an inductively coupled plasma (ICP). A CCP produces an electric field by applying an oscillating voltage to a pair of electrodes. This then allows for the electrons to energise and collide with the background gas creating reactive species. An ICP on the other hand, which is the plasma source used within this study, creates the electric field by passing a varying electric current through a coil. This then produces an oscillating magnetic field which induces the electric field within the gas.

Similarly, to the CCP this causes the energised electrons to collide with the background gas forming reactive species. It is these reactive species which then interact with the deposited

precursor allowing for the formation of the desired film. As these species carry chemical energy, processes have the potential to be conducted at lower temperatures compared to the TALD as heat is not as critical in driving the chemical reactions.

The use of plasma enhances the reactivity of precursors and can often facilitate the application of a wider range of materials due to a reduced temperature dependence. It is the radicals and other energetic species within the plasma itself which serve to drive reactions which are not possible using thermal energy alone [132,133].

Additionally, plasma sources can be used in the generation of hydrogen radicals which can act to reduce metal or semiconductor precursors [124]. PEALD can also lead to faster deposition rates however it can add complexity to the deposition process with the plasma parameters needing to be precisely controlled. The advantages typically outweigh the disadvantages, with PEALD ultimately yielding cleaner films compared to those obtained via TALD, with carbon being a key impurity left behind following incomplete reactions which can occur in the conventional TALD regime [134,135].

The choice between the use of TALD or PEALD depends on the requirements of the application in addition to the requirements for the resulting film. TALD is typically applied wherein excellent uniformity and conformality are required with PEALD being more dependent on line-of-sight and exacting chamber geometry [130]. The chamber geometry can affect the transport of precursor gases and plasma species as well as reaction by-products. The loss of neutral species within the chamber has an appreciable effect on PEALD depositions with the reactor walls themselves being a critical loss mechanism and ultimately determining the flux of neutral species to the substrate surface [136].

PEALD is preferential for applications requiring a wider range of precursor chemistries, faster deposition rates or in cases where high temperatures such as those needed for TALD could negatively affect materials within the process such as resulting in decomposition [137–142]. PEALD is also reported to yield films which exhibit higher density than those obtained via TALD as well as being capable of producing improved electrical properties [134,143–148].

It is evident that ALD is a well-suited technique for the deposition of thin protective films for the passivation of water splitting photoelectrodes. Being that ALD is somewhat of a new technique being a variation of the more traditional chemical vapor deposition (CVD) technique, the deposition of these protective and even catalytic films for water splitting applications had previously been performed via alternative techniques such as pulsed laser deposition (PLD), spin coating and sputtering with spin coating being the more common approach due to its comparative simplicity and equipment requirements [115–118]. However, spin coating falls short in offering a high level of controllability on film thickness as well as poor surface coverage and wettability particularly when the base substrate is especially rough resulting in the introduction of interfacial defects [119,120].

Both PLD and sputtering are prone to the formation of pinholes throughout the films resulting in undesirable performance for PEC or PSC applications [121]. As a result of the above mentioned shortcomings of these different film deposition techniques, ALD emerges as an attractive alternative owing to its layer by layer self-limiting deposition, which results in a high level of controllability both in terms of film thickness and properties at the atomic level [122–126]. The sequential admittance of vapor phase ALD products to the deposition chamber enables highly controllable and conformal film growth [123,126]. ALD has also become a favorable technique for the fabrication of thin films on non-planar surfaces due its

conformality allowing for depositions on textured surfaces or those with complex surface morphology such as multiwalled carbon nanotubes and fullerenes amongst others [127–129].

It is these distinct advantages in terms of controllability and layer by layer growth of ALD thin films which makes this technique so valuable in this work. Through fine detail analysis of film composition and nucleation studies on a layer-by-layer basis using the vacuum coupled x-ray characterisation (XPS) it becomes possible to investigate and characterize thin protective films in an effort to enhance and prolong the performance of water splitting photoelectrodes.

1.9 Thesis Layout and Overview of Results

In Chapter 2, the principles behind the operation of the deposition and characterisation techniques are presented. The deposition technique used was atomic layer deposition (ALD) while the primary characterisation techniques for the analysis for deposited ALD films were x-ray photoelectron spectroscopy (XPS) and photoelectrochemical cell testing. To supplement these characterisation techniques other techniques were implemented including synchrotron based XPS (HAXPES), atomic force microscopy (AFM), Fourier transform infra-red spectroscopy (FTIR) and ellipsometry.

This thesis presents its findings through 3 distinct results chapters, all aimed at the overarching goal: the characterisation of deposited thin films for safeguarding photoelectrodes used in water splitting. Analysis of these films is performed to gain insights into their stoichiometry, nucleation, and growth characteristics before subjecting them to simulated water splitting testing to establish their efficacy as protective layers.

Chapter 3 focuses on the characterisation of TiO_2 deposited using two different precursor materials being titanium isopropoxide (TTIP) and tetrakis(dimethylaminol) titanium (TDMAT). These precursors were characterised and compared against one another within the same system via both conventional thermal ALD (TALD) using H_2O and plasma enhanced ALD (PEALD) using O_2 plasma allowing for a direct and accurate analysis of these materials side by side. through concurrently depositing and characterising these two commonly used TiO_2 ALD precursors, this study eliminated potential discrepancies arising from the use of different deposition chambers and techniques employed by others within the field. Furthermore, the impact of applying post deposition annealing treatments via H_2 plasma annealing and ambient air annealing was studied to gain an understanding on the

effect on PEC performance based on discussion within the literature citing potential scope for improvement utilising such annealing processes.

Chapter 4 looks to the PEALD deposition and characterisation of NiO using bis(cyclopentadienyl)nickel(II) or nickelocene ($NiCp_2$) as the chosen precursor material and O_2 as the coreactant. NiO is a material that which has garnered attention for its potential application in both PEC and perovskite solar cells which warrants a detailed investigation into its growth chemistry and performance characteristics as a protective layer for PEC water splitting photoelectrodes. This chapter also explores the effect of H_2 plasma annealing on the stoichiometry and PEC performance of deposited protective films as well as investigating the performance of metallic Ni films deposited via modified ALD deposition recipes which are referred to as 'supercycles' within the field of ALD. Additionally, depth profiling analysis via slow argon milling was performed with results contrary to those reported within the field observed based on sputtering effects of the milling process.

After extensively examining the performance of oxide and metallic films in this thesis, Chapter 5 shifts focus towards the investigation of PEALD nitride films, specifically CoN deposited using cobaltocene ($CoCp_2$) as the cobalt precursor and NH_3 plasma as a co-reactant. Within the field of water splitting, the study of nitrides has been limited, with only a few reports highlighting their potential. Therefore, conducting a comprehensive analysis on these films was considered valuable. The growth chemistry of CoN films was characterised using both traditional XPS as well as synchrotron studies using HAXPES which enabled a more accurate and detailed investigation of film stoichiometry. These films were subsequently tested for their PEC performance in the same manner of the previously studied oxide and

metal films building upon the findings for these materials in earlier chapters and the field as a whole.

In Chapter 6 the primary discoveries of this study are consolidated, and potential avenues for future research are outlined.

1.10 References

(1)   Electricity Market Report. *Electr. Mark. Rep.* **2020**. https://doi.org/10.1787/f0aed4e6-en.

(2)   Lynas, M.; Houlton, B. Z.; Perry, S. Greater than 99% Consensus on Human Caused Climate Change in the Peer-Reviewed Scientific Literature. *Environ. Res. Lett.* **2021**, *16* (11). https://doi.org/10.1088/1748-9326/ac2966.

(3)   McMichael, A. J.; Woodruff, R. E. Climate Change and Human Health. *Encycl. Earth Sci. Ser.* **2005**, 209–213. https://doi.org/10.1007/1-4020-3266-8_41.

(4)   Jan Van Oldenborgh, G.; Krikken, F.; Lewis, S.; Leach, N. J.; Lehner, F.; Saunders, K. R.; Van Weele, M.; Haustein, K.; Li, S.; Wallom, D.; Sparrow, S.; Arrighi, J.; Singh, R. K.; Van Aalst, M. K.; Philip, S. Y.; Vautard, R.; Otto, F. E. L. Attribution of the Australian Bushfire Risk to Anthropogenic Climate Change. *Nat. Hazards Earth Syst. Sci.* **2021**, *21* (3), 941–960. https://doi.org/10.5194/nhess-21-941-2021.

(5)   Perera, A. T. D.; Nik, V. M.; Chen, D.; Scartezzini, J. L.; Hong, T. Quantifying the Impacts of Climate Change and Extreme Climate Events on Energy Systems. *Nat. Energy* **2020**, *5* (2), 150–159. https://doi.org/10.1038/s41560-020-0558-0.

(6)   Koetse, M. J.; Rietveld, P. The Impact of Climate Change and Weather on Transport: An Overview of Empirical Findings. *Transp. Res. Part D Transp. Environ.* **2009**, *14* (3), 205–221. https://doi.org/10.1016/j.trd.2008.12.004.

(7)   Hashim, J. H.; Hashim, Z. Climate Change, Extreme Weather Events, and Human Health Implications in the Asia Pacific Region. *Asia-Pacific J. Public Heal.* **2014**, *28*, 8S-14S. https://doi.org/10.1177/1010539515599030.

(8)   Diffenbaugh, N. S.; Field, C. B. Changes in Ecologically Critical Terrestrial Climate Conditions. *Science (80-.).* **2013**, *341* (6145), 486–492. https://doi.org/10.1126/science.1237123.

(9)   Coumou, D.; Rahmstorf, S. A Decade of Weather Extremes. *Nat. Clim. Chang.* **2012**, *2* (7), 491–496. https://doi.org/10.1038/nclimate1452.

(10)   Rahmstorf, S.; Coumou, D. Increase of Extreme Events in a Warming World. *Proc. Natl. Acad. Sci. U. S. A.* **2011**, *108* (44), 17905–17909. https://doi.org/10.1073/pnas.1101766108.

(11) Hansen, J.; Sato, M.; Ruedy, R. Perception of Climate Change. *Proc. Natl. Acad. Sci. U. S. A.* **2012**, *109* (37). https://doi.org/10.1073/pnas.1205276109.

(12) Tomas, R. A.; Deser, C.; Sun, L. The Role of Ocean Heat Transport in the Global Climate Response to Projected Arctic Sea Ice Loss. *J. Clim.* **2016**, *29* (19), 6841–6859. https://doi.org/10.1175/JCLI-D-15-0651.1.

(13) Box, J. E.; Fettweis, X.; Stroeve, J. C.; Tedesco, M.; Hall, D. K.; Steffen, K. Greenland Ice Sheet Albedo Feedback: Thermodynamics and Atmospheric Drivers. *Cryosphere* **2012**, *6* (4), 821–839. https://doi.org/10.5194/tc-6-821-2012.

(14) Maykut, G. A. Chapter 5 the Surface Heat and Mass Balance 5.1 Introduction. **1986**.

(15) Taghizadeh-Hesary, F.; Taghizadeh-Hesary, F. The Impacts of Air Pollution on Health and Economy in Southeast Asia. *Energies* **2020**, *13* (7). https://doi.org/10.3390/en13071812.

(16) Perera, F.; Nadeau, K. Climate Change, Fossil-Fuel Pollution, and Children's Health. *N. Engl. J. Med.* **2022**, *386* (24), 2303–2314. https://doi.org/10.1056/nejmra2117706.

(17) Lee, H. H.; Iraqui, O.; Wang, C. The Impact of Future Fuel Consumption on Regional Air Quality in Southeast Asia. *Sci. Rep.* **2019**, *9* (1), 1–20. https://doi.org/10.1038/s41598-019-39131-3.

(18) Raza, W.; Saeed, S.; Saulat, H.; Gul, H.; Sarfraz, M.; Sonne, C.; Sohn, Z. H.; Brown, R. J. C.; Kim, K. H. A Review on the Deteriorating Situation of Smog and Its Preventive Measures in Pakistan. *J. Clean. Prod.* **2021**, *279*, 123676. https://doi.org/10.1016/j.jclepro.2020.123676.

(19) Malik, M. I. SMOG AND HEALTH. **2022**, *33* (02), 2022.

(20) Leikauf, G. D.; Kim, S. H.; Jang, A. S. Mechanisms of Ultrafine Particle-Induced Respiratory Health Effects. *Exp. Mol. Med.* **2020**, *52* (3), 329–337. https://doi.org/10.1038/s12276-020-0394-0.

(21) Rasoulinezhad, E.; Taghizadeh-Hesary, F.; Taghizadeh-Hesary, F. How Is Mortality Affected by Fossil Fuel Consumption, CO2 Emissions and Economic Factors in CIS Region? *Energies* **2020**, *13* (9). https://doi.org/10.3390/en13092255.

(22) Rahman, M. M.; Begum, B. A.; Hopke, P. K.; Nahar, K.; Newman, J.; Thurston, G. D. Cardiovascular Morbidity and Mortality Associations with Biomass-and Fossil-Fuel-Combustion Fine-Particulate-Matter Exposures in Dhaka, Bangladesh. *Int. J.*

Epidemiol. **2021**, *50* (4), 1172–1183. https://doi.org/10.1093/ije/dyab037.

(23)   Kotcher, J.; Maibach, E.; Choi, W. T. Fossil Fuels Are Harming Our Brains: Identifying Key Messages about the Health Effects of Air Pollution from Fossil Fuels. *BMC Public Health* **2019**, *19* (1), 1–12. https://doi.org/10.1186/s12889-019-7373-1.

(24)   Lelieveld, J.; Klingmüller, K.; Pozzer, A.; Burnett, R. T.; Haines, A.; Ramanathan, V. Effects of Fossil Fuel and Total Anthropogenic Emission Removal on Public Health and Climate. *Proc. Natl. Acad. Sci. U. S. A.* **2019**, *116* (15), 7192–7197. https://doi.org/10.1073/pnas.1819989116.

(25)   Delbeke, J.; Runge-Metzger, A.; Slingenberg, Y.; Werksman, J. The Paris Agreement. *Towar. a Clim. Eur. Curbing Trend* **2019**, 24–45. https://doi.org/10.4324/9789276082569-2.

(26)   Shepard, J. U.; Pratson, L. F. The Myth of US Energy Independence. *Nat. Energy* **2022**, *7* (6), 462–464. https://doi.org/10.1038/s41560-022-01053-2.

(27)   Eberhard, A.; Naude, R. The South African Renewable Energy Independent Power Producer Procurement Programme: A Review and Lessons Learned. *J. Energy South. Africa* **2016**, *27* (4), 1–14. https://doi.org/10.17159/2413-3051/2016/v27i4a1483.

(28)   Barone, G.; Buonomano, A.; Forzano, C.; Giuzio, G. F.; Palombo, A. Increasing Renewable Energy Penetration and Energy Independence of Island Communities: A Novel Dynamic Simulation Approach for Energy, Economic, and Environmental Analysis, and Optimization. *J. Clean. Prod.* **2021**, *311* (April), 127558. https://doi.org/10.1016/j.jclepro.2021.127558.

(29)   Żuk, P.; Żuk, P. National Energy Security or Acceleration of Transition? Energy Policy after the War in Ukraine. *Joule* **2022**, *6* (4), 709–712. https://doi.org/10.1016/j.joule.2022.03.009.

(30)   Van De Krol, R.; Grätzel, M. *Photoelectrochemical Hydrogen Production*, First.; Krol, R. van de, Gra¨tzel, M., Eds.; Springer US. https://doi.org/10.1007/978-1-4614-1380-6.

(31)   IEA. International Energy Agency World Energy Outlook. **2004**.

(32)   Winzer, C. Conceptualizing Energy Security. *Energy Policy* **2012**, *46*, 36–48. https://doi.org/10.1016/j.enpol.2012.02.067.

(33)   Staffell, I.; Scamman, D.; Velazquez Abad, A.; Balcombe, P.; Dodds, P. E.; Ekins, P.;

Shah, N.; Ward, K. R. The Role of Hydrogen and Fuel Cells in the Global Energy System. *Energy Environ. Sci.* **2019**, *12* (2), 463–491. https://doi.org/10.1039/c8ee01157e.

(34) Andreas, Z.; Borgschulte, A. *Handbook of Fuels Beyond Oil and Gas : The Methanol Economy Molten Carbonate Fuel Cells*; 2008.

(35) Jensen, S. H.; Larsen, P. H.; Mogensen, M. Hydrogen and Synthetic Fuel Production from Renewable Energy Sources. *Int. J. Hydrogen Energy* **2007**, *32* (15 SPEC. ISS.), 3253–3257. https://doi.org/10.1016/j.ijhydene.2007.04.042.

(36) Solar hydrogen: Moving beyond fossil fuels (Book) | OSTI.GOV https://www.osti.gov/biblio/6280248 (accessed May 25, 2023).

(37) Pellow, M. A.; Emmott, C. J. M.; Barnhart, C. J.; Benson, S. M. Hydrogen or Batteries for Grid Storage? A Net Energy Analysis. *Energy Environ. Sci.* **2015**, *8* (7), 1938–1952. https://doi.org/10.1039/c4ee04041d.

(38) Ferrario, A. M.; Jos, F.; Manzano, F. S.; Manuel, J.; Bocci, E.; Martirano, L. A Comparative Between Energy Management Strategies for Hybrid Renewable Microgrids. *Electronics* **2020**, *9* (698), 27.

(39) NaturePortfollio. Turbines Driven Purely by Hydrogen in the Pipeline. *Nature* **2022**, 1–6.

(40) Uliasz-Misiak, B.; Lewandowska-Śmierzchalska, J.; Matuła, R.; Tarkowski, R. Prospects for the Implementation of Underground Hydrogen Storage in the EU. *Energies* **2022**, *15* (24). https://doi.org/10.3390/en15249535.

(41) Han, S. S.; Mendoza-Cortés, J. L.; Goddard, W. A. Recent Advances on Simulation and Theory of Hydrogen Storage in Metal–Organic Frameworks and Covalent Organic Frameworks. *Chem. Soc. Rev.* **2009**, *38* (5), 1460–1476. https://doi.org/10.1039/b802430h.

(42) Hu, Z.; Sheng, J.; Xu, M. Review of Hydrogen Fuel Cell Vehicles. **2023**, *29*.

(43) Mahajan, D.; Tan, K.; Venkatesh, T.; Kileti, P.; Clayton, C. R. Hydrogen Blending in Gas Pipeline Networks—A Review. *Energies* **2022**, *15* (10). https://doi.org/10.3390/en15103582.

(44) Florin, N. and Dominish, E. Sustainability Evaluation of Energy Storage Technologies. *Inst. Sustain. Futur. Aust. Counc. Learn.* **2017**, 78.

(45) Becherif, M.; Ramadan, H. S.; Cabaret, K.; Picard, F.; Simoncini, N.; Bethoux, O. Hydrogen Energy Storage: New Techno-Economic Emergence Solution Analysis. *Energy Procedia* **2015**, *74* (0), 371–380. https://doi.org/10.1016/j.egypro.2015.07.629.

(46) Meda, U. S.; Bhat, N.; Pandey, A.; Subramanya, K. N.; Lourdu Antony Raj, M. A. Challenges Associated with Hydrogen Storage Systems Due to the Hydrogen Embrittlement of High Strength Steels. *Int. J. Hydrogen Energy* **2023**, No. xxxx, 1–20. https://doi.org/10.1016/j.ijhydene.2023.01.292.

(47) Pradhan, A.; Vishwakarma, M.; Dwivedi, S. K. A Review: The Impact of Hydrogen Embrittlement on the Fatigue Strength of High Strength Steel. *Mater. Today Proc.* **2019**, *26*, 3015–3019. https://doi.org/10.1016/j.matpr.2020.02.627.

(48) Xiuqing, X.; Junwei, A.; Chen, W.; Jing, N. Study on the Hydrogen Embrittlement Susceptibility of AISI 321 Stainless Steel. *Eng. Fail. Anal.* **2021**, *122* (October 2020), 105212. https://doi.org/10.1016/j.engfailanal.2020.105212.

(49) Laureys, A.; Depraetere, R.; Cauwels, M.; Depover, T.; Hertelé, S.; Verbeken, K. Use of Existing Steel Pipeline Infrastructure for Gaseous Hydrogen Storage and Transport: A Review of Factors Affecting Hydrogen Induced Degradation. *J. Nat. Gas Sci. Eng.* **2022**, *101* (March). https://doi.org/10.1016/j.jngse.2022.104534.

(50) Li, X.; Ma, X.; Zhang, J.; Akiyama, E.; Wang, Y.; Song, X. Review of Hydrogen Embrittlement in Metals: Hydrogen Diffusion, Hydrogen Characterization, Hydrogen Embrittlement Mechanism and Prevention. *Acta Metall. Sin. (English Lett.* **2020**, *33* (6), 759–773. https://doi.org/10.1007/s40195-020-01039-7.

(51) Tanwar, H.; Singh, T.; Khichi, B.; Singh, R. C.; Singari, R. M. *Study and Design Conceptualization of Compliant Mechanisms and Designing a Compliant Accelerator Pedal*; 2021. https://doi.org/10.1007/978-981-15-8542-5_24.

(52) Briottet, L.; Moro, I.; Lemoine, P. Quantifying the Hydrogen Embrittlement of Pipeline Steels for Safety Considerations. *Int. J. Hydrogen Energy* **2012**, *37* (22), 17616–17623. https://doi.org/10.1016/j.ijhydene.2012.05.143.

(53) Nykyforchyn, H.; Unigovskyi, L.; Zvirko, O.; Tsyrulnyk, O.; Krechkovska, H. Pipeline Durability and Integrity Issues at Hydrogen Transport via Natural Gas Distribution Network. *Procedia Struct. Integr.* **2021**, *33* (C), 646–651.

https://doi.org/10.1016/j.prostr.2021.10.071.

(54) Nanninga, N.; Slifka, A.; Levy, Y.; White, C. A Review of Fatigue Crack Growth for Pipeline Steels Exposed to Hydrogen. *J. Res. Natl. Inst. Stand. Technol.* **2010**, *115* (6), 437–452. https://doi.org/10.6028/jres.115.030.

(55) Venezuela, J.; Liu, Q.; Zhang, M.; Zhou, Q.; Atrens, A. A Review of Hydrogen Embrittlement of Martensitic Advanced High-Strength Steels. *Corros. Rev.* **2016**, *34* (3), 153–186. https://doi.org/10.1515/corrrev-2016-0006.

(56) Djukic, M. B.; Bakic, G. M.; Sijacki Zeravcic, V.; Sedmak, A.; Rajicic, B. The Synergistic Action and Interplay of Hydrogen Embrittlement Mechanisms in Steels and Iron: Localized Plasticity and Decohesion. *Eng. Fract. Mech.* **2019**, *216* (June), 106528. https://doi.org/10.1016/j.engfracmech.2019.106528.

(57) Ohaeri, E.; Eduok, U.; Szpunar, J. Hydrogen Related Degradation in Pipeline Steel: A Review. *Int. J. Hydrogen Energy* **2018**, *43* (31), 14584–14617. https://doi.org/10.1016/j.ijhydene.2018.06.064.

(58) Megia, P. J.; Vizcaino, A. J.; Calles, J. A.; Carrero, A. Hydrogen Production Technologies: From Fossil Fuels toward Renewable Sources. A Mini Review. *Energy and Fuels* **2021**, *35* (20), 16403–16415. https://doi.org/10.1021/acs.energyfuels.1c02501.

(59) He, W.; Zheng, Y.; You, S.; Strbac, G.; Therkildsen, K. T.; Olsen, G. P.; Howie, A.; Byklum, E.; Sharifabadi, K. T. Case Study on the Benefits and Risks of Green Hydrogen Production Co-Location at Offshore Wind Farms. *J. Phys. Conf. Ser.* **2022**, *2265* (4). https://doi.org/10.1088/1742-6596/2265/4/042035.

(60) Wind Energy Ireland. Seizing Our Green Hydrogen Opportunity.

(61) Himpsel, F. J.; McFeely, F. R.; Taleb-Ibrahimi, A.; Yarmoff, J. A.; Hollinger, G. Microscopic Structure of the SiO2/Si Interface. *Phys. Rev. B* **1988**, *38* (9), 6084–6096. https://doi.org/10.1103/PhysRevB.38.6084.

(62) Generation, T. S.; Photoelectrolysis, W. *Light , Water , Hydrogen.*

(63) Dawood, F.; Anda, M.; Shafiullah, G. M. Hydrogen Production for Energy: An Overview. *Int. J. Hydrogen Energy* **2020**, *45* (7), 3847–3869. https://doi.org/10.1016/j.ijhydene.2019.12.059.

(64) The Future of Hydrogen. *Futur. Hydrog.* **2019**, No. June.

https://doi.org/10.1787/1e0514c4-en.

(65) Barelli, L.; Bidini, G.; Gallorini, F.; Servili, S. Hydrogen Production through Sorption-Enhanced Steam Methane Reforming and Membrane Technology: A Review. *Energy* **2008**, *33* (4), 554–570. https://doi.org/10.1016/j.energy.2007.10.018.

(66) Alqahtani, M. M. Photoelectrochemical Water Splitting for Hydrogen Production Using III-V Semiconductor Materials, 2019, Vol. 6.

(67) Adris, A. M.; Pruden, B. B.; Lim, C. J.; Grace, J. R. On the Reported Attempts to Radically Improve the Performance of the Steam Methane Reforming Reactor. *Can. J. Chem. Eng.* **1996**, *74* (2), 177–186. https://doi.org/10.1002/cjce.5450740202.

(68) Howarth, R. W.; Jacobson, M. Z. How Green Is Blue Hydrogen? *Energy Sci. Eng.* **2021**, *9* (10), 1676–1687. https://doi.org/10.1002/ese3.956.

(69) Noussan, M.; Raimondi, P. P.; Scita, R.; Hafner, M. The Role of Green and Blue Hydrogen in the Energy Transition—a Technological and Geopolitical Perspective. *Sustain.* **2021**, *13* (1), 1–26. https://doi.org/10.3390/su13010298.

(70) Hermesmann, M.; Müller, T. E. Green, Turquoise, Blue, or Grey? Environmentally Friendly Hydrogen Production in Transforming Energy Systems. *Prog. Energy Combust. Sci.* **2022**, *90* (October 2021), 100996. https://doi.org/10.1016/j.pecs.2022.100996.

(71) Diab, J.; Fulcheri, L.; Hessel, V.; Rohani, V.; Frenklach, M. Why Turquoise Hydrogen Will Be a Game Changer for the Energy Transition. *Int. J. Hydrogen Energy* **2022**, *47* (61), 25831–25848. https://doi.org/10.1016/j.ijhydene.2022.05.299.

(72) Pruvost, F.; Cloete, S.; Arnaiz del Pozo, C.; Zaabout, A. Blue, Green, and Turquoise Pathways for Minimizing Hydrogen Production Costs from Steam Methane Reforming with CO2 Capture. *Energy Convers. Manag.* **2022**, *274* (June), 116458. https://doi.org/10.1016/j.enconman.2022.116458.

(73) Ajanovic, A.; Sayer, M.; Haas, R. The Economics and the Environmental Benignity of Different Colors of Hydrogen. *Int. J. Hydrogen Energy* **2022**, *47* (57), 24136–24154. https://doi.org/10.1016/j.ijhydene.2022.02.094.

(74) Valencia, S.; Marín, J. M.; Restrepo, G. Study of the Bandgap of Synthesized Titanium Dioxide Nanoparticules Using the Sol-Gel Method and a Hydrothermal Treatment. *Open Mater. Sci. J.* **2010**, *4*, 9–14.

https://doi.org/10.2174/1874088X01004020009.

(75)   Newborough, M.; Cooley, G. Developments in the Global Hydrogen Market: The Spectrum of Hydrogen Colours. *Fuel Cells Bull.* **2020**, *2020* (11), 16–22. https://doi.org/10.1016/S1464-2859(20)30546-0.

(76)   Petrunin, V. V.; Marov, I. V.; Kodochigov, N. G. Hydrogen Energy and Large Scale Hydrogen Production with Nuclear Power Plants Based on High-Temperature Reactors. *J. Phys. Conf. Ser.* **2020**, *1683* (4). https://doi.org/10.1088/1742-6596/1683/4/042031.

(77)   Friederich, S.; Boudry, M. Ethics of Nuclear Energy in Times of Climate Change: Escaping the Collective Action Problem. *Philos. Technol.* **2022**, *35* (2), 1–27. https://doi.org/10.1007/s13347-022-00527-1.

(78)   Kermisch, C.; Taebi, B. Sustainability, Ethics and Nuclear Energy: Escaping the Dichotomy. *Sustain.* **2017**, *9* (3), 1–13. https://doi.org/10.3390/su9030446.

(79)   Naidu, L.; Moorthy, R. Ethics and Risks in Sustainable Civilian Nuclear Energy Development in Vietnam. *Ethics Sci. Environ. Polit.* **2022**, *22*, 1–12. https://doi.org/10.3354/esep00198.

(80)   Nuclear Power in a Clean Energy System. *Nucl. Power a Clean Energy Syst.* **2019**. https://doi.org/10.1787/fc5f4b7e-en.

(81)   Cozzi, L.; Arsalane, Y.; Mcglade, C.; Vass, T.; Crow, D. The Sustainable Development Scenario. **2019**, No. December.

(82)   Lewis, N. S.; Crabtree, G. *Basic Research Needs for Solar Energy Utilization*; 2005.

(83)   Walter, M. G.; Warren, E. L.; McKone, J. R.; Boettcher, S. W.; Mi, Q.; Santori, E. A.; Lewis, N. S. Solar Water Splitting Cells. *Chem. Rev.* **2010**, *110* (11), 6446–6473. https://doi.org/10.1021/cr1002326.

(84)   Mekhilef, S.; Saidur, R.; Safari, A. A Review on Solar Energy Use in Industries. *Renew. Sustain. Energy Rev.* **2020**, *15* (4), 1777–1790. https://doi.org/10.1016/j.rser.2010.12.018.

(85)   Kannan, N.; Vakeesan, D. Solar Energy for Future World : - A Review. **2016**, *62*, 1092–1105. https://doi.org/10.1016/j.rser.2016.05.022.

(86)   Yung, K.; Huin, H. Solar Energy-Powered Battery Electric Vehicle Charging Stations : Current Development and Future Prospect Review. **2022**, *169* (March).

https://doi.org/10.1016/j.rser.2022.112862.

(87)   Kammen, D. M. The Rise of Renewable Energy. *Sci. Am.* **2006**, *295* (3), 84–93.

(88)   Outlook, W. E. World Energy Outlook 2018. **2018**.

(89)   Mohsin, M.; Ishaq, T.; Bhatti, I. A.; Jilani, A.; Melaibari, A. A.; Abu-hamdeh, N. H. Semiconductor Nanomaterial Photocatalysts for Water-Splitting Hydrogen Production : The Holy Grail of Converting Solar Energy to Fuel. **2023**.

(90)   Nocera, D. G. Solar Fuels and Solar Chemicals Industry. **2017**, 21–24. https://doi.org/10.1021/acs.accounts.6b00615.

(91)   Currao, A. Photoelectrochemical Water Splitting. *Chimia (Aarau).* **2007**, *61* (12), 815–819. https://doi.org/10.2533/chimia.2007.815.

(92)   Zhebo Chen Eric Miller; Dinh, H. N. *Photoelectrochemcial Water Splitting Standards, Experimental Methods, and Protocols*; Springer, 2013.

(93)   Turner, J. A. A Realizable Renewable Energy Future. *Science (80-.).* **1999**, *285* (5428), 687–689. https://doi.org/10.1126/science.285.5428.687.

(94)   Taylor, R. A.; Ramasamy, K. Colloidal Quantum Dots Solar Cells. *SPR Nanosci.* **2017**, *4* (March), 142–168. https://doi.org/10.1039/9781782620358-00142.

(95)   FUJISHIMA, A.; HONDA, K. Electrochemical Photolysis of Water at a Semiconductor Electrode. *Nature* **1972**, *238* (5358), 37–38. https://doi.org/10.1038/238037a0.

(96)   Khaselev, O.; Turner, J. A. A Monolithic Photovoltaic-Photoelectrochemical Device for Hydrogen Production via Water Splitting Author (s): Oscar Khaselev and John A . Turner Published by : American Association for the Advancement of Science Stable URL : Http://Www.Jstor.Org/Stable/. *Science (80-.).* **2016**, *280* (5362), 425–427.

(97)   Brinkworth, B. J. Solar Energy. *Nature* **1974**, *249* (5459), 726–729. https://doi.org/10.1038/249726a0.

(98)   Jones, H. *Introduction to Solid State Physics by C. Kittel* ; 1957; Vol. 10. https://doi.org/10.1107/s0365110x57001280.

(99)   Song, H.; Luo, S.; Huang, H.; Deng, B.; Ye, J. Solar-Driven Hydrogen Production: Recent Advances, Challenges, and Future Perspectives. *ACS Energy Lett.* **2022**, *7* (3), 1043–1065. https://doi.org/10.1021/acsenergylett.1c02591.

(100) Moshinsky, M. *On Solar Hydrogen & Nanotechnology*; Vayssieres, L., Ed.; 2010; Vol. 13.

(101) Bard, A. J.; Fox, M. A. Artificial Photosynthesis: Solar Splitting of Water to Hydrogen and Oxygen. *Acc. Chem. Res.* **1995**, *28* (3), 141–145. https://doi.org/10.1021/ar00051a007.

(102) Scheuermann, A. G.; Prange, J. D.; Gunji, M.; Chidsey, C. E. D.; McIntyre, P. C. Effects of Catalyst Material and Atomic Layer Deposited TiO2 Oxide Thickness on the Water Oxidation Performance of Metal-Insulator-Silicon Anodes. *Energy Environ. Sci.* **2013**, *6* (8), 2487–2496. https://doi.org/10.1039/c3ee41178h.

(103) Scheuermann, A. G.; Lawrence, J. P.; Kemp, K. W.; Ito, T.; Walsh, A.; Chidsey, C. E. D.; Hurley, P. K.; McIntyre, P. C. Design Principles for Maximizing Photovoltage in Metal-Oxide-Protected Water-Splitting Photoanodes. *Nat. Mater.* **2016**, *15* (1), 99–105. https://doi.org/10.1038/nmat4451.

(104) Bronneberg, A. C.; Höhn, C.; Van De Krol, R. Probing the Interfacial Chemistry of Ultrathin ALD-Grown TiO2 Films: An In-Line XPS Study. *J. Phys. Chem. C* **2017**, *121* (10), 5531–5538. https://doi.org/10.1021/acs.jpcc.6b09468.

(105) O'Donnell, S.; Jose, F.; Shiel, K.; Snelgrove, M.; McFeely, C.; McGill, E.; O'Connor, R. Thermal and Plasma Enhanced Atomic Layer Deposition of Ultrathin TiO2on Silicon from Amide and Alkoxide Precursors: Growth Chemistry and Photoelectrochemical Performance. *J. Phys. D. Appl. Phys.* **2022**, *55* (8). https://doi.org/10.1088/1361-6463/ac360c.

(106) Satterthwaite, P. F.; Scheuermann, A. G.; Hurley, P. K.; Chidsey, C. E. D.; McIntyre, P. C. *Engineering Interfacial Silicon Dioxide for Improved Metal-Insulator-Semiconductor Silicon Photoanode Water Splitting Performance*; 2016; Vol. 8. https://doi.org/10.1021/acsami.6b03029.

(107) Met Eireann - The Irish Meteorological Service. Solar Radiation www.met.ie/science/valentia/solar-radiation.

(108) Cheng, C.; Zhang, W.; Chen, X.; Peng, S.; Li, Y. Strategies for Improving Photoelectrochemical Water Splitting Performance of Si-Based Electrodes. *Energy Sci. Eng.* **2022**, *10* (4), 1526–1543. https://doi.org/10.1002/ese3.1087.

(109) Kahn, A. Fermi Level, Work Function and Vacuum Level. *Mater. Horizons* **2016**, *3*

(1), 7–10. https://doi.org/10.1039/c5mh00160a.

(110) MOTT, N. F. The Theory of Crystal Rectifiers. **1995**, *1*, 153–165. https://doi.org/10.1142/9789812794086_0013.

(111) Mott, N. F. Note on the Contact between a Metal and an Insulator or Semi-Conductor. *Math. Proc. Cambridge Philos. Soc.* **1938**, *34* (4), 568–572. https://doi.org/10.1017/S0305004100020570.

(112) Schottky, W. Anm. Beg Der Korrektur. **1938**, *26* (8), 938.

(113) Schottky, W. Halbleitertheorie Der Sperrschicht. *Naturwissenschaften* **1938**, *26* (52), 843. https://doi.org/10.1007/BF01774216.

(114) Zhang, Z.; Yates, J. T. Band Bending in Semiconductors: Chemical and Physical Consequences at Surfaces and Interfaces. *Chem. Rev.* **2012**, *112* (10), 5520–5551. https://doi.org/10.1021/cr3000626.

(115) Gupta, S.; Kulbak, M.; Cahen, D. Pin-Hole-Free, Homogeneous, Pure CsPbBr3 Films on Flat Substrates by Simple Spin-Coating Modification. *Front. Energy Res.* **2020**, *8* (June), 1–6. https://doi.org/10.3389/fenrg.2020.00100.

(116) Qiu, Z.; Gong, H.; Zheng, G.; Yuan, S.; Zhang, H.; Zhu, X.; Zhou, H.; Cao, B. Enhanced Physical Properties of Pulsed Laser Deposited NiO Films via Annealing and Lithium Doping for Improving Perovskite Solar Cell Efficiency. *J. Mater. Chem. C* **2017**, *5* (28), 7084–7094. https://doi.org/10.1039/c7tc01224a.

(117) Chen, H. L.; Lu, Y. M.; Hwang, W. S. Characterization of Sputtered NiO Thin Films. *Surf. Coatings Technol.* **2005**, *198* (1-3 SPEC. ISS.), 138–142. https://doi.org/10.1016/j.surfcoat.2004.10.032.

(118) Zorkipli, N. N. M.; Kaus, N. H. M.; Mohamad, A. A. Synthesis of NiO Nanoparticles through Sol-Gel Method. *Procedia Chem.* **2016**, *19*, 626–631. https://doi.org/10.1016/j.proche.2016.03.062.

(119) Chen, K.-T.; Hsu, C.-H.; Ren, F.-B.; Wang, C.; Gao, P.; Wu, W.-Y.; Lien, S.-Y.; Zhu, W.-Z. Influence of Annealing Temperature of Nickel Oxide as Hole Transport Layer Applied for Inverted Perovskite Solar Cells. *J. Vac. Sci. Technol. A* **2021**, *39* (6), 062401. https://doi.org/10.1116/6.0001191.

(120) Park, B.; Na, S. Y.; Bae, I. G. Uniform and Bright Light Emission from a 3D Organic Light-Emitting Device Fabricated on a Bi-Convex Lens by a Vortex-Flow-Assisted

Solution-Coating Method. *Sci. Rep.* **2019**, *9* (1), 1–10. https://doi.org/10.1038/s41598-019-54820-9.

(121) Camacho-Espinosa, E.; Oliva-Avilés, A. I.; Oliva, A. I. Effect of the Substrate Cleaning Process on Pinhole Formation in Sputtered CdTe Films. *J. Mater. Eng. Perform.* **2017**, *26* (8), 4020–4028. https://doi.org/10.1007/s11665-017-2842-0.

(122) Cremers, V.; Puurunen, R. L.; Dendooven, J. Conformality in Atomic Layer Deposition: Current Status Overview of Analysis and Modelling. *Appl. Phys. Rev.* **2019**, *6* (2). https://doi.org/10.1063/1.5060967.

(123) Snelgrove, M.; McFeely, C.; Mani-Gonzalez, P. G.; Lahtonen, K.; Lundy, R.; Hughes, G.; Valden, M.; McGlynn, E.; Yadav, P.; Saari, J.; Morris, M. A.; O'Connor, R. Aluminium Oxide Formation via Atomic Layer Deposition Using a Polymer Brush Mediated Selective Infiltration Approach. *Appl. Surf. Sci.* **2020**, *515* (March), 145987. https://doi.org/10.1016/j.apsusc.2020.145987.

(124) George, S. M. Atomic Layer Deposition: An Overview. *Chem. Rev.* **2010**, *110* (1), 111–131. https://doi.org/10.1021/cr900056b.

(125) Kim, H.; Lee, H.-B.-R.; Maeng, W.-J. Applications of Atomic Layer Deposition to Nanofabrication and Emerging Nanodevices. *Thin Solid Films* **2009**, *517* (8), 2563–2580. https://doi.org/10.1016/j.tsf.2008.09.007.

(126) Johnson, R. W.; Hultqvist, A.; Bent, S. F. A Brief Review of Atomic Layer Deposition: From Fundamentals to Applications. *Mater. Today* **2014**, *17* (5), 236–246. https://doi.org/10.1016/j.mattod.2014.04.026.

(127) Dandley, E. C.; Taylor, A. J.; Duke, K. S.; Ihrie, M. D.; Shipkowski, K. A.; Parsons, G. N.; Bonner, J. C. Atomic Layer Deposition Coating of Carbon Nanotubes with Zinc Oxide Causes Acute Phase Immune Responses in Human Monocytes in Vitro and in Mice after Pulmonary Exposure. *Part. Fibre Toxicol.* **2016**, *13* (1), 1–17. https://doi.org/10.1186/s12989-016-0141-9.

(128) Herrmann, C. F.; Fabreguette, F. H.; Finch, D. S.; Geiss, R.; George, S. M. Multilayer and Functional Coatings on Carbon Nanotubes Using Atomic Layer Deposition. *Appl. Phys. Lett.* **2005**, *87* (12), 1–3. https://doi.org/10.1063/1.2053358.

(129) Justh, N.; Firkala, T.; László, K.; Lábár, J.; Szilágyi, I. M. Photocatalytic C 60 - Amorphous TiO 2 Composites Prepared by Atomic Layer Deposition. *Appl. Surf. Sci.*

2017, *419*, 497–502. https://doi.org/10.1016/j.apsusc.2017.04.243.

(130) Akter, T.; Bagheriasl, R.; Caballero, F. .; Edmonds, D. .; Friebe, H.; Garcia-Mateo, C.; Haider, J.; Hallfeldt, T.; Hashmi, M. S. .; Hotz, W.; Keller, S.; Kurukuri, S.; Kuwabara, T.; Lance, M. .; Leppin, C.; Lucon, E.; Matlock, D. .; Militzer, M.; Muller, R.; Plummer, C. J. .; Rahman, M.; Schajer, G. .; Speer, J. .; Stoughton, T. .; Tari, D. .; Till, E. .; Van Tyne, C. .; Vegter, H.; Vucetic, M.; Wang, L.; Watkins, T. .; Worswick, M. .; Yoon, J. . *COMPREHENSIVE MATERIALS PROCESSING*; Hashimi, S., Batalha, F. G., Van Tyne, C. J., Yilbas, B., Eds.

(131) Transactions, E. C. S.; Society, T. E. Industrial Applications of Atomic Layer Deposition. *ECS Trans.* **2009**, *25* (8), 641–652.

(132) Li, M.; Jin, Z. X.; Zhang, W.; Bai, Y. H.; Cao, Y. Q.; Li, W. M.; Wu, D.; Li, A. D. Comparison of Chemical Stability and Corrosion Resistance of Group IV Metal Oxide Films Formed by Thermal and Plasma-Enhanced Atomic Layer Deposition. *Sci. Rep.* **2019**, *9* (1), 1–12. https://doi.org/10.1038/s41598-019-47049-z.

(133) Profijt, H. B.; Potts, S. E.; van de Sanden, M. C. M.; Kessels, W. M. M. Plasma-Assisted Atomic Layer Deposition: Basics, Opportunities, and Challenges. *J. Vac. Sci. Technol. A Vacuum, Surfaces, Film.* **2011**, *29* (5), 050801. https://doi.org/10.1116/1.3609974.

(134) Koo, J.; Kim, Y.; Jeon, H. ZrO2 Gate Dielectric Deposited by Plasma-Enhanced Atomic Layer Deposition Method. *Japanese J. Appl. Physics, Part 1 Regul. Pap. Short Notes Rev. Pap.* **2002**, *41* (5 A), 3043–3046. https://doi.org/10.1143/jjap.41.3043.

(135) Qu, C.; Sakiyama, Y.; Agarwal, P.; Kushner, M. J. Plasma-Enhanced Atomic Layer Deposition of SiO 2 Film Using Capacitively Coupled Ar/O 2 Plasmas: A Computational Investigation . *J. Vac. Sci. Technol. A* **2021**, *39* (5), 052403. https://doi.org/10.1116/6.0001121.

(136) Boris, D. R.; Wheeler, V. D.; Nepal, N.; Qadri, S. B.; Walton, S. G.; Eddy, C. (Chip) R. The Role of Plasma in Plasma-Enhanced Atomic Layer Deposition of Crystalline Films. *J. Vac. Sci. Technol. A* **2020**, *38* (4), 040801. https://doi.org/10.1116/6.0000145.

(137) Puurunen, R. L. Surface Chemistry of Atomic Layer Deposition: A Case Study for the

Trimethylaluminum/Water Process. *J. Appl. Phys.* **2005**, *97* (12). https://doi.org/10.1063/1.1940727.

(138) Ji, Y. J.; Kim, K. S.; Kim, K. H.; Byun, J. Y.; Yeom, G. Y. A Brief Review of Plasma Enhanced Atomic Layer Deposition of Si3N4. *Appl. Sci. Converg. Technol.* **2019**, *28* (5), 142–147. https://doi.org/10.5757/ASCT.2019.28.5.142.

(139) Elam, J. W.; Routkevitch, D.; Mardilovich, P. P.; George, S. M. Conformal Coating on Ultrahigh-Aspect-Ratio Nanopores of Anodic Alumina by Atomic Layer Deposition. *Chem. Mater.* **2003**, *15* (18), 3507–3517. https://doi.org/10.1021/cm0303080.

(140) Dufond, M. E.; Diouf, M. W.; Badie, C.; Laffon, C.; Parent, P.; Ferry, D.; Grosso, D.; Kools, J. C. S.; Elliott, S. D.; Santinacci, L. Quantifying the Extent of Ligand Incorporation and the Effect on Properties of TiO2 Thin Films Grown by Atomic Layer Deposition Using an Alkoxide or an Alkylamide. *Chem. Mater.* **2020**, *32* (4), 1393–1407. https://doi.org/10.1021/acs.chemmater.9b03621.

(141) Musschoot, J.; Xie, Q.; Deduytsche, D.; Van den Berghe, S.; Van Meirhaeghe, R. L.; Detavernier, C. Atomic Layer Deposition of Titanium Nitride from TDMAT Precursor. *Microelectron. Eng.* **2009**, *86* (1), 72–77. https://doi.org/10.1016/j.mee.2008.09.036.

(142) Hornsveld, N.; Put, B.; Kessels, W. M. M.; Vereecken, P. M.; Creatore, M. Plasma-Assisted and Thermal Atomic Layer Deposition of Electrochemically Active Li2CO3. *RSC Adv.* **2017**, *7* (66), 41359–41368. https://doi.org/10.1039/c7ra07722j.

(143) Kim, D.-H.; Kim, Y. J.; Song, Y. S.; Lee, B.-T.; Kim, J. H.; Suh, S.; Gordon, R. Characteristics of Tungsten Carbide Films Prepared by Plasma-Assisted ALD Using Bis(Tert-Butylimido)Bis(Dimethylamido)Tungsten. *J. Electrochem. Soc.* **2003**, *150* (10), C740. https://doi.org/10.1149/1.1610000.

(144) Kim, K. M.; Jang, J. S.; Yoon, S. G.; Yun, J. Y.; Chung, N. K. Structural, Optical and Electrical Properties of HfO2 Thin Films Deposited at Low-Temperature Using Plasma-Enhanced Atomic Layer Deposition. *Materials (Basel).* **2020**, *13* (9). https://doi.org/10.3390/MA13092008.

(145) Kwon, O.-K.; Kwon, S.-H.; Park, H.-S.; Kang, S.-W. PEALD of a Ruthenium Adhesion Layer for Copper Interconnects. *J. Electrochem. Soc.* **2004**, *151* (12), C753.

https://doi.org/10.1149/1.1809576.

(146) Ding, S. F.; Xie, Q.; Chen, F.; Lu, H. S.; Deng, S. R.; Deduytsche, D.; Detavernier, C.; Qu, X. P. Improved Thermal Stability and Electrical Performance by Using PEALD Ultrathin Al2O3 Film with Ta as Cu Diffusion Barrier on Low k Dielectrics. *ECS Solid State Lett.* **2012**, *1* (3), 98–100. https://doi.org/10.1149/2.006203ssl.

(147) Kim, H. J. K.; Kaplan, K. E.; Schindler, P.; Xu, S.; Winterkorn, M. M.; Heinz, D. B.; English, T. S.; Provine, J.; Prinz, F. B.; Kenny, T. W. Electrical Properties of Ultrathin Platinum Films by Plasma-Enhanced Atomic Layer Deposition. *ACS Appl. Mater. Interfaces* **2019**, *11* (9), 9594–9599. https://doi.org/10.1021/acsami.8b21054.

(148) Zhu, Z.; Sippola, P.; Lipsanen, H.; Savin, H.; Merdes, S. Influence of Plasma Parameters on the Properties of Ultrathin Al2O3 Films Prepared by Plasma Enhanced Atomic Layer Deposition below 100 °c for Moisture Barrier Applications. *Jpn. J. Appl. Phys.* **2018**, *57* (12), 2–8. https://doi.org/10.7567/JJAP.57.125502.

(149) Ni, M.; Leung, M. K. H.; Leung, D. Y. C.; Sumathy, K. A Review and Recent Developments in Photocatalytic Water-Splitting Using TiO2 for Hydrogen Production. *Renew. Sustain. Energy Rev.* **2007**, *11* (3), 401–425. https://doi.org/10.1016/j.rser.2005.01.009.

(150) Lee, K.; Mazare, A.; Schmuki, P. One-Dimensional Titanium Dioxide Nanomaterials: Nanotubes. *Chem. Rev.* **2014**, *114* (19), 9385–9454. https://doi.org/10.1021/cr500061m.

(151) Chen, S.; Thind, S. S.; Chen, A. Nanostructured Materials for Water Splitting - State of the Art and Future Needs: A Mini-Review. *Electrochem. commun.* **2016**, *63*, 10–17. https://doi.org/10.1016/j.elecom.2015.12.003.

(152) Hoang, S.; Guo, S.; Hahn, N. T.; Bard, A. J.; Mullins, C. B. Visible Light Driven Photoelectrochemical Water Oxidation on Nitrogen-Modified TiO 2 Nanowires. *Nano Lett.* **2012**, *12* (1), 26–32. https://doi.org/10.1021/nl2028188.

(153) Shankar, K.; Basham, J. I.; Allam, N. K.; Varghese, O. K.; Mor, G. K.; Feng, X.; Paulose, M.; Seabold, J. A.; Choi, K. S.; Grimes, C. A. Recent Advances In the Use of TiO 2 Nanotube and Nanowire Arrays for Oxidative Photoelectrochemistry. *J. Phys. Chem. C* **2009**, *113* (16), 6327–6359. https://doi.org/10.1021/jp809385x.

(154) Cho, I. S.; Choi, J.; Zhang, K.; Kim, S. J.; Jeong, M. J.; Cai, L.; Park, T.; Zheng, X.;

Park, J. H. Highly Efficient Solar Water Splitting from Transferred TiO2 Nanotube Arrays. *Nano Lett.* **2015**, *15* (9), 5709–5715. https://doi.org/10.1021/acs.nanolett.5b01406.

(155) Amano, F.; Tian, M.; Wu, G.; Ohtani, B.; Chen, A. Facile Preparation of Platelike Tungsten Oxide Thin Film Electrodes with High Photoelectrode Activity. *ACS Appl. Mater. Interfaces* **2011**, *3* (10), 4047–4052. https://doi.org/10.1021/am200897n.

(156) Thind, S. S.; Tian, M.; Chen, A. Direct Growth and Photo-Electrochemical Study of WO3 Nanostructured Materials. *Electrochem. commun.* **2014**, *43*, 13–17. https://doi.org/10.1016/j.elecom.2014.03.002.

(157) Seabold, J. A.; Choi, K. S. Effect of a Cobalt-Based Oxygen Evolution Catalyst on the Stability and the Selectivity of Photo-Oxidation Reactions of a WO3 Photoanode. *Chem. Mater.* **2011**, *23* (5), 1105–1112. https://doi.org/10.1021/cm1019469.

(158) Boettcher, S. W.; Warren, E. L.; Putnam, M. C.; Santori, E. A.; Turner-Evans, D.; Kelzenberg, M. D.; Walter, M. G.; McKone, J. R.; Brunschwig, B. S.; Atwater, H. A.; Lewis, N. S. Photoelectrochemical Hydrogen Evolution Using Si Microwire Arrays. *J. Am. Chem. Soc.* **2011**, *133* (5), 1216–1219. https://doi.org/10.1021/ja108801m.

(159) Ding, Q.; Meng, F.; English, C. R.; Cabán-Acevedo, M.; Shearer, M. J.; Liang, D.; Daniel, A. S.; Hamers, R. J.; Jin, S. Efficient Photoelectrochemical Hydrogen Generation Using Heterostructures of Si and Chemically Exfoliated Metallic MoS2. *J. Am. Chem. Soc.* **2014**, *136* (24), 8504–8507. https://doi.org/10.1021/ja5025673.

(160) Shaner, M. R.; McKone, J. R.; Gray, H. B.; Lewis, N. S. Functional Integration of Ni-Mo Electrocatalysts with Si Microwire Array Photocathodes to Simultaneously Achieve High Fill Factors and Light-Limited Photocurrent Densities for Solar-Driven Hydrogen Evolution. *Energy Environ. Sci.* **2015**, *8* (10), 2977–2984. https://doi.org/10.1039/c5ee01076d.

(161) Morales-Guio, C. G.; Tilley, S. D.; Vrubel, H.; Graïzel, M.; Hu, X. Hydrogen Evolution from a Copper(I) Oxide Photocathode Coated with an Amorphous Molybdenum Sulphide Catalyst. *Nat. Commun.* **2014**, *5* (I), 1–7. https://doi.org/10.1038/ncomms4059.

(162) Paracchino, A.; Laporte, V.; Sivula, K.; Grätzel, M.; Thimsen, E. Highly Active Oxide Photocathode for Photoelectrochemical Water Reduction. *Nat. Mater.* **2011**, *10* (6),

456–461. https://doi.org/10.1038/nmat3017.

(163) Liu, R.; Zheng, Z.; Spurgeon, J.; Yang, X. Enhanced Photoelectrochemical Water-Splitting Performance of Semiconductors by Surface Passivation Layers, 2014, Vol. 7. https://doi.org/10.1039/c4ee00450g.

(164) Liu, T.; Cai, S.; Mei, Z.; Zhao, G.; Xu, L.; An, Q.; Fu, Y.; Wang, H.; Li, M.; Guo, H. Boosting the Water Splitting Activity of Cobalt Nitride through Morphological Design: A Comparison of the Influence of Structure on the Hydrogen and Oxygen Evolution Reactions. *Sustain. Energy Fuels* **2021**, *5* (14), 3632–3639. https://doi.org/10.1039/D1SE00616A.

2 Experimental Techniques

Once deposited, ALD protective films were subjected to a range of characterisation techniques to perform analysis to gain an insight into their chemistry and performance. This chapter outlines the theoretical principles of each technique applied.

Being that films under investigation were thin, or ultrathin, and coupled with the importance of surface interactions on the overall experimental results, the primary form of characterisation was the photoemission technique called x-ray photoelectron spectroscopy (XPS). XPS is a valuable tool which provides a great deal of chemical information on thin films including elemental composition and chemical bonding as well as depth profiling in some instances. For analysis deeper into the bulk of a sample of interest, hard x-ray photoelectron spectroscopy (HAXPES) was used and offers further insights into the nature and quality of ALD grown films. XPS was paired with additional characterisation techniques such as Fourier transform infrared spectroscopy (FTIR) which offered additional insight into chemical bonding.

Film thicknesses were closely monitored during deposition using the Thickogram which is a simple graphical and mathematical method of film thickness determination using XPS peak ratios [1]. This method allowed for in-situ monitoring of ALD depositions and was verified using ex-situ ellipsometry. Atomic force microscopy (AFM) was utilized to assess the surface roughness of deposited films as well as to verify homogenous growth.

Once deposited and analyzed, films were subjected to electrical measurements in simulated real-world conditions such as to ascertain the effectiveness of applied protective films. Electrical measurements consisted of chronoamperometry (CA) and cyclic voltammetry (IV) stress testing with the aim of observing enhanced chemical stability or photocurrent output.

2.1 Atomic Layer Deposition System

The deposition system utilized within this study is an Oxford Instruments FlexAl II coupled via robotic vacuum transfer to the Scienta Omicron monochromated x-ray photoelectron spectroscopy (XPS) system. The FlexAl is a versatile process station which is capable of depositing a wide range of precursor materials and automatically transfers wafers between the deposition chamber, transfer station and analysis stations. This system has the ability to perform plasma enhanced (PEALD) or the conventional thermally enhanced (TALD) processes. The basic principle of operation of the FlexAl II deposition system is detailed in Figure 2.1
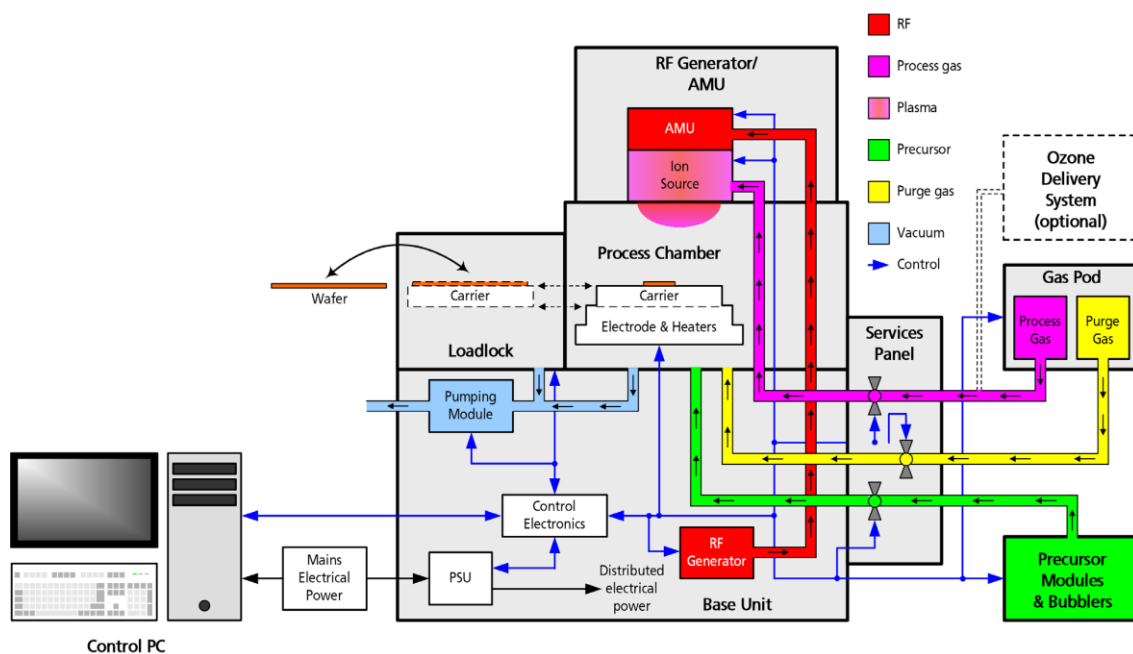
Figure 2.1 Principle of operation of the FlexAl II atomic layer deposition system [2]*.*

The basic operation of a typical ALD deposition begins with the fitting of the required precursor bottle within the precursor cabinet using the manufacturer supplied detachable

glove box for safe material handling. The operator can then select the required ALD recipe using the desired precursor material using the control PC. A full sized 4 inch deposition wafer or series of samples upon a carrier wafer are placed inside the loadlock which is then evacuated. The tool then automatically takes the wafer from the loadlock through the vacuum hex handler to the process chamber to undergo deposition. The tool evacuates the process chamber and readies for either PEALD or TALD depending on the operator recipe selection before proceeding with the deposition. Once the process is complete the tool purges the chamber before the tool transfers the wafer to either another process station, analysis chamber or back to the loadlock. If the wafer is to be removed from the system, the operator then vents the load lock and manually removes the now processed wafer.

2.1.1 Thermal Atomic Layer Deposition (TALD) Process

As noted above the FlexAL II system used within this work is capable of deposition via both the conventional TALD or PEALD regimes. During TALD the deposition is carried out through the repeated exposure of the substrate or samples to two precursors sequentially admitting one following the other until a desired number of ALD cycles is completed. The key within ALD versus the alternative CVD is that the precursor materials used never mix directly within gas phase. The substrate and samples are heated to provide the correct conditions for the reaction to proceed. A basic schematic of the TALD configuration is shown in Figure 2.2
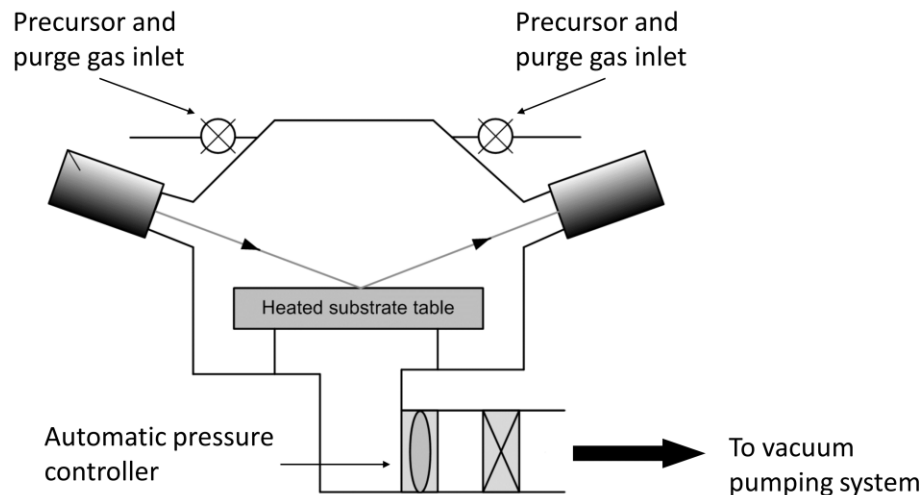
Figure 2.2 FlexAl II process chamber during TALD depositions [2].

A typical TALD process consists of four basic steps beginning with flowing the first precursor into the chamber which deposits a monolayer of intermediate material on the substrate material. This is followed by a purge of the unreacted precursor material as well as any reaction byproducts. The second precursor is then admitted to the process chamber which reacts with the existing monolayer deposited by the first precursor thus forming the required film. The chamber is purged again after this second precursor to again remove unreacted material and reaction byproducts. Each ALD cycle deposits an atomic monolayer of the desired film material with increasing the number of cycles acting to increase the thickness of the desired material and film one layer at a time.

2.1.2 Plasma Enhanced Atomic Layer Deposition (PEALD) Process

In addition to the conventional TALD deposition process, the FlexAl II system is also equipped in this case to deposit via the plasma enhanced regime following the same basic

principles of the TALD counterpart of the sequential admittance of the two precursors one

after another depositing monolayer by monolayer. Figure 2.3 shows a simplified schematic

of the process chamber equipped with the PEALD components where it is shown that

precursors and purge gas can flow into the chamber via two inlets with gas also able to be

admitted at the top of the inductively coupled plasma (ICP) source [2].
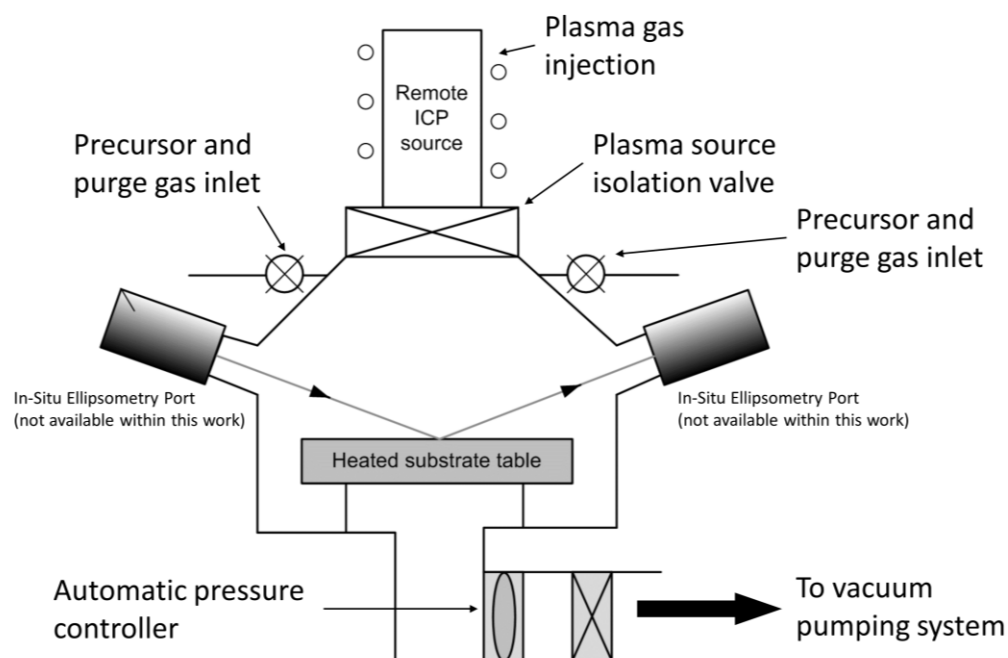
Figure 2.3 FlexAl II process chamber during PEALD depositions [2].

The PEALD process is not too dissimilar form that of the TALD regime and begins with

flowing the first precursor material into the process chamber which deposits a monolayer of

material on the substrate surface before the chamber is purged to remove unreacted material

and reaction byproducts. The second precursor is admitted into the plasma source to produce

a precursor species which reacts with the monolayer deposited by the first precursor thus

forming the required ALD film. The process chamber is then purged following this second precursor admittance before the process repeats for a user defined number of cycles corresponding to a desired film thickness.

2.1.3 Process Chamber
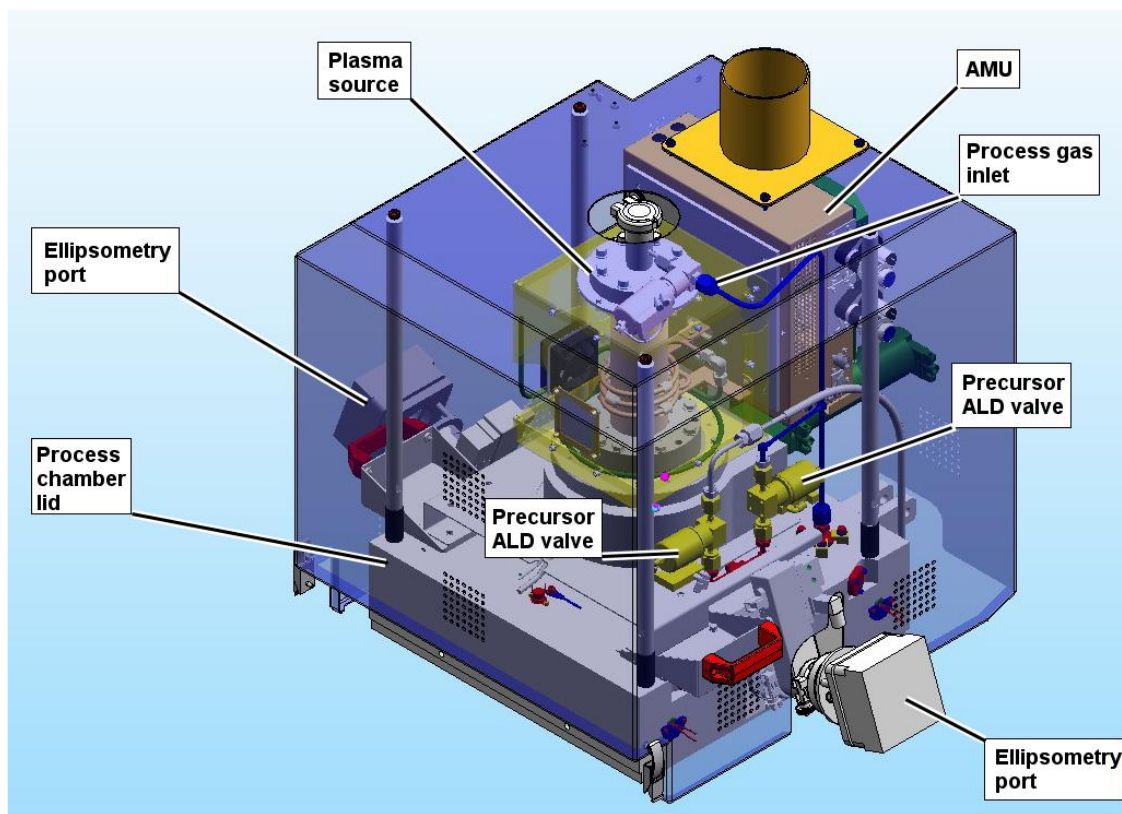
Figure 2.4 Process chamber and key components [2].

The schematic above in Figure 2.4 gives an overview of the FlexAl II process chamber showing the precursor inlet ports for the delivery of the precursor material during depositions, the 100 mm pumping port for the extraction of gases from the deposition process and the wafer transfer slot which is a pneumatically operated slit valve allow for the insertion of the wafers to the chamber. Also shown is the plasma source which creates the plasma from the RF power and process gas, the gate valve used to obstruct flow of the precursor during a

plasma or process step to avoid coating the ICP tube with precursor and the automatic matching unit (AMU). The FlexAl II within this work incorporates a low power AMU which is a vane type using air cooled impedance-matching capacitors and is rated for 300 W [2]. Ellipsometry ports are also included on the FlexAl II for the integration of in-situ ellipsometry which was unavailable during this work.

Shown below in Figure 2.5 is the lower electrode of the process chamber which is a disc of 240 mm on which the wafer is placed during depositions. The lower electrode can be heated electrically to a temperature of 400 °C or higher for the enhancement of deposition efficiency [2]. The electrode temperature is controlled via programmable logic controller (PLC) with the lower electrode also being electrically grounded. The wafer lift mechanism highlighted in Figure 2.5 is responsible for raising the wafer by 15 mm above the process chamber table in order to create space for the robotic transfer handler arm to move in below the wafer before the pneumatically actuated wafer lift mechanism lowers the wafer onto the robotic arm.
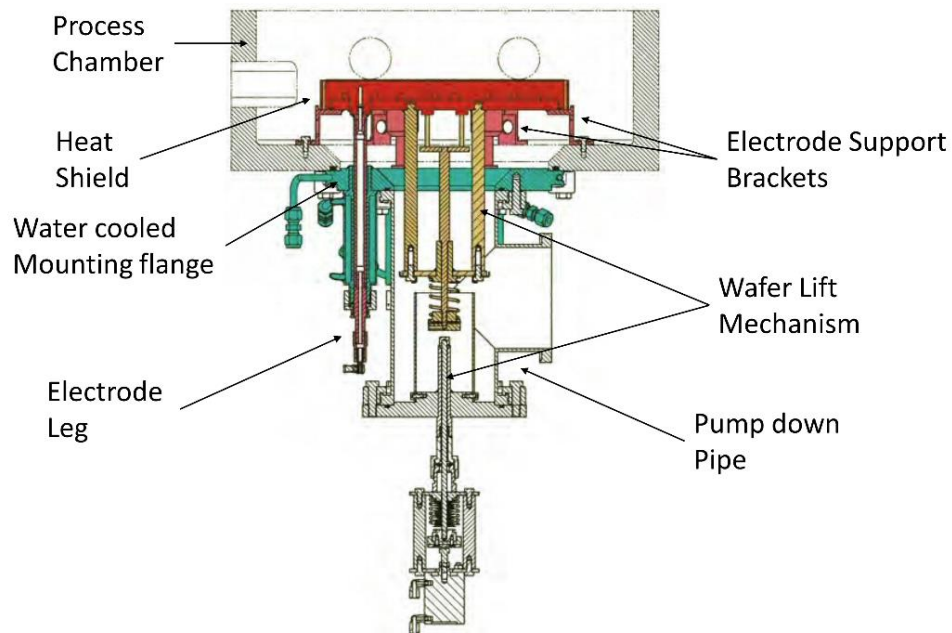
Figure 2.5 Lower electrode of the process chamber [2].

2.1.4 ICP Plasma Source and RF Generator

For purposes of PEALD the FlexAl II is equipped with an RF generator which produces a 13.56 MHz output which is fed via the automatch to the driven electrode which creates the plasma. The automatch is responsible for adjusting the impedance of its output as well as the impedance of the lower electrode to ensure maximum power transfer. The ICP 65 inductively coupled plasma (ICP) is shown in Figure 2.6 and has a maximum power output of 300 W. The tool manufacturer states typical process operating ranges for the ICP source with a total gas flow range from 10 – 200 sccm and the typical pressure range stated is 1 – 60 mTorr [2]. The RF generated power is fed via the AMU to the RF coil of the plasma source as shown in Figure 2.6. This results in the formation of the plasma in the insulating tube of the source which is held under vacuum. The process gas is supplied to the top of the insulating tube as well as to the gas ring in the process chamber also shown in Figure 2.6. There is a screening box which includes a NW40 pumping port for the extraction of generated ozone.
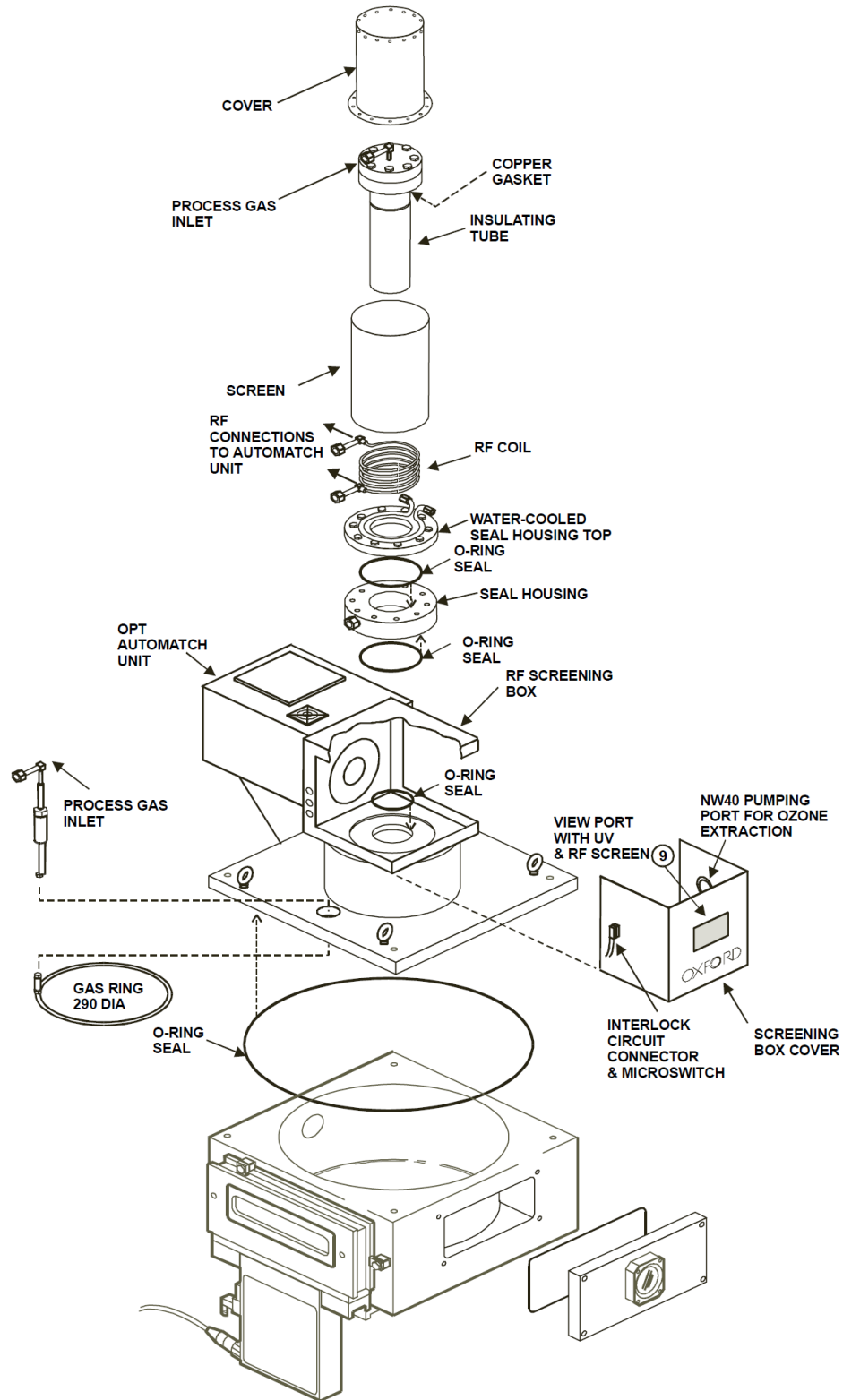
Figure 2.6 Exploded schematic of the Oxford Instruments Plasma Technology (OIPT) ICP 65 plasma source used within this work [2].

2.2 X-ray Photoelectron Spectroscopy

2.2.1 Overview

X-ray photoelectron spectroscopy (XPS) which has its roots in electron spectroscopy for chemical analysis (ESCA) is a long established highly surface sensitive characterisation technique providing a range of chemical information on solid materials. Being that XPS is highly dependent on the mean free path of photoelectrons, this technique is sensitive to the top $8 - 10$nm of the surface region of a given material, given the energy range of the electrons involved.

XPS, also known as photoemission spectroscopy, is essentially the energy analysis of photoexcited electrons of sufficient energy to escape the surface of a solid. XPS is a powerful characterisation technique which is capable of providing information on the presence of various elements at a sample surface, the states each of these elements occupy, the quantity of each element, crystal band structure, bonding occurring between surface atoms and adsorbed molecules and the three-dimensional spatial distribution [3]. Furthermore, when looking to films as is the focus of this study, information on the film thickness and uniformity of thickness and chemical composition can be established.

XPS is based on the fundamental concept of the photoelectric effect which involves the emission of electrons from a material under photon radiation of sufficient energy. This was first discovered by Heinrich Hertz in 1887 when he observed the emission of electrons from a surface due to exposure to irradiance [4,5]. The concept was more formally described in 1905 by Albert Einstein for which he was awarded the Nobel prize in physics in 1921 [4]. It was Kai Siegbahn that carried out the bulk of the work which developed XPS as the technique it

is today for which he was awarded the Nobel prize in 1981 for his efforts in high resolution electron spectroscopy which was referred to as ESCA initially [4].

The incoming photon energy acts to ionize an atom through promoting the removal of a free electron of kinetic energy K_E. When an x-ray of a known energy of hv interacts with an atom a photoelectron may be emitted as per the photoelectric effect and its kinetic energy is dependent on the core level from which it originated, and how strongly bound that electron is known as the binding energy B_E. the binding energy may be regarded as the difference in energy between the initial and final states following the ejection of a photoelectron.

The relationship between the incoming photon energy, binding and kinetic energy is described using Eq 2.1

$$E_B = hv - E_K - \Phi_{sp} \tag{2.1}$$

where Φ_{sp} is the spectrometer work function and hv is the photon energy as the product of Planck's constant times the frequency of the incoming photon. All of the quantities on the right side of Eq 2.1 are known or measurable leaving the calculation of the binding energy to be trivial [3]. The most common x-rays used in conventional XPS setups are Mg Kα (1253.6 eV) and Al Kα (1486.6 eV)

2.2.2 Technical Details

2.2.2.1 Theoretical Basics

Through measuring the kinetic energy of photoelectrons emitted due to irradiation of monoenergetic soft x-rays of a known energy, Eq 2.1 allows for the determination of the binding energy of the core level from which the electron originated. Thus, the kinetic energy of the emitted electron is directly proportional to their binding energy. All electrons within an atom have a distinct binding energy associated with it which is determined by various

mechanisms. It is this discrete binding energy of every energy level of every element which allows for the determination of the elemental compositions of a sample by comparing against binding energies of known spectra. The primary effect in determining binding energy is the core level it is located in within the atom which specifies its proximity to the nucleus . As seen in Figure 2.7 the *1s* shell is closer to the atomic nucleus than the *2p* shells. For example, a nickel sample irradiated by a Mg Kα (1253.6 eV) source will exhibit binding energy spectral peaks at 1009 eV and 853 eV for the *2s* and *2p$_{3/2}$* components respectively [6,7]. This illustrates that the *2s* requires additional incoming energy compared to the *2p* to liberate it from its core level in close proximity to the nucleus.

This is due to the effective nuclear charge experienced by an electron which is the amount of positive nuclear charge experience by a given electron in a multi electron atom – the strength of electrostatic attraction between a nucleus and orbiting electrons [8]. It is referred to as effective charge as all electrons within the atom present a shielding effect of inner electrons preventing outer electrons from experiencing the full nuclear charge of the nucleus. The resulting effective nuclear charge is dependent on various factors including the nuclear charge, atom size and the screening effect of inner shell electrons.

Binding energy is also intrinsically linked to the atom from which the electron originated with, for example, the Ni *2p$_{3/2}$* binding energy of 853 eV being greater than that of the Ti *2p$_{3/2}$* at 454 eV as a result of their atomic numbers of 28 amu and 22 amu respectively.
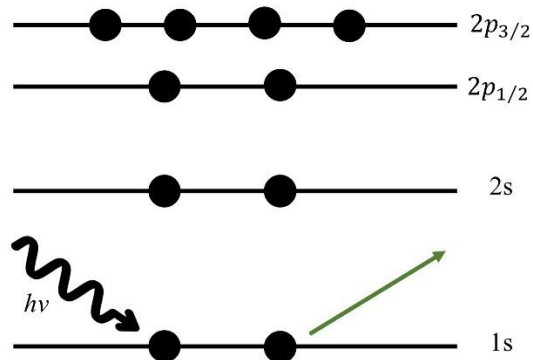
Figure 2.7 Basic principle of XPS showing the photoelectric effect and the emission of a photoelectron as a result of incoming x-ray radiation.

Therefore, XPS can provide a detailed analysis of the elements present within a sample as well as additional chemical information such as bonding. Through measuring the kinetic energy of emitted photoelectrons, converting to binding energy and referring to available databases one can determine elemental composition of a sample with the inclusion of a so-called relative sensitivity factor (RSF) in the calculation to account for sensitivity due to electron scattering.

During XPS measurement, there is likely to be chemical shifting present as a result of the binding energy of an electron within an atom being affected by its chemical environment and can provide valuable information about the chemical state of atoms within a sample. Among the most widely studied and commonly referenced spectral lines within the field of XPS is that of the Si *2p* doublet peak. Silicon atoms in covalent bonds with neighbouring silicon atoms in a crystal exhibit a binding energy of 99.4 eV [9]. This binding energy changes once the Si atoms begin bonding with other elements present in a sample, for example oxygen.

The binding energy of the Si *2p* core level for Si atoms bonded to oxygen as would be expected in SiO_2 is 103.5 eV [10]. In a Si-Si crystal the electrons are shared equally with the addition of oxygen causing a shift in the electron density from the Si atom towards the O atom resulting in a reduction of the kinetic energy and as per Eq 2.1 an increase in the binding energy. The electronegativity of oxygen is higher than that of silicon meaning it attracts more electrons compared to the Si atom due to its valence shell being less occupied. Electronegativity is a measure of the tendency of an atom to attract electrons towards itself via chemical bonding describing the strength if electron attraction [11]. Introduced by Linus Pauling in 1932 and measured on the Pauling scale with a numerical value assigned to each element based on its relative attraction for electrons [12]. This Si-O example illustrates the dependence of binding energy on the chemical environment – the dependence being termed "chemical shift".

2.2.2.2 Experimental Setup

As will be discussed in more detail later, the mean free path of emitted photoelectrons is crucial in order to ensure a sufficient quantity of those ejected are available for detection by the spectrometer. Therefore, XPS requires low pressure environments of at least high vacuum (HV) to operate satisfactorily in the region of 1×10^{-8} mbar or better such as to allow the electron transit from sample to detector with a low scattering probability. There are some exceptions to this rule with a new method of ambient pressure photoelectron spectroscopy (AP-XPS) becoming more common [13,14]. While not implemented within this study, AP-XPS is an interesting and valuable derivative of conventional XPS which enables photoemission studies of samples not suited to HV environments such as liquids with its original concept being developed by Hans and Kai Siegbahn [15–18]. AP-XPS involves placing

the sample in an elevated pressure enclosure with the x-ray source and electron energy analyser isolated due to their requirement of UHV for safe and effective operation [19]. The x-ray source is housed in UHV with the x-rays being transmitted to the sample via x-ray transparent window. The photoelectrons are directed through a small aperture to the differentially pumper analyser which isolates it from the elevated pressure environment of the sample.

An additional importance of the HV requirement of conventional XPS relates to the possibility for sample contamination due to atoms found in ambient air such as N, H, O and C which readily interact and form chemical bonds upon reaching a samples surface which can act to alter the chemical makeup of a given sample thus providing misguiding information. As it is desirable to extract information about the uncontaminated sample it is vital to ensure these contaminant atoms are not present within the XPS chamber through pumping to a sufficiently high vacuum. XPS equipment often requires HV in order to operate, for example the XPS anode contains a filament and similar to the requirement of a lightbulb filament to be isolated from atmosphere and high pressure, the same is true for an x-ray filament which will burn out if exposed to suboptimal vacuum conditions. The XPS analyser as well as gauges are also susceptible to damage unless operated in HV.

The basic principle of XPS is the irradiation of a sample with soft x-ray radiation and the collection and measurement of the emitted photoelectrons the principal components are shown in Figure 2.8. The x-rays themselves are generated through bombarding a metal coated copper target with a stream of electrostatically accelerated high energy electrons which is created using a high potential tungsten filament (approximately 10 -15 kV). As noted earlier, typical anodes used for this metal target are coated in Mg or Al which ultimately

determines the x-ray frequency generated. Since the majority of the incident electron energy is converted to heat, anodes are water cooled to prevent degradation [20]. A thin 2μm foil, commonly Al, is placed between the anode and the sample to minimize contamination of the sample by the x-ray source and vice versa as well as to reduce the flux of electrons and unwanted Bremsstrahlung reaching the sample which may cause the appearance of satellite peaks or sample degradation [20]. Due to the photoemission process and the emission of negatively charged photoelectrons from the sample surface, an insulating sample may undergo electrostatic charging resulting in peaks shifting to higher binding energies. To overcome this, charge compensation must be performed through sample grounding or the application of an electron flood gun so as to replace lost electrons and avoid sample charging [3]. The x-rays are focused before being directed onto the sample surface which results in the photoemission process emitting photoelectrons of kinetic energy described by Eq 2.1.
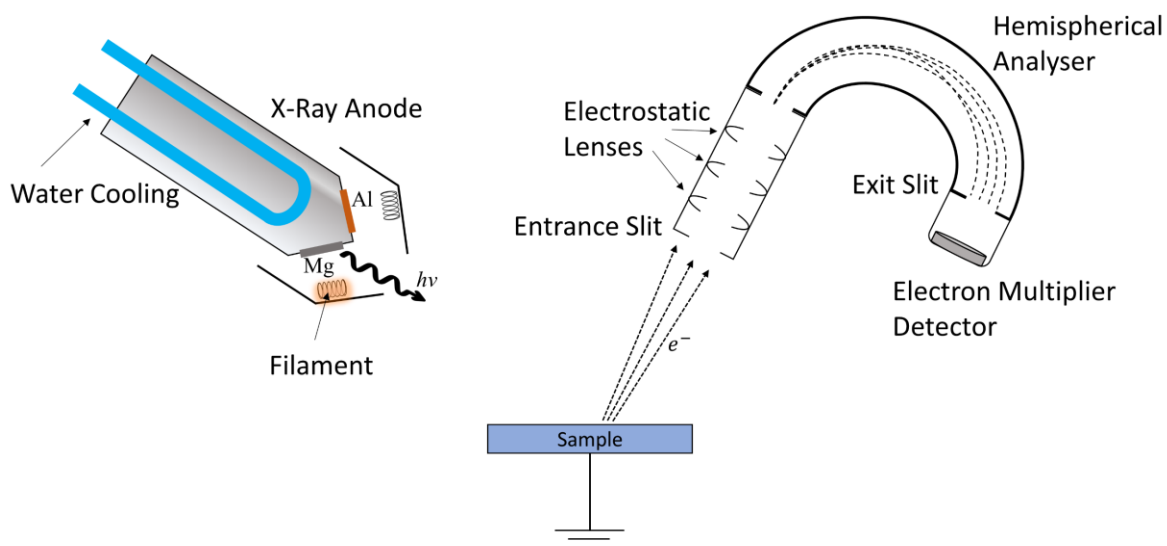
Figure 2.8 Schematic detailing the experimental setup for a conventional XPS system.

It is worth highlighting the influence of x-ray monochromators in XPS and their impact on spectra. The utilization of a non-monochromatic x-ray source can result in the excitation of the sample by x-ray components at higher energies [21]. Consequently, these low-intensity x-rays may generate secondary photoemission peaks, approximately 10 eV higher in kinetic energy compared to the primary peak. However, employing an x-ray monochromator which uses a quartz crystal to effectively eliminate residual Bremsstrahlung mitigating the presence of these additional features and substantially reducing the width of the photoemission lines thus enhancing their resolution [21,22].

Once generated, the photoelectrons must now be collected and measured to determine their kinetic energy and convert to binding energy thus revealing the atom and core level from which they originated. This collection and measurement is performed using an electron energy analyzer which consists of 3 primary components being the collection lens optics, the energy analyzer itself and finally the detector [20,23]. The collection lens has a collection angle within which electrons can enter which controls the area of analysis and so a larger acceptance or collection angle leads to an increased quantity of electrons collected. Alongside collecting photoelectrons, the lens also acts to retard the kinetic energy of the electrons down to the analyzer pass energy – the pass energy being the parameter which determines the range of electron energies which can be detected by the analyzer with a higher pass energy leading to higher intensity but a reduced resolution. Pass energy is a balance between resolution, spectra acquisition time and sensitivity.

The electrostatic hemispherical analyzer is the most common type and is made up of a pair of inner and outer concentric hemispheres of radius R_1 and R_2 respectively the space between them being the path along which the photoelectron passes of R_0 [20]. A potential ΔV is applied

across the hemispheres with the outer being negatively charged (V1) and the inner being positive (V2). Electron energy analyzers have two modes of operation being constant analyzer energy (CAE) and constant retard ratio (CRR). When operating under the CAE mode the photoelectrons are accelerated or retarded based on an energy defined by the user – the pass energy as mentioned earlier being the energy the electrons will traverse the analyzer with and affects the analyzer transmission and resolution. Small pass energies lead to higher resolution with reduced transmission while the opposite is true for high pass energies [3]. Conversely the CRR mode retards the photoelectrons by dividing the incoming kinetic energy by a user defined fraction. The CAE mode was employed within this work as it provides constant resolution.

Once collected by the analyzer the electrons are directed to the detector itself where they are counted. In most spectrometers the individual electrons which arrive at the detector are counted using electron multipliers with the two main types being channel plates and channel electron multiplier commonly referred to as channeltrons [3].

2.2.3 XPS Data Analysis

When performing XPS characterization of a sample, the first step is the identification of all the elements present in the sample which is done by recording a so-called survey spectrum or wide scan from 0 eV to approximately 1000 eV depending on the sample and the elements expected to be present. An example of a typical XPS survey spectrum is shown in Figure 2.9, plotting photoelectron counts per second as a function of electron binding energy. Though the electron energy analyzer measures kinetic energy, the norm within the field is to plot binding energy as it is more indicative and intuitive for the reader. The photoemission process causes electrons of specific energies related to their atomic core levels to be emitted with

additional electrons which have lost energy as a result of collisions contributing to the background. The background is continuous due to the randomness of the loss processes within the sample [20]. As is indicated within Figure 2.9, the primary peaks of the sample are O, C, and Si which emerge sharply from the background. Along with the primary excitation peaks it is common to observe an array of satellite peaks, when using a non-monochromated x-ray source, which appear near to the primary XPS peaks and typically occur when the energy of the incident photons is high enough to result in inner-shell ionisations within the sample.
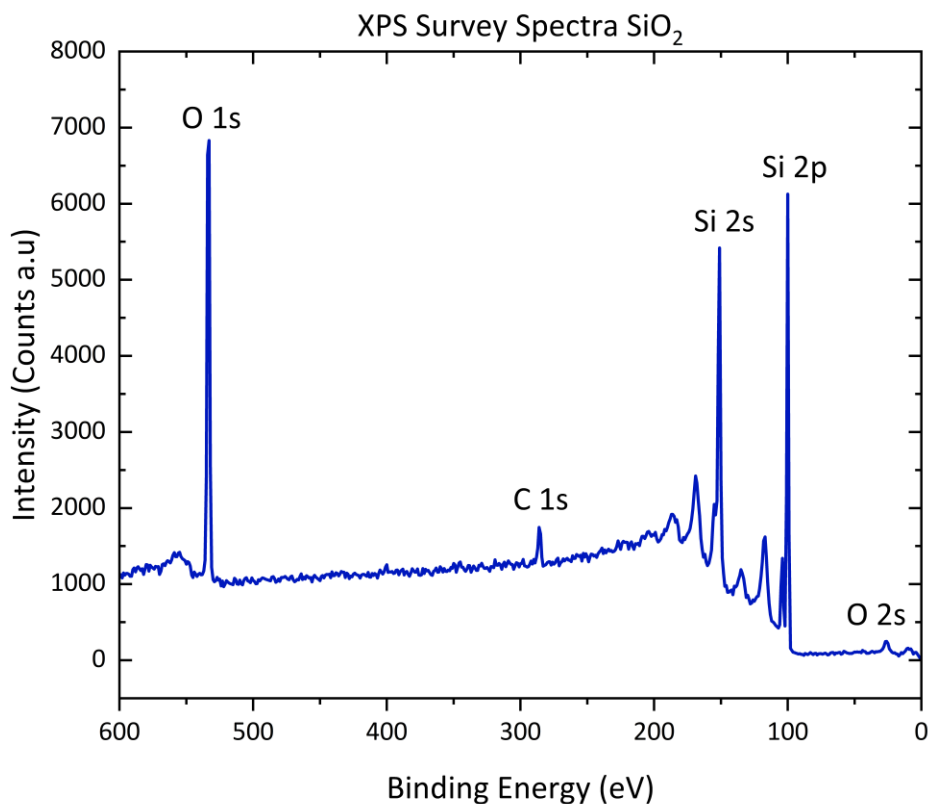
Figure 2.9 Exemplar XPS survey spectra showing a scan of a silicon sample. Both silicon bulk from the underlying substrate along with silicon oxide at the surface in addition to the carbon peak indicating a layer of contamination due to atmospheric exposure.

The main photoemission peak, as discussed, corresponds to the emission of an electron from the outermost energy level of the atom or molecule however in some cases the incoming x-ray may ionize an inner shell electron leaving a hole in the inner energy level. The rearrangement of electrons between energy levels to fill this inner shell can lead to the emission of further photoelectrons from a higher energy level leading to additional spectral features such as satellites. Satellite peak binding energies are most often higher than that of the main photoemission peak with the energy difference related to the difference between the inner and outer energy levels. Satellite peak intensity is typically diminished compared to that of the main peak. Satellite features can be removed using an x-ray monochromator which uses a quartz crystal to remove residual Bremsstrahlung and also acts to narrow photoemission peak width [24].

A core hole is formed through the excitation and subsequent emission of a core electron. Through filling this hole with an electron from the valence band the ionized state relaxes. It is the relaxation process which releases energy in one of two competing processes of either by the emission of an Auger electron or via x-ray fluorescence [4]. Since the XPS uses an electron energy analyser, x-ray fluorescence is not detected and does not contribute to the spectrum. Auger electrons on the other hand are detected and are used in qualitative XPS analysis and their notation relies on the K, L, and M nomenclature for atomic orbitals [4]. Taking oxygen as an example, its Auger peak is denoted KLL which implies that the first electron ejected came from the K orbital before being filled by an electron from an L orbital and the final Auger electron emitted in the process also came from the L orbital as illustrated in Figure 2.10. It is possible to distinguish between photoemission and Auger peaks through changing the energy of the x-ray source with the position of the Auger lines remaining

constant due to their dependence on the energy separation of the core levels with the photoemission peaks shifting based on the incoming x-ray energy.
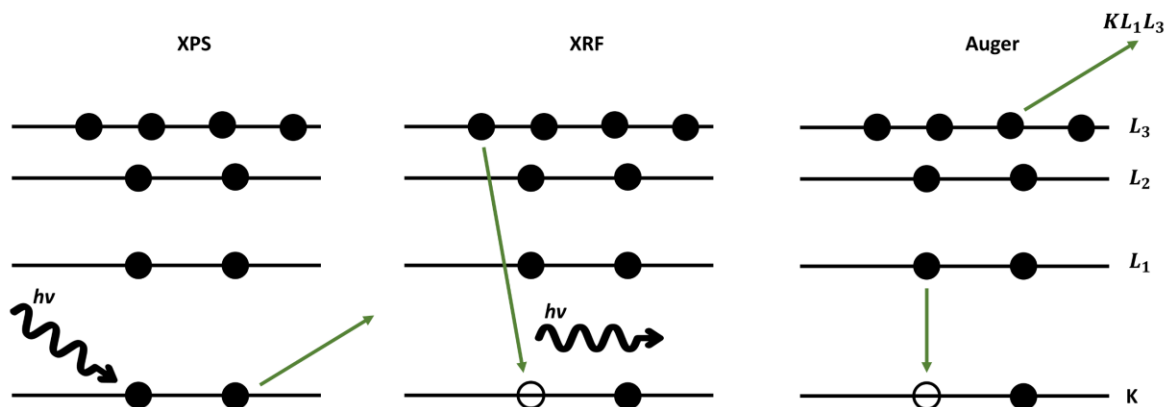
Figure 2.10 Illustration of the XPS, XRF and Auger emission processes.

In some cases, satellite peaks can provide additional chemical information about the sample in question beyond what can be obtained from the main peak alone though they can also complicate XPS spectra interpretation and data analysis.

2.2.3.1 Inelastic Mean Free Path and Analysis Depth

Due to the reliance of the XPS analysis technique on the excitation and emission of photoelectrons from within the sample surface, the inelastic mean free path (IMFP) of these electrons within a sample is a vitally important factor which ultimately determines the effective sampling depth of the technique as a whole. Although the photons generated by the Mg and Al Kα sources have energies (approximately 1 KeV) sufficient to penetrate and excited electrons in most materials to a depth of around 1 μm, it is only those photoelectrons generated in the surface region of approximately 8 – 10 nm which manage to escape from the sample due to their IMFP. The IMFP states the average distance an electron will travel within a solid material before undergoing an inelastic scattering event where it loses a

significant quantity of energy which is described in Beer's Law in Eq 2.2. The IMFP ultimately affects the intensity and shape of the measured photoemission peaks. It is the IMFP which affected the attenuation of a signal as it traverses a material undergoing a series of inelastic scattering events which result in losses in energy and changes in direction.

$$I_k = I_0 e^{(-\frac{d}{\lambda_{IMFP} cos\theta})} \tag{2.2}$$

With I_k and I_0 being the final and initial intensity of the photoemission signal respectively, λ_{IMFP} is the IMFP of the given material, d is the distanced travelled by the electron and θ is the angle of emission from the sample surface with respect to the normal with the normal being 90° perpendicular to the sample surface. The normal represents the shortest path along which photoelectrons from the greatest depth within the sample may take to escape the solid. Upon being irradiated with x-rays of a sufficient energy, a flux of electrons I_0 is generated at a depth d which is the distance through the sample they must travel without being scattered which leads to a final intensity or electron flux of I_k. a variation in the so called take off angle from the sample surface and deviation from the normal results in decreased peak intensity and increased surface sensitivity. By varying the angle as shown in Figure 2.11 the effective sampling depth of the system can be altered in what is called angularly resolved XPS (ARXPS). Going to a large take off angle of say 60° off angle, meaning going to 60° away from the perpendicular to the surface, results in spectra which are dominated by signals originating near the surface. Conversely, low take off angle spectra such as those measured at 15° off angle result in spectra being dominated by bulk features deeper within the sample.
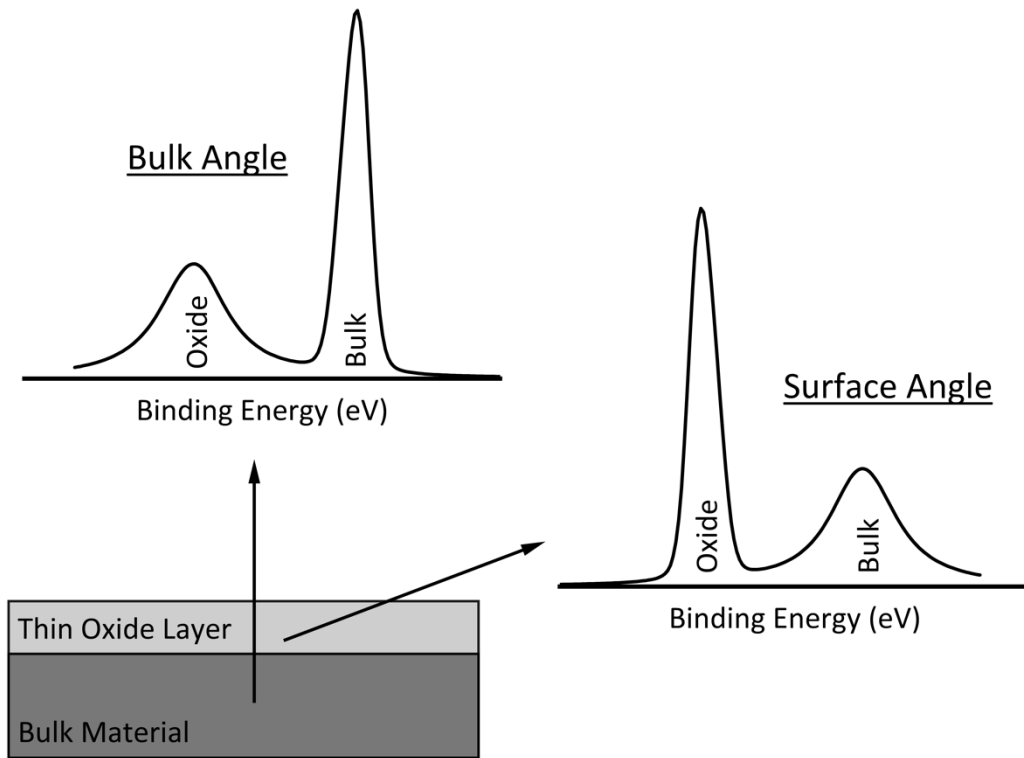
Figure 2.11 Sampling depth dependence on analyser take-off angle with respect to the surface normal.

The dependence on the IMFP is clear from Eq 2.2 which is intuitive as it describes the likelihood of an electron to undergo scattering events which will change the kinetic energy with which it escapes from the sample. The probability of such interactions can be predicted statistically and depends itself on the initial energy of the electron in addition to the nature of the material being traversed and is represented graphically by Figure 2.12 wherein the universal mean free path curve seen shown . The universal mean free path curve shows the mean free path of ejected electrons within a solid as a function of electron energy above the fermi energy. Electrons which undergo elastic scattering do not incur energy loss, only a

change in their direction. Inelastic scattering involves electron-phonon interactions known as quasi-elastic scattering which slightly effect the energy of the electrons. However, a considerable amount of energy is lost through two forms of electron-electron scattering events one of which involves the formation of an electron hole pair via the collision of an electron with a bound electron within the solid with the alternative being through plasmon excitation. If the energy of a photoexcited electron within a solid is insufficient to form an electron hole pair or to generate plasmons this results in a reduced probability of inelastic scattering. The change in mean free path for inelastically scattered electrons as a function of energy is shown in Figure 2.12.
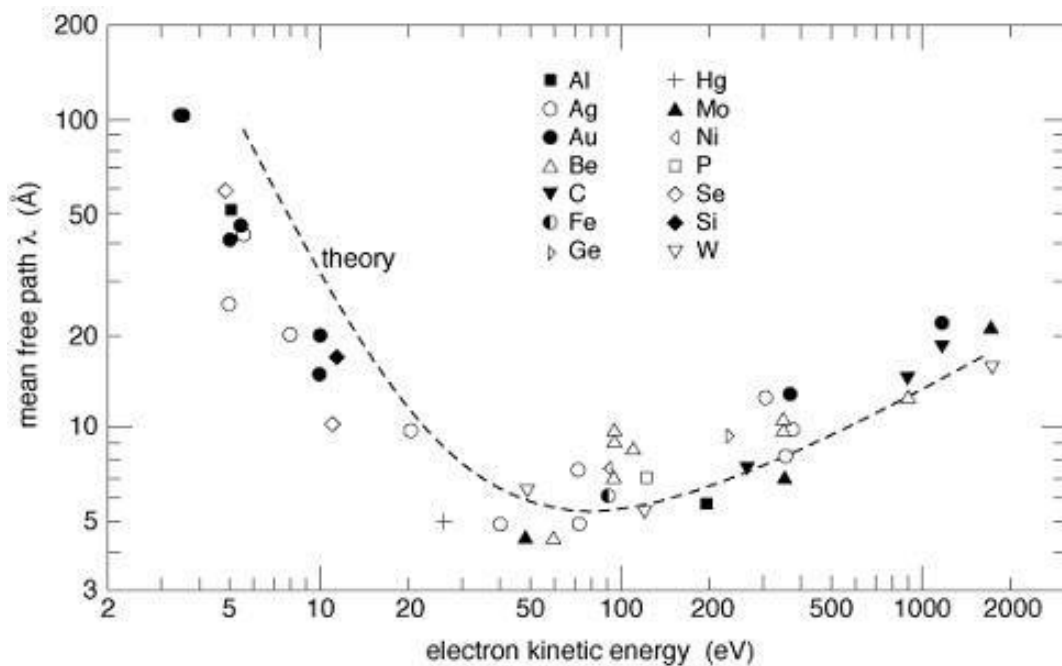
Figure 2.12 Universal curve for the electron mean free path in solids as a function of their energy.

The mean free path (λ) of inelastically scattered photoexcited elelctrons deends strongly on the electron energy itself with the expression for the IMFP is given in Eq 2.3

$$P(d) = \exp\left(-\frac{d}{\lambda}\right)$$ (2.3)

with $P(d)$ being the probability of an electron traversing a distance d without undergoing a scattering event with λ being the energy of the electron. Therefore, while the x-ray penetrates deep within a sample it is only the electrons from the near surface region which statistically likely to be emitted and detected. The low energy limit of these scattering mechanisms corresponds to the long mean free path seen at the left of Figure 2.12 while beyond this threshold energy the mean free path is seen to reduce drastically to being only of the order of a few Ångstroms with this mean free path corresponding to the topmost atomic layers of a solid under investigation. Looking to Figure 2.12 it is evident that electrons with kinetic energies in the 20 – 200 eV range which escape from the solid have originated from the atomic layers closest to the solid surface.

2.2.3.2 Elemental Sensitivity and Cross Sections

A powerful tool in XPS data analysis is the ability to determine sample stoichiometry which is most commonly referred to as elemental composition and is highly dependent on the elemental sensitivity of the XPS. As discussed at the outset of this chapter, the complete XPS spectrum contains peaks associated with all elements present with in a sample, aside from H and He with the area under each peak relating to the quantity of each element present – elemental composition. Through measuring the peak area and correcting for instrumental and chemical factors their percentages can be accurately determined.

It is insufficient to ratio all observed peaks from a spectrum as they are due to some elements such as nickel and titanium having high XPS sensitivity while elements such as fluorine and carbon have comparatively low sensitivity. This variation in XPS sensitivity depends on a number of factors including the binding energy, x-ray photoionisation cross section as well

as the emission probability. The emission probability refers to the likelihood of a specific x-ray emission process occurring once an atom or molecule has been ionized by the incoming x-ray. The cross section is defined as the probability of excitation of a photoelectron from the core level under x-ray irradiation with every element and core level having a distinct cross section with small values indicating small probability of excitation and the occurrence of photoemission. The cross section is dependent on various factors including the element in question and the orbital an electron is ejected from as well as the incoming photon energy [3]. Assuming the sample is homogeneous then the intensity I of a photoelectron peak is given as;

$$I = J\rho\sigma K\lambda \tag{2.4}$$

with J being the photon flux, σ the cross-section, ρ the atomic concentration, λ the effective attenuation length of the electron and K being a constant which accounts for instrumental factors related to the spectrometer. The intensity of the peak can either be taken as the peak height but more commonly and more accurately the intensity refers to the integrated area under the peak with a background subtraction applied. Taking the photon flux to be constant, the cross section, attenuation length and instrumental factors from Eq 2.4 are combined in an experimentally derived relative sensitivity factor (RSF). A database of relative sensitivity factors used were obtained from Wagner et al [25]. The constant photon flux assumption and database of RSF values for all elements and orbitals enable the determination of an adjusted peak intensity given by Eq 2.5;

$$Relative\ Peak\ Intensity = \frac{Measured\ Peak\ Intensity}{RSF} \tag{2.5}$$

This then allows for the calculation of the elemental composition;

$$Elemental\ Composition = \frac{Relative\ Peak\ Intensity}{Sum\ of\ Relative\ Peak\ Intensities} \times 100 \qquad (2.6)$$

2.2.3.3 Peak Fitting

It is possible to gain a much greater amount of information about a film under investigation than just its elemental composition through the use of peak fitting. Peak fitting is the deconvolution of a photoemission spectra into single peaks in order to interpret them accurately and establish the chemical interactions of the sample in question. The overall shape of the spectra is affected by more than just the bonding or chemical states occupied, with spin orbit splitting and charging also influencing spectral shape.

2.2.3.3.1 Line Shape and Peak Width

At this point it is important to consider the spectral peak width which is defined as the full width at half-maximum (FWHM) ΔE given as Eq 2.7.

$$\Delta E = \sqrt{\Delta E_n^2 + \Delta E_p^2 + \Delta E_a^2} \qquad (2.7)$$

where ΔE_n is the inherent core level width, ΔE_p is the width of the photon source with ΔE_a being the resolution of the analyzer. It is assumed for the purposes of Eq 2.7 that all components included bear Gaussian line shape.

Every photoemission peak has a specific line shape made up of a mixture of Gaussian and Lorentzian components which combine to form what is referred to as a Voigt function with the final Voigt curve peak width given in Eq 2.8;

$$\Gamma_V = \sqrt{\Gamma_{Gaussian}^2 + \Gamma_{Lorentzian}^2} \qquad (2.8)$$

The resolution of the system determines the Gaussian component and is dependent on the instrumental broadening of the peaks and is therefore generally constant for all peaks for a given system. Phonon broadening effects may also contribute to Gaussian broadening and the final width of the Gaussian component is given by Eq 2.9;

$$\Gamma_{Gaussian} = \sqrt{\Gamma_c^2 + \Gamma_a^2 + \Gamma_p^2} \qquad (2.9)$$

Where the Γ_c^2, Γ_a^2 and Γ_p^2 components correspond to phonon-broadening, non-perfect analyzer resolution and x-ray spectral line width respectively. This results in there being and effective minimum Gaussian value for a system although this can in some cases increase depending on the efficiency of the electrostatic lenses within the electron energy analyzer to focus electrons across the full range of incoming kinetic energy to the same focal point on the detector thus directly influencing the resolution of the system. This efficiency of the electrostatic lenses to perform this focusing is tested at higher electron kinetic energies which can traverse greater distances through the generated magnetic field before the lens can compensate for their motion resulting in changes in the acceptance angle in the lens system which leads to a spread in the electron energies as they pass the focal point of the analyzer. The intrinsic photoemission line shape is Lorentzian in nature and is a direct reflection of the uncertainty in the lifetime, from Heisenberg's uncertainty principle, of a core-hole following its emission from an atom. Core hole lifetimes reduce with increasing atomic number along with proximity of the atomic level to the nucleus due to the increased availability of electrons to fill the core hole – the deeper the orbital the larger the peak width and shorter the lifetime for example 4f < 4d < 4p < 4s. Therefore, the line width is obtained from the uncertainty principle:

$$\Gamma_{Lorentzian} = \frac{h}{\tau} \qquad\qquad (2.10)$$

where h is Planck's constant and τ is the core hole lifetime measured in seconds. As this Lorentzian value is dependent on intrinsic core level properties it is therefore theoretically consistent across various XPS setups.

The processes of dissipation or decay of excess energy which occur following photoemission govern core hole lifetimes. There are three mechanisms which may account for this, which consist of x-ray fluorescence, Auger emission, and the Coster-Kronig process which is a special variant of the Auger process. The main process of dissipation of excess energy post photoemission is the Auger process as was discussed earlier however, it is possible for one or sometimes two holes (Super Coster-Kronig) following an auger process to be in the same shell as that of the initial vacancy named after Dirk Coster and Ralph Kronig who first detailed this phenomenon [26–28]. The outcome of the Coster-Kronig effect in XPS leads to a difference in the peak width of two spin orbit doublet peaks which is exclusively observed in 2 p spectra of 1st row transition metals .

2.2.3.3.2 Spin Orbit Splitting

The fine structure features of XPS spectra of bound electrons with the same n but different l quantum numbers are a result of an effect called spin-orbit splitting or sometimes spin-orbit coupling. Spin-orbit splitting at its most fundamental level comes about as a result of the interaction of electron spin and its orbital motion around the nucleus. Electron spin is an intrinsic property of electrons described as the electrons spin around its own axis.

The electron spin interacts with its orbital motion due to the electromagnetic field created by the positive charge of the nucleus. This spin orbit interaction causes the splitting of energy levels within an atom which is known as the fine structure and leads to the splitting of energy

levels into multiple sub-levels. The magnitude of the induced splitting is dependent on the strength of the spin-orbit coupling and the quantum numbers associated with the electron. This is made possible as all spinning charged bodies induce a magnetic field.

The nomenclature for describing core levels are n, l and j with n being the principal quantum, number, l is the orbital angular momentum and j is defined as the sum of the orbital and spin angular momentum as in Eq 2.11;

$$j = l + s \qquad (2.11)$$

All orbitals within an atom have two possible j values except for s-orbitals which have an orbital angular momentum equal to zero. The two possible states of these subshells exhibit different binding energies which is known as spin-orbit splitting and gives rise to doublets. The degeneracy being the number of electrons in each state is approximated using either j-j or L-S coupling arguments The most common example of a doublet is that of the Si $2p$ which is made up of $p_{3/2}$ and $p_{1/2}$ components as seen in Figure 2.13.
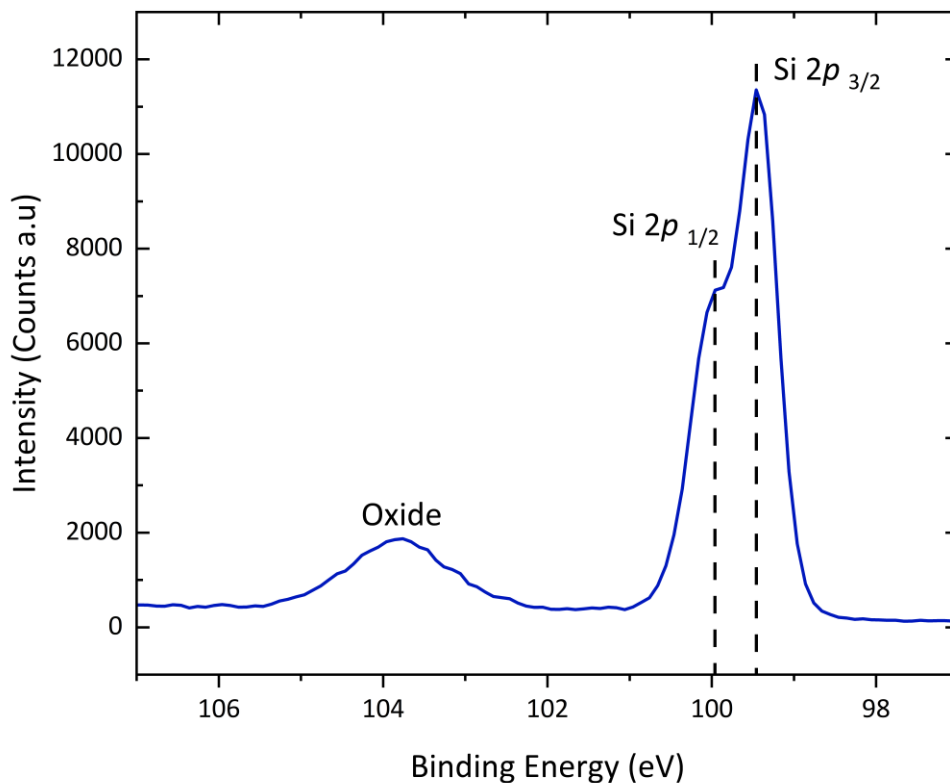
Figure 2.13 High resolution XPS spectra of the Si 2p region of a bare SiO₂ sample detailing the spin-orbit splitting of the Si bulk photoemission peak.

The j value, which itself depends on the subshell, determines the area ratio of the two components as well as the binding energy difference. The subshells and their corresponding j values and peak ratios are shown in Table 2.1. The binding energy difference of the doublet components in the Si $2p$ spectra seen in Figure 2.13 is approximately 0.55 eV. The spin orbit splitting of doublet components varies depending on the element in question and other factors, with for example, TiO_2 having a binding energy separation of its $p1/2$ and $p3/2$ components of approximately 5.9 eV.

Table 2. 1 Spin-orbit splitting parameters [28].

Subshell	j Value	Peak Area Ratio
s	1/2	—
p	1/2 , 3/2	1 : 2
d	3/2 , 5/2	2 : 3
f	5/2 , 7/2	3 : 4

2.2.3.3.3 Background

XPS spectra exhibit a background which refers to binding energy regions where no photoemission peak is present. The background is random, and counts are attributed to photoelectrons which have lost a significant portion of their original kinetic energy from the photoemission process due to inelastic scattering events before being emitted from the material under investigation. Looking to the earlier Figure 2.9 which shows an exemplar spectrum, the background is seen to increase on the higher binding energy side of all major photoemission peaks due to the inelastically scattered electrons from that core level now contributing to the background rather than the primary emission peak itself [29].

The accurate removal of this background contribution is vital to allowing precise analysis of the data as when incorrectly removed the background may act to distort the data [28]. There are three main types of background which have been most popular within XPS studies; the simple linear background, the integral background based on the Shirley method and the Tougaard background [30].

The linear background is deemed a crude method of background subtraction which is achieved via a straight line drawn between the start and end data points of a peak fit, the main benefit of this method being that the original data is not altered. This gross oversimplification of the background subtraction is not typically favoured in XPS peak

fitting software and is used only when little change in the background has occurred which is uncommon in XPS. For these reasons the Shirly and Tougaard approaches are favoured in specialist fitting software and literature.

The Shirley integral background subtraction is an iterative approach which assumes the background at a given binding energy position in the photoelectron peak is proportional to the integrated intensity of the same peak at lower binding energy [31]. This approach results in a background subtraction which increases as a function of the peak area [28].

The Tougaard background is based on the elastic and inelastic loss processes investigated by Tougaard and co-workers to account for the intrinsic loss processes contributing to the background in metals. This method is successful for large background regions while the Shirley approach is more suitable for narrow binding energy windows [28,32].

2.2.4 Precision and Accuracy in XPS

Provided sufficient signal to noise within the obtained spectra, precision within the field of XPS is quite good with a series of spectra performed on the same area of the same sample or series of identical samples essentially yielding the same result with marginal deviation. However, in some cases depending on the sample and its material makeup exposure to x-rays over time can act to alter the sample itself, though this was not a concern within this study due to the sample materials not being susceptible to this effect being robust under x-ray photoemission studies. Accuracy within XPS spectra and interpretation depends on several factors one of which and among the most important is that of the relative sensitivity factor (RSF) which for the most common elements is well known and studied while for some of the more rare elements this can be an issue due to a lack of reference spectra to refer to [33]. For elements such as those of interest within this work being O, C, Si, Ni, Ti and Co the RSF

values which have been empirically derived as well as cross referenced with reference spectra within the literature both binding energy as well as RSF values are very well known. A further implication on the accuracy of spectra is the angle of acceptance of the analyser during the spectra acquisition with off-angle or the so-called angularly resolved variant of the XPS technique being more prone to low signal to noise ratios thus limiting the certainty in measurements – this was not a technique applied within this work and is therefore discounted with all spectra obtained at normal emission which yield the highest photoelectron counts and thus best signal to noise.

A further consideration for the precision of XPS spectra is that of element photoelectron cross section, with elements such as N and B being in this group which are susceptible to error in this manner. Moreover, the background subtraction selected is also important and choosing between the Shirley, linear, and Tougaard background can influence the overall analysis [33]. For the majority of elements especially those with strong photoelectron cross-sections precision will vary only by a few tenths of a percent though for lower photoelectron cross-section elements this can increase [33]. As a means of illustrating the precision and accuracy of the XPS technique Figure 2.14 shows the high resolution XPS spectra of two NiO samples which received the same deposition simultaneously and were subsequently scanned one after the other following deposition. As can be seen from the spectra, there is extremely small divergence between the spectra showing consistency both in the ALD deposition conformality as well as accuracy in the characterisation of the XPS measurements.
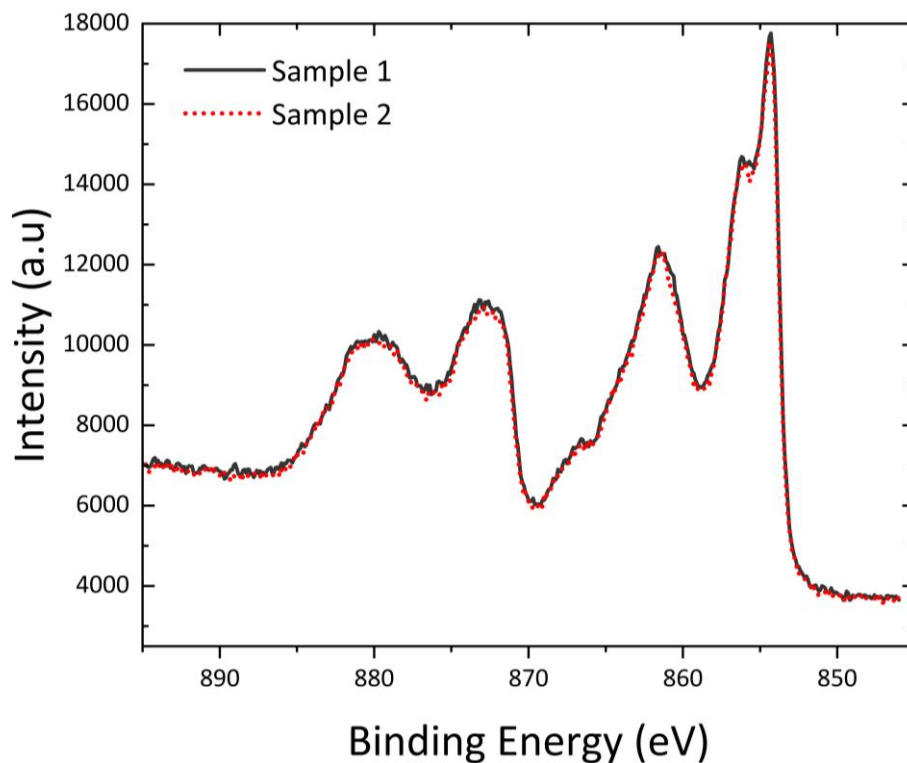
Figure 2.14 XPS Ni 2p high resolution spectra showing Sample 1 and Sample 2 from a batch of depositions which were scanned consecutively

Expanding on that mentioned above, semi-quantitative analysis is possible through measuring the peak areas and intensities of specific element core lines and through applying the RSF values it is possible to calculate the atomic fraction or so-called elemental composition of a given sample and spectra. The RSF values may be obtained through theory via empirical derivation or through the use of reference samples. The peak area and its calculation relies heavily on the background subtraction selection as highlighted earlier there are 3 main backgrounds being the simple straight line which lacks accuracy due to its blunt approach in subtraction across a straight line from where the peak begins at its lower binding energy shoulder to where it ends at the higher binding energy [34–36]. The Shirley background in which the intensity at a given binding energy is proportional to the intensity of the total

peak area above the background at that point meaning that the background rises as a function of the total number of secondary electrons at that point in the spectra [34]. The Tougaard is a more complex approach not often applied [34].

In terms of elemental stoichiometry determination which is a common analysis tool used within the field of XPS and within this work, this technique operates via a determination of the peak areas (or intensity) of each elemental peak within a recorded spectra which are then corrected using their corresponding RSF values before being mathematically manipulated to represent the spectra in elemental percentages. These percentages are dependent on the calculation of the respective peak area of all other elements within that one spectra and so any error within the compositions for one spectra will be consistent throughout that calculation as the calculation is a ratio against itself and a conservative estimate of error on these compositions is typically $\pm$ 5 %.

2.3 Hard X-ray Photoelectron Spectroscopy

2.3.1 Overview

Hard X-ray Photoelectron Spectroscopy (HAXPES) is variation of photoemission spectroscopy which utilises synchrotron radiation (SR) photons in the hard x-ray range for the excitation of photoelectrons in contrast to XPS as has been detailed earlier which uses soft x-rays. Both XPS and HAXPES are spectroscopic characterisation techniques which allow for in depth surface analysis and operate under the same principles of the photoelectric effect. Some key differences exist between the two primarily being the ability of HAXPES SR to be tuned to a range of photon energies of approximately 2 – 10 KeV allowing for variation in sampling depth due to this enhanced excitation energy as one example.

2.3.2 Technical Details

2.3.2.1 Synchrotron Radiation

When relativistic electrons undergo centripetal acceleration a form of electromagnetic radiation is emitted called synchrotron radiation (SR) which generates photons in the hard x-ray regime. Though originally the primary energy loss mechanism experienced by large accelerators with significant injection of additional energy required to compensate for this loss, specific SR source facilities have been constructed with storage rings which do not require the continual supplemental injection and acceleration of electrons. Though soft x-rays from Mg and Al Kα sources as mentioned earlier have been the most common sources for the facilitation of the photoemission process, they simply cannot compete with the broad spectral range, tunability, intensity, stability and therefore resolution of SR sources. The electron beam within the storage ring is transversely accelerated via deflection in a magnetic

field thus creating SR which is collimated and polarized as it emerges tangentially from the synchrotron ring.

A schematic of a synchrotron set up is shown in Figure 2.15 with the primary components numbered. Electrons are accelerated with an energy of 0.1 GeV (1) which are then injected into a booster synchrotron (2) before entering the main synchrotron ring (3) where magnets and undulators are used for the manipulation and oscillation of the beam respectively (4). Radiofrequency cavities are used to compensate for the inevitable energy loss of the system. Several beamlines (5) are located around the ring which harness the SR for use in a variety of techniques such as HAXPES.
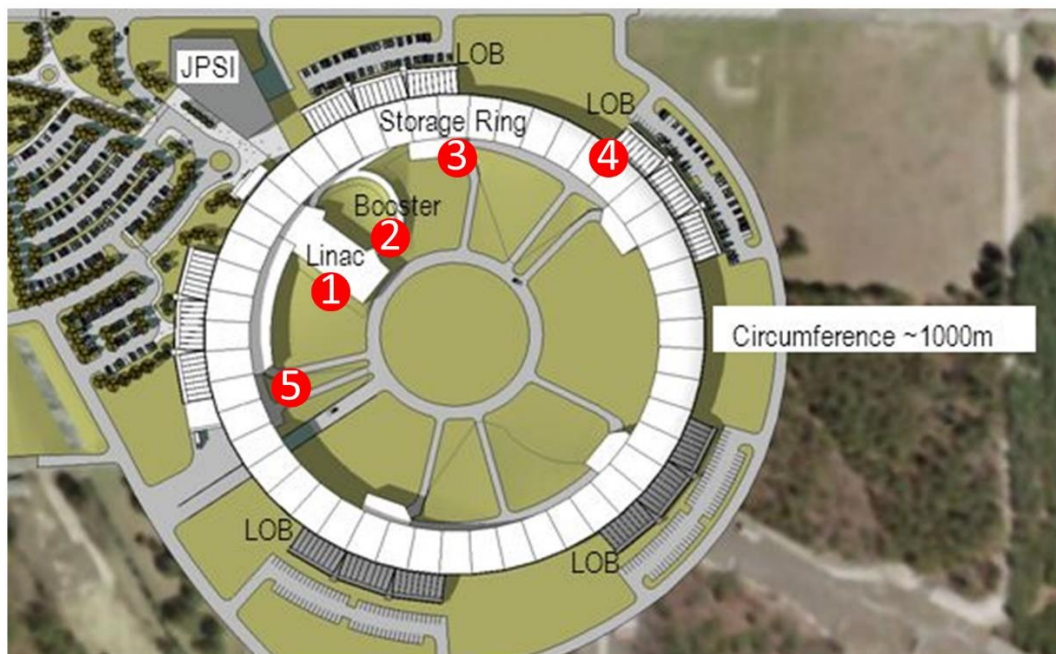
Figure 2.15 Overview of the synchrotron at Brookhaven National Laboratory [37].

2.3.2.2 HAXPES Beamline Characteristics

The purpose of the beamline is the collection, focusing and application of the emitted SR from the ring in a variety of x-ray-based applications. As has been discussed already at length, the effect of the IMFP significantly limits the effective sampling depth of the XPS analysis technique leading to an upper limit of depth analysis of approximately 10 nm. It is the sampling depth limitation which led to the formation of the HAXPES technique which applies SR to achieve ethe photoemission required for sample analysis. While lab based XPS systems rely of soft x-ray sources of ~ 1 KeV, HAXPES is capable of producing an incident beam over a ranger of higher energies with the HAXPES studies performed within this study being carried out in Brookhaven National Laboratory (BNL) which can operate over a range of 2 – 7.5 KeV. The ability firstly to be tuned to a user defined energy within this range coupled with the overall increased energy allows for the acquisition of core levels not possible with conventional XPS. The most important difference between XPS and HAXPES then is the kinetic energy of photoelectrons being significantly higher in the HAXPES setup, though all other basic principles of operation remain consistent between XPS and HAXPES. The conclusion from Figure 2.16 being that the only way to increase bulk as well as interface sensitivity across all materials is to go to higher photon energy such as to ultimately enhance the emitted kinetic energy [38].
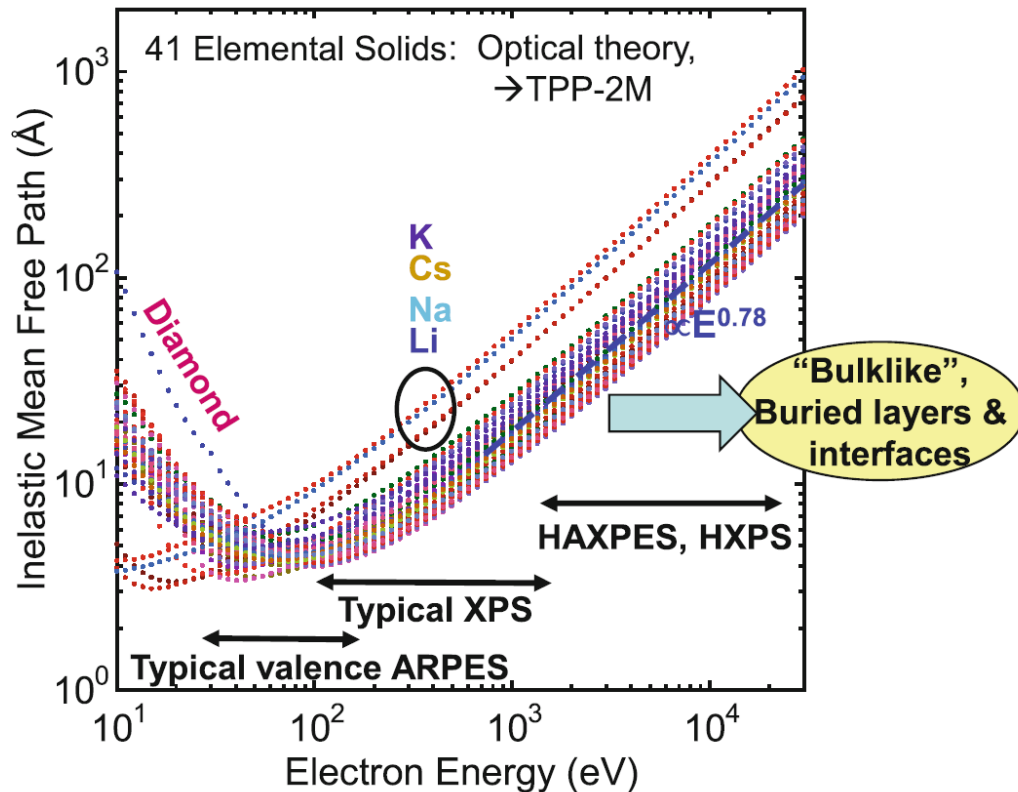
Figure 2.16 IMFP as a function of electron energy [38]

From earlier discussions within this chapter, the dependence of the photoemission signal on the depth from which it originated within the solid being the distance it must traverse to reach the detector coupled with a dependence on the IMFP which itself is correlated to the photon energy which initiated the photoemission in the first place and results in the kinetic energy of the emitted photoelectrons. This relationship between IMFP and electron energy detailed in Figure 2.16 with the typical XPS and HAXPES electron energies highlight clearly indicating the ability of HAXPES to investigate bulklike features deeper within the film compared to the 10 nm theoretically imposed limits of conventional XPS [38].

Moving to HAXPES measurements and the hard x-rays and higher photon energies can lead to more simplified spectral analysis owing to several distinct advantages:

- Increase of the EAL and IMFP as a function of rising photon beam energies.

- Fitting and broader analysis of spectral features becomes less complex through the significant reduction in the inelastic background of spectra generated making the determination of various peak intensities easier.

- Higher resolution spectra than that available via conventional XPS.

- Brightness and photoemission intensities which are orders of magnitude higher than conventional XPS sources.

- Analysers utilised in HAXPES beamlines are much more sophisticated than lab based XPS detectors allowing for further improvements in resolution.

2.4 Thickness Determination

2.4.1 Overview

As discussed, the thickness employed for the protection of the underlying photoanode itself is vital for optimal performance of both the protective layer and the anode. It is important to ensure films are sufficiently thick such as to effectively distance the OER from the anode and prevent passivation however, increasing the overlayer thickness can bring many side effects and ultimately can act to outweigh the benefits of passivation [39]. Typically as overlayer thickness increases so too does the reflectivity of the film coupled with a reduction of transmission with TiO_2 being cited in the literature to exhibit this behaviour [39,40]. Furthermore, sticking with the TiO_2 example, thicker layers can act to increase charge transfer resistance leading to charge tunnelling becoming unlikely if the thickness exceeds a so-called critical thickness reported to be sub 10 nm alongside an increase in the overpotential resulting in voltage loss [39,41–43].

Therein, the requirement for precise thickness control of ultrathin (ca. 2 nm) films is evident. Given the unique advantage presented by the ALD-XPS system utilised within this study which allows for in-situ photoemission studies of deposited films without the exposure to atmosphere the ability to also determine film thicknesses while held under vacuum is also critically advantageous. The most common method of thickness measurement employed in thin film studies is that of ellipsometry which in most cases is ex-situ thus resulting in inaccuracy associated with the absorption of adventitious contamination from atmospheric exposure. Ellipsometry measurements can be performed in-situ via the installation of purpose built vacuum compatible setup however, this was unavailable within this study. In-situ real time thickness calculations were performed using the Thickogram method

developed by Peter J. Cumpson with these calculations being verified with ex-situ ellipsometry [1].

2.4.2 Thickogram

The Thickogram is described by its creator as a simple graphical method of thin film thickness measurement via XPS [1]. The method was developed to overcome the issue of converting XPS peak intensity into film thickness. A previous popular method for this conversion from intensity to thickness for oxide films was developed by Hill *et al* outlined in Eq 2.12 [44].

$$t = -\lambda \cos\theta \, ln\left(1 + \frac{I_o/S_o}{I_s/S_s}\right) \qquad (2.12)$$

where t denotes film thickness, λ is the attenuation length of the photoelectrons within the film and θ is the angle of emission from the material with respect to the normal. I_o and I_s refer to the measured peak intensities from the overlayer film and substrate respectively with S_o and S_s being their sensitivity factors.

This equation and measurement approach set out by Hill was popular for several useful features:

- Assuming uniform surface contamination, adventitious contaminants can be accounted for uniformly across the film.

- Instrumental factors which are common to the overlayer, and substrate peak measurement cancel out.

- The equation is simplistic with only one logarithm required and simple variables for the user to input.

However, the key shortcoming of this method is it does not account for variations in the attenuation lengths of photoelectrons in each material and are therefore assumed identical. Due to the dependence of IMFP on photoelectron energy, this means that measured overlayer and substrate peaks must be of almost identical kinetic energy. This is of course problematic as often it is necessary to utilise peaks which vary widely in energy.

This requirement for the inclusion of the varying attenuation lengths adds complexity to Eq 2.12 which will be further explored. The Thickogram presents a nomogram as shown in Figure 2.17 as a straightforward graphical solution. A nomogram being a plot designed to provide a value depending on two or more user defined measurements which in the case of the Thickogram are peak intensity ratio along with peak energy ratio [1].
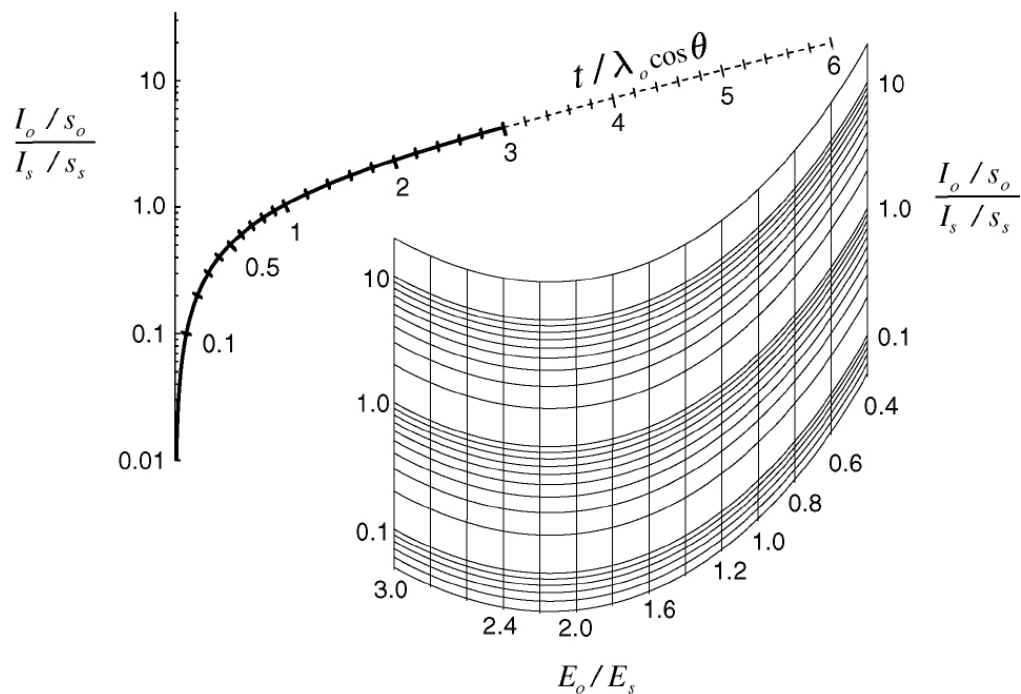
Figure 2.17 Nomogram utilised for a graphical application of the Thickogram method [1].

Utilisation of the nomogram seen in Figure 2.17 first requires the user to determine the value on the vertical axis on the left which corresponds to the measured peak intensities divided by their corresponding sensitivity factors which provides point 'A'. The next step is to determine the point in the curved logarithmic grid to yield point 'B' which corresponds to the same ratio of overlayer and substrate intensities against the ratio of their kinetic energies. A straight line between points 'A' and 'B' will intersect the curved thickness scale at a point 'C', the value of which being the thickness in units of $\lambda_o cos\theta$ with θ being the angle of emission with respect to the normal to the film surface. The attenuation lengths were obtained using the National Institute of Standards and Technology (NIST) Standard Reference Database 82 which provides effective attenuation lengths (EAL) for electrons in solids elements and compounds for electron energies between 50 and 2,000 eV which was established for applications in surface analysis via techniques such as XPS. Applying user data with reference EAL values the Thickogram can provide a geometric solution and thickness approximation given by Eq 2.13

$$ ln\left(1 + \frac{I_o/S_o}{I_s/S_s}\right) - \left[\left(\frac{E_o}{E_s}\right)^{0.75} - \frac{1}{2}\right]\frac{t}{\lambda_o cos\theta} - \ln 2 = \ln sinh\left(\frac{t}{2\lambda_o cos\theta}\right) \qquad (2.13) $$

Thus, the Thickogram represents and fast and easy to use thickness measurements using photoemission peak intensities which is more widely applicable than the previously reported method through being applicable over more energetically distributed peaks. Thickogram values were calculated and periodically verified using ex-situ ellipsometry confirming its operation and allowing for use throughout this work.

2.4.3 Ellipsometry

2.4.3.1 Overview

Ellipsometry is among the most common optical characterisation techniques capable of non-destructive determination of various characteristics of thins and interfaces. Ellipsometry is based on the analysis of the change of polarisation of light as it is reflected or transmitted through a sample. Through measuring this change in polarisation, ellipsometry can provide information on the optical constants such as refractive index as and extinction coefficient in addition to crystallinity, morphology and even doping concentration.
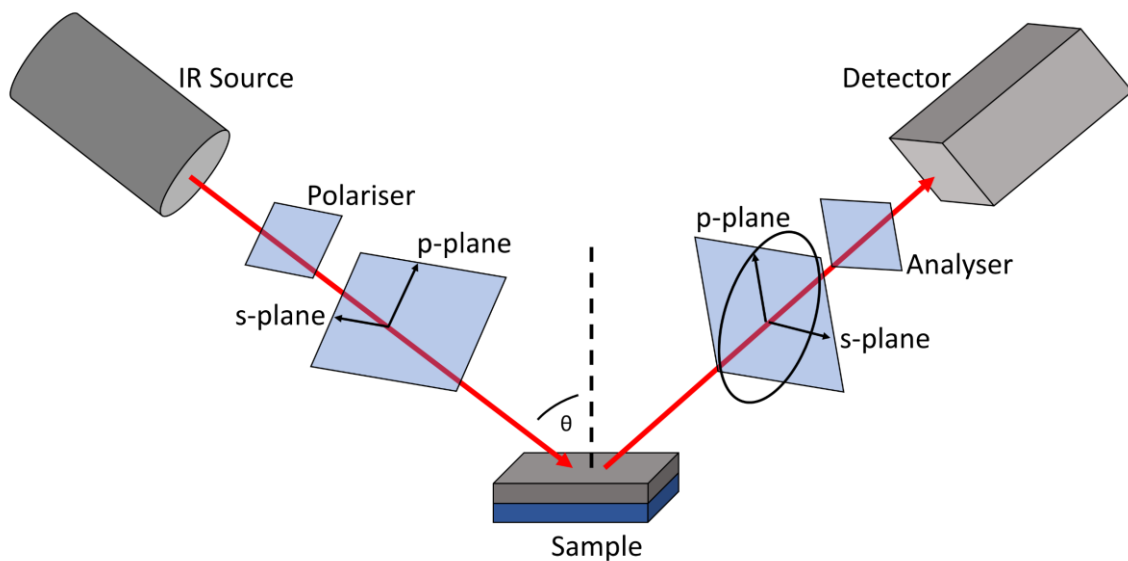
Figure 2.18 Basic ellipsometry set up showing polarized light incident on a sample surface with any and all changes in polarisation as a result of the interaction with the sample measured by the detector.

A simplified interpretation of the basic principles of operation of an ellipsometer are shown in Figure 2.18 wherein light is first passed through a polariser which linearly polarizes it such as to normalize the incoming light to a known constant polarisation therefore any deviation

from this system defined polarisation may be observed. Upon interacting with the sample surface via reflection and absorption processes the light becomes elliptically polarised with the variation in polarisation depending on the sample under investigation. The light is then collected by the analyzer and detector where the degree of polarisation is determined and compared to the original incoming linearly polarised light.

2.4.3.2 Technical Details

Ellipsometry operates by measuring the degree of polarisation of reflected light. Given that incoming linearly polarised light is known and made up of two in phase orthogonal waves one of which oscillates perpendicular (*s* component) to the plane of incidence and the other is parallel (*p* component).

During reflection from the sample surface, it is possible that the *s* and *p* waves may undergo a shift in phase which may not be equal which must be accounted for. It is through measuring the elliptically polarised light and comparing to the original incoming light which allows specific sample characteristic information to be extracted with the change in polarization of the *s* and *p* components with respect to each other. By defining the phase difference between the *s* and *p* waves prior to reflection as δ_1 and the difference in phase following reflection as δ_2 leads to the delta Δ parameter [45];

$$\Delta = \delta_1 - \delta_2 \qquad (2.1)$$

In addition to the phase shift, the wave amplitude may also be affected to varying degrees. The ratio of the magnitudes of the total reflection coefficients is defined as $\tan \Psi$ while ρ is the complex ratio of same yielding the fundamental equation of ellipsometry described by Eq 2.15 [45];

$$\rho = \frac{r_s}{r_p} = \tan \Psi e^{i \Delta p} \qquad \qquad (2.15)$$

The measured variables in Eq 2.15 are Ψ the amplitude and Δ_p the phase shift induced by the reflection which are related to the amplitudes of the incoming s and p components denoted as r_s and r_p. Eq 2.15 is therefore a ratio of these r_s and r_p components and depends on many factors such as the film thickness (t) as well as the refractive index of both the overlayer film, substrate materials and ambient air, the wavelength (λ)of the incident linearly polarised light and the angle of incidence (θ). Given that the refractive indices of the ambient environment and substrate in question are known and the measurement of Ψ and Δ_p allows for the determination of the refractive index of the film and ultimately the thickness of the film through comparison of experimentally acquired data to mathematical equations [46].

Once measured, a mathematical model is constructed and varied so as to describe the sample in question. The model is used to predict the response to the Fresnel equations which describe a material based on its thickness and optical constants, which if unknown can be estimated for preliminary fitting and varied based on fit performance. For a single wavelength ellipsometry arrangement only two unknown material properties (Ψ and Δ_p) may be determined.

The fit is between the model and experimental data is improved through regression with the mean square error (MSE) estimator used for the quantification of variation between the experimental and model data with the unknown material property parameters allowed to vary until the lowest MSE is achieved. A wide variety of models have been established to this end in experimental data fitting such as the Cauchy and Sellmeier equations being cited as applicable in the description of transparent materials with the Lorentz, Harmonic and

Gaussian equations applied to describe resonant absorption processes in addition to Tauc-Lorentz and Cody-Lorentz used for amorphous semiconductors [47].

2.5 Fourier Transform Infrared Spectroscopy (FTIR)

2.5.1 Overview

FTIR is an established technique for the study of molecular vibrations with the frequency dependent interaction of the incident IR radiation being the fundamental principle of the technique. This is a versatile non-destructive technique which offers information on the molecular vibrations of as range of solids, liquids and gases and gives insight into molecular structure and compositions. In FTIR infrared radiation is passed through a sample, a portion of this radiation at specific frequencies is absorbed by molecules within the material while the remainder is transmitted. The spectrum which results represents the molecular absorption and transmission which produces a molecular fingerprint of the sample. The frequencies at which absorption occurs corresponds to vibrational modes and are dependent on the molecular characteristics such as atomic mass of elements within a given molecule as well as the bond of molecular bonding and the environment of the material.

IR spectra obtained from this technique are composed of various peaks or troughs which depends on whether the instrument was configured for transmission or reflection mode with the peak and trough features indicating the wavelength given in units of wavenumber where a molecule has absorbed that frequency of the IR spectrum. This suggests that the frequency absorbed corresponds to a fundamental vibrational mode of the molecule present. These vibrational modes are classified into two main types of mode called stretching and bending. Stretching modes involve the elongation or contraction of bonds within a molecule and occur

along the bond axis resulting in changes in the bond length. Stretching vibrational modes are further classified into two further subgroups of symmetric and asymmetric with symmetric stretching occurring when both atoms either side of a bond move simultaneously in the same direction. Asymmetric stretching is therefore the opposite and corresponds to the atoms on either side of the bond moving in opposing directions. Bending vibrations on the other hand involves the deformation of a molecule which alters the bond angle and occurs when the vibrating atoms move beyond the plane defined by the bond axis. As with stretching modes, bending modes are also further classified into two subgroups of in-plane bending which describes when atoms move within the bond axis plasma and out-of-plane bending wherein they move out of the plane defined by the bond axis. Through analysing the intensities of patterns of these stretching and bending vibrational modes within the FTIR spectrum it is possible to extract useful information pertaining to the functional groups and molecular structure of a sample.

2.5.2 Technical Details

2.5.2.1 Theoretical Principles

In order to be available to interact with the incoming IR radiation a molecule must have a dipole moment which in FTIR refers to the separation of positive and negative charges within the molecule or bond. Molecules with a dipole moment have an uneven distribution of charge which results in a positive and negative end which occurs when the distribution of electron density within the material is asymmetric. Molecular vibrations are induced when the IR radiation causes a change in the dipole moment due IR radiation consisting of electromagnetic waves with specific frequencies which match that of molecular bonds. As the IR radiation traverses the material it interacts with it and its molecules causing the dipole

moment of the molecules to oscillate which results in either the absorption or scattering of light. The dipole moment strength affects the intensity of the absorption or scattering event, and the frequency of the vibrational mode is described by Eq 2.16;

$$v = \frac{1}{2\pi}\sqrt{\left(\frac{k}{\mu}\right)} \tag{2.16}$$

where k is the restoring force constant from Hooke's law, μ is the reduced mass which is given itself by Eq 2.17 with m_1 and m_2 denoting the mass of the oscillating atoms at either end of the bond;

$$Reduced\ Mass = \mu = \frac{m_1 m_2}{m_1 + m_2} \tag{2.17}$$

2.5.2.2 FTIR Setup

The FTIR spectrometer utilises an interferometer, an optical instrument capable of measuring and manipulating the properties of incoming light waves, the most common of which is the Michelson interferometer and is shown in Figure 2.19. The interferometer consists of an IR radiation source, a series of collimators and beam splitters with the final major component being the detector. IR radiation is generated at the source before being passed through a collimating mirror to make the light parallel before it strikes the beamsplitter. The beam is divided into two equal energy beams which travel on different paths after being either reflected or transmitted by the beamsplitter. One of these beams is reflected off of a fixed mirror while the other strikes a moving mirror, both tracing some distance before being reflected back to the beamsplitter. The two beams then recombine where they interfere depending on the difference in path of each and the recombined beam is then passed through the sample as a single wave and finally to the detector. By changing the position of the

moveable mirror throughout the measurement it is ensured that the recombined wave will exhibit an intensity profile consistent with a cosine wave once plotted versus the path difference both beams travelled before recombining. It is this plot of intensity as a function of path difference at a given wavelength which produces the interferogram. Through varying the wavelength of the incident IR radiation multiple interferograms are produced and combined by the detector to produce a complete spectrum. A Fourier transform is used to convert the series of interferograms into an absorption spectrum.
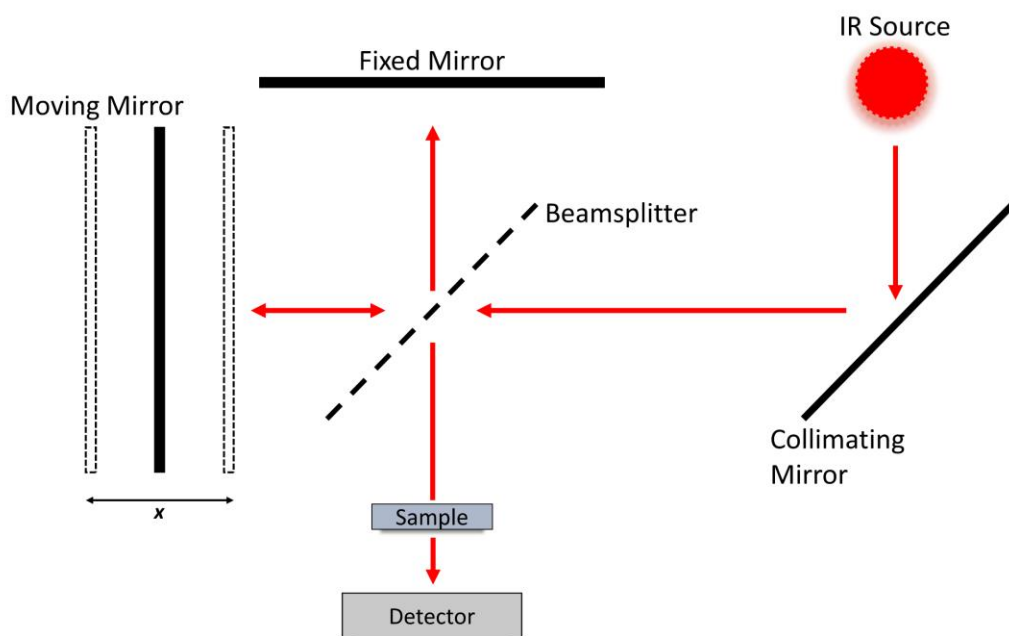
Figure 2.19 Schematic of typical Michelson interferometer components set up for FTIR.

2.5.2.3 Principles of Attenuated Total Reflection

Attenuated total reflectance (ATR) is among the most widely adopted forms of IR spectroscopy which acts to overcome some of the difficulties which arise during FTIR analysis particularly for thin films. As a result of the reduced thickness of thin films and therefore the decreased quantity of molecules available to interact with the IR radiation, the

resultant absorption signal intensity is low and can be indistinguishable among the noise of the spectra. The typical FTIR operational mode is referred to as single pass whereas ATR, using total internal reflection, causes IR radiation to travel through the sample many times as shown in Figure 2.20 thus increasing the distance travelled through a thin film to many times greater than if it just passed a single time. It is the principle of total internal reflection (TIR) which forms the basis of the ATR technique which occurs when light is travelling through an optically dense medium toward a rare medium at an angle of incidence (θ_i) greater than or equal to the critical angle (θ_c). At sites of TIR an evanescent wave is formed in the lower refractive index medium.
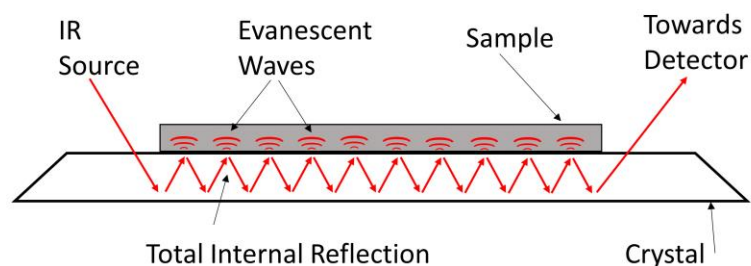
Figure 2.20 Illustration of the IR radiation path travelled in the ATR mode of operation for thin film investigation using FTIR.

As can be seen, the incoming IR beam undergoes TIR causing it to traverse the sample many times. Downward pressure is exerted onto the sample which ensures solid contact between the sample and the underlying material of high refractive index, often a Ge crystal is used to this end. Selecting a material with a high refractive index such as the Ge crystal ensures that the sample in contact with it is lower to enable the TIR mechanism. Upon TIR an evanescent wave is created within the sample which decays exponentially before recombining with the sample and may be partially absorbed by molecules within the sample.

It is the absorption of the evanescent wave which attenuates the TIR beam which is then compared to the background spectrum which the user collects prior to performing the FTIR measurement on the sample. It is the TIR which results in a greater level of absorption by the sample due to repeated evanescent wave interaction which have a penetration depth within a sample ranging from 10 μm to < 1 μm. Through directing the IR radiation at a shallow angle of incidence the FTIR technique can be further improved for thin nanometre scale film studies in what is called grazing angle FTIR (GA-FTIR). This requires analysing the interaction of the IR radiation with a sample when the angle of incidence is close to or near the critical angle needed for TIR which allows for multiple internal reflections thus enhancing sensitivity to surface localised phenomena such as surface reactions and adsorption.

2.6 Atomic Force Microscopy

2.6.1 Overview

Atomic force microscopy (AFM) is a powerful surface sensitive characterisation and imaging technique which allows for the investigation of surfaces at the atomic and molecular scales which yields 3D topographical profiles of a sample surface. The schematic shown in Figure 2.21 shows the basic setup and operating principle of a modern AFM.
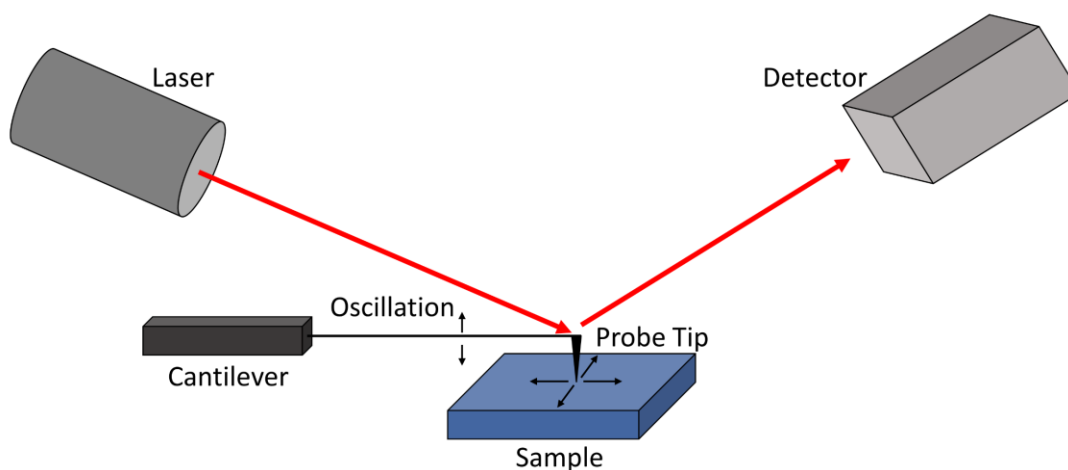
Figure 2.21 Simplified schematic of the AFM set up.

At its core, AFM provides topographical information on a sample through measuring the forces experienced by a sharp probe at the sample surface. The AFM setup consists of a cantilever with a sharp point of radius less than 10 nm attached to its free end and acts as a sort of spring which undergoes deflection as a result of sample interaction either physically or via Van der Waals, electrostatic and magnetic forces. Interatomic forces are exerted when

two materials are brought into close proximity to one another, and AFM operates through measuring these to determine the characteristics of the surface under investigation. The magnitude of these deflections as the cantilever and probe is raster scanned across the surface is quantified through shining a laser onto the back of the cantilever with the light being reflected into a four-quadrant photodetector. The force causing the deflection and up and down movement of the probe causes the reflected laser light to be altered is described using Hooke's law;

$$F = -kx \qquad (2.18)$$

wherein F is the force, k is the spring constant corresponding to the cantilever and x is the deflection experienced by the probe as a function of surface interactions. The force is measured through continually monitoring the variations in the reflected laser light and produces a 3D topographical profile of the scanned area in the nanometre scale.

2.6.2 Technical Details

AFM can be operated in three different modes being contact mode, non-contact mode and tapping mode. Alongside a broader assessment of the topography of a sample surface, AFM can be sued to provide information on the surface roughness which is obtained through AFM height images. This is an important factor for thin film analysis in verifying film homogeneity.

2.6.2.1 Contact Mode

In contact moder the distance between the AFM tip and the sample surface is < 0.5 nm. Through maintaining an extremely low force on the cantilever the tip is pushed against the sample as it raster's across the sample with changes in deflection due repulsion by the sample being monitored and yielding an image of the sample surface. This mode allows for rapid

imaging times however due to being in contact with the sample surface directly is only suitable for hard surfaces which will not become damaged through the contact of the tip.

2.6.2.2 Non-Contact Mode

This mode sees the probe – sample separation being maintained at approximately 0.1 – 10 nm. This results in very weak interactions between the sample and probe which ultimately reduces spatial resolution but is preferential when the sample in question is susceptible to being damaged or deformed were the probe to be in physical contact with it.

2.6.2.3 Tapping Mode

This mode of AFM involves the intermittent contact of the cantilever with the sample surface through oscillating the probe with a frequency of hundreds of kHz close to its resonant frequency which is held constant throughout the measurement via altering the probe – sample separation throughout scanning. The oscillation is produced using a piezoelectric crystal which causes the cantilever to oscillate with a high amplitude of approximately 20 – 100 nm when the tip is not in contact with the sample. As a result of the instantaneous contact time between the probe and the sample, there is insufficient time for the probe to be deflected laterally which enhances resolution. This mode of operation overcomes the issues of sample degradation mentioned in contact mode AFM as the cantilever only makes contact momentarily as the bottom of each oscillation thus preventing damage and contamination and so is suited to scanning of delicate samples which may be sensitive to contamination such as biological samples.

2.7 Photoelectrochemical Cell Testing

2.7.1 Overview

Although a lot of advancement has been made in computational materials science, it remains that the primary tool for investigating the properties and performance of photoelectrodes is photocurrent measurements within the simulated environment of the photoelectrochemical cell. The best test for a PEC device or candidate electrode material is establishing its behaviour and electrical performance under simulated solar irradiation. Figure 2.22 details an overview of the primary components in PEC measurements.
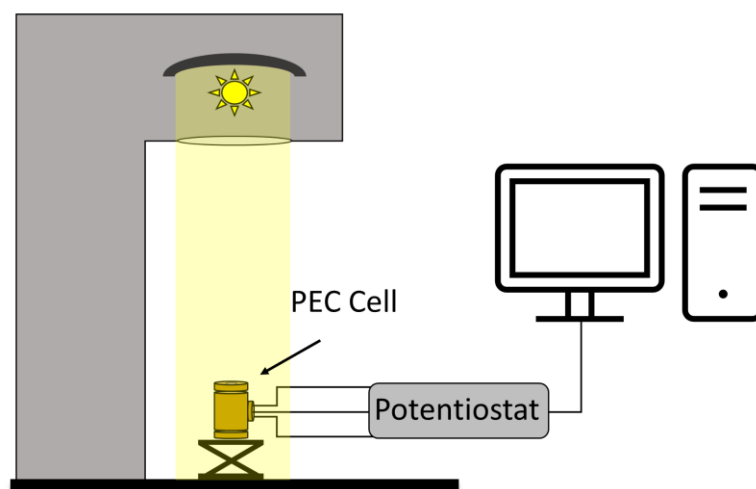
Figure 2.22 Typical experimental setup for PEC testing showing the simulated sun irradiating the PEC cell in the three-electrode configuration.

From Figure 2.22 it can be seen that the entire apparatus is centred around the photoelectrochemical cell (PEC cell) in which the photoanode or photocathode sample is mounted for testing. The PEC cell in its simplest form consists of a volume of electrolyte

solution, the sample under investigation, which is referred to as the working electrode, a counter electrode which supplies current to the system, a reference electrode and a transparent window which admits solar irradiance to the sample surface. A schematic of the PEC cell used in this work is shown in Figure 2.23. The PEC cell has many more complex forms which implement additional electrodes for further measurement techniques and often gas circulation and purging mechanisms to rid the electrolyte of gas build up during extended electrochemical testing.
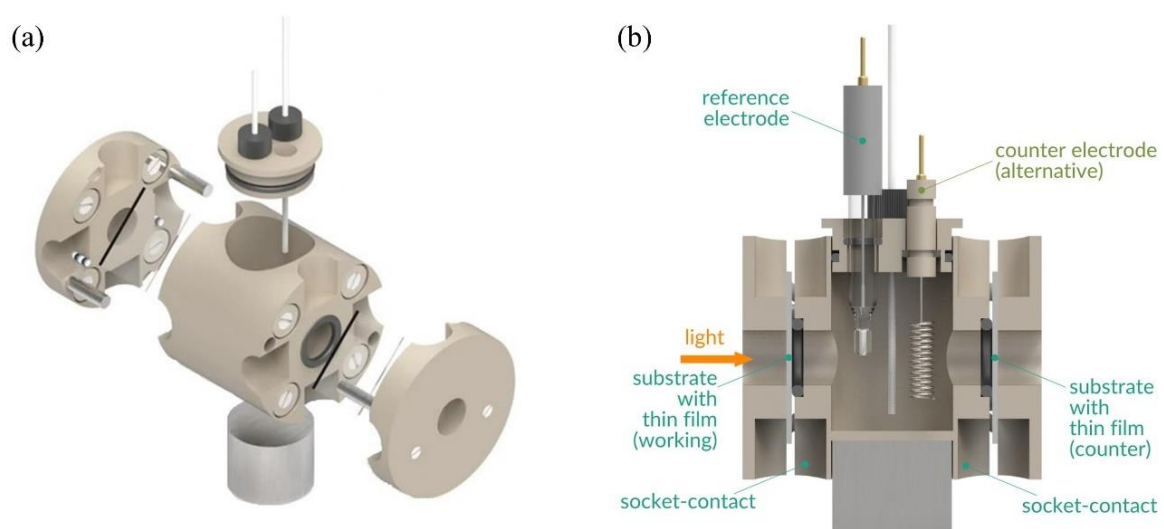
Figure 2.23 Adapted manufacturer illustrations of the PEC device used within this work (a) an exploded view detailing assembly and insertion of transparent window and sample for measurement [48] *and (b) a cross section wherein the inner workings of the PEC cell are shown indicating the immersion of the counter and reference electrodes within the electrolyte solution with the surface of the sample being measured also in contact with the solution* [48].

Due to the impracticalities of testing using natural sunlight, PEC laboratory setups utilise a solar simulator which provides high intensity light usually 1000 W/m^2 which corresponds to 1 sun at AM1.5G. This AM1.5G stands for Air Mass 1.5 Global which refers to the spectral distribution and intensity of solar irradiance on a south-facing surface which has been tilted

to 37° after travelling through 1.5 times the thickness of the earth's atmosphere. AM1.5G is a benchmark standard reference spectrum used in the PEC and PV fields to represent the average solar irradiance at sea level with the sun at an average angle of 48.2° above the horizon and allows for meaningful comparisons of device performances from various labs. Looking to Figure 2.22 once more, among the most important components of the PEC apparatus is the potentiostat. Most potentiostats, including the one used in this work, have three test leads which consist of the working, reference and counter electrodes denoted as WE, REF and CE respectively. The role of the potentiostat is to control the potential difference between the WE and REF with the WE being the photoelectrode under investigation.

This is performed through applying a controlled voltage or potential to the reference electrode, the voltage of which can be set to a specific value or varied over a range of values to assess the photoelectrode response and performance. The role of the REF is to act as to act as the reference in measuring and controlling the potential of the WE without passing any current. The control and feedback units within the potentiostat ensure the potentiostat continuously adjusts the current flowing through the WE to maintain the user defined potential.

2.7.2 Photocurrent – Voltage Sweeps (Voltammetry)

2.7.2.1 Theoretical Basics

IV measurements are the most important method of PEC performance determination which allows for the investigation of the performance characteristics of photoanodes or photocathodes [49]. These PEC IV measurements allow for the acquisition and determination of the following;

- Photocurrent density as a function of applied potential

- Dark current as a function of applied potential

- Photocurrent onset potential

- Transport limitations of electrons and holes

In the three-electrode configuration of the PEC testing apparatus the reference electrode is used rather obviously to provide the reference potential for the system. Then using a potentiostat the working electrode, which as mentioned is the photoelectrode under scrutiny, has a potential set against the reference electrode which is fixed and the current at the potential is measured. In this measurement the performance of the counter electrode is unimportant and the potentiostat is used to maintain the potential of the working electrode at the user defined value and gives a read out of the current at that potential and supplies whatever voltage between the working and counter electrodes to maintain that current [50].

These measurements are performed through measuring the output photocurrent while sweeping across a range of potentials. This can be performed under solar illumination, in the dark, or a combination of the two by chopping the light on and off at a fixed frequency throughout the scan. In linear sweep voltammetry the potential is swept from the starting user defined potential E_1 to some end potential E_2, if at E_2 the scan is reversed back to E_1

while maintaining the same scan rate the technique is referred to as cyclic voltammetry. Scans are recorded as current vs potential and both linear and cyclic variations of voltammetry testing are used to evaluate the photoelectrochemical activity of a material being tested for its application as a HER or OER candidate. Through comparing reference voltammograms of the bare substrate on its own against a material under investigation materials are screened for their catalytic and protective characteristics.

By plotting the photocurrent as a function of varying applied voltages PEC IV curves provide a range of information about the overall performance of a PEC system. Firstly, the measurement allows for the determination of the photocurrent density which represents the current produced by the PEC photoelectrode per unit area with higher photocurrent output indicating more efficient utilization of the oncoming incident light thus leading to a better performing water splitting device.

2.7.3 Time Degradation Testing (Chronoamperometry)

2.7.3.1 Theoretical Basics

Chronoamperometry (CA) is commonly referred to as time degradation testing as it evaluates the photoelectrochemical performance of a sample as a function of time such as to determine its stability under real world conditions and involves monitoring the cells performance over an extended period of time under continuous illumination. CA testing involves applying a constant user defined potential across the WE and measuring the corresponding change in current as a function of time. CA testing is used in the investigation of electrochemical reaction kinetics as well as to establish electrode stability and evaluate response to changes in current or potential. The primary objective for CA testing is the determination of the cells long term stability and durability.

2.7.4 Efficiency Determination

Within the field of water splitting various practices have been developed for testing measurements and environments which therefore makes it essential to have standardized methods for the evaluation and comparison of their efficiency of a wide variety of PEC testing set ups. This being said, as a result of the complexity and multifaceted nature of the PEC process there have been several efficiency definitions devised such as to capture the various aspects of the system performance. for a fair and accurate evaluation several efficiency metrics have been developed with some of the most commonly used and widely accepted variants are described herein.

The first and potentially the most commonly cited is the Solar-to-Hydrogen (STH) Efficiency which represents the fraction of the incoming solar energy which has been effectively converted to chemical energy in the form of hydrogen gas. It is deemed a comprehensive metric which considers the light absorption efficiency as well as the efficiency of converting the now absorbed photons into hydrogen as it is a crucial parameter for the evaluation of the overall photoelectrochemical performance of the PEC cell. STH efficiency is the single value which can be applied in the comparison of all PEC devices and is therefore the benchmark value with the methods described to follow being defined as demonstrated research efficiency [51].

Following on from the STH method, the Incident-Photon-to-Current-Efficiency (IPCE) is a measure of the efficiency with which the incident photons are converted into electrical current within the cell. This parameter quantifies the cell's ability to absorb photons and generate the charge carriers necessary for efficiency water splitting and adds in providing information on the light harvesting efficiency across various wavelengths. This IPCE is often

applied in the assessment of specific photoactive materials for electrode fabrication. IPCE is the efficiency of the overall process taking into consideration the efficiency of light absorption, charge carrier generation and injection ultimately describing the ratio of output electrons to input photons which is unlike STH which ratios the incoming light energy to outgoing chemical energy.

Quantum efficiency (QE) is the last of the most popular efficiency measurements and measures the efficiency of the PEC cell in generating chare carriers as a function of incoming photons. This acts to quantify the absorption efficiency of a given material and offers insights into the overall performance of the system at a variety of wavelengths.

The Energy Conversion Efficiency (ECE) represents the ratio of the energy stored in the chemical products, being the hydrogen and oxygen, to the total incident solar energy. This considers the electrical and thermal energy contributions and provides a measure of how effectively the PEC cell converts the incoming solar energy into chemical energy.

Faradaic efficiency (FE) is concerned with the fraction of the total charge which is involved in the desired photoelectrochemical reaction compared to the quantity of energy used in side reactions or losses within the system. FE quantifies the electrochemical reaction efficiency at the electrodes toward measuring the selectivity of the PEC cell towards the desired product of either hydrogen or oxygen.

All of these metrics for efficiency allow for the assessment of a variety of aspects of the PEC water splitting process which aids in a comprehensive understanding of the performance of a given system and allows for the comparison with different systems and the identification of areas for improvement which can lead to more efficient and sustainable PEC architectures.

As mentioned, the STH efficiency is the most important of the evaluation methods and as such will be developed further here. To recap the STH efficiency details the overall efficiency of a PEC system being defined as the ratio of the stored chemical energy in the hydrogen gas formed to the overall solar energy input under zero bias. The stored chemical energy in the generated hydrogen gas may be calculated from the product rate of hydrogen production (r_{H_2}) and the change in Gibbs free energy (ΔG) per mol of H_2 – this is divided by the product of the solar energy illumination power density (P) and the illuminated electrode area (S) as described in Eq 2.19 [52];

$$STH\ Efficiency\ =\ \frac{r_{H_2} \times \Delta G}{P \times S}$$ (2.19)

It is also possible to express the stored chemical energy as a product of the current voltage and faradaic efficiency for hydrogen evolution given in its new form in Eq 2.20;

$$STH\ Efficiency\ =\ \frac{1.23 \times J \times \eta}{P}$$ (2.20)

The 1.23 constant is the thermodynamic water splitting potential with J being the photocurrent density without an applied voltage and η is the faradaic efficiency and P is still the power density as in Eq 2.19 [52].

Although the highlighted metrics play a crucial role in evaluating the efficiency of solar-to-hydrogen conversion, it is important to acknowledge that they are not employed in this study due to their inability to be accurately calculated for a single electrode configuration. In lieu of reporting misleading efficacy claims, the performance of (PEC) electrodes is assessed and analysed comparatively using current-voltage (IV) and chronoamperometry (CA) measurements. These measurements allow for an investigation into the influence of different protective layer materials on the current and stability of PEC photoelectrodes.

2.8 References

(1)   Cumpson, P. J.; Zalm, P. C. Thickogram: A Method for Easy Film Thickness Measurement in XPS. *Surf. Interface Anal.* **2000**, *29* (6), 403–406. https://doi.org/10.1002/1096-9918(200006)29:6<403::AID-SIA884>3.0.CO;2-8.

(2)   Instruments, O.; Technology, P. Oxford Instruments Plasma Technology. *Technology* **1996**, *7* (383).

(3)   Watts, F.; Wolstenholme, J. *Surface Analysis by XPS and AES*; 2015; Vol. 1.

(4)   Stevie, F. A.; Donley, C. L. Introduction to X-Ray Photoelectron Spectroscopy. *J. Vac. Sci. Technol. A* **2020**, *38* (6), 063204. https://doi.org/10.1116/6.0000412.

(5)   Alov, N. V. Fifty Years of X-Ray Photoelectron Spectroscopy. *J. Anal. Chem.* **2005**, *60* (3), 297–300. https://doi.org/10.1007/s10809-005-0087-9.

(6)   Morales-Guio, C. G.; Mayer, M. T.; Yella, A.; Tilley, S. D.; Grätzel, M.; Hu, X. An Optically Transparent Iron Nickel Oxide Catalyst for Solar Water Splitting. *J. Am. Chem. Soc.* **2015**, *137* (31), 9927–9936. https://doi.org/10.1021/jacs.5b05544.

(7)   Hannula, M.; Ali-Löytty, H.; Lahtonen, K.; Sarlin, E.; Saari, J.; Valden, M. Improved Stability of Atomic Layer Deposited Amorphous TiO2 Photoelectrode Coatings by Thermally Induced Oxygen Defects. *Chem. Mater.* **2018**, *30* (4), 1199–1208. https://doi.org/10.1021/acs.chemmater.7b02938.

(8)   *Physical Chemistry*; 1961; Vol. 272. https://doi.org/10.1016/0016-0032(61)90576-2.

(9)   Himpsel, F. J.; McFeely, F. R.; Taleb-Ibrahimi, A.; Yarmoff, J. A.; Hollinger, G. Microscopic Structure of the SiO2/Si Interface. *Phys. Rev. B* **1988**, *38* (9), 6084–6096. https://doi.org/10.1103/PhysRevB.38.6084.

(10)   NIST X-ray Photoelectron Spectroscopy (XPS) Database, Version 3.5 https://srdata.nist.gov/xps/Default.aspx (accessed May 5, 2023).

(11)   Mulliken, R. S. A New Electroaffinity Scale; Together with Data on Valence States and on Valence Ionization Potentials and Electron Affinities. *J. Chem. Phys.* **1934**, *2* (11), 782–793. https://doi.org/10.1063/1.1749394.

(12)   Pauling, L.; Wheland, G. W. The Nature of the Chemical Bond. V. *J. Chem. Phys.* **1934**, *2* (8), 482. https://doi.org/10.1063/1.1749514.

(13)   Kokkonen, E.; Kaipio, M.; Nieminen, H. E.; Rehman, F.; Miikkulainen, V.; Putkonen, M.; Ritala, M.; Huotari, S.; Schnadt, J.; Urpelainen, S. Ambient Pressure X-Ray

Photoelectron Spectroscopy Setup for Synchrotron-Based in Situ and Operando Atomic Layer Deposition Research. *Rev. Sci. Instrum.* **2022**, *93* (1). https://doi.org/10.1063/5.0076993.

(14) Trotochaud, L.; Head, A. R.; Karslioğlu, O.; Kyhl, L.; Bluhm, H. Ambient Pressure Photoelectron Spectroscopy: Practical Considerations and Experimental Frontiers. *J. Phys. Condens. Matter* **2017**, *29* (5), 0–71. https://doi.org/10.1088/1361-648X/29/5/053002.

(15) Fellner-Feldegg, H.; Siegbahn, H.; Asplund, L.; Kelfve, P.; Siegbahn, K. ESCA Applied to Liquids IV. A Wire System for ESCA Measurements on Liquids. *J. Electron Spectros. Relat. Phenomena* **1975**, *7* (5), 421–428. https://doi.org/https://doi.org/10.1016/0368-2048(75)85006-7.

(16) Siegbarn, H.; Asplund, L.; Kelfve, P.; Hamrin, K.; Karlsson, L.; Siegbahn, K. ESCA Applied to Liquids. II. Valence and Core Electron Spectra of Formamide. *J. Electron Spectros. Relat. Phenomena* **1974**, *5* (1), 1059–1079. https://doi.org/https://doi.org/10.1016/0368-2048(74)85065-6.

(17) Siegbahn, H.; Siegbahn, K. ESCA Applied to Liquids. *J. Electron Spectros. Relat. Phenomena* **1973**, *2* (3), 319–325. https://doi.org/https://doi.org/10.1016/0368-2048(73)80023-4.

(18) Siegbahn, H.; Asplund, L.; Kelfve, P.; Siegbahn, K. Esca Applied to Liquids III. ESCA Phase Shifts in Pure and Mixed Organic Solvents. *J. Electron Spectros. Relat. Phenomena* **1975**, *7* (5), 411–419. https://doi.org/https://doi.org/10.1016/0368-2048(75)85005-5.

(19) Starr, D. E.; Bluhm, H.; Liu, Z.; Knop-gericke, A.; Hävecker, M. APPLICATION OF AMBIENT-PRESSURE X-RAY PHOTOELECTRON SPECTROSCOPY FOR THE IN-SITU INVESTIGATION OF HETEROGENEOUS CATALYTIC REACTIONS. 315–343.

(20) Vickerman, J. C.; Gilmore, I. S. *Surface Analysis - The Principal Techniques: Second Edition*; 2009. https://doi.org/10.1002/9780470721582.

(21) Bogan, J. Growth and Chemical Characterisation Studies of Mn Silicate Barrier Layers on SiO2 and CDO, Dublin City University, 2012.

(22) Snelgrove, M. Characterising Infiltration Techniques in Polymer Science for Area

Selective Deposition, Dublin City Univsersity, 2021.

(23) Anderson, S. G.; Sohlberg, K. W.; Howard, S. L.; Shukla, A. K.; Futrell, J. H. A High Transmission Hemispherical Energy Analyzer for Ion Spectrometry. *J. Am. Soc. Mass Spectrom.* **1991**, *2* (6), 506–510. https://doi.org/10.1016/1044-0305(91)80039-A.

(24) Nefedov, V. . *X-Ray Photoelectron Sepctroscopy of Solid Surfaces*; CRC Press.

(25) Wagner, C. D.; Davis, L. E.; Zeller, M. V; Taylor, J. A.; Raymond, R. H.; Gale, L. H. Empirical Atomic Sensitivity Factors for Quantitative Analysis by Electron Spectroscopy for Chemical Analysis. *Surf. Interface Anal.* **1981**, *3* (5), 211–225. https://doi.org/https://doi.org/10.1002/sia.740030506.

(26) Coster, D.; L. Kronig, R. De. New Type of Auger Effect and Its Influence on the X-Ray Spectrum. *Physica* **1935**, *2* (1–12), 13–24. https://doi.org/10.1016/S0031-8914(35)90060-X.

(27) Hantsche, H. High Resolution XPS of Organic Polymers, the Scienta ESCA300 Database. By G. Beamson and D. Briggs, Wiley, Chichester 1992, 295 Pp., Hardcover, £ 65.00, ISBN 0-471-93592-1. *Advanced Materials*. 1993, pp 778–778. https://doi.org/10.1002/adma.19930051035.

(28) Briggs, D.; Seah, M. . *Practical Surface Analysis*, Second.; Wiley & Sons, 1994.

(29) Engelhard, M. H.; Baer, D. R.; Herrera-Gomez, A.; Sherwood, P. M. A. Introductory Guide to Backgrounds in XPS Spectra and Their Impact on Determining Peak Intensities. *J. Vac. Sci. Technol. A* **2020**, *38* (6), 063203. https://doi.org/10.1116/6.0000359.

(30) Sherwood, P. M. A. The Use and Misuse of Curve Fitting in the Analysis of Core X-Ray Photoelectron Spectroscopic Data. *Surf. Interface Anal.* **2019**, *51* (6), 589–610. https://doi.org/10.1002/sia.6629.

(31) Proctor, A.; Sherwood, P. M. A. Data Analysis Techniques in X-Ray Photoelectron Spectroscopy. *Anal. Chem.* **1982**, *54* (1), 13–19. https://doi.org/10.1021/ac00238a008.

(32) Sherwood, P. M. A. Curve Fitting in Surface Analysis and the Effect of Background Inclusion in the Fitting Process. *J. Vac. Sci. Technol. A Vacuum, Surfaces, Film.* **1996**, *14* (3), 1424–1432. https://doi.org/10.1116/1.579964.

(33) X-ray Photoelectron Spectroscopy (XPS) Reference Pages: Precision and Accuracy in XPS http://www.xpsfitting.com/2011/09/precision-and-accuracy-in-xps.html

(accessed Aug 25, 2023).

(34) X-ray Photoelectron Spectroscopy (XPS) Reference Pages: Backgrounds http://www.xpsfitting.com/search/label/Backgrounds (accessed Aug 25, 2023).

(35) Briggs, D. X-Ray Photoelectron Spectroscopy (XPS). *Handb. Adhes. Second Ed.* **2005**, 621–622. https://doi.org/10.1002/0470014229.ch22.

(36) Greczynski, G.; Hultman, L. Towards Reliable X-Ray Photoelectron Spectroscopy: Sputter-Damage Effects in Transition Metal Borides, Carbides, Nitrides, and Oxides. *Appl. Surf. Sci.* **2021**, *542*. https://doi.org/10.1016/j.apsusc.2020.148599.

(37) BNL | About NSLS-II https://www.bnl.gov/nsls2/about-nsls-ii.php (accessed Aug 8, 2023).

(38) Woicik, J. *Hard X-Ray Photoelectron Spectroscopy (HAXPES)[1] J. Woicik, Hard X-Ray Photoelectron Spectroscopy (HAXPES). Nueva York: Springer, 2016.*; 2016.

(39) Cui, F.; Zhang, Y.; Fonseka, H. A.; Promdet, P.; Channa, A. I.; Wang, M.; Xia, X.; Sathasivam, S.; Liu, H.; Parkin, I. P.; Yang, H.; Li, T.; Choy, K. L.; Wu, J.; Blackman, C.; Sanchez, A. M.; Liu, H. Robust Protection of III-V Nanowires in Water Splitting by a Thin Compact TiO_2 Layer. *ACS Appl. Mater. Interfaces* **2021**, *13* (26), 30950–30958. https://doi.org/10.1021/acsami.1c03903.

(40) Li, L. F.; Li, Y. F.; Liu, Z. P. CO_2 Photoreduction via Quantum Tunneling: Thin TiO_2-Coated GaP with Coherent Interface to Achieve Electron Tunneling. *ACS Catal.* **2019**, *9* (6), 5668–5678. https://doi.org/10.1021/acscatal.9b01645.

(41) Hu, S.; Shaner, M. R.; Beardslee, J. A.; Lichterman, M.; Brunschwig, B. S.; Lewis, N. S. Amorphous TiO_2 Coatings Stabilize Si, GaAs, and GaP Photoanodes for Efficient Water Oxidation. *Science (80-.).* **2014**, *344* (6187), 1005–1009. https://doi.org/10.1126/science.1251428.

(42) Scheuermann, A. G.; Prange, J. D.; Gunji, M.; Chidsey, C. E. D.; McIntyre, P. C. Effects of Catalyst Material and Atomic Layer Deposited TiO_2 Oxide Thickness on the Water Oxidation Performance of Metal-Insulator-Silicon Anodes. *Energy Environ. Sci.* **2013**, *6* (8), 2487–2496. https://doi.org/10.1039/c3ee41178h.

(43) Cao, S.; Kang, Z.; Yu, Y.; Du, J.; German, L.; Li, J.; Yan, X.; Wang, X.; Zhang, Y. Tailored TiO_2 Protection Layer Enabled Efficient and Stable Microdome Structured P-GaAs Photoelectrochemical Cathodes. *Adv. Energy Mater.* **2020**, *10* (9), 1–7.

https://doi.org/10.1002/aenm.201902985.

(44)   Hill, J. M.; Royce, D. G.; Fadley, C. S.; Wagner, L. F.; Grunthaner, F. J. Properties of Oxidized Silicon as Determined by Angular-Dependent X-Ray Photoelectron Spectroscopy. *Chem. Phys. Lett.* **1976**, *44* (2), 225–231. https://doi.org/10.1016/0009-2614(76)80496-4.

(45)   Tompkins, H. G.; Hilfiker, J. N. *Spectroscopic Ellipsometry - Practical Application to Thin Film Characterization*; 2016.

(46)   Azzam, R. M. A. Arrangement of Four Photodetectors for Measuring the State of Polarization of Light. *Opt. Lett.* **1985**, *10* (7), 309. https://doi.org/10.1364/ol.10.000309.

(47)   Hilfiker, J. N.; Tiwald, T. Dielectric Function Modeling. In *Spectroscopic Ellipsometry for Photovoltaics: Volume 1: Fundamental Principles and Solar Cell Characterization*; Fujiwara, H., Collins, R. W., Eds.; Springer International Publishing: Cham, 2018; pp 115–153. https://doi.org/10.1007/978-3-319-75377-5_5.

(48)   redox.me   https://redox.me/collections/photo-electrochemical-cells/products/mm-pec-15-ml-double-sided-magnetic-mount-photo-electrochemical-cell (accessed May 25, 2023).

(49)   Van De Krol, R.; Grätzel, M. *Photoelectrochemical Hydrogen Production*, First.; Krol, R. van de, Gra¨tzel, M., Eds.; Springer US. https://doi.org/10.1007/978-1-4614-1380-6.

(50)   Hodes, G. Photoelectrochemical Cell Measurements: Getting the Basics Right. *J. Phys. Chem. Lett.* **2012**, *3* (9), 1208–1213. https://doi.org/10.1021/jz300220b.

(51)   Sankir, N. D.; Sankir, M. *Photoelectrochemical Solar Cells: Advances in Solar Cell Materials and Storage*; 2018.

(52)   Holmes-Gentl, I.; Alhersh, F.; Bedoya-Lora, F.; Klaus Hellgardt, D. of C. E. I. C. L. *Photoelectrocchemical Solar Cells*, First.; Nurdan Sankir, M. S., Ed.; Wiley & Sons, 2018. https://doi.org/10.1016/B978-0-12-814134-2.00028-0.

3 Deposition and Characterisation of TiO_2 Thin Films from Amide and Alkoxide Precursors for Photoelectrode Passivation

3.1 Introduction

This chapter presents the results of the growth and characterisation of TiO_2 thin films for the passivation and protection of silicon photoelectrodes during solar water splitting. Firstly, the characterisation of the deposited films is discussed before the effects of the use of such films on the performance of the photoelectrodes during simulated water splitting in the PEC testing is shown.

The particular focus of this chapter is to detail an in-line x-ray photoelectron spectroscopy analysis of the nucleation and growth of ultra-thin (ca. 2nm) TiO_2 films on silicon from two ALD precursor molecules, titanium isopropoxide (TTIP) and tetrakis(dimethylamido)titanium (TDMAT). This investigation focuses on the impact of precursor choice, and the use of thermal ALD (TALD) vs plasma-enhanced ALD (PEALD), on the chemistry of the produced films, and how this impacts the photoelectrochemical performance of silicon photoanodes.

ALD of TiO_2 was performed in a unique, custom-designed Oxford Instruments ALD reactor which is coupled in-vacuum to a Scienta Omicron monochromated X-ray photoelectron spectrometer (XPS) by a fast-transfer robotic handler. This setup allows for rapid cycle-by-cycle XPS analysis of the ALD films during nucleation and growth, and a robust comparison of process parameters.

The results in this chapter show significant differences in film chemistry between PEALD and TALD derived films, including reduced ligand incorporation and increased interaction

with the underlying silicon - identified as titanium suboxide formation during PEALD. There are also subtle differences between the chemistry of the films resulting from the two precursors.

Photoelectrochemical testing also shows some differences in photo-current between the processes. In all cases, following an appraisal of the photo-electrochemical performance of the as-deposited layers, the films were exposed to a post deposition H_2 plasma anneal and a high-temperature air anneal in order to examine the effect of annealing on the individual ALD films, and how the annealing impacts photoelectrochemical performance and stability. Results show good correlation to those observed by Hannula et al for much thicker (ca 30 nm) films.

3.2 Experimental Details

3.2.1 ALD

Atomic layer deposition took place in an Oxford Instruments FlexAl ALD Reactor (base pressure $3.8 \times 10^{-7} Torr$), using titanium isopropoxide [TTIP, Sigma Aldrich 97%, Figure 3.1 (a)] and tetrakis(dimethylaminol) titanium [TDMAT, Sigma Aldrich 99.999 Figure 3.1 (b)] as precursors and H_2O and O_2 ICP generated plasma as co-reactants for TALD and PEALD, respectively. The substrate was heated to 270°C and 250°C for plasma and thermally grown films, respectively. The recipes, as shown in *Table 3.1 ALD deposition parameters detailing individual process recipes with P and T referring to either the PEALD or thermal deposition processes respectively.*, were designed based on the ALD tool manufacturer's optimized recipes. Bubbler and purge flows were carried out using Ar at 100 sccm and 200 sccm respectively. Resulting growth rates are reported in the 'Results and Discussion' section.
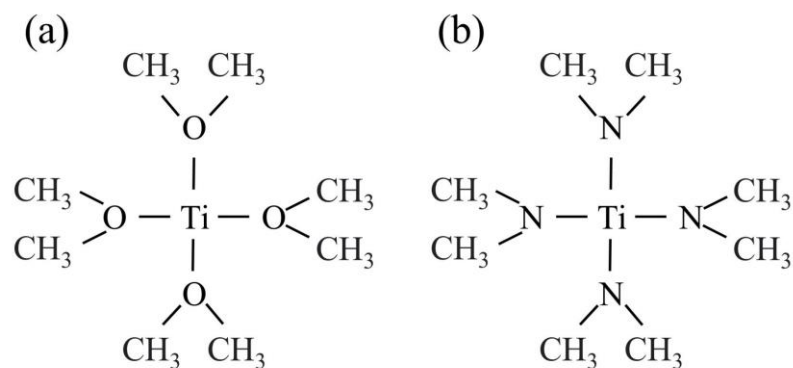
Figure 3.1 Precursor molecules utilised (a) titanium isopropoxide (TTIP) (b) tetrakis(dimethylaminol) titanium (TDMAT).

TiO$_2$ films were deposited on n-Si (100) ($\rho = 5 - 9 \, \Omega cm^2$). Samples were cut from the wafer in 2.5 × 2.5 cm^2 coupons. Prior to ALD processing, samples were exposed for 5 minutes to a 300 W RF remote H$_2$ ICP plasma in the FlexAl ALD deposition chamber in order to remove adventitious carbon and increase surface hydroxyl groups to improve nucleation during the ALD process.

Table 3.1 ALD deposition parameters detailing individual process recipes with P and T referring to either the PEALD or thermal deposition processes respectively.

Variable	TDMAT-P	TDMAT-T	TTIP-P	TTIP-T
Precursor Dose	0.5	1	2	2
Precursor Purge	3	5	6	5
Co-reactant Dose	4	0.15	5	0.15
Co-reactant Purge	2	0.02	4	20
Deposition Temp	270	250	270	250

3.2.2 FTIR

Grazing-angle ATR FTIR was performed using a Nicolet iS50 FTIR Spectrometer in conjunction with a Harrick VariGATR attachment. The germanium crystal was cleaned using butanone which removed any contaminants prior to a background scan being taken. Samples were placed face down on the crystal and a force of ~700N was applied to ensure good contact between the sample and crystal. A total of 128 scans were performed per sample at an 8cm^{-1} resolution with an unpolarized angle of incidence of 65°.

3.2.3 XPS

The primary characterisation technique employed in this investigation is X-ray photoelectron spectroscopy (XPS), which allowed for chemical composition and thickness determination of the TiO$_2$ films. XPS was performed using a Scienta Omicron XPS (Monochromated Al

Kα source, base pressure of 6.5×10^{-7} Pa) with a 128 channel Argus CU detector. The XPS is coupled in-vacuum by a robotic wafer handler allowing for sample transfer from ALD to XPS in approximately 1 minute without the need for breaking vacuum. Survey scan and high-resolution spectra were taken at normal emission from the sample using 1 and 0.1 eV step sizes, respectively. All spectral fits utilised a Shirley – Sherwood type background in conjunction with Voigt profiles. XPS data analysis was carried out using Aanalyzer fitting software with photoemission peaks shifted in accordance with the Si^0 $2p_{3/2}$ signal at 99.4 eV binding energy (BE) [1, 2].

3.2.4 AFM

Morphological images were obtained using a Bruker Icon Atomic Force Microscope (AFM) in tapping mode operation. Data were collected from a surface area of 1×1 μm^2 at 256 Samples/Line. Studies were performed in air using Si cantilevers with a 30nm Al reflex coating with a tip radius of < 10nm. Acquired AFM and root mean squared (RMS) surface roughness were treated by Gwyddion analysis software [3].

3.2.5 Photoelectrochemical Testing

Photoelectrochemical cell testing was carried out in a Redoxme AB MM 15 ml double-sided photoelectrochemical cell with a Pt counter electrode (99.9%) and a Ag/AgCl (1 mol KCl) reference electrode. The electrolyte was a 0.5 M phosphate buffer solution (pH 7.4). The electrodes were irradiated with 1000W/m^2 AM 1.5 G simulated sunlight from an Oriel Instruments xenon arc lamp solar simulator in a top-down configuration with 1cm^2 of illuminated sample area during testing. Linear sweep voltammetry (*I-V)* testing is performed for the acquisition of key photoanode material characteristics such as photocurrent density, onset potential and dark current outputs as a function of an applied potential [4].

In this study, samples were studied under constant illumination. In addition to this linear sweep voltammetry, chronoamperometric detection was also carried out on separate samples to those which had been *I-V* tested. Amperometry involves the application of a constant potential to a working electrode and the measurement of the output steady – state current [5]. Samples in this investigation were subjected to this constant potential for 100 seconds which offers some insight into the potential durability of the photoanodes.

3.3 Results

3.3.1 FTIR

Figure 3.2 shows the FTIR absorbance spectra for the four-deposition processes *as-deposited*. The four deposition processes consist of growing 2 nm films using both TDMAT and TTIP via thermal and plasma enhanced ALD. Resulting FTIR spectra are similar for all TiO_2 growth processes. Marginal deviations are observed in carbon and oxygen bonding with additional C = O observed in TDMAT PEALD which correlates with XPS analysis of the C1s region shown later in this study.

The dominant peak in the spectra shown in Figure 3.2 occurs at 877 cm^{-1}, representing Ti – O – Si bonds, which confirms a chemical interaction between the deposited TiO_2 films and the underlying SiO_2 [6]. The shoulder feature at 728 cm^{-1} corresponds to Ti – O bonds with Si – O observed at 825cm^{-1} [7]. A peak at 1172 cm^{-1} is attributed to C – O stretching bonds linked to the TiO_2 film. The spectrum features peaks at 1452 cm^{-1} and 1644 cm^{-1}, which are in line with expected values for OH groups (hydroxyls) [6]. These peaks indicate the chemisorption of O – H molecules in the deposited TiO_2 overlayer. The broad band from 3000 – 3640 cm^{-1} also indicates strong interactions through hydrogen bonding between the TiO_2 film and surface hydroxyls [7].
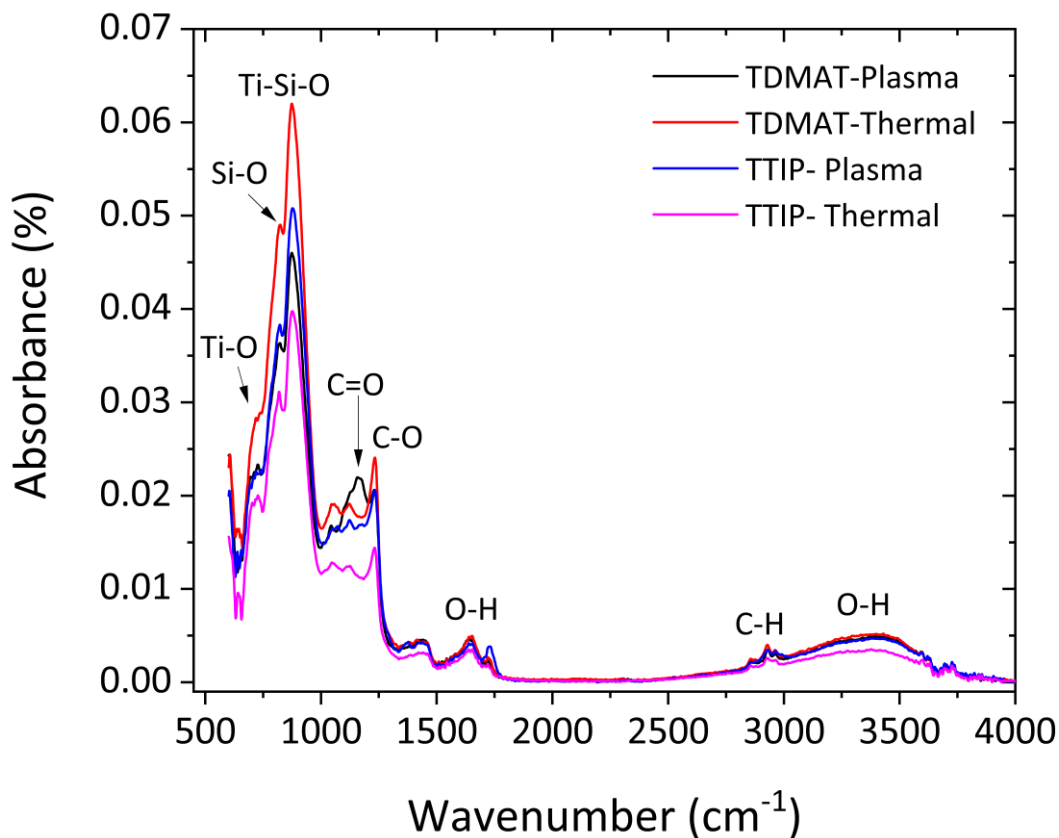
Figure 3.2: FTIR spectra of as deposited TiO$_2$ films from all deposition processes.

3.3.2 XPS

XPS analysis was carried out on samples *as loaded* as well as following a plasma cleaning step prior to ALD to prepare samples for deposition. In addition to this, samples were later subjected to annealing treatments both *in* and *ex-situ* and again photoemission analysis was performed to study effects of the post-deposition treatments. As deposited samples were analysed using AFM to check for agglomerations on the film surfaces and also showed highly uniform surfaces with 102.5pm, 144.3 pm, 87.95 pm and 178.2pm for TDMAT plasma grown (TD-P), TDMAT thermally grown (TD-T), TTIP plasma grown (TT-P) and TTIP

thermally grown (TT-T) respectively, as shown in Figure 3.3. It is evident from Figure 3.3 that the PEALD process yields smoother films a benefit stemming from the enhanced reactivity of the process due to the higher energy providing higher energy to reactive species aiding in mobility and diffusion thus aiding in improved surface coverage, film-substrate adhesion and surface cleaning through a reduction of surface localized contaminants allowing for the densification of deposited films [8].
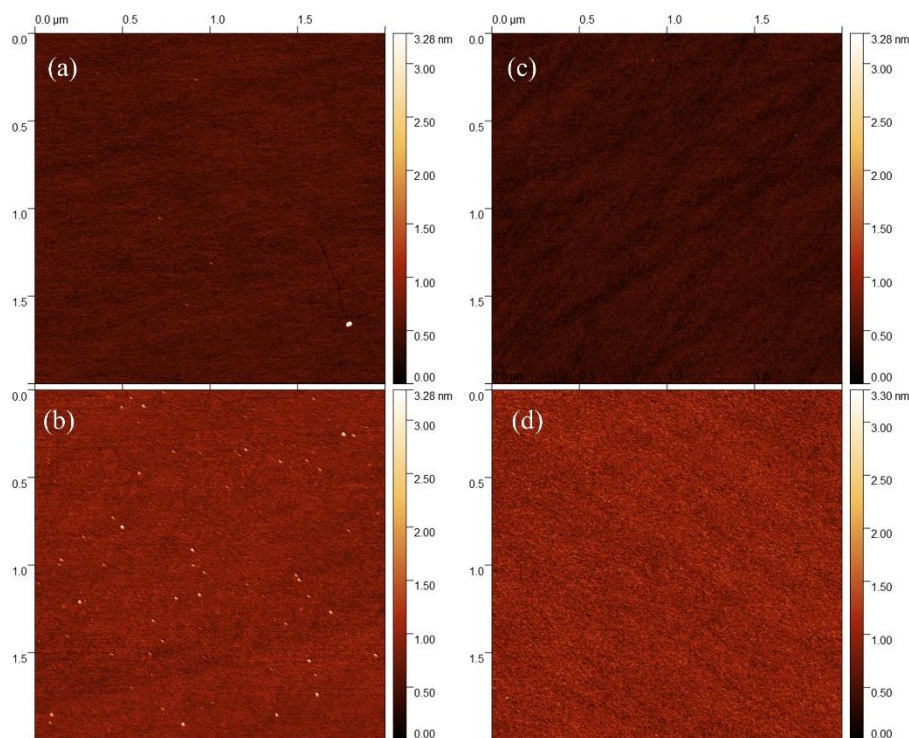
Figure 3.3 AFM images showing all four growth processes in their as deposited states (a) TDMAT PEALD, (b) TDMAT TALD, (c) TTIP PEALD and (d) TTIP TALD. Mean Roughness values were as follows; 74.3pm, 108.7pm, 69.7pm and 141.7pm for TD-P, TD-T, TT-P and TT-T respectively.

In order to develop an understanding of the early-stage growth kinetics for each process and for accurate determination of growth per cycle (GPC) rates, a set of films were grown sequentially, with the deposition process periodically interrupted so that they could be

analysed using the integrated XPS. Attention was focused primarily on the Si $2p$, Ti $2p,$ C $1s$ and O $1s$ core levels to monitor for any development of additional oxidation states in the case of Ti $2p$ or evidence of titanium silicate formation for low cycle numbers in the Si $2p$ peak. This is particularly important, as hole transport to the electrode surface will rely heavily on the quality and chemistry of the interface between the TiO_2 film and the underlying silicon.

Figure 3.4 shows the representative GPC for all four processes as deposited. More consistent, linear early-stage growth is observed for PEALD processes. Additionally, thermally grown TTIP displayed evidence of nucleation delay and subsequent enhanced growth in the latter stages. Thicknesses were determined using the Thickogram method, allowing for in-situ thickness determination for precise deposition control [9]. These sequential-growth depositions were used in order to investigate the early state growth characteristics and allowed for the determination of exact growth rates for each process to allow for precise thickness deposition later on for purposes of photoelectrochemical cell testing wherein accurate film thickness is necessary to compare the processes. In all cases, XPS growth rates were cross referenced with those obtained through spectroscopic ellipsometry.
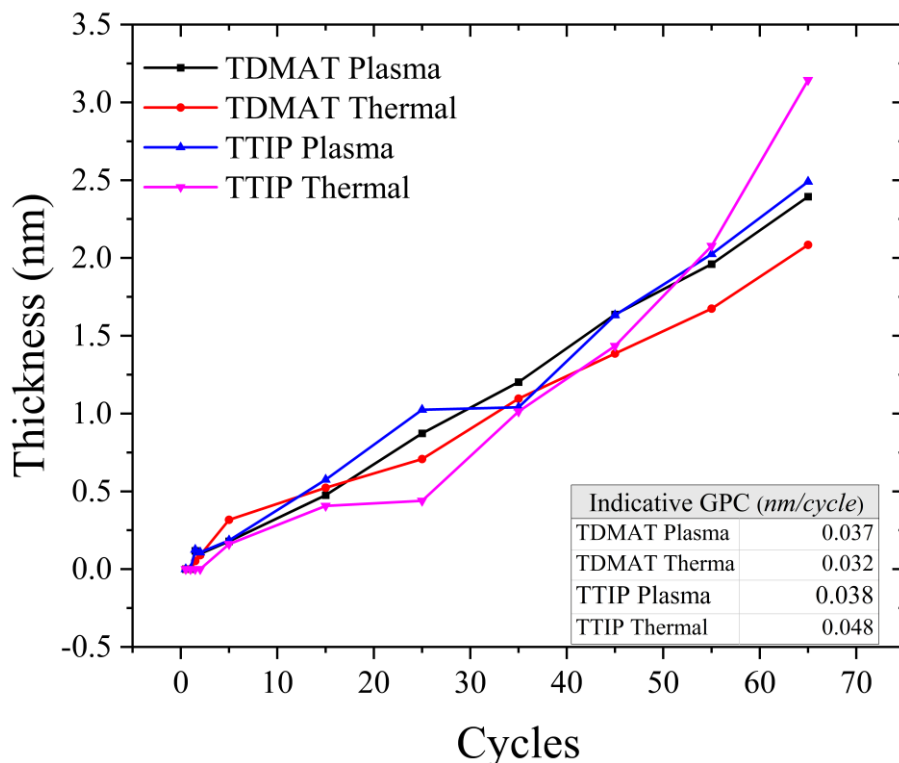
Figure 3.4 Representative growth characteristics showing sequentially grown ALD TiO$_2$ films for 4 processes detailing the evolution of indicative GPC rates for the various recipes. For clarity, error bars, which range between ± 0.02Å/cycle and ± 0.04Å/cycle based on the standard error from multiple deposition, are not shown.

The GPC rates presented within Figure 3.4 are in line with those expected based on literature reported values. The measured GPC for TTIP thermally grown of 0.048 nm (± 0.02Å) is consistent with reports from the literature with Chiappim et al as well as Diouf et al and others detailing ALD recipes for thermally grown TTIP aligned with those in this study yielding similar GPC rates [10–14]. Additionally, the measured GPC rate for TTIP plasma of 0.036 nm (± 0.02Å) is also verified by literature reports with Kilic et al and others reporting on an in-situ ellipsometry study yielding GPC rates in line with those reported in Figure 3.4 [12,15–18]. The same can be said for the measured GPC rate of 0.032 nm (± 0.02Å) for TDMAT

136

thermally grown shown above in Figure 3.4 with this experimental value corroborated within the literature [13,14,19,20]. The final deposition process for consideration from Figure 3.4 is that of TDMAT plasma enhanced with a measured GPC within this work of 0.037 nm ($\pm$ 0.04Å) which is also within the range of that expected based on literature reports [14,21,22]. Reported error within the literature for ALD depositions is typically very low owing to the monolayer by monolayer self-limiting growth characteristics and therefore yields error within the $\pm$ 0.02Å range with which all measured GPC rates within Figure 3.4 are consistent[23].

Figure 3.5 (a) shows the evolution of the O 1s peak as a function of increasing number of ALD cycles for the TDMAT thermal process. In this figure, two dominant oxygen peaks are observed, the first being oxygen in SiO_2 at a binding energy position at approximately 533 eV and the second is oxygen in TiO_2 at approximately 531 eV. Figure 3.5 (b) shows the Si 2p evolution, where the SiO_2 peak is seen to attenuate rapidly, due to suppression of the substrate signal during the growth of the TiO_2 overlayer. Also in Figure 3.5 (b) we see a shifting of the silicon oxide peak towards lower binding energy as the number of cycles increases suggesting the formation of silicon suboxides or titanium silicate at the interface, as suggested in Figure 3.2.

Figure 3.5 (c) shows the sequential growth of the Ti 2p region. Growth can be seen to initiate as early as after the first half cycle of the sequential deposition with consistent peak evolution observed throughout. In the case of the TALD processes for both TTIP and TDMAT, a low binding energy shoulder is seen to form as early as 5 cycles into the deposition, attributable to titanium in the 3+ oxidation state.

Figure 3.5 (d) shows the C 1s as a function of cycle number, with an increase in carbon composition with increasing cycles, despite the film not leaving vacuum between ALD and XPS analysis. Having started from a clean H$_2$ plasma treated samples surface with negligible carbon contribution, the C 1s region grows steadily leaving a significant composition after 65 cycles of approximately 16% for this particular process. This suggests incomplete reactions in the ALD process leading to ligand incorporation which in previous photoemission studies is not highlighted, with this level of carbon often attributed to atmospheric contamination in *ex-situ* studies [24].
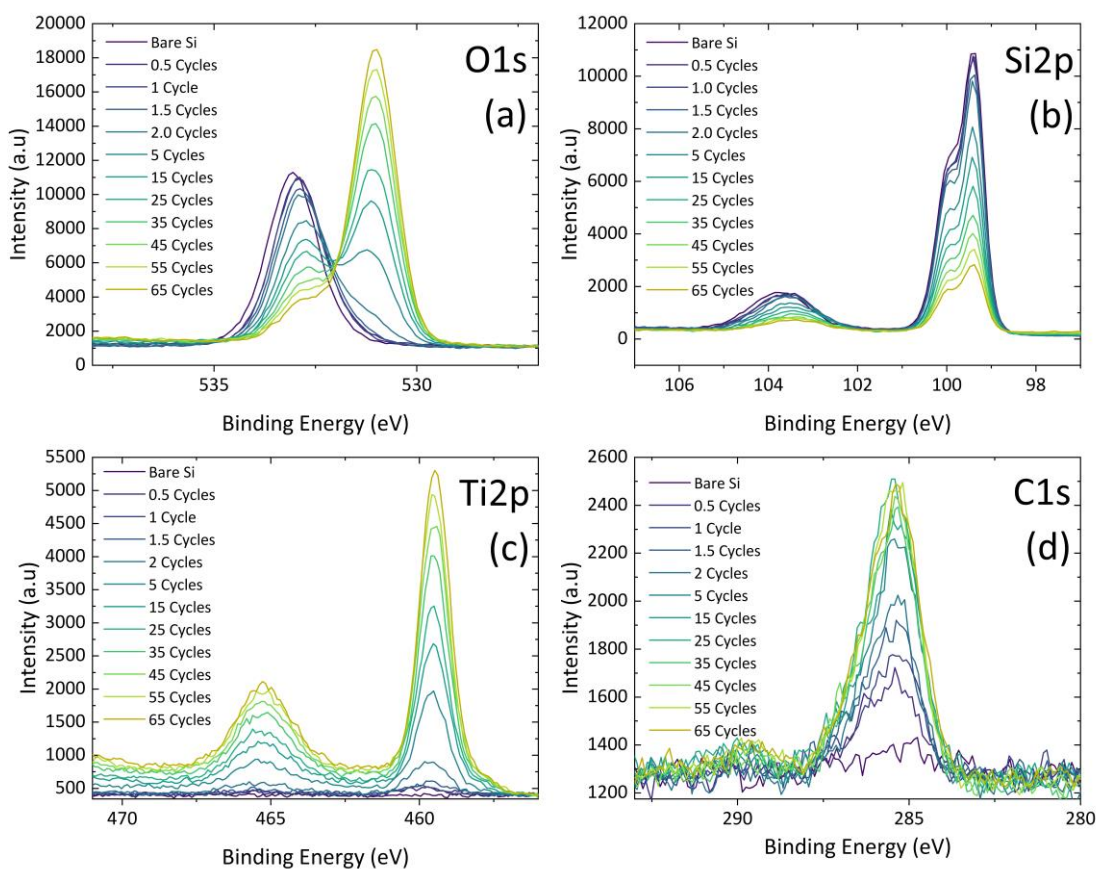
Figure 3.5 Thermal TDMAT sample evolution as a function of increasing number of ALD cycles depicting the change in composition as the thickness of the titanium overlayer increases. (a) Evolution of the O 1s photoemission peak as it changes from a SiO2 dominant peak TiO_2 dominant (b) Attenuation of the SiO_2 peak is shown (c) Ti 2p region showing peak intensity with increasing cycles (d) C 1s peak showing remnant carbon incorporation in the film.

The corresponding PEALD growth of TDMAT is shown in Figure 3.6. The same comparison on thermal and plasma enhanced ALD is shown for TTIP in Figure 3.7 and Figure 3.8 respectively. In all cases the attenuation of the Si 2*p* as a function of increasing ALD cycles is observed with a simultaneous increase in Ti 2*p* intensity.
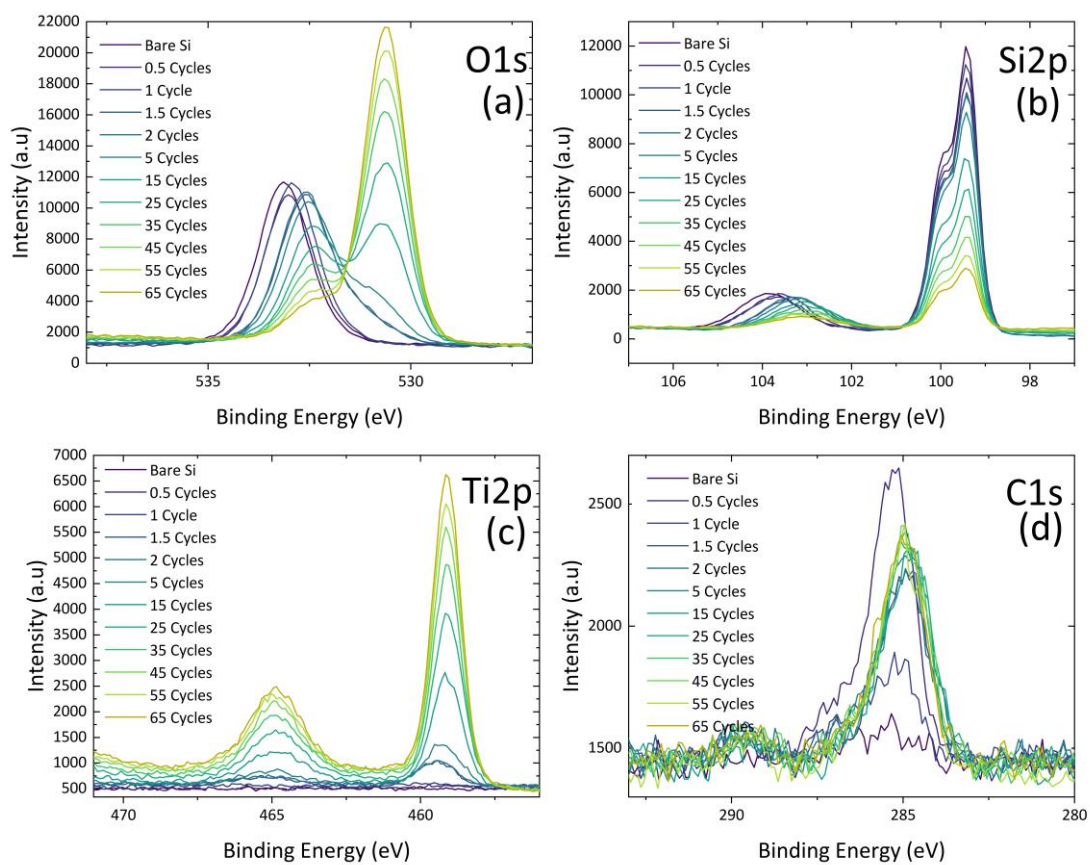
Figure 3.6 : XPS high resolution spectra of PEALD TDMAT showing sample evolution as a function of increasing of cycles (a) O 1s (b) Si 2p (c) Ti 2p (d) C 1s.
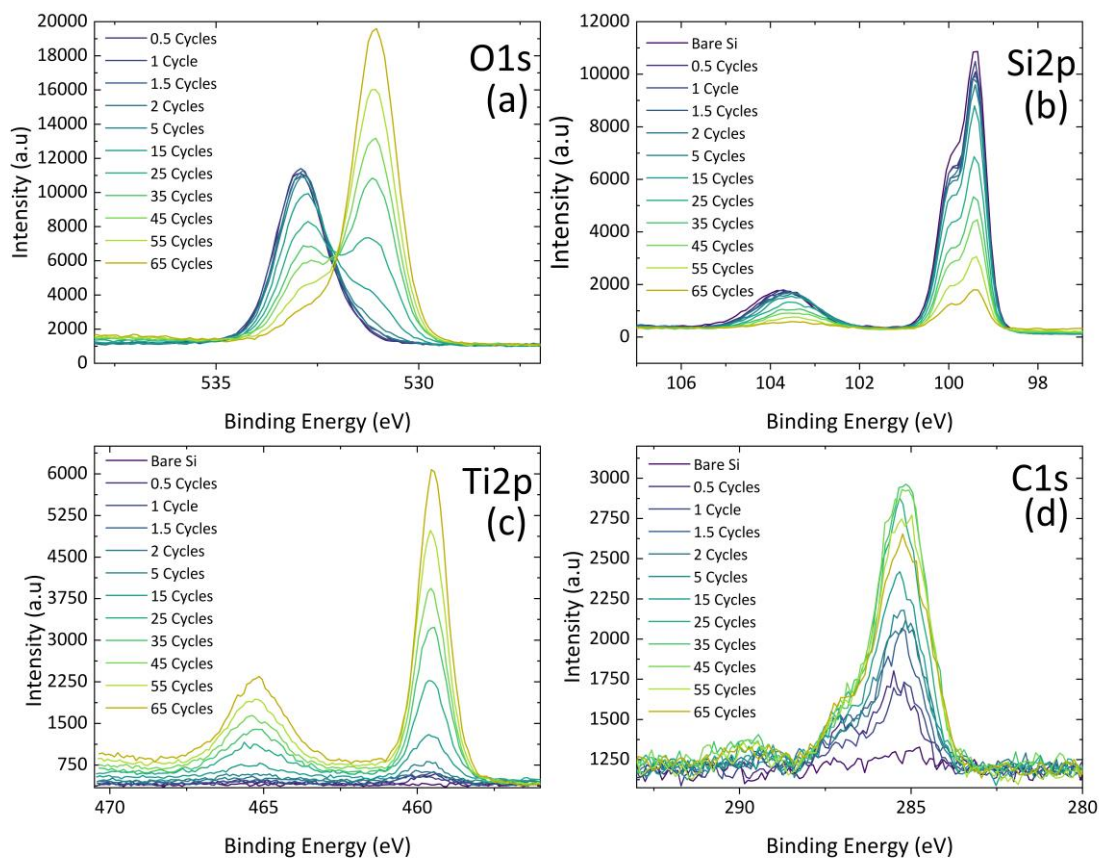
Figure 3.7 XPS high resolution spectra of TALD TTIP showing sample evolution as a function of increasing cycles (a) O 1s (b) Si 2p (c) Ti 2p (d) C 1s.
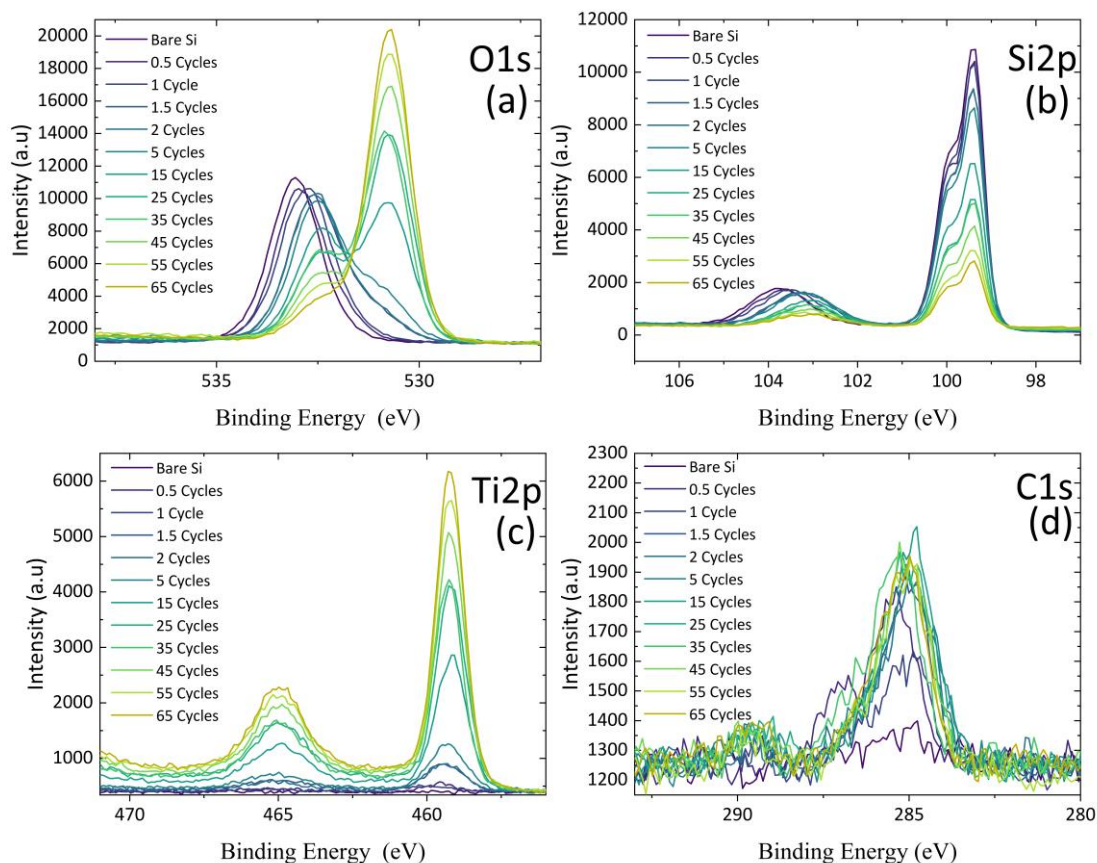
Figure 3.8 XPS high resolution spectra of PEALD TTIP showing sample evolution as a function of increasing number of cycles (a) O 1s (b) Si 2p (c) Ti 2p (d) C 1s.

In order to further illustrate the complications in interpreting carbon and oxygen spectra that can be avoided by analysing ALD processes without breaking vacuum, Figure 3.9 shows an example of a 2nm TiO_2 layer which was scanned post deposition and following exposure to atmosphere for 5 minutes. The *as deposited* sample shows a significant carbon signal. Once exposed to atmosphere there is a further growth in the C 1*s*. Note however that the growth of adventitious carbon can mask the carbon associated with ligand incorporation, though many works attribute the entirety of the C 1*s* peak area to adventitious carbon.

In many processes, up to 30% carbon can be observed which, if incorporated in the film will significantly impact the material properties and the suitability of the ALD process under investigation [24].
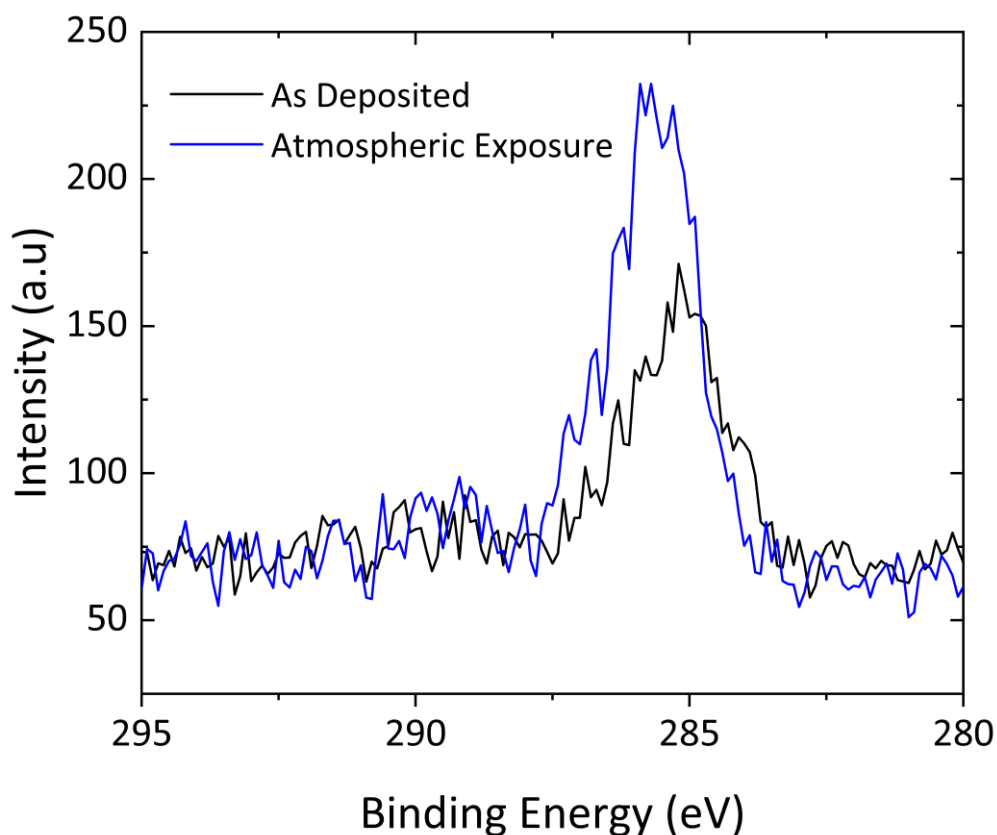
Figure 3.9 : High resolution XPS spectra for the C 1s region showing the carbon contribution of a TiO2 film grown using TDMAT PEALD at two stages:- as deposited and post atmospheric exposure, showing the importance of in-situ studies of ALD films.

In this investigation all growth processes show less than 20% carbon within the film as a result of remnant ligands trapped during the deposition. Depth profiling of ALD films with XPS is often carried out using Ar-ion sputtering, but given the ion beam's tendency to change the film's structure as it removes material, this is not a wholly reliable indicator of the chemical composition of bulk films [25,26]. The degree of incorporation of the ligands in these

films is evident in Figure 3.5 (d) with the sequential deposition of a TiO$_2$ film and the steady growth of the C 1s peak. The observation in Figure 3.5 (d) which suggests continuous carbon incorporation is expanded upon in Figure 3.10 which details the carbon concentration as a function of the number of cycles observed in the sequentially grown films for all process. From a theoretical viewpoint during an ideal ALD process, on every oxidant pulse remnant CH$_3$ groups of the TTIP and TDMAT molecules respectively should be removed in addition to N from the TDMAT molecule as shown in Figure 3.1. It is already clear from Figure 3.10 that this is not the case given the consistent growth of the carbon peak throughout the deposition for all processes.

One point to note is that there appears to be reduced ligand incorporation in the PEALD grown layers when compared to TALD as is seen from their overall lower relative sample carbon content and the rate at which the carbon contribution in these plasma grown samples stabilizes. This is due to the comparatively larger redeposition of carbon within the TALD films which is reduced in PEALD due to reactive species present in the plasma blocking the reaction leading to the excess carbon incorporation. Furthermore, the presence of N within either the TALD or PEALD deposition processes is not observed during the deposition of TDMAT which suggests that the precursor molecule is breaking down and reacting as expected.
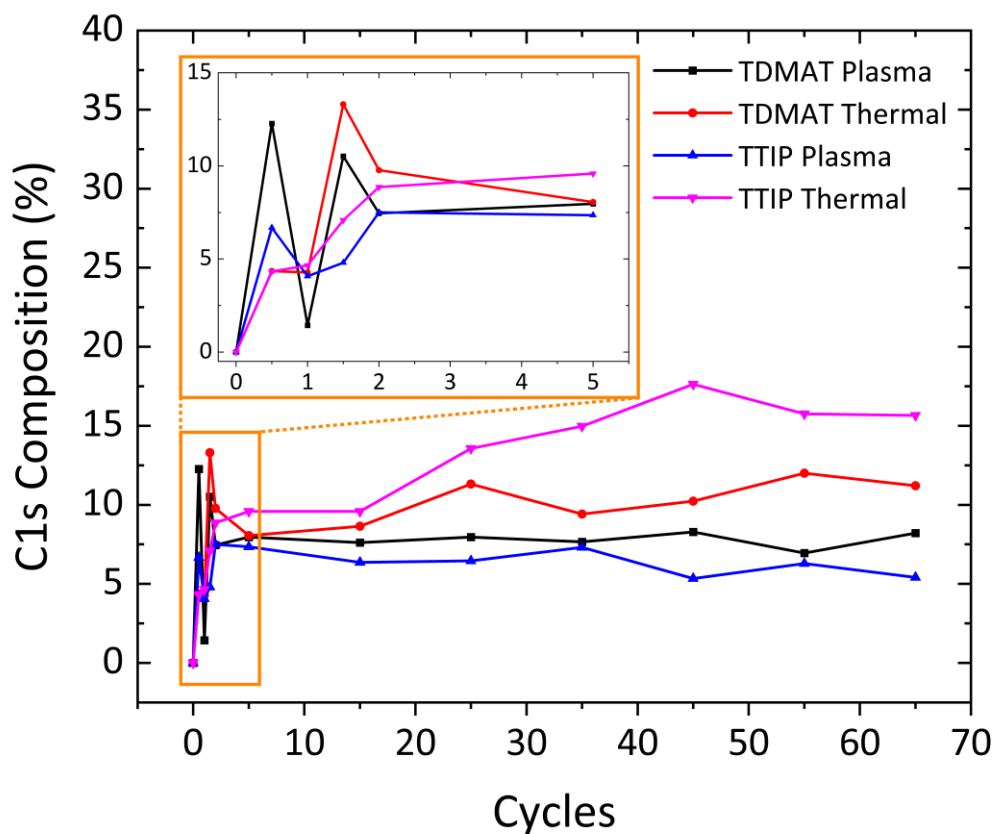
Figure 3.10 High resolution XPS spectra for the C 1s region showing the carbon contribution of a TiO2 film grown using TDMAT PEALD at two stages: - as deposited and post atmospheric exposure, showing the importance of in-situ studies of ALD films.

Following the sequential depositions detailed above, a series of conventional depositions were performed to confirm GPC values and to confirm consistency of the TiO_2 deposition processes. A temperature of 270°C was selected for sample temperature which is within the ALD window for both TDMAT and TTIP which provided suitable growth rates and minimal remnant carbon ligands from the ALD process [7]. From this point forward all XPS binding energy positions and electrochemical measurements discussed pertain specifically to the 'straight-through' 2 nm thick layers as opposed to those grown sequentially.

As shown in Figure 3.11, for both PEALD processes, Ti was present only in the Ti^{4+} state with TDMAT plasma (TD-P) at 458.9 eV and TTIP plasma (TT-P) at 459.2 eV which are consistent with previous reports [27,28,29,13]. These two plasma processes exhibit Ti^{4+} only, in contrast to the TALD processes which show the presence of Ti^{3+} at 458.2 eV and 458.1 eV for TDMAT (TD-T) and TTIP (TT-T) respectively in addition to Ti^{4+}. The literature indicates the binding energy position of Ti^{3+} to be in the region of 1.3 – 2.3 eV lower than Ti^{4+} [13,28,27]. The measured spin orbit splitting for the TD-P, TT-P and TT-T is 5.7 eV with the TD-T found to be 5.18 eV, again consistent with values reported in the literature [27,28]. High resolution Ti 2p spectra were fitted as two singlet peaks, with the peak area of the Ti $2p_{1/2}$ being 0.43 of that of the Ti $2p_{3/2}$ rather than the expected 0.5 and the FWHM of the Ti $2p_{3/2}$ being higher.

This approach to peak fitting is used in order to account for the Coster – Kronig effect which leads to a difference in the peak width and branching ratio of two spin-orbit doublet peaks which occurs in 2p spectra of first row transition metals [29] [30] [28]. Figure 3.11 shows the fitted Ti 2p peaks for all 4 processes which shows the good quality single state nature of PEALD grown films in contrast with the TALD films which exhibit 3+.
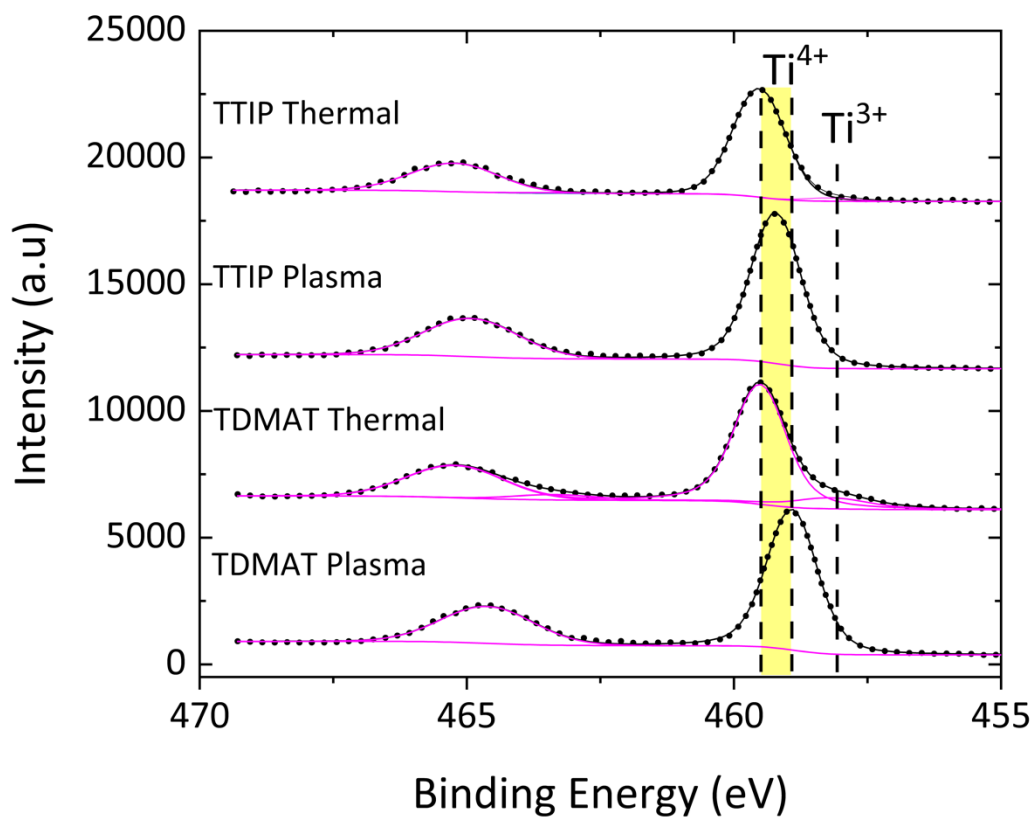
Figure 3.11 Comparative figure of 4 processes showing Ti 2p fits.

Samples with Ti^{3+} present exhibited a blue tint when viewed with the naked eye, compared to those without it [31] [32]. An exemplar fitted spectrum of a TALD grown sample using TDMAT as the precursor is shown in Figure 3.12 which clearly shows the presence of the Ti^{3+} state.
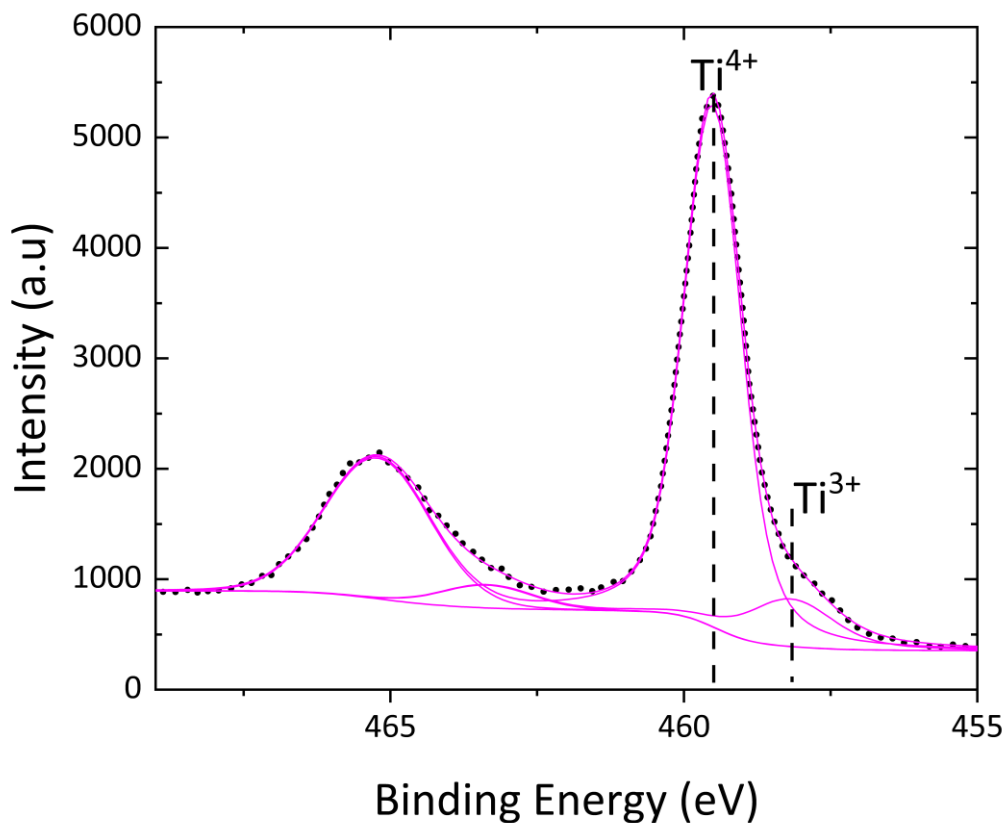
Figure 3.12 Ti 2p high resolution photoemission peak from TDMAT thermally grown film showing the presence of Ti3+.

Using the established growth rates, we deposited films of 2 nm for purposes of electrochemical testing and XPS characterisation. These films were grown in a straight through deposition wherein the ALD process continues uninterrupted to a desired number of cycles as per the required calculated number based on the previously calculated growth rates.

Once depositions had been completed for each process, and the samples were scanned with XPS to verify thickness and composition, they were removed from vacuum and stored in atmosphere prior to receiving subsequent annealing treatments.

In order to understand the effects of annealing in oxidizing and reducing ambients on the thin TiO$_2$ films, high temperature anneals were carried out both in atmosphere, and in H$_2$ plasma under vacuum, respectively. Upon being reinserted into the ALD-XPS system for H$_2$ plasma annealing, XPS scans were performed on all samples to determine their reaction to atmospheric exposure prior to annealing. Once annealed, samples underwent additional photoemission analysis to study the effect of the H$_2$ treatment.

Given that the performance of the TiO$_2$ films in atmosphere is of interest, it is important to understand the surface chemistry of the TiO$_2$ when it has been re-exposed to atmosphere following the H$_2$ annealing step. As the samples are so thin, if the H$_2$ exposure causes any reduction in the films, one may expect partial or full re-oxidizing of the reduced films upon atmospheric exposure. Therefore, samples were moved to the system load lock where they were exposed to atmosphere for 5 minutes before being loaded once more to vacuum for a final XPS scan.

Firstly, addressing the samples post- H$_2$ plasma anneal but prior to exposure to atmospheric conditions as seen in Figure 3.13, the Ti 2p peak showed the presence of the Ti^{2+} state at 457 eV for all process along with the aforementioned Ti^{4+} and Ti^{3+} states at the previously mentioned binding energies which dominate the spectra. In all cases Ti^{4+} is the dominant species followed by Ti^{3+} and then Ti^{2+}.
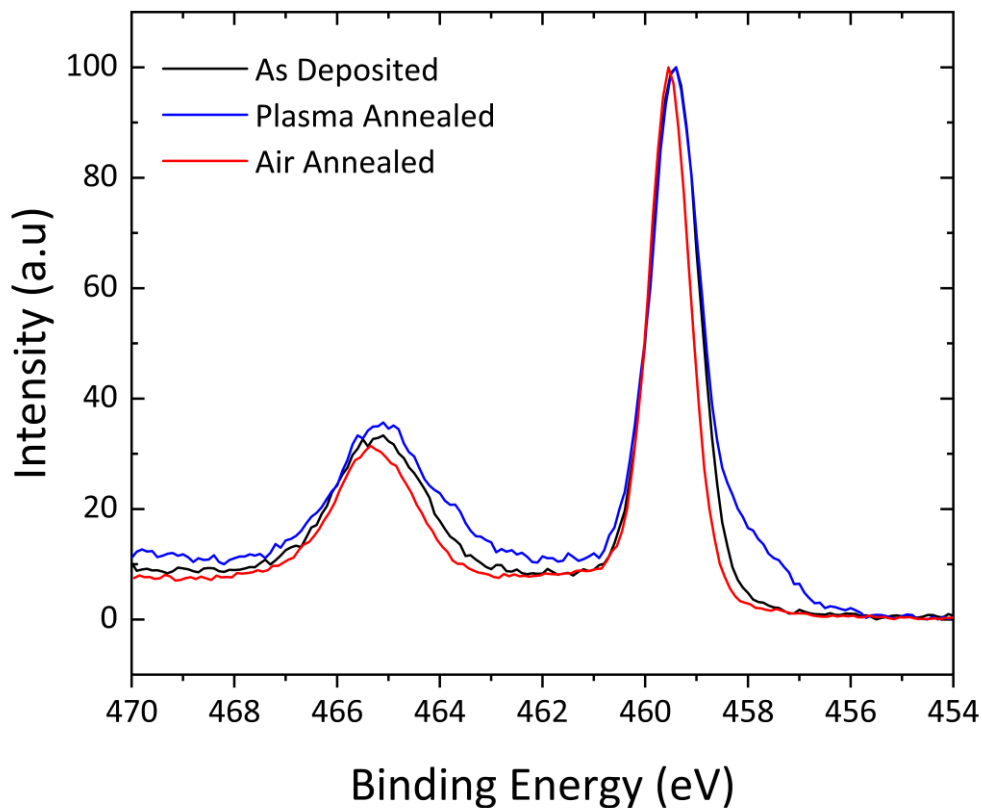
Figure 3.13 High resolution XPS scan of the Ti 2p region showing all stages of treatment for a TTIP plasma grown sample.

Following subsequent exposure to atmosphere all samples see a drastic reduction in Ti^{3+} and Ti components with their composition being made up almost entirely of Ti^{4+}. This is key information from an *in-situ* perspective as it shows the true state of the titania films in atmosphere following plasma annealing and the significant degree of re-oxidation upon atmospheric exposure. An example of the effect of annealing treatments is shown in Figure 3.13 where TTIP plasma grown titanium oxide films at all stages of treatment show the change in state of the Ti 2p state for each stage. The remaining growth processes at all stages of treatment are shown in Figure 3.14 and shows that PEALD grown plasma annealed

150

samples remain at higher binding energy compared to the *as deposited* and air annealed samples due to the main formation of silicates having taken place during film growth rather than annealing.
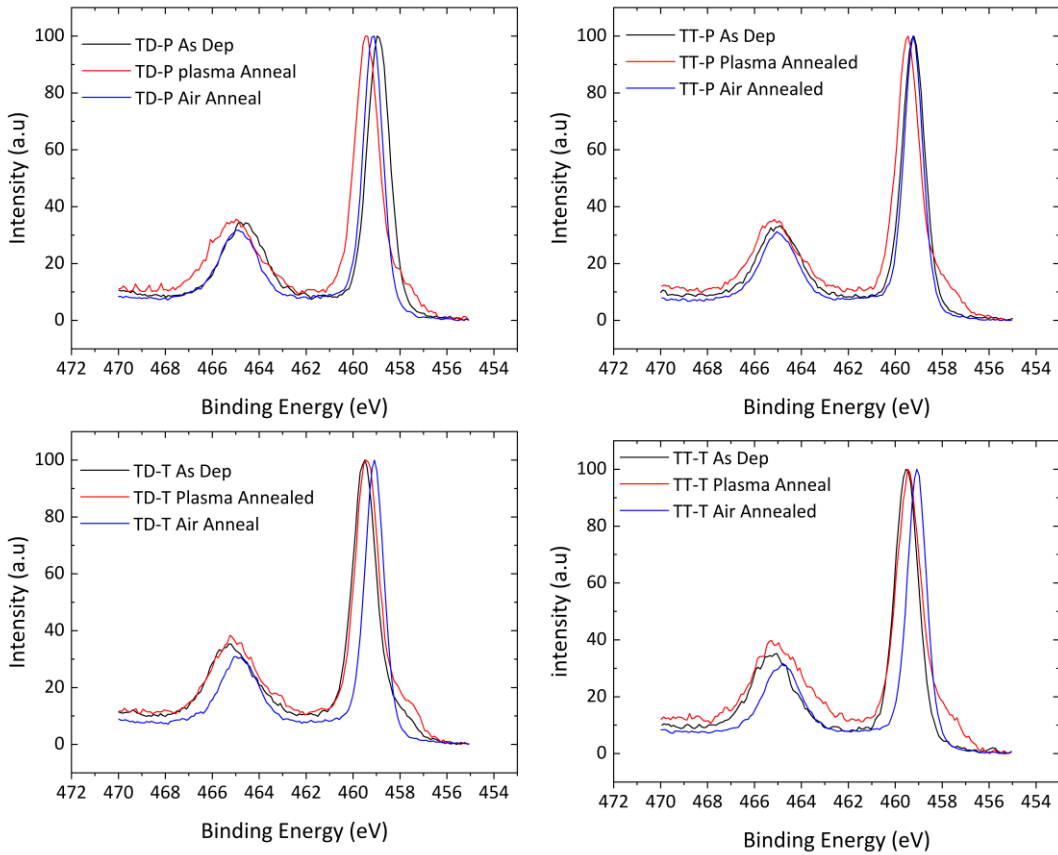
Figure 3.14 Ti 2p core level spectra for all growth processes and treatment stages aligned to the Si 2p peak at 99.4 eV.

Along with plasma annealing in vacuum, layers grown via all processes were exposed to an atmospheric anneal and were also analysed using XPS. This annealing treatment results in Ti existing predominantly in the Ti^{4+} state with TD-T and TT-P exhibiting marginal contributions of Ti^{2+} and TT-T presenting Ti^{3+}. This is in line with what is to be expected, the plasma anneal being the reducing environment causes the formation of oxygen vacancies

resulting in the Ti^{3+} and Ti^{2+}. Annealing in atmosphere results in the Ti film moving towards a more stoichiometric state, which occurs due to the formation of a significant contribution of silicate which causes the BE to decrease relative to what would be expected for a typical Ti^{4+} dominated film.
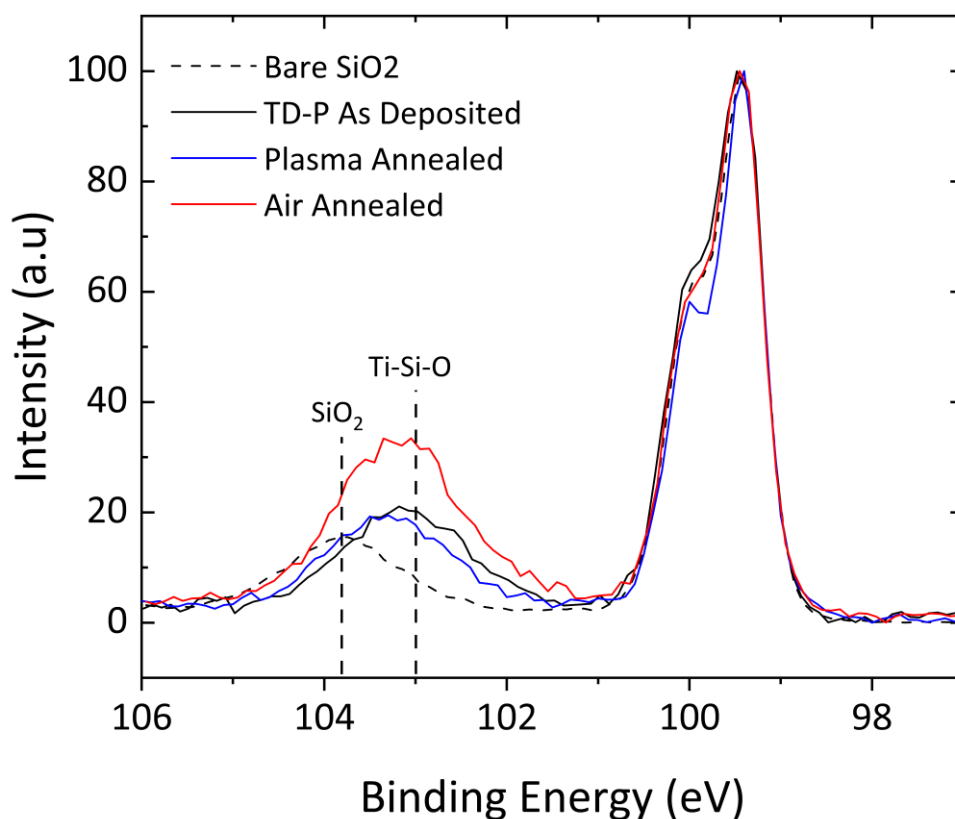
Figure 3.15 XPS high resolution spectra of the Si 2p region showing the evolution of the oxide peak with each stage of sample treatment with bare SiO2 shown for reference.

Figure 3.15 shows typical XPS spectra for the Si *2p* core level of titanium oxide films in their as deposited state, post plasma annealing and post air annealing stages. The presence of titanium silicates within the films shown in Figure 3.15 is evident from the shift in binding energy position of the oxide peak which move from higher to lower energy starting from

approximately 103.8 eV in the case of bare SiO_2. The air annealed sample showed the strongest silicate contribution, with XPS fitting of this peak showing the silicate contribution to be centred at a lower value of approximately 103 eV which is in line with literature values [33]. Briefly looking again to films deposited in a cycle by cycle regime with photoemission analysis performed between batches of ALD cycles, Figure 3.16 shows the change in binding energy separation of the Si $2p$ bulk and oxide peaks as a function of deposition cycles and includes the post plasma and air annealed sample binding energy separations for all processes. This binding energy shift is also observed for sequential depositions as is seen from Figure 3.5 (b) where the shift of the Si^{4+} oxide peak to lower BE as a function of ALD cycles and can be attributed to the formation of interfacial Ti-Si-O bonds during the deposition of TiO_2, which have a lower binding energy than bulk SiO_2 [34].
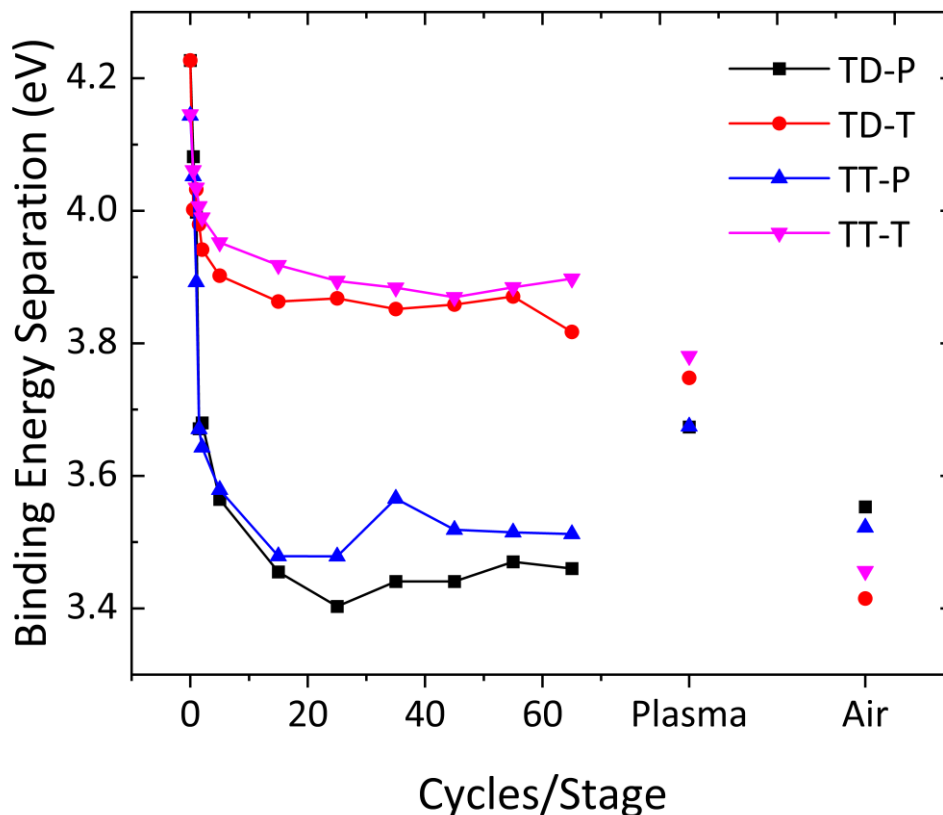
Figure 3.16 : For all four growth processes the binding energy separation of the silicon oxide and bulk peak positions is shown as a function of increasing number of cycles for sequentially grown samples as well as positions for continuously grown 2 nm films following post deposition annealing in vacuum and ambient air conditions.

In the case of TTIP via both PEALD (Figure 3.8) and TALD (Figure 3.7), XPS core level spectra clearly show the presence of Ti $2p_{3/2}$ and Ti $2p_{1/2}$ peaks after the first half cycle. For TDMAT both processes (PEALD Figure 3.6 and TALD Figure 3.5) show the presence of the Ti $2p_{1/2}$ peak whereas the Ti $2p_{3/2}$ signal-to-noise ratio (SNR) is too low to clearly distinguish its precise position. However, it confirms that for both precursors and deposition processes that growth initiates as early as the first reactant dose. Additionally, during nucleation the Ti $2p$ peak exhibits high binding energy suggesting the dominance of the Ti^{4+} state before

shifting to lower binding energy with increasing ALD cycles during a sequential growth investigation. The shift is evident from Figure 3.16 and it is seen to approach a limiting value in all process following 25 ALD cycles. A similar finding was reported by Methaapanon *et al* wherein the shift of the Ti $2p$ peak was shown for $TiCl_4$ samples grown via TALD with an approximate shift of the peak of 0.5 eV [34]. In the case of the TDMAT and TITP precursors investigated here we observe that for samples grown via PEALD the Ti *2p* peak shifts by ~0.85 eV with TALD samples shifting by ~0.43 eV similar to that shown in the afore mentioned literature value. The behaviour of both the Si $2p$ and Ti $2p$ peaks during early stage depositions can be explained by Si-O-Ti silicate bonds which form at the Si – Ti interface [34]. The binding energy positions of both peaks reduces from that of the stoichiometric 4+ oxide in both cases, in line with the reduced electronegativity of silicon and titanium when compared with oxygen. The behaviour is consistent with that in Figure 3.16 where the saturation of the BE separation is shown at ~ 25 cycles as well as with Figure 3.17 where at 25 ALD cycles the shift in BE of the Ti *2p3/2* also stabilises.
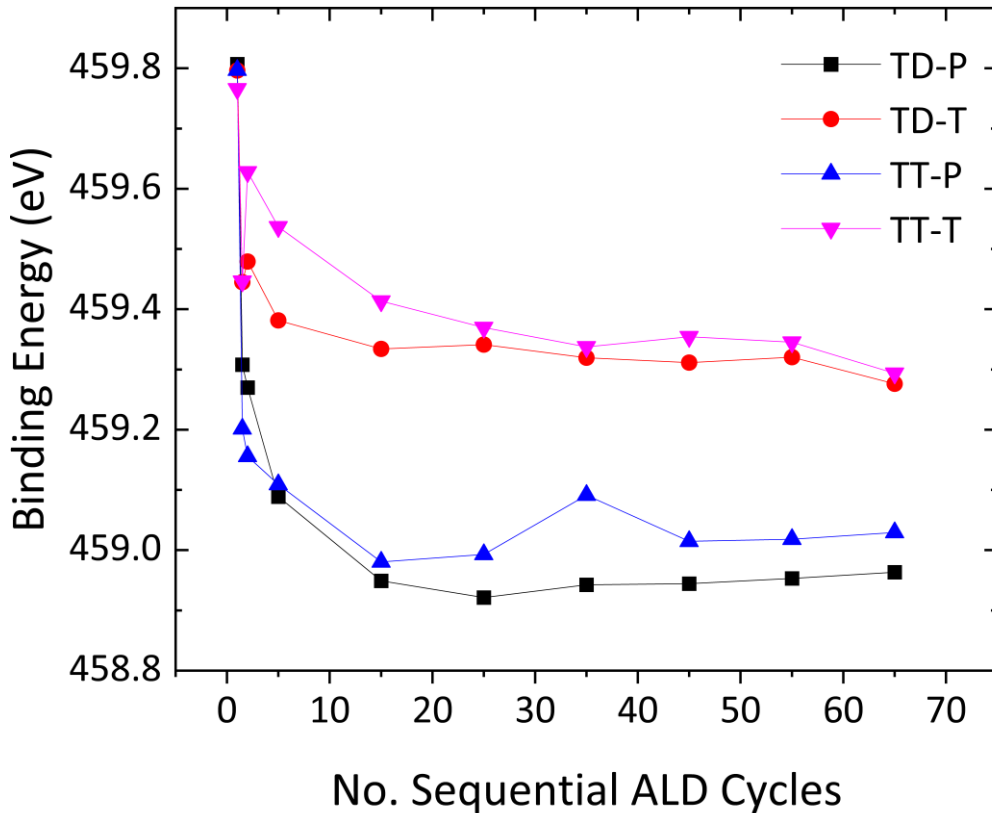
Figure 3.17 Shift of the Ti 2p3/2 peak binding energy position from 1-25 ALD cycles.

In the case of the O 1*s* spectra shown in Figure 3.18 three discrete chemical states were identified. For all deposition processes in their *as deposited* state Figure 3.18 (a), the dominant peak corresponded to Ti - O bonding centred at approximately 531 eV. Plasma enhanced ALD processes yield a slightly lower binding energy, likely due to the formation of more titanium silicate and silicon suboxides than the thermal processes.

The peak observed in the O 1*s* spectra at 532 eV is attributed to remaining SiO_x contribution, which is in line with prior reports [29] [35]. Following H_2 plasma annealing Figure 3.18 (b) the oxygen peaks are observed to converge and align to 531 eV, whereas following air annealing a shift of all O 1*s* peaks to lower binding energy is observed. This is consistent with the Ti

$2p$ spectra highlighted earlier, in that the reducing environment of the vacuum plasma anneal causes the creation of oxygen vacancies in the film which results in the Ti^{3+} and Ti^{2+} states. Whereas in the air annealing treatment Figure 3.18 (c) the abundance of oxygen in the atmosphere allows for the conversion of the film to Ti^{4+}. In the *as deposited* state not all processes showed their O $1s$ to be precisely aligned to O in TiO_2 and only after annealing in air did they conform suggesting incomplete reaction during the ALD deposition process.
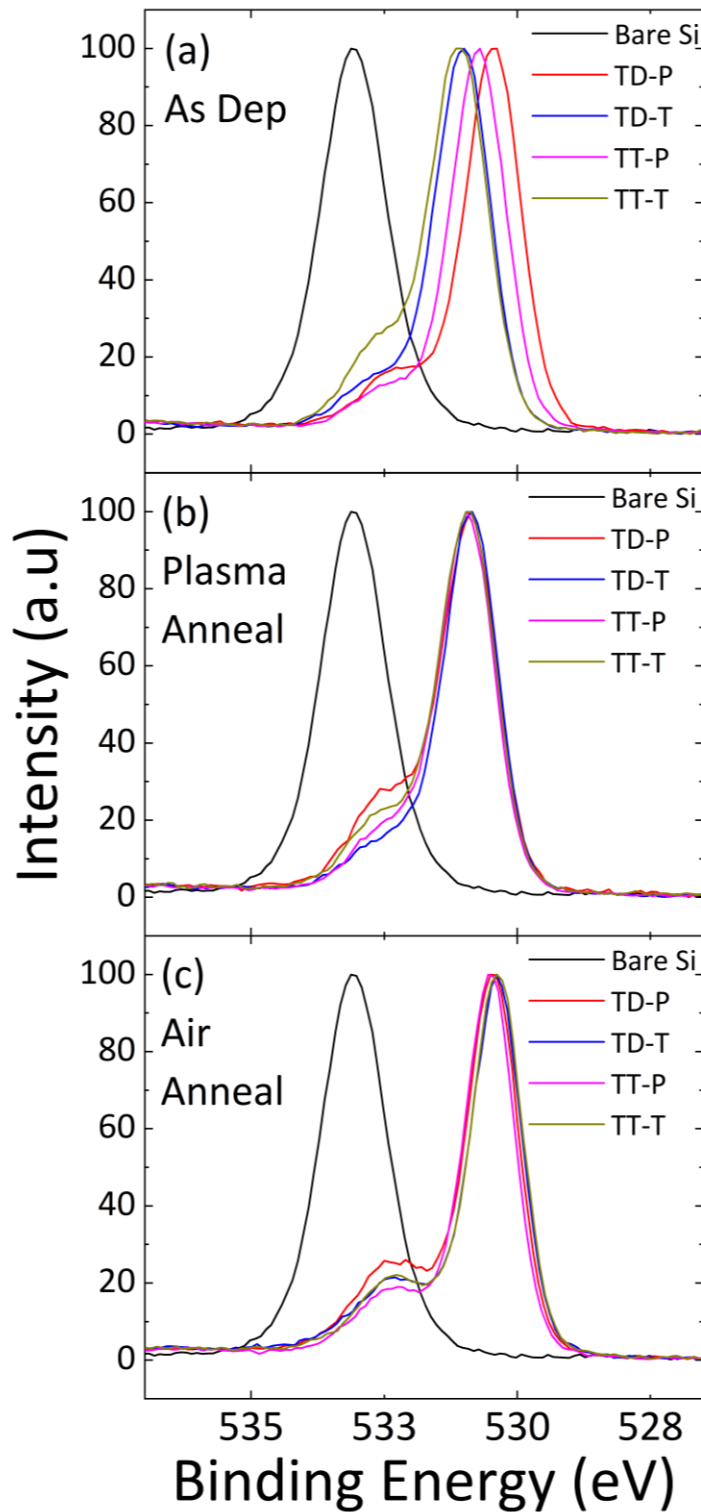
Figure 3.18 O 1s spectra of (a)as deposited, (b) plasma annealed and (c) air annealed samples showing the shift in oxygen binding energy as a function of their annealing environment.

3.3.3 Photoelectrochemical Testing

Following verification of film thickness using ellipsometry and XPS, 2 nm thick TiO_2 films were subjected to PEC testing to study the influence of ALD process parameters and post deposition annealing treatments on their electrical performance. A thickness of 2 nm has been widely identified as being an optimal thickness for photoanode performance enhancement [36]. Chronoamperometry tests were carried out using an applied voltage of 1 V vs Ag/AgCl which corresponds to 1.67 V vs the reversible hydrogen electrode (RHE), over a period of 100 seconds. Linear sweep voltammetry tests were carried out from 0 – 4.17V vs RHE. Figure 3.19 shows the voltammograms for all deposition processes which corresponds to Figure 3.20 by displaying the current density measurements with matching data symbols.
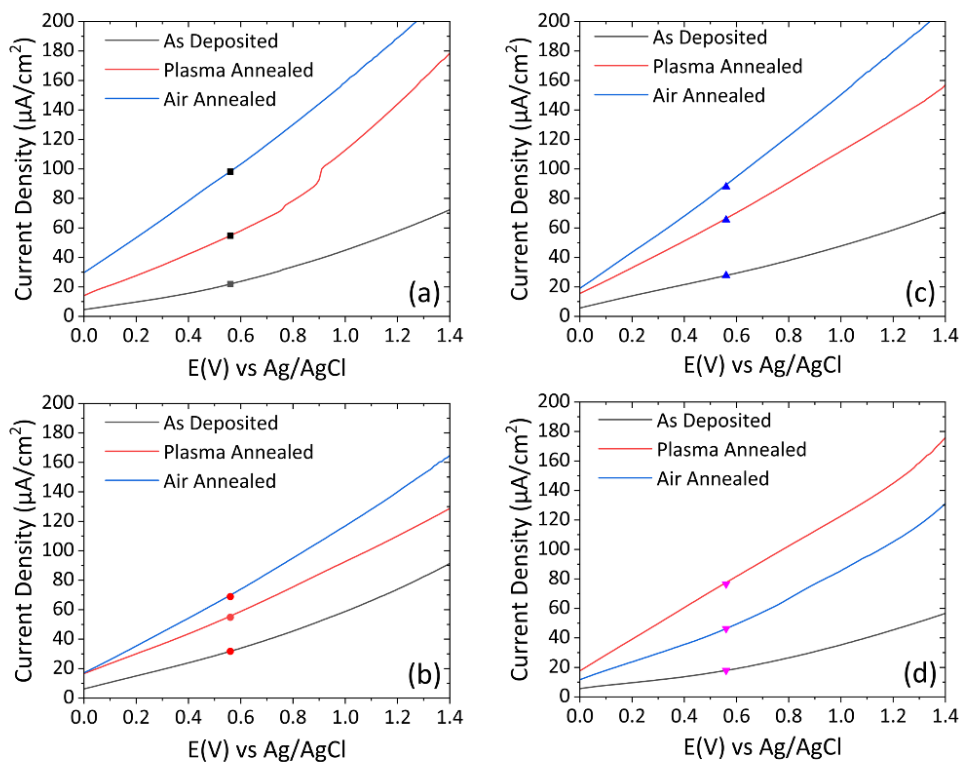
Figure 3.19 Linear sweep voltammetry measurements for all processes and treatment stages (a)TDMAT PEALD, (b) TDMAT TALD, (c) TTIP PEALD and (d) TTIP TALD.

159

As a means of data simplification for the display of the peak performance of all sample processes and stages of treatment, Figure 3.20 shows the current density of each sample at 1.23V vs RHE for all four processes. It is clear from this figure that all growth processes benefitted greatly from post deposition annealing treatments, with the air annealing showing the most significant increase when compared to the *as deposited* samples. Prior to annealing neither precursor, nor the choice of plasma enhanced, or thermal ALD appeared to show consistent improvement performance over the others.
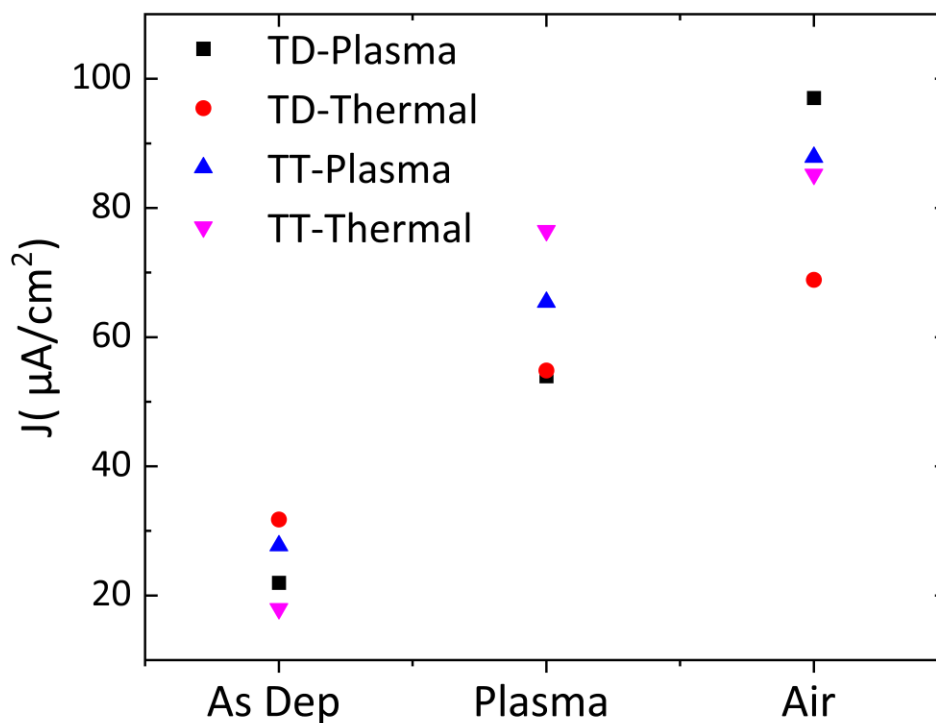
Figure 3.20 Cyclic voltammetry measured photocurrent at 1.23 V vs. RHE as a function of sample treatment stage. See Figure 3.21 for additional information.

Examining the TiO$_2$ films in their *as deposited* state shows a significant degradation in photocurrent over the short 100 second testing period, the extent of this degradation is shown in Figure 3.21 wherein the amperometric performance all films in their as deposited, post plasma anneal and post annealing in atmosphere states are shown. This highlights the necessity for post deposition film treatments to stabilise currents and sustain high current output over an extended period of PEC operation. Most importantly from Figure 3.21, a significant improvement in sample stability is seen in air annealed samples when compared to their plasma annealed counterparts. This a good demonstration of the superior performance, both in terms of gross current output along with ability to sustain this increased output, of annealed over *as deposited* counterparts.

This is followed by the plasma annealed sample which exhibits a high initial output current however, its output rapidly decreases after just 10 seconds of testing before beginning to stabilize at approximately 70 µA/cm^2. The H$_2$ plasma annealed sample stability shows improved performance over as deposited films when comparing start and end current output as an indication of stability. Although beginning at an initially high current competing even with that of the plasma annealed sample, the *as deposited* film showed a sharp decrease in current density in as little as 20 seconds.
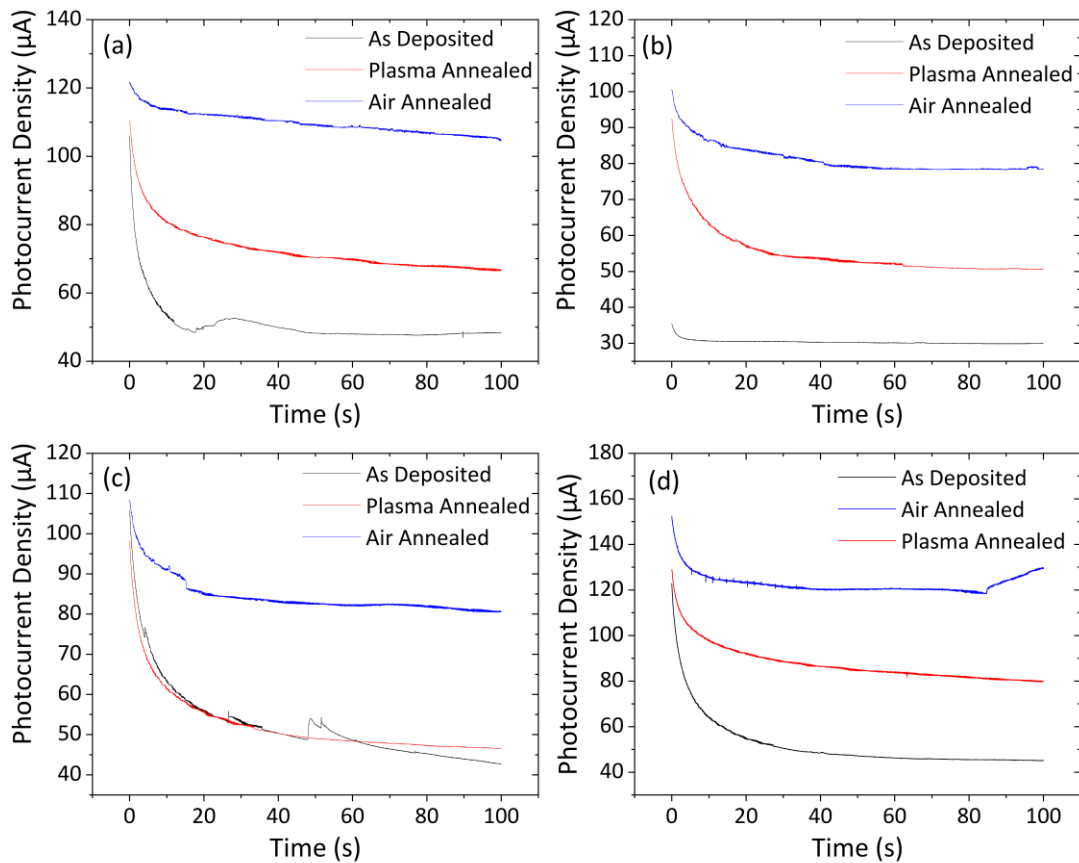
Figure 3.21 Exemplar amperometric curves from all treatment stages of (a) TDMAT PEALD (b) TDMAT TALD (c) TTIP PEALD & (d) TTIP TALD illustrating that air annealed samples exhibit the greatest and most stable current output.

These stability improvements are in line with findings from Hannula *et al* where they show vacuum annealing of titania films at 500 °C results in superior performance than is achieved by similar films which have received plasma annealing, no anneal or annealing at a reduced temperature of 400 °C [29]. All processes exhibit results which follow this pattern of air annealed samples outperforming the alternate treatments. It is worth noting that these concise evaluations offer limited insights into the long-term reliability of the protective films in question. Their primary purpose of these PEC stability tests within this work lies in

comparing the initial phases of each respective film rather than establishing extended reliability and stability benchmarks.

This PEC testing illustrates the performance enhancements obtained through applying post deposition treatments, with the air annealing of all samples producing the highest current output for all deposition processes.

3.4 Discussion

Overall, H_2 plasma annealing results in an almost 3x increase in photocurrent over as-deposited samples and a 4x increase in the case of air annealing. In the context of the XPS analysis in this work, we have shown significant differences in the spectra of all elements following annealing. In the context of plasma annealed films, the main observation is the presence of a 2+ and 3+ component in the Ti $2p$ spectra indicating the presence of oxygen vacancies in the films. Improved charge transport through insulating and semiconducting films is often linked to oxygen vacancies in the material. Density functional theory calculations, performed using Quantum Espresso*, show that removing an oxygen atom from the TiO_2 unit cell yields an increase in Ti d and O p states approximately 0.5 eV above the water oxidation energy, shown in Figure 3.22, which would explain the increased photocurrent observed in Figure 3.21 for the H_2 plasma annealed samples which causes a reduction of the TiO_2. XPS valence band spectra (not shown) confirm an increased density of states approximately 2 eV above the Fermi energy.
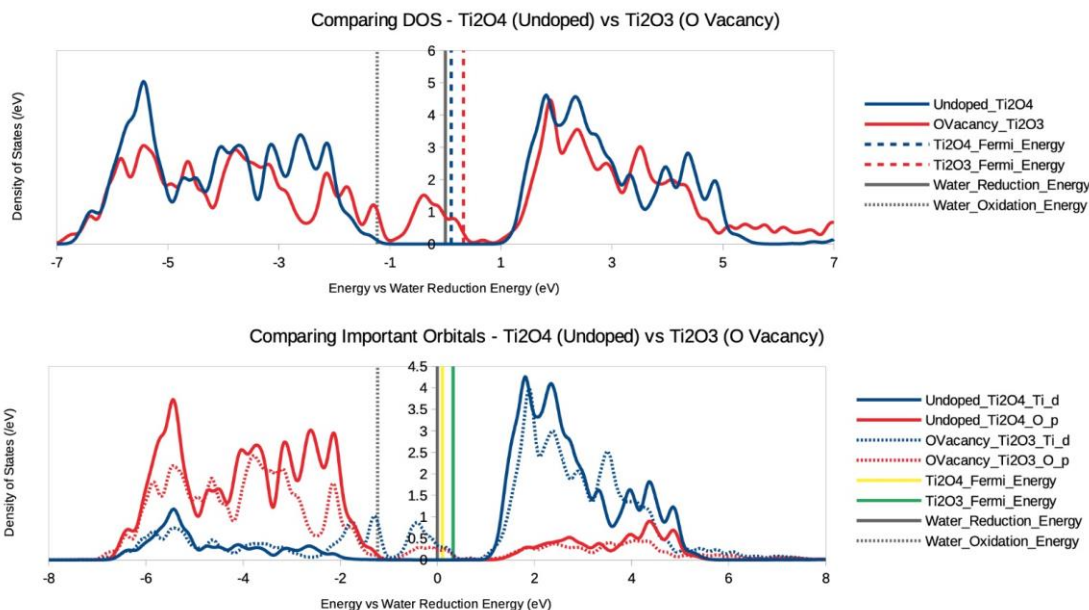
Figure 3.22 Density functional theory calculations produced using Quantum Espresso show that the removal of an oxygen atom from the TiO₂ unit cell yields an increase in Ti d and O p states approximately 0.5 eV above the water oxidation energy.

However, this does not explain why air annealing should further increase the photocurrent, as we have shown that air annealing yields stoichiometric TiO₂ with no mid-gap states present.

The main difference in the film chemistry between the plasma and air annealed samples can be concluded from an analysis of Figure 3.15 and Figure 3.16. There is a significant increase in titanium silicate growth following atmospheric annealing, and the binding energy separation between the silicon bulk and oxide peaks reduce by approximately 0.2 eV. The binding energy position of the Si *2p* oxide peak is similar to that of films grown by plasma enhanced ALD with no annealing treatment.

From this we can conclude that we see more titanium silicate growth during PEALD than thermal ALD, but an atmospheric anneal results in significant silicate growth regardless of

the deposition process. When comparing the area of the bulk and oxide peaks for the air annealed sample in Figure 3.15, the relative areas are consistent with what one would observe for an SiO_2 film of approximately 2 nm, suggesting that there is almost complete conversion to titanium silicate.

While it may sometimes be the case that plasma enhanced processes may proceed satisfactorily with low remnant precursor incorporation and therefore low carbon incorporation within the deposited film this may not always be the case as was observed within this work, with the temperature used for plasma enhanced processes being marginally elevated versus that of the thermally grown counterpart. It has been previously reported within the literature that plasma enhanced processes may suffer from poor growth nucleation at lower temperature which is contradictory from the expected outcome and has been shown within the literature and within this work [37]. Furthermore, precursor molecules are highly complex, and their reaction mechanisms vary widely even for those engineered to yield the same resultant compound. For example, this is well highlighted by Astanasov et al wherein TiO_2 films are prepared via thermally enhanced ALD using TTIP and $TiCl_4$ precursors using H_2O as the co-reactant [38]. Within this report it is shown that their precursor materials exhibit opposing growth characteristics with $TiCl_4$ showing a decrease in GPC as a function of increasing deposition temperature while the opposite is true for TTIP. This shows the complexity of the ALD deposition process and high degree of variability of behaviour of the technique from process to process and makes characterising precursors and deposition processes before performing investigations important rather than relying on theoretical assumptions of potential deposition characteristics and dependencies.

Therefore, during early testing and precursor characterisation it was deemed that plasma enhanced processes benefitted from the higher temperature of 270 °C such as to ensure no precursor condensation was occurring which would be contributing to excessive carbon incorporation which is undesirable particularly for PEC testing purposes and as such a temperature at the higher end of the ALD temperature window for PEALD processes was selected [37]. This temperature selection is within the range suggested in the literature with Lee et al reporting on a PEALD TTIP deposition temperature window of up to 300 °C [37].

From Table 3.1 presented earlier it can be seen that the deposition recipes varied across all precursors and deposition methods. This was necessary in order to obtain acceptable and comparable film stoichiometry, quality and thickness which required modifications of the deposition parameters for all. It is deemed more vital within this work to prepare films of comparable nature rather than assessing the films based on identical growth parameters regardless of the implications on the overall films produced. Precursors were under examination for their performance as protective layers rather than for their performance at an exacting set of deposition parameters which all must satisfy as such is not the nature of the technique and therefore recipes varied across all processes.

3.5 Conclusion

The presented results detail an *in-situ* study on the deposition of amide and alkoxide based precursors grown via PEALD and TALD processes, in contrast to some previous literature reports which detail only the comparison of two precursors for a single growth process or vice versa. Characterisation of these deposition processes with *in-situ* XPS allows for unique understandings of film chemistry in their as deposited states without the added complexity of film contamination via atmospheric exposure while sequential growth of all processes allowed for precise monitoring of film nucleation.

The primary variations in stoichiometry of deposited films between the plasma and air annealed sampled showed a significant increase in the growth of titanium silicate in samples which received the air annealing treatment. This is highlighted by the reduction in the Si bulk and oxide binding energy separation by approximately 0.2 eV. The relationship between the development of titanium silicate and enhanced photoelectrochemical effectiveness and stability indicates that achieving maximum photocurrent from silicon photoanodes, which are shielded by ultra-thin films, necessitates a high-temperature annealing process that allows for the transformation of the mixed phase material into titanium silicate. Furthermore, after undergoing such a treatment, films produced using both precursors and through both atomic layer deposition (ALD) techniques become chemically indistinguishable. The application of post deposition annealing treatments were revealed through photoelectrochemical testing to enhance both current output and stability under test conditions. Of the annealing treatments, air annealing at 500°C for 1 hour yielded both the most stable and efficient titania films grown from either precursor material and deposition process with plasma grown films showing only marginally higher current outputs versus thermally grown films.

3.6 References

(1)   Herrera-Gomez, A.; Bravo-Sanchez, M.; Ceballos-Sanchez, O.; Vazquez-Lepe, M. O. Practical Methods for Background Subtraction in Photoemission Spectra. *Surf. Interface Anal.* **2014**, *46* (10–11), 897–905. https://doi.org/https://doi.org/10.1002/sia.5453.

(2)   Himpsel, F. J.; McFeely, F. R.; Taleb-Ibrahimi, A.; Yarmoff, J. A.; Hollinger, G. Microscopic Structure of the SiO2/Si Interface. *Phys. Rev. B* **1988**, *38* (9), 6084–6096. https://doi.org/10.1103/PhysRevB.38.6084.

(3)   Nečas, D.; Klapetek, P. Gwyddion: An Open-Source Software for SPM Data Analysis. *Cent. Eur. J. Phys.* **2012**, *10* (1), 181–188. https://doi.org/10.2478/s11534-011-0096-2.

(4)   Van De Krol, R.; Grätzel, M. *Photoelectrochemical Hydrogen Production*, First.; Krol, R. van de, Gra¨tzel, M., Eds.; Springer US. https://doi.org/10.1007/978-1-4614-1380-6.

(5)   Adeloju, S. B. AMPEROMETRY. In *Encyclopedia of Analytical Science (Second Edition)*; Worsfold, P., Townshend, A., Poole, C., Eds.; Elsevier: Oxford, 2005; pp 70–79. https://doi.org/https://doi.org/10.1016/B0-12-369397-7/00012-1.

(6)   Zhuiykov, S.; Akbari, M. K.; Hai, Z.; Xue, C.; Xu, H.; Hyde, L. Wafer-Scale Fabrication of Conformal Atomic-Layered TiO2 by Atomic Layer Deposition Using Tetrakis (Dimethylamino) Titanium and H2O Precursors. *Mater. Des.* **2017**, *120*, 99–108. https://doi.org/10.1016/j.matdes.2017.02.016.

(7)   Zhuiykov, S.; Akbari, M. K.; Hai, Z.; Xue, C.; Xu, H.; Hyde, L. Wafer-Scale Fabrication of Conformal Atomic-Layered TiO2 by Atomic Layer Deposition Using Tetrakis (Dimethylamino) Titanium and H2O Precursors. *Mater. Des.* **2017**, *120*, 99–108. https://doi.org/10.1016/j.matdes.2017.02.016.

(8)   Oke, J. A.; Jen, T. C. Atomic Layer Deposition and Other Thin Film Deposition Techniques: From Principles to Film Properties. *J. Mater. Res. Technol.* **2022**, *21*, 2481–2514. https://doi.org/10.1016/j.jmrt.2022.10.064.

(9)   Cumpson, P. J.; Zalm, P. C. Thickogram: A Method for Easy Film Thickness Measurement in XPS. *Surf. Interface Anal.* **2000**, *29* (6), 403–406.

https://doi.org/10.1002/1096-9918(200006)29:6<403::AID-SIA884>3.0.CO;2-8.

(10)   Diouf, M. W.; Dufond, M. E. Atomic Layer Deposition of TiO 2 : Effects of the Precursor , Deposition Temperature and Annealing on the Film Quality.

(11)   Chiappim, W.; Fraga, M. A.; Maciel, H. S.; Pessoa, R. S. An Experimental and Theoretical Study of the Impact of the Precursor Pulse Time on the Growth Per Cycle and Crystallinity Quality of TiO2 Thin Films Grown by ALD and PEALD Technique. *Front. Mech. Eng.* **2020**, *6* (October). https://doi.org/10.3389/FMECH.2020.551085.

(12)   Das, C.; Henkel, K.; Tallarida, M.; Schmeißer, D.; Gargouri, H.; Kärkkänen, I.; Schneidewind, J.; Gruska, B.; Arens, M. Thermal and Plasma Enhanced Atomic Layer Deposition of TiO2: Comparison of Spectroscopic and Electric Properties. *J. Vac. Sci. Technol. A Vacuum, Surfaces, Film.* **2015**, *33* (1). https://doi.org/10.1116/1.4903938.

(13)   Dufond, M. E.; Diouf, M. W.; Badie, C.; Laffon, C.; Parent, P.; Ferry, D.; Grosso, D.; Kools, J. C. S.; Elliott, S. D.; Santinacci, L. Quantifying the Extent of Ligand Incorporation and the Effect on Properties of TiO2 Thin Films Grown by Atomic Layer Deposition Using an Alkoxide or an Alkylamide. *Chem. Mater.* **2020**, *32* (4), 1393–1407. https://doi.org/10.1021/acs.chemmater.9b03621.

(14)   Gent, U.; Wetenschappen, F.; Vaste-stofwetenschappen, V. Jan Musschoot. *Kernenergie* **2011**.

(15)   Kilic, U.; Mock, A.; Sekora, D.; Gilbert, S.; Valloppilly, S.; Ianno, N.; Langell, M.; Schubert, E.; Schubert, M. Precursor-Surface Interactions Revealed during Plasma-Enhanced Atomic Layer Deposition of Metal Oxide Thin Films by in-Situ Spectroscopic Ellipsometry. *Sci. Rep.* **2020**, *10* (1), 1–12. https://doi.org/10.1038/s41598-020-66409-8.

(16)   Xie, Q.; Musschoot, J.; Deduytsche, D.; Van Meirhaeghe, R. L.; Detavernier, C.; Van den Berghe, S.; Jiang, Y.-L.; Ru, G.-P.; Li, B.-Z.; Qu, X.-P. Growth Kinetics and Crystallization Behavior of TiO[Sub 2] Films Prepared by Plasma Enhanced Atomic Layer Deposition. *J. Electrochem. Soc.* **2008**, *155* (9), H688. https://doi.org/10.1149/1.2955724.

(17)   Chiappim, W.; Testoni, G. E.; Doria, A. C. O. C.; Pessoa, R. S.; Fraga, M. A.; Galvão, N. K. A. M.; Grigorov, K. G.; Vieira, L.; Maciel, H. S. Relationships among Growth Mechanism, Structure and Morphology of PEALD TiO2 Films: The Influence of O2

Plasma Power, Precursor Chemistry and Plasma Exposure Mode. *Nanotechnology* **2016**, *27* (30), 1–15. https://doi.org/10.1088/0957-4484/27/30/305701.

(18) Rai, V. R.; Agarwal, S. Surface Reaction Mechanisms during Plasma-Assisted Atomic Layer Deposition of Titanium Dioxide. *J. Phys. Chem. C* **2009**, *113* (30), 12962–12965. https://doi.org/10.1021/jp903669c.

(19) Xie, Q.; Jiang, Y. L.; Detavernier, C.; Deduytsche, D.; Van Meirhaeghe, R. L.; Ru, G. P.; Li, B. Z.; Qu, X. P. Atomic Layer Deposition of Ti O2 from Tetrakis-Dimethyl-Amido Titanium or Ti Isopropoxide Precursors and H2 O. *J. Appl. Phys.* **2007**, *102* (8). https://doi.org/10.1063/1.2798384.

(20) Abendroth, B.; Moebus, T.; Rentrop, S.; Strohmeyer, R.; Vinnichenko, M.; Weling, T.; Stöcker, H.; Meyer, D. C. Atomic Layer Deposition of TiO2 from Tetrakis(Dimethylamino) Titanium and H2O. *Thin Solid Films* **2013**, *545*, 176–182. https://doi.org/10.1016/j.tsf.2013.07.076.

(21) Van Meter, K. E.; Chowdhury, M. I.; Sowa, M. J.; Kozen, A. C.; Grejtak, T.; Babuska, T. F.; Strandwitz, N. C.; Krick, B. A. Effects of Deposition Temperature on the Wear Behavior and Material Properties of Plasma Enhanced Atomic Layer Deposition (PEALD) Titanium Vanadium Nitride Thin Films. *Wear* **2023**, *523*, 204731. https://doi.org/10.1016/J.WEAR.2023.204731.

(22) Song, H.; Shin, D.; Jeong, J. E.; Park, H.; Ko, D. H. Growth Behavior and Film Properties of Titanium Dioxide by Plasma-Enhanced Atomic Layer Deposition with Discrete Feeding Method. *AIP Adv.* **2019**, *9* (3). https://doi.org/10.1063/1.5085801.

(23) Angelidis, A. Area-Selective Atomic Layer Deposition of Al2O3, 2019.

(24) Smieszek, A.; Seweryn, A.; Marcinkowska, K.; Sikora, M.; Lawniczak-Jablonska, K.; Witkowski, B. S.; Kuzmiuk, P.; Godlewski, M.; Marycz, K. Titanium Dioxide Thin Films Obtained by Atomic Layer Deposition Promotes Osteoblasts' Viability and Differentiation Potential While Inhibiting Osteoclast Activity—Potential Application for Osteoporotic Bone Regeneration. *Materials (Basel).* **2020**, *13* (21), 1–20. https://doi.org/10.3390/ma13214817.

(25) Harvey, S. P.; Zhang, F.; Palmstrom, A.; Luther, J. M.; Zhu, K.; Berry, J. J. Mitigating Measurement Artifacts in TOF-SIMS Analysis of Perovskite Solar Cells. *ACS Appl. Mater. Interfaces* **2019**, *11* (34), 30911–30918.

https://doi.org/10.1021/acsami.9b09445.

(26)   Jeynes, C.; Colaux, J. L. Thin Film Depth Profiling by Ion Beam Analysis. *Analyst* **2016**, *141* (21), 5944–5985. https://doi.org/10.1039/c6an01167e.

(27)   Jackman, M. J.; Thomas, A. G.; Muryn, C. Photoelectron Spectroscopy Study of Stoichiometric and Reduced Anatase TiO2(101) Surfaces: The Effect of Subsurface Defects on Water Adsorption at near-Ambient Pressures. *J. Phys. Chem. C* **2015**, *119* (24), 13682–13690. https://doi.org/10.1021/acs.jpcc.5b02732.

(28)   Marchant, S.; Foot, P. J. S. Poly(3-Hexylthiophene)-Zinc Oxide Rectifying Junctions. *J. Mater. Sci. Mater. Electron.* **1995**, *6* (3), 144–148. https://doi.org/10.1007/BF00190545.

(29)   Hannula, M.; Ali-Löytty, H.; Lahtonen, K.; Sarlin, E.; Saari, J.; Valden, M. Improved Stability of Atomic Layer Deposited Amorphous TiO2 Photoelectrode Coatings by Thermally Induced Oxygen Defects. *Chem. Mater.* **2018**, *30* (4), 1199–1208. https://doi.org/10.1021/acs.chemmater.7b02938.

(30)   Coster, D.; L. Kronig, R. De. New Type of Auger Effect and Its Influence on the X-Ray Spectrum. *Physica* **1935**, *2* (1–12), 13–24. https://doi.org/10.1016/S0031-8914(35)90060-X.

(31)   Di Valentin, C.; Pacchioni, G.; Selloni, A. Reduced and N-Type Doped TiO2: Nature of Ti3+ Species. *J. Phys. Chem. C* **2009**, *113* (48), 20543–20552. https://doi.org/10.1021/jp9061797.

(32)   Khomenko, V. M.; Langer, K.; Rager, H.; Fett, A. Electronic Absorption by Ti3+ Ions and Electron Delocalization in Synthetic Blue Rutile. *Phys. Chem. Miner.* **1998**, *25* (5), 338–346. https://doi.org/10.1007/s002690050124.

(33)   Brassard, D.; El Khakani, M. A.; Ouellet, L. Substrate Biasing Effect on the Electrical Properties of Magnetron-Sputtered High-k Titanium Silicate Thin Films. *J. Appl. Phys.* **2007**, *102* (3). https://doi.org/10.1063/1.2759196.

(34)   Methaapanon, R.; Bent, S. F. Comparative Study of Titanium Dioxide Atomic Layer Deposition on Silicon Dioxide and Hydrogen-Terminated Silicon. *J. Phys. Chem. C* **2010**, *114* (23), 10498–10504. https://doi.org/10.1021/jp1013303.

(35)   Bronneberg, A. C.; Höhn, C.; Van De Krol, R. Probing the Interfacial Chemistry of Ultrathin ALD-Grown TiO2 Films: An In-Line XPS Study. *J. Phys. Chem. C* **2017**,

121 (10), 5531–5538. https://doi.org/10.1021/acs.jpcc.6b09468.

(36) Bras, J. A. Understanding Titanium Dioxide Passivation on Silicon Photoanodes in Photoelectrochemical Cells, Delft University of Technology, 2015.

(37) Lee, J.; Lee, S. J.; Han, W. B.; Jeon, H.; Park, J.; Jang, W.; Yoon, C. S.; Jeon, H. Deposition Temperature Dependence of Titanium Oxide Thin Films Grown by Remote-Plasma Atomic Layer Deposition. *Phys. Status Solidi Appl. Mater. Sci.* **2013**, *210* (2), 276–284. https://doi.org/10.1002/pssa.201228671.

(38) Atanasov, S. E.; Kalanyan, B.; Parsons, G. N. Inherent Substrate-Dependent Growth Initiation and Selective-Area Atomic Layer Deposition of TiO2 Using "Water-Free" Metal-Halide/Metal Alkoxide Reactants. *J. Vac. Sci. Technol. A Vacuum, Surfaces, Film.* **2016**, *34* (1). https://doi.org/10.1116/1.4938481.

4 Plasma Enhanced Atomic Layer Deposition of Nickel and Nickel Oxide on Silicon for Photoelectrochemical Applications

4.1 Introduction

Nickel oxide (NiO) has attracted a great deal of attention for its use in PEC water splitting as well as a hole transport layer (HTL) for perovskite solar cells (PSCs) thus warranting additional understanding of its growth chemistry and performance characteristics [1,2]. The effect of post deposition annealing treatment parameters and their implication on film properties and subsequent performance is also of interest in such fields [3]. Interest in NiO in the fields of PSCs and PECs stems primarily from its ability to provide enhanced device stability, decreased absorption losses and its ease of deposition commonly achieved using plasma enhanced atomic layer deposition (PEALD) [4]. Furthermore, its suitably wide bandgap of 3.4 – 4eV for light transmission coupled with suitable energy level alignment which facilitates hole transportation makes this transition metal oxide one of relevance within the field [5].

NiO is highlighted within the literature as having potential to be implemented in PEC water splitting setups as a surface coating for n-Si photoanodes typically being applied for its electrocatalysts properties as detailed by Sun et al. however, He et al also report on the application of NiO for its potential as a protective layer in which thin films were deposited via pulsed laser deposition (PLD) [6,7]. As mentioned earlier within the Introduction section, Si is not the only photoelectrode substrate material of interest with others such as GaN also under investigation with NiO also being applied to this alternative as reported by Kang et al wherein NiO cocatalyst was applied via chemical vapor deposition (CVD) to doped GaN [8].

NiO has also been deposited in non-planar form as reported by Babar et al wherein NiO nanoflakes were spray-coated onto FTO glass slides [9].

While a great many studies have been reported on the application of NiO for its application in water splitting PEC systems, the majority detail its efficacy purely with regard to its performance as an electrocatalyst with few exploring its potential as a protective film such as to protect the underlying photoelectrode rather than purely seeking to enhance gross photocurrent output. Furthermore, fewer still offer detailed analysis with a focus on in-situ cycle-by-cycle early-stage nucleation studies to gain in-depth information on the growth kinetics and the development of the very crucial interfacial region between the underlying substrate and any applied coating. This chapter details an in-line x-ray photoelectron spectroscopy (XPS) analysis of the growth of bulk ALD grown Ni films with additional focus on the nucleation of ultra-thin (ca. 2nm) Ni films on Si using Bis(cyclopentadienyl)nickel(II) or nickelocene ($NiCp_2$) as the chosen precursor. Films were grown via PEALD. The effect of various growth parameters such as deposition temperature, reactant and co-reactant dose times are detailed.

Films are characterized using *in-situ* XPS to avoid undesirable and often misleading effects of atmospheric contamination of deposited films. Nucleation of NiO was studied through a sequential growth experiment which involved performing a half cycle of ALD followed by XPS scanning. This was repeated for every half cycle up to 5 ALD cycles in total then proceeding with regular full cycles for the remainder of the film deposition. This approach allowed for the analysis of the early-stage growth at the Ni-Si interface during the first 5 cycles.

Argon milling was also utilized to study and confirm the composition of deposited NiO films. Analysis of the impact of post deposition plasma annealing treatments on film stoichiometry and electrochemical performance is shown in addition to that of plasma annealing steps interspersed within the film growth recipe in so-called 'supercycles'.

The effect of applying post deposition annealing treatments to deposited films as well as the optimization of the deposition recipe used in the study are also presented. There is little to be found in literature reports on the performance of Ni- metal in water splitting applications and as such this has been explored to determine its efficacy. Deposited oxide and metal films are tested under simulated sunlight conditions to study their performance as water splitting photoelectrodes.

4.2 Experimental

4.2.1 ALD of NiO

n-Si (100 $\rho = 5 - 9\Omega cm^2$) N(Phos) doped reclaim grade wafers were purchased from PI-KEM Ltd. The 4-in. diameter Si of centre thickness from $425 - 550 \, \mu m$ were cleaved into $2.5 \times 2.5 \, cm^2$ squares before being loaded into the ALD system in their as received state after being blown with N_2 to remove Si particles created during the cleaving. NiO deposition was performed via PEALD in the Oxford Instruments FlexAl ALD Reactor using Bis(cyclopentadienyl)nickel(II) (nickelocene STREM 99%) and a 300 W O_2-plasma as the reactant and co-reactant species respectively, with N_2 as the carrier gas. A 300 W hydrogen plasma of varying duration was applied for mid-recipe and post deposition annealing where required. Substrate temperatures of 200, 250 and 300 degrees were applied to determine the ALD window for nickelocene in the reactor.

Reactant dose lengths of $0.25 - 5$ seconds were investigated to establish precursor dose saturation while O_2-plasma steps of 1-15 seconds were similarly tested. Growth per cycle (GPC) rates were also determined using these investigations. These saturation curves and GPC rates combined with ALD tool manufacturer suggested parameters and literature reports aided in the selection of final process parameters used for subsequent sequential and continually grown films. A form of sequential 'supercycling' was carried out in an effort to explore methods of depositing Ni-metal. The supercycle involved 4 standard ALD cycles of reactant and co-reactant using the parameters shown in Table 1, followed by a 5-minute 300 W H_2-plasma anneal. The precursor bottle, manifold, lines, and chamber walls were set to 90, 65, 75 and 120 °C respectively.

This series of 4 deposition and 1 annealing step was continued for a total of 20, 40, 80 and finally 120 cycles with XPS scanning performed between these steps to study the film formation during its growth. The same was performed with XPS scanning only following the full 120 cycles. A deposition of 250 cycles with identical parameters to those used in the 120 supercycle process was carried out however cycles were completed in 50 supercycle batches with 15 minutes of plasma annealing performed following each 50 cycles and scanned after each annealing step. Again, the same 250 cycles process was subjected to the same total amount of annealing of 75min at the end of the deposition to compare the effect of the same amount of time of anneal at the end of deposition versus interspersed in the deposition and its effect on the resulting films.

Table 4.1 ALD process parameters used for the deposition of thin films in this study.

Variable (s)	Value
Precursor Dose	5
Precursor Purge	4
Gas Stabilization	6
Co-reactant Dose	10
Co-reactant Purge	1
Deposition Temperature °C	250

4.2.2 Characterisation Techniques

In-line photoemission analysis was performed on films post deposition as well as post plasma annealing treatments and photoelectrochemical cell testing. XPS allowed for the determination of film composition as well as a method of real time thickness approximation. XPS was carried out using a Scienta Omicron (Monochromated Al Kα source 1486.74 eV,

$6.5 \times 10^{-7} \, Pa$ base pressure) with a 128 channel Argus CU detector. As discussed previously, the XPS is coupled via vacuum held robotic wafer transfer system allowing for sample transfer between XPS and ALD in less than 1 minute without the need for vacuum break and unwanted contamination of wafer surfaces. Wide energy survey spectra as well as high resolution narrow window spectra were taken with step sizes of 1 and 0.1 eV respectively. Analysis was performed using AAnalyser peak fitting software with a Shirley-Sherwood background and Voigt profiles applied [10]. All spectra were shifted such that the Si^0 $2p_{3/2}$ component was placed at 99.4 eV binding energy (BE)[11–13] .

Thickness values were approximated mathematically using the Thickogram method [14], which by measuring the suppression of the substrate peak as a function of the deposition of an overlayer and knowing material properties such as electron mean free path allows for thickness approximations. The method was derived to compare peak intensity of a substrate and overlayer peak for a given take off angle which when combined with the effective attenuation lengths (EAL) of the materials in question allows for the determination of the thickness of the overlayer based on the mean free path of the substrate electrons in the overlayer material. EAL values were obtained from the NIST EAL database with the XPS relative sensitivity factors being taken from the database of empirically derived atomic sensitivity factors [15]. In order to verify the accuracy of the Thickogram method, film thicknesses were also measured using an ex-situ ellipsometer, which showed that Thickogram obtained thickness approximations were satisfactory. Spectroscopic ellipsometry was carried out using a Woollam XLS-100 multi-wavelength system. XPS scans were carried out after 0, 2 4,6,8,13,18,23 and 33 minutes of milling using a Focus GmbH FDG 150 Ion Source at 3.5 keV and a pressure of $3 \times 10^{-5} Pa$.

Photoelectrochemical cell testing of films in order to measure the comparative chemical stability and photocurrent output of the deposited films was carried out in the Redoxme AB MM 15 ml double sided photoelectrochemical cell (PEEK constructed body, in 3 electrode configuration) with Pt counter electrode (99.9%) and a Ag/AgCl (1 mol/KCl) reference electrode. The electrolyte solution used was a 0.5 M phosphate buffer solution (pH 7.4) with the electrodes being irradiated with 1000 Wm^{-2} AM 1.5 G simulated sunlight supplied by an Oriel Instruments xenon arc lamp. Samples were irradiated in the PEC cell in a top-down configuration with 1 cm^2 of exposed sample surface. I-V linear sweep voltammetry PEC tests were performed to determine the photocurrent density of deposited films to screen their effectiveness as photoanode materials with this test sweeping from -0.7 – 3.5 V vs Ag/AgCl. Samples were also subjected to chronoamperometric testing at 1 V vs Ag/AgCl for 1000 seconds such as to determine the chemical stability of films under PEC conditions.

4.3 Results & Discussion

4.3.1 XPS Characterisation

4.3.1.1 Cycle-by-Cycle Growth Chemistry

XPS was carried out on Ni films at all stages of deposition and treatment from as deposited, post plasma annealing, and following exposure to atmosphere such as to investigate the state of Ni films in these environments before any photoelectrochemical testing. Prior to depositing Ni films for characterisation and later PEC testing, an investigation into acquiring optimal deposition parameters for the ALD FlexAl system such as the $NiCp_2$ dose time was performed. The saturation point was determined using a combination of ex-situ ellipsometry alongside the complementary Thickogram method of thickness approximation through monitoring the ratio of the Ni $2p$ overlayer peak with that of the substrate Si $2p$ peak analyzing its rate of attenuation as a function of increasing ALD cycles and therefore overlayer film thickness. An initial substrate temperature of 250°C was chosen for characterisation studies which is within the ALD window for PEALD of NiO from nickelocene and O_2 plasma and provided a suitable starting temperature for nucleation studies [16–18]. This temperature was used during the acquisition of reactant and co-reactant saturation curves as shown in Figure 4.1, such as to characterise the nickelocene precursor on the ALD system being that variations in chamber geometry between ALD systems can influence film growth rates. It can be seen from Figure 4.1 that film thickness increases sharply with increasing reactant dose time up until 3 *s* wherein the growth rate begins to diminish. Based on the dose saturation curve and owing to relatively low levels of carbon incorporation within deposited films of approximately 4%, reactant and co-reactant dose times of 1 *s* and 10 *s* respectively were chosen for all further film depositions.
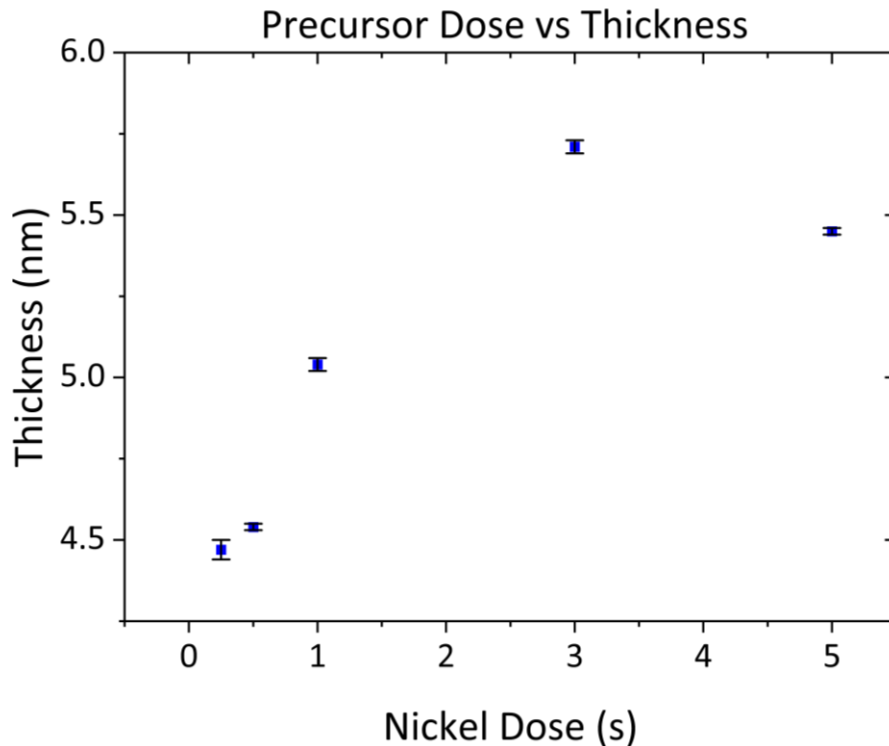
Figure 4.1 Nickelocene reactant dose time saturation curve for 100 cycle processes from 0.25 – 5 s doses, with the co-reactant dose time set at 10 s. Error for these ellipsometry thickness measurements was determined through calculating the standard error of the mean value of three individual measurements for each sample.

The co-reactant dose of 10 *s* selected based on ALD recipes within the literature as well as saturation studies performed within this work as shown in Figure 4.2 and was shown to yield a suitable growth rate, film stoichiometry and efficient sample processing time [19]. The film growth rate as a function of increasing O2 plasma coreactant dose duration is not the typical plateau which is often observed in ALD precursor recipe characterisation studies this is due to an effect called soft saturation [20]. For both the nickel and plasma coreactant dose saturations the measured experimental results seen in Figure 4.1 and Figure 4.2 are in line with those expected based on reports within the literature [19,21–23].
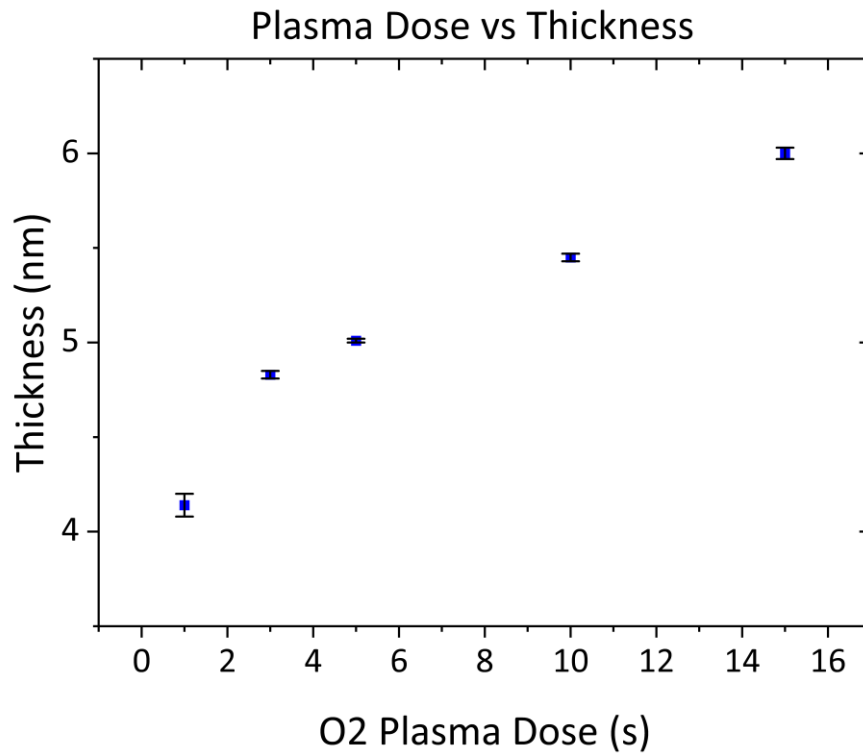
Figure 4.2 O2 plasma co-reactant characterisation showing soft-saturation behaviour. Error for these ellipsometry thickness measurements was determined through calculating the standard error of the mean value of three individual measurements for each sample.

To gain further insight into the early-stage growth kinetics of the Ni deposition process, sequential PEALD depositions were performed and analysed throughout the process at regular intervals using XPS. These measurements focused on the Si $2p$, O $1s$, Ni $2p_{3/2}$ and C $1s$ core levels such as to closely monitor the film growth and to identify any evidence of additional oxidation states or silicides in the case of the Ni peak. The formation of oxidation states is of particular relevance due to the hole transport to the electrode surface relying heavily on the interfacial chemistry between the overlying Ni protective layer and underlying Si substrate.

The characterisation of the precursor within the ALD system allowed for the investigation of the nucleation of NiO thin films for a variety of substrate temperatures consisting of 200, 250 and 300 °C. Guided by literature reports and combined with investigations within this study of both higher and lower substrate temperatures, 250 °C was found to be the optimal deposition temperature. This is based on growth per cycle deposition rate as well as stoichiometry evaluations finding remnant carbon incorporation to be sufficiently low in the sub 5% following variations in recipe parameters to reduce this and was therefore chosen for the remainder of the depositions performed throughout.

The films used in the investigation of nucleation were grown via sequential deposition. This consisted of performing half-ALD cycles of alternating reactant and co-reactant up to a total of 5 full ALD cycles with *in-situ* XPS scanning after each half cycle. An additional 5 full ALD cycles were performed on the existing 5 to bring the sum to 10 cycles with XPS scanning performed at this stage as well. Cycles were then performed in batches of 10 full ALD cycles at a time with XPS scanning after each batch until the final total of 100 cycles was reached.

An example of these nucleation studies is shown in Figure 4.3 and Figure 4.4. It can be seen from Figure 4.3 that the sample shows measurable quantities of Ni following 3 full ALD cycles from the elemental compositions obtained using XPS.
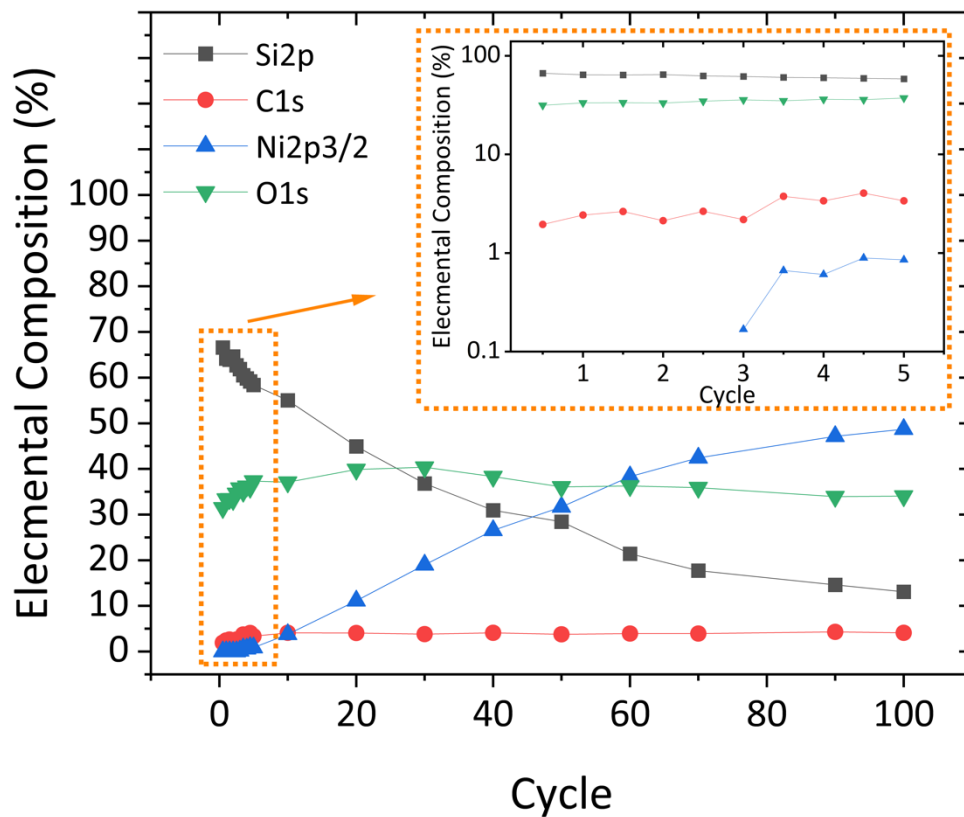
Figure 4.3 Elemental compositions of 250 °C grown sample substrate with inset enhanced view of the initial half cycles.

These compositions were calculated using XPS measurements, an example of which seen in Figure 4.4 which confirms this with the evolution of the Ni $2p_{3/2}$ peak as a function of increasing ALD cycles. Sequentially grown films allowed for the determination of growth per cycle (GPC) rates for the deposition recipe used which later facilitated accurate deposition of a desired film thickness.
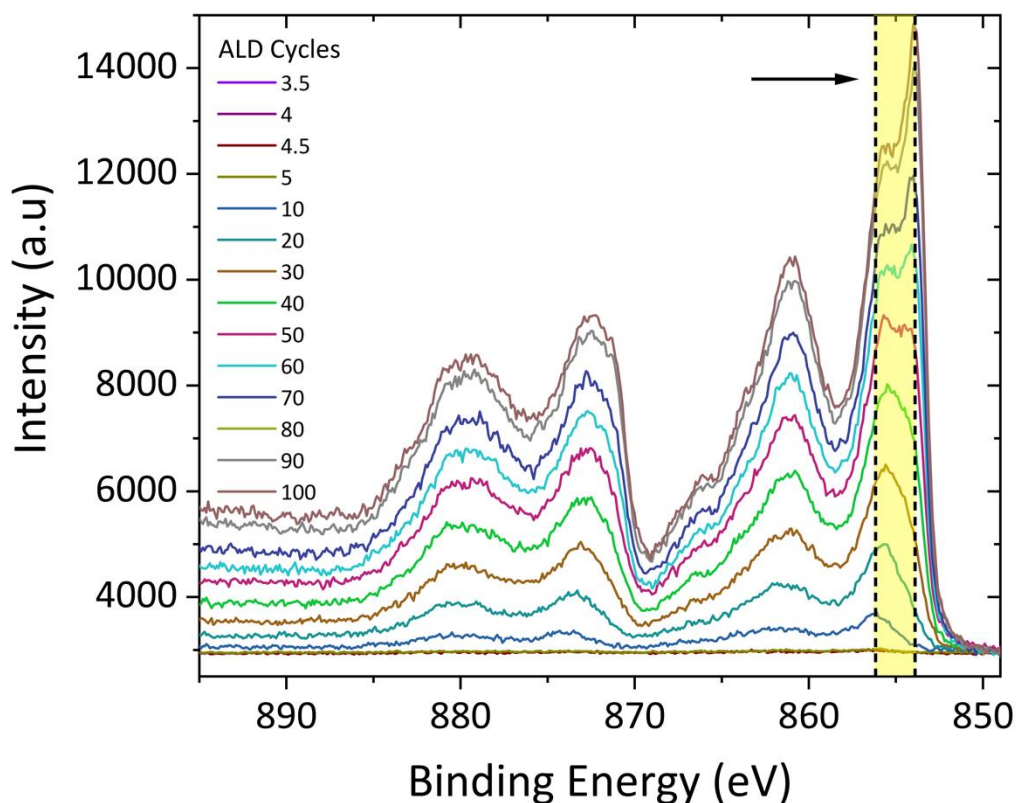
Figure 4.4 High resolution narrow energy region XPS spectra showing sequential growth of NiO with evidence of nucleation delay verified with growth undetectable before 3 ALD cycles with area highlighted indicating BE shift of Ni peak from early thru to final ALD cycle.

XPS analysis of the sequentially grown Ni film shows the first detectable Ni 2p signal appeared at 856.1 eV following 3.5 ALD cycles and shifts gradually to lower BE over the course of the deposition to the position of NiO at 854.2 eV illustrated in the yellow window in Figure 4.4, a BE position which is consistent with literature reports [24–27]. This BE shift over the course of the film deposition is indicative of the complex interaction between the first few monolayers of Ni-containing species with the underlying Si substrate. A similar effect is observed in the Si 2p peak with the oxide BE position starting out at 103.6 eV for bare untreated reference Si substrate which, over the course of the deposition shifts to the lower BE position of 102.9 eV at the peak maximum. This shift of the oxide component in

the Si peak is a further indication of the strong interactions between the Si and Ni. The formation of suboxides at the Si/Ni interface results in the suppression of the bare Si oxide peak as a function of ALD cycles as the presence of these suboxides, silicates, or silicides becomes dominant in that BE region. The extent of the BE shift of the oxide component of the Si $2p$ peak is illustrated in Figure 4.5 (a) wherein normalized XPS spectra of a bare Si reference sample is compared to that of 100 cycles of NiO as well as the tracking of the BE shift over the full course of the sequential deposition. Figure 4.5 (b) tracks the BE shift of the Si oxide component as a function of ALD cycle with the inset showing a detailed view of the early half cycles where we observe the BE of the oxide decreasing following each co-reactant pulse while the reactant dose causes the BE to increase relative to the previous co-reactant half cycle. While counterintuitive, this suggests that $NiCp_2$ doses promote a reaction at the interface which causes the breaking of some Ni-O bonds, with the released oxygen bonding to Si. It is possible that this is accompanied by the formation of Ni-Ni bonds, but the Ni2p signal is too weak to confirm this. Subsequently, during the oxidation step the donation of oxygen to nickel and reduction of the silicon oxide appears to be occurring. The similar electronegativity of Si and Ni and the instability of the respective suboxides support the hypothesis that oxygen is routinely transferred between the elements. This result was observed for all substrate deposition temperatures of 200, 250 and 300 °C.
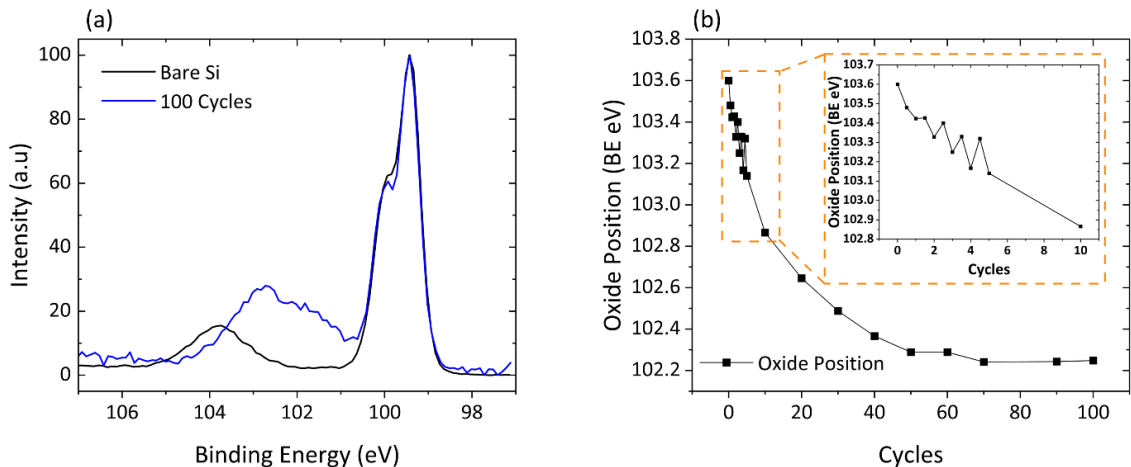
Figure 4.5 (a) Normalized XPS spectra of bare reference Si substrate vs 100 cycles of NiO (b) Si 2p oxide BE as a function of Ni ALD cycles.

The evolution of the O $1s$ peak is depicted in Figure 4.6 as a function of increasing number of ALD cycles for the same sequentially grown samples. In the O $1s$ spectrum the two primary peaks observed are at approximately 533 eV corresponding to oxygen present in the substrate and 529 eV as a result of the oxygen in NiO. The intensity of the O $1s$ peak corresponding to SiO_x can be seen to rapidly decrease as it is attenuated as early as the first half ALD cycle and then increase, while shifting to lower BE, indicating significant restructuring at the interface with the substrate. At lower BE, the NiO contribution is seen to increase steadily throughout the deposition, becoming measurable after approximately 10 full cycles.
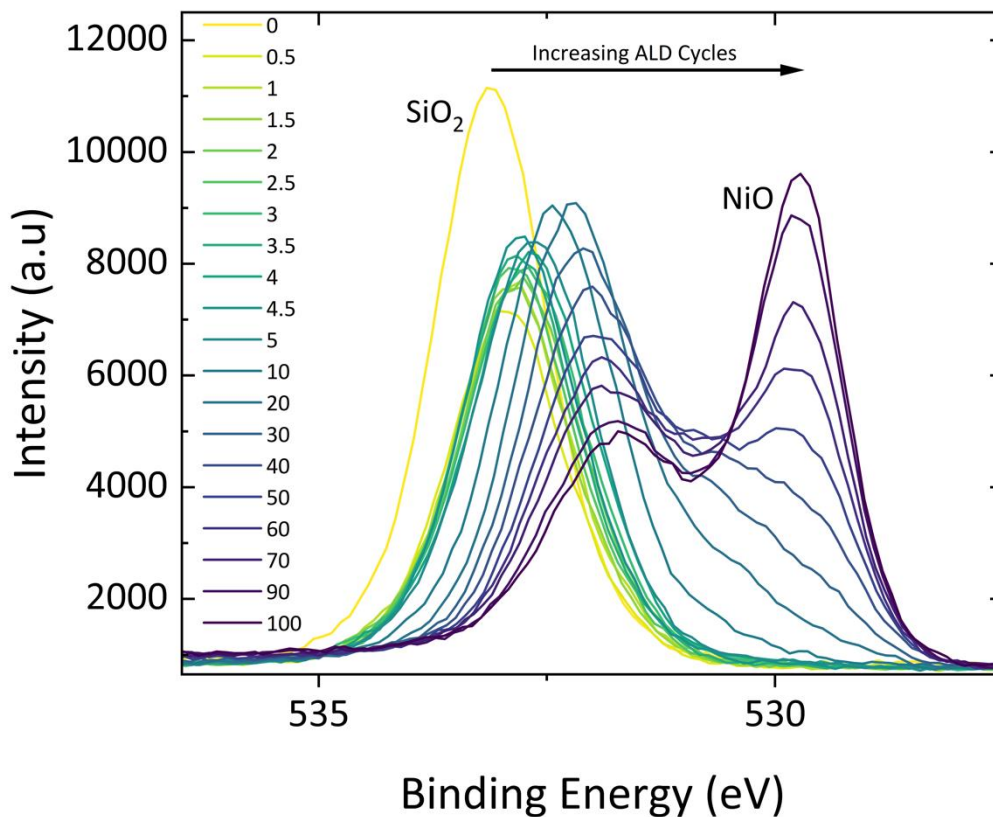
Figure 4.6 O1s XPS high resolution spectra as a function of increasing ALD cycles for sequentially grown NiO at 250 °C substrate temperature.

4.3.1.2 Post Deposition Annealing to Form Metallic Ni

Films were removed from vacuum and stored in atmosphere before being rescanned to determine the extent of atmospheric contamination, prior to being subjected to a series of plasma annealing stages in an effort to reduce the film to Ni-metal. A 20 and 40 minute 300W H_2 plasma anneal was carried out at 250 °C with *in-situ* XPS analysis performed before and after. Samples were removed from vacuum and exposed to atmosphere then reloaded for XPS analysis one final time to determine the extent of sample contamination and susceptibility to carbon incorporation and re-oxidation post plasma annealing.
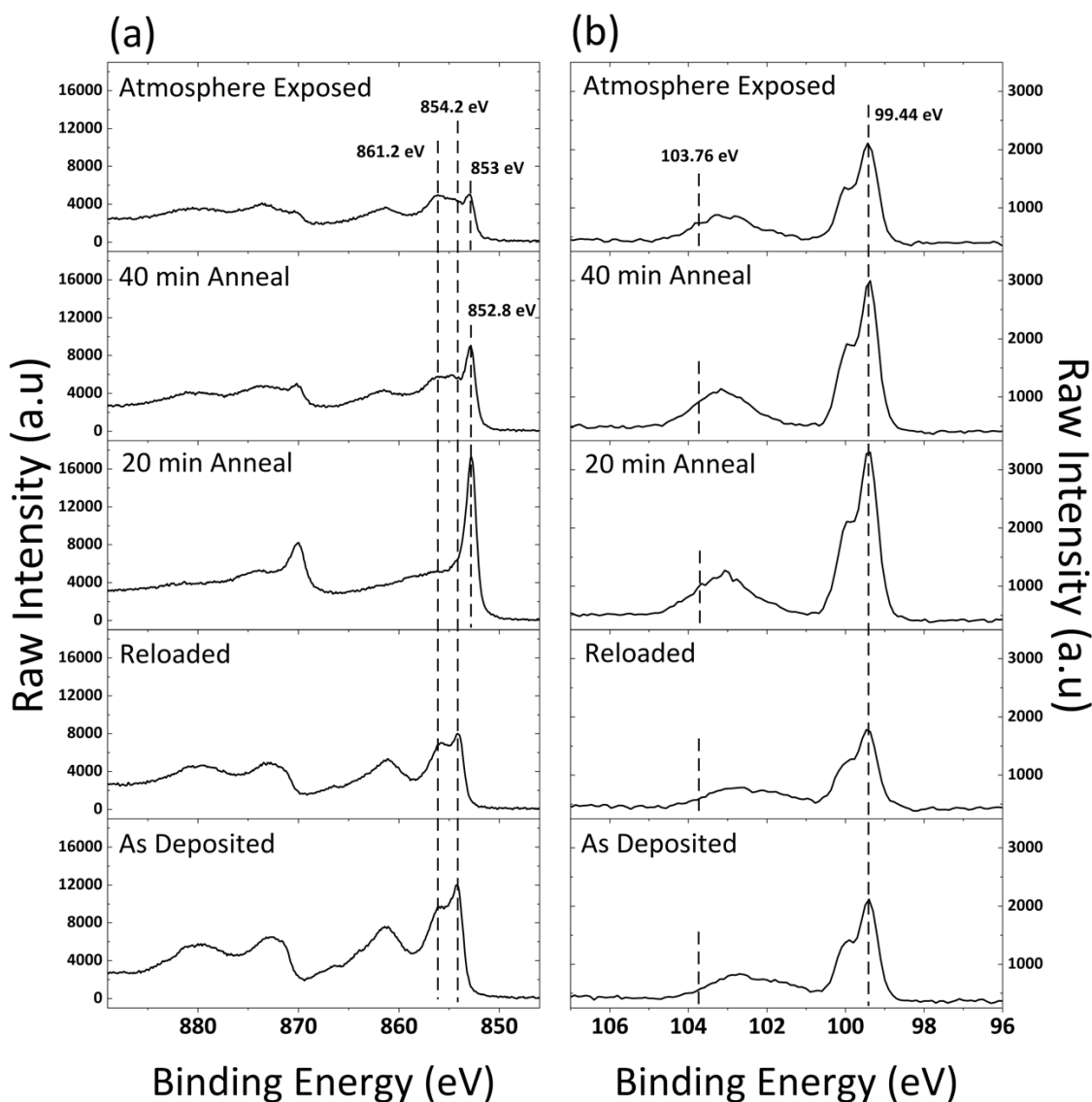
Figure 4.7 High resolution normalized XPS spectra for all stages of treatment on the same sample (a) Ni 2p (b) Si 2p. In (b) the BE positions of the Si^0 and Si^{4+} are shown for reference.

Figure 4.7 shows the XPS spectra throughout all stages of treatment. High resolution spectra of the Ni $2p$ peak verifies the presence of NiO with the peak centered at 854.2 eV as expected shown in Figure 4.7 (a). Films subjected to H_2 plasma annealing for 20 minutes are largely reduced to metallic nickel as shown in Figure 4.7 (a) with the Ni $2p_{3/2}$ BE centered at 852.9

eV separated by 18 eV from the Ni $2p_{1/2}$ component at 870.1 eV. The Ni metal $2p_{3/2}$ peak is observed at 852.9 eV which falls within the literature range of 852.7 eV $\pm$ 0.4 eV [28,29]. Following the 40-minute H_2 anneal there are no significant improvements in the reduction of the film seen compared to the 20 minute process but rather results in a considerable etching effect on the film shown by the reemergence of the Si $2p$ peak following this treatment. Additionally, the 40-minute annealed sample appears to reintroduce the presence of the NiO component seen in the as deposited state at 854.2 eV and 861.2 eV which may suggest that although receiving an extended plasma annealing stage, 20 minutes was not sufficient to reduce the bulk film in its entirety. It is clear from the 20-minute plasma annealed sample that there are remnants of the NiO features in the Ni $2p_{3/2}$ component still present which further indicates that the film was not fully reduced, potentially suggesting that some fully or partially oxidized nickel remains deeper within the film with only the surface of the Ni film being reduced fully. The 40-minute annealed sample is seen to uncover these buried features through removing the overlying metallic Ni through film etching, which is confirmed as mentioned by the reappearance of the Si film upon completion and uncovering the underlying Ni silicate which appears more stable and therefore more difficult to reduce due to it remaining even following the extensive plasma annealing.

Figure 4.7 (b) shows the high-resolution spectra for the Si $2p$ region as a function of sample treatment over the course of the plasma annealing investigation, with that of a bare Si sample included for reference. All data has been shifted to align the bulk to 99.4 eV [11]. It is clear when looking at the as deposited film as well as that of the film post-exposure to atmosphere that there is a significant shift of the higher BE oxide peak to a lower BE suggesting the

presence of additional Si oxidation states as seen from the deconvolution shown in Figure 4.8.
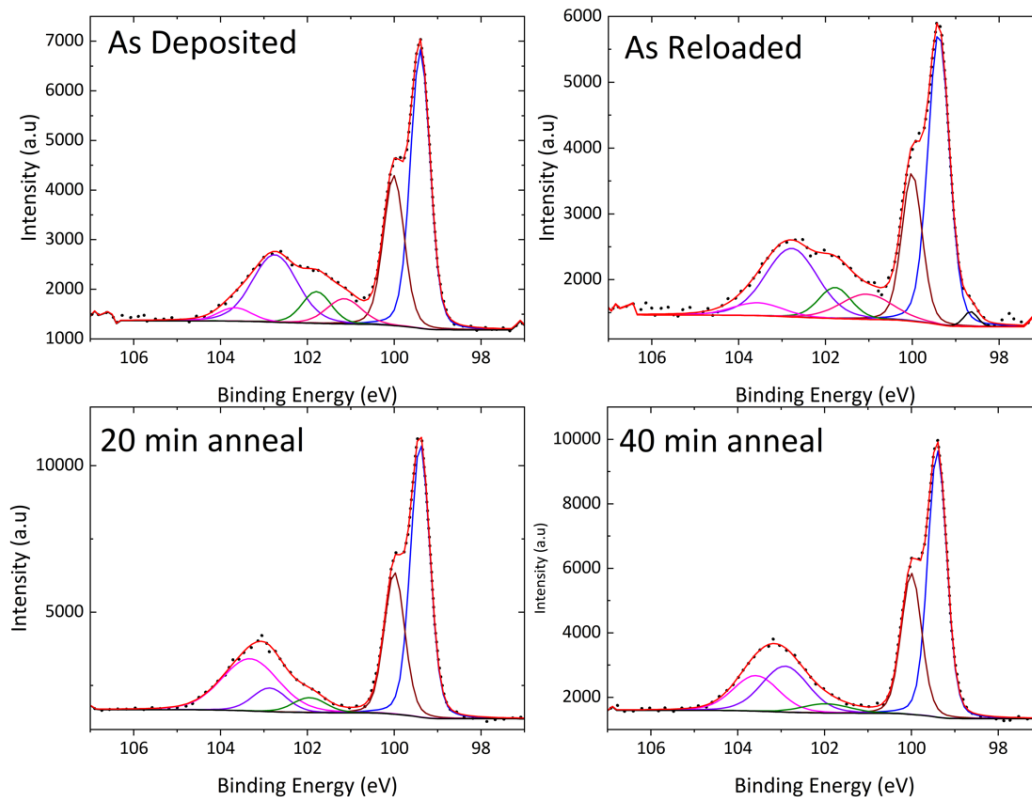
Figure 4.8 High resolution XPS spectra and peak deconvolution for various stages of sample treatment for the 250 degree substrate temperature sample.

Beginning from bare Si with the expected single 4+ oxidation state at 103.8 eV, the silicon oxide component in the as deposited film is seen to be dominated by 3+ and 2+ oxidation states at 102.5 eV and 101.3 eV respectively with that of the 4+ being diminished almost into the noise. Upon exposure of the film to atmosphere, the peak intensity as a whole is diminished due to carbon contamination on the films with the 4+ seen to be suppressed and the increased contribution from the 1+ state at approximately 100.6 eV. 20 minutes of plasma annealing is sufficient to remove this 1+ oxide component and only that of the 2+, 3+ and 4+

components are observed. The 40 minute anneal, further reduces the contribution of 2+ oxide with the film now dominated by the 4+ and 3+ states. Robust deconvolution of XPS spectra of Ni is found to be highly complex owing to the numerous satellite features present within the peak envelope in addition to their tendency to overlap one another making indisputable assertions on their identification difficult. This is reflected within the literature with many reports presenting deconvolution of the Ni $2p_{3/2}$ region solely with little or no analysis of the Ni $2p_{1/2}$ region [29]. Furthermore, general consistency within the literature on the quantity of fit peaks within the envelope is lacking and there appears an acceptance of deviation of the data set and the fit envelope with it being cited as a result of the fit complexity of the Ni region [30–32]. As such, it is more reasonable to analyse XPS spectra of this region qualitatively rather than quantitatively due to the inherent unreliability. However, Grosvenor et al present perhaps the most complete assessment of the fitting of the Ni region which was the basis and reference source utilized in this work for a satisfactory example of a Ni $2p_{3/2}$ deconvolution as seen in Figure 4.9 showing only marginal deviation of the fit envelope from the data set [33].
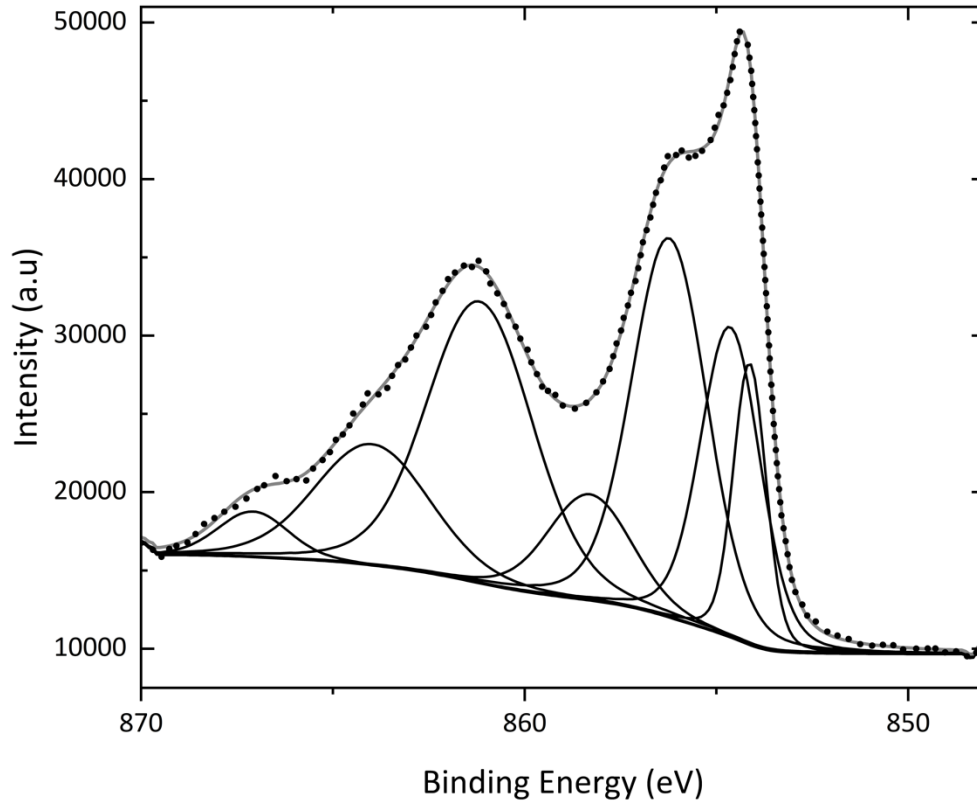
Figure 4.9 High resolution spectra of Ni 2p 3/2 peak showing deconvolution fit for NiO in its as deposited state.

Figure 4.10 shows deconvolution of high-resolution spectra for the remaining stages of sample treatment associated with the sample shown in Figure 4.9 above.
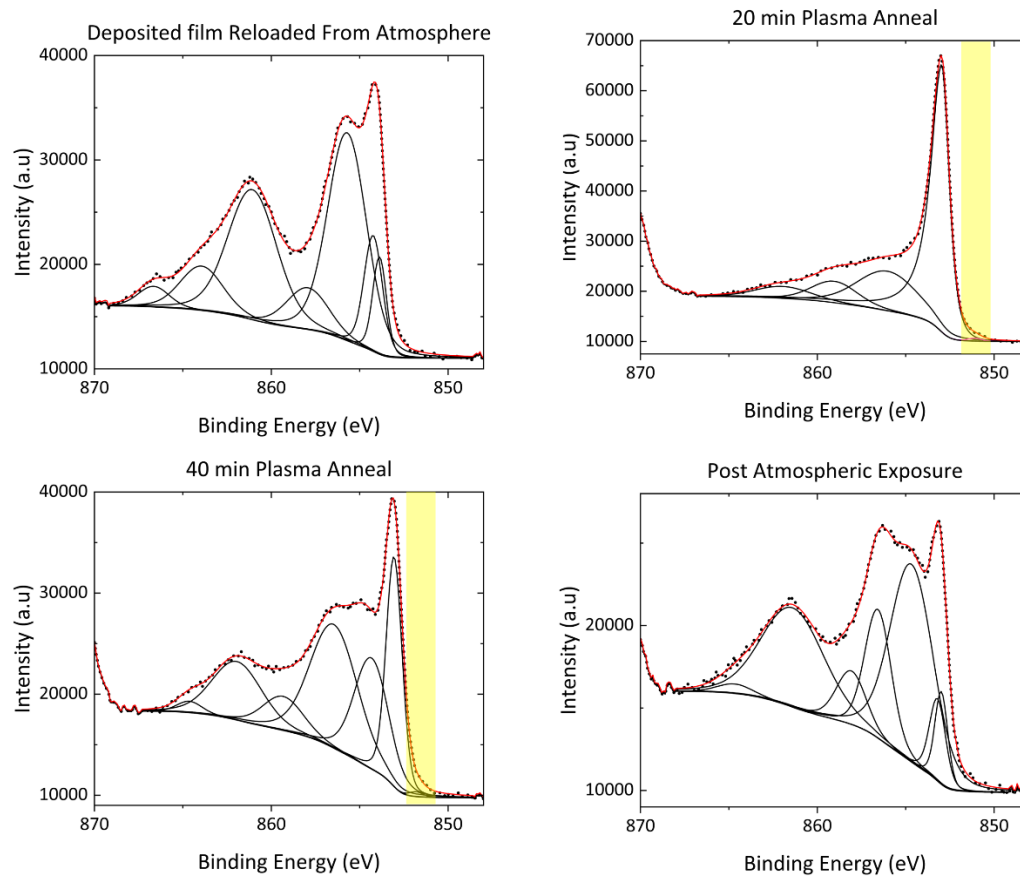
Figure 4.10 Ni 2p XPS spectra showing peak deconvolutions for all stages of sample treatment with yellow highlighted region indicating the presence of the lower binding energy component associated with silicide formation.

4.3.1.3 Comparison Between Depth Profiling by Ar Milling and Cycle-by-cycle

Growth

Ar ion bombardment in conjunction with XPS is regularly employed as a method of depth profiling deposited thin films. In order to compare the depth profile information that our cycle-by-cycle approach yielded with the more traditional method, we carried out slow Ar milling coupled with XPS depth profiling on the same films. Figure 4.11 (a) & (c) show XPS high resolution Ni2p spectra for a NiO film before and after slow Ar milling totalling 33

minutes. The data appears to show an overlayer of NiO, with metallic nickel metal underneath, with the predominant peak appearing at approximately 853 eV, the BE expected with Ni-metal rather than the 854 eV which is consistent with NiO. Ar milling was performed in short, repeated exposures to a total time of 2, 4, 6, 8, 13, 18, 23 and 33 minutes, with in-situ XPS analysis after each. Figure 4.11 (d) shows the BE shift from a higher to lower BE as a function of Ar milling time, indicating a greater metallic contribution as a function of time.
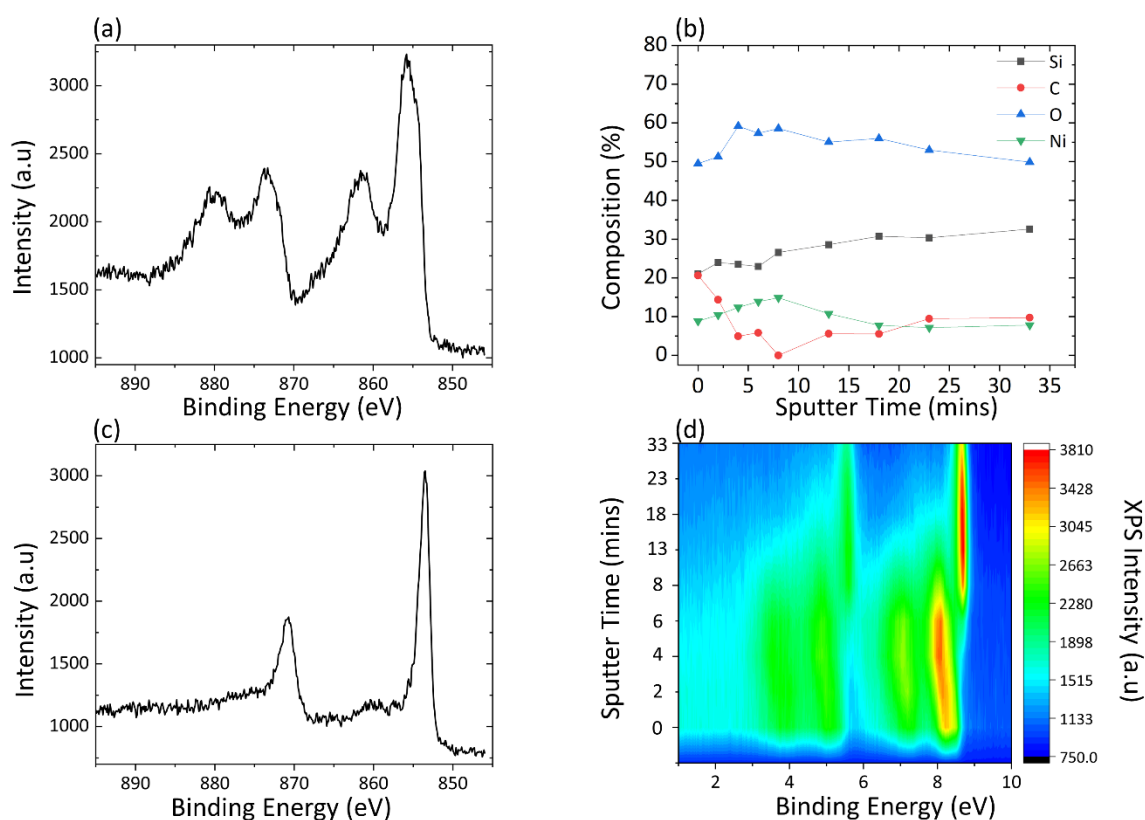
Figure 4.11 (a) & (c) XPS high resolution spectra argon milled NiO in its as deposited and post 33 minutes of sputtering respectively (b) Elemental compositions as a function of argon milling (d) Contour plot showing film conversion from nickel oxide to nickel metal as a function of increasing argon milling.

This analysis is consistent with data from Kenney *et al* wherein the film is reported to remain metallic below a thin layer of oxide, even following long duration photoelectrochemical

testing in a harshly oxidizing environment [34]. However, both our data and that of Kenney et al shows no presence of metallic nickel before Ar milling, despite the entire film being well within the sampling depth of XPS. Our sequential growth studies have shown that the films under consideration are oxidized throughout the growth process, but Ar depth profiling suggests the presence of metal. NiO films have been shown within the literature to readily reduce to metallic Ni upon ion bombardment [35]. The reducing effect and preferential sputtering of oxygen in NiO and other transition metals and oxides such as Fe, Cu, Mo and V is widely reported with MoO_3 , V_2O_5, Fe_2O_3 and CuO being reported to reduce to MoO_2 , V_2O_3 , Fe and Cu respectively [36,37]. Although an inert gas itself, Ar^+ induces chemical reactions within the target material and as a result of the high sputtering yield and volatility of oxygen it is more likely to escape from a bombarded material than heavier atoms of the same material. As a consequence of these factors, the material undergoes a gradual reduction. However, the theoretical mechanisms of preferential sputtering in metal oxides are not well developed or agreed upon fully in the literature. It has previously been attributed to diffusion of lattice oxygen alongside sputtering enhanced vaporization and thermal sputtering [38]. Thermal sputtering being that caused through the momentary temperature spike as a result of incident ions at the impact site. These impact induced temperature spikes have the capability to result in a range of effects from disordering, stoichiometry alteration and primarily the sputtering effect [39]. A similar reducing effect observed within this work is illustrated by Chen et al wherein the reduction of the NiO film observed following as little as 1000 seconds [40]. Malherbe et al present a detailed comparison between theoretical and experimental data on the effects of sputtering of oxides wherein it is reported that although as mentioned above the process of sputtering is rather complex a broad consensus agree that

there are two primary mechanisms which result in the preferential sputtering which are surface binding effects and mass difference effects [41,42]. Malherbe goes on to conclude that the preferential sputtering of oxides may be reasonably quantitatively explained by Sigmund's equation for cascade sputtering which shows that the dominant effect for the preferential sputtering effect is due to the mass difference between the metal and oxygen atoms [42]. The preferential sputtering effect is further discussed and developed by Mende et al wherein Monte Carlo simulations are compared to XPS obtained experimental data further verifying this process [43]. Moreover, Betz and Wehner provide a comprehensive overview of sputtering by particle bombardment with a key finding relevant to this thesis being the assertion within this overview that multicomponent solids do in fact show preferential sputtering with sputtering yields of various species within a target material being disproportionate to their atomic concentrations [44].

Figure 4.11 (b) tracks the elemental composition of the Ni film as a function of Ar milling time with values calculated using XPS. This shows the rapid removal of carbon during initial milling stages with the Ni simultaneously increasing during early milling steps due to a reduction in its attenuation by overlying carbon. Following the first 8 minutes of milling the Ni signal is seen to diminish due to the etch back of the Ni film. The Si peak is seen to increase consistently as the Ni film is milled away exposing more of the underlying substrate, consistent with reports from Kenney et al [34]. Oxygen is seen to increase initially as C-C bonds are removed uncovering the underlying NiO before the O in the NiO is preferentially removed leaving behind Ni-Ni bonds with the remaining O being from SiO_2 and the interfacial region of the Ni and Si. This comparison between live 'during growth' depth profiling and traditional Ar milling shows the risks in making assumptions about film

chemistry using the latter approach. The XPS findings which support the theory of preferential oxygen sputtering have been verified by computationally using SRIM (Stopping Range of Ions in Matter) software commonly applied in the simulation of a range of ion based sample effects from ion stopping and range within targets, ion implantation, ion transmission and crucially to this investigation it yields simulations on the effects of ion sputtering [45]. An exemplar simulation using the above mentioned SRIM software is shown below *Figure 4.12* highlighting the preferential sputtering effect of O vs Ni as indicated by the atoms/ion sputtering yield of O being 3.66 atoms/ion compared to the 2.26 atoms/ion of Ni.
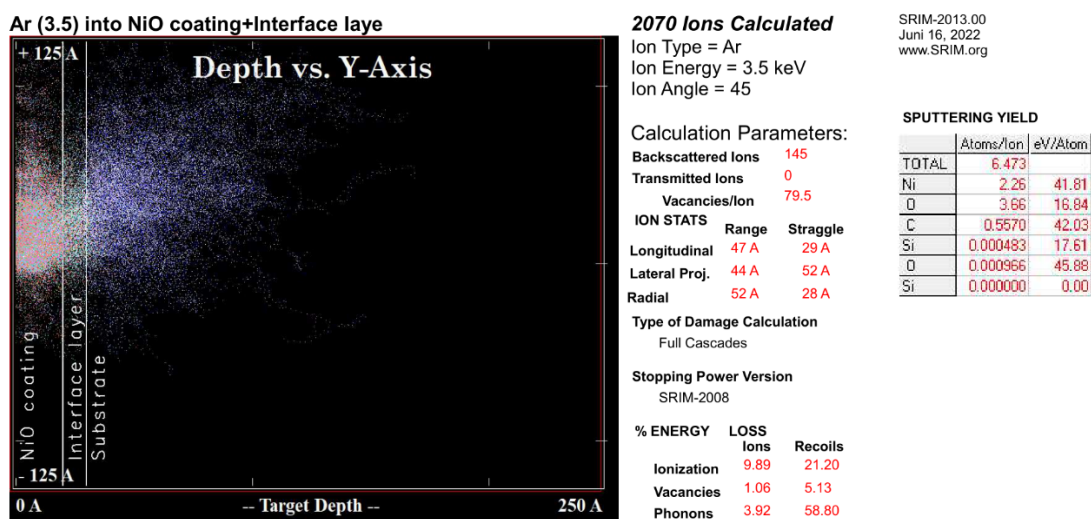
Figure 4.12 SRIM simulation illustrating preferential sputtering effect of argon ion sputtering..

4.3.1.4 Ni Metal Growth by Annealing vs. Supercycles

The majority of investigations into Ni with regard to water splitting applications detail only the performance of NiO [26,46–50]. Therefore, we investigate the effect of Ni-metal in water splitting with metallic films deposited via supercycle depositions. It was observed through

earlier investigations within this work that NiO films are readily reduced to Ni-metal through the application of H_2 plasma annealing post deposition. However, we endeavoured to grow metallic Ni rather than forming it through the application of this post deposition annealing. We compare the performance of metallic Ni films deposited in the traditional cycle by cycle ALD regime with a post deposition H_2 annealing applied along with so called supercycle depositions with H_2 plasma annealing stages interspersed within the ALD deposition process. This supercycle regime was explored in order to ensure all unreacted remnant carbon-containing ligands were removed throughout the growth of the film. An additional motive for the investigation into supercycle depositions was to compare the reduction of films via post deposition anneals of the bulk film as opposed to the reduction of several monolayers at a time and the effect, if any, of this on film stoichiometry.
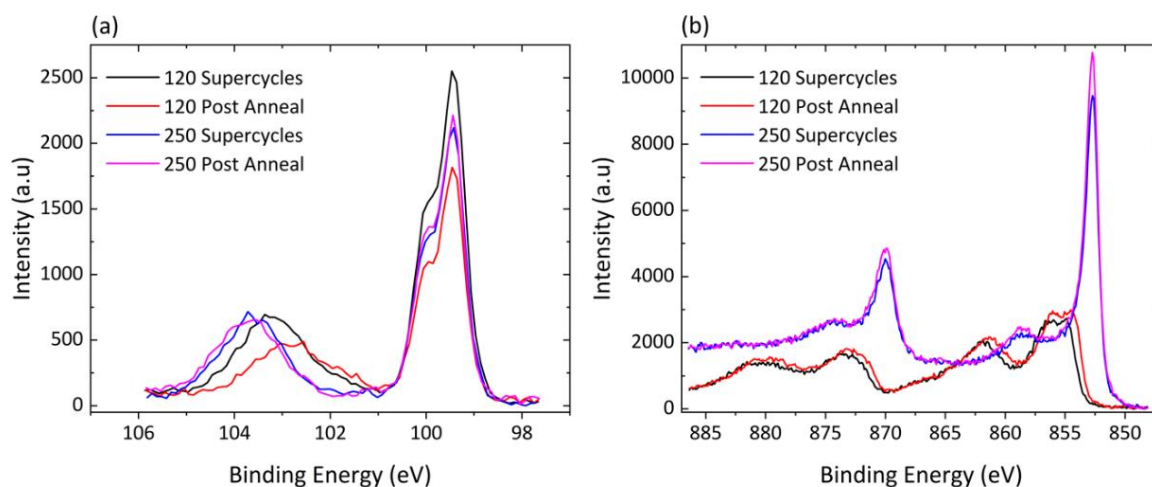
Figure 4.13 XPS high resolution spectra showing the 4 supercycle samples in their as deposited state (a) Si 2p (b) Ni 2p 3/2.

The 120 supercycle and 120 post anneal samples yielded 2.9 nm and 3.2 nm respectively while the 250 supercycle and 250 post anneal yielded 5.6 nm and 6.4 nm. From Figure 4.13 (a) showing the high resolution spectra for the Si 2p of the 4 variations of the supercycle

samples, it can be seen that the 120 supercycle sample exhibits the least attenuated Si signal due to the marginally reduced GPC when compared to its 120 post anneal counterpart. Furthermore, the 120 cycle samples both show a reduction in the energy separation between the bulk and oxide peaks of the Si $2p$ region due to the reduced film thickness resulting in smaller attenuation of the lower BE oxidation states in the Si region.

The reduced growth rate obtained through ellipsometry measurements is verified in Figure 4.13 (b) which shows the Ni $2p_{3/2}$ of the 120 supercycle sample to be decreased versus the 120 post anneal sample. The large attenuation difference seen in the Si peak is verified as being due to the enhanced growth of the Ni film when looking to Figure 4.14 where the C1s contribution of the 120 supercycle and 120 post anneal samples are approximately equal. Figure 4.14 shows that as thickness increases the level of carbon incorporation within the film continues to rise regardless of being deposited with interspersed plasma annealing steps or waiting for complete deposition before a final annealing stage.
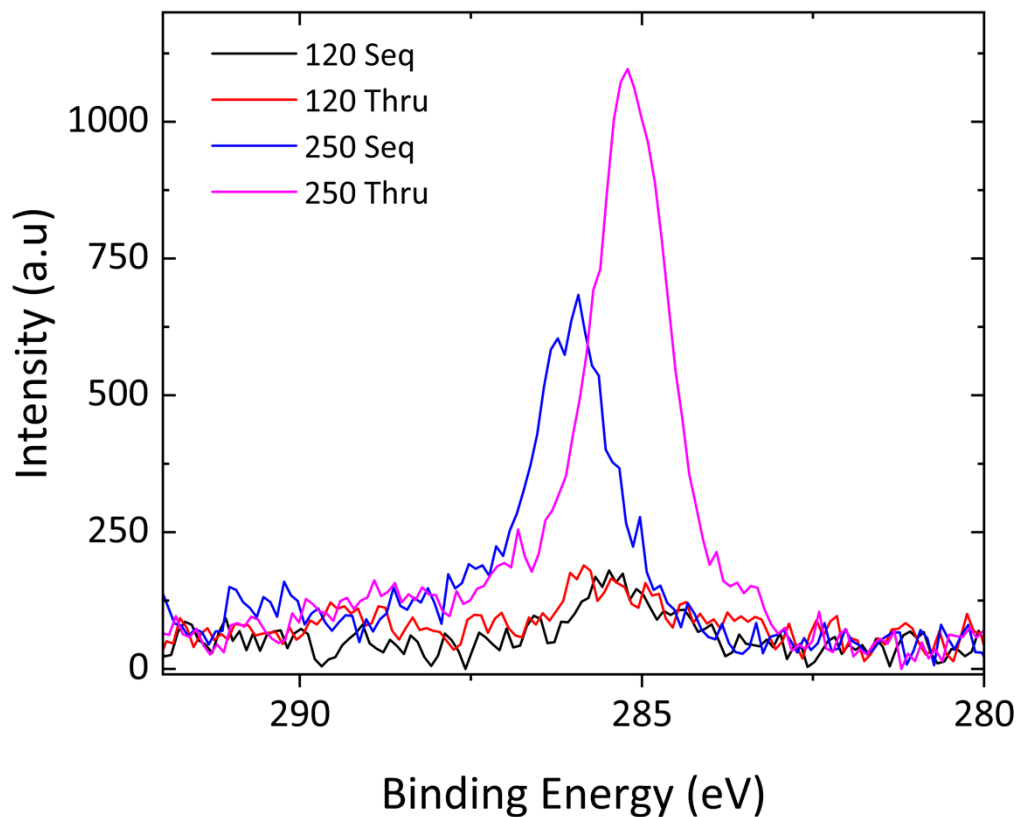
Figure 4.14 High resolution XPS spectra for the C 1s region of all 4 sample deposition variations with 250 cycle samples seen to retain larger contributions of carbon within the deposited film.

Figure 4.15 (a) shows the high-resolution spectra for the Ni $2p_{3/2}$ region wherein both the 250 supercycle and 250 post anneal samples are seen to form strong lower BE peaks consistent with the presence of Ni-metal. It also shows a similar trend for both of the 120 cycle samples with the post anneal variant in both cases demonstrating both enhanced growth and marginal but measurable shift to lower BE. Figure 4.15 shows XPS spectra for the 250 supercycle and post anneal samples following exposure to atmosphere, wherein a rapid attenuation of the Ni $2p_{3/2}$ peak is observed alongside the partial conversion of the films

from Ni-metal to NiO through the oxidation of the film with the post annealed sample showing greater resistance to oxidation due to its greater thickness.
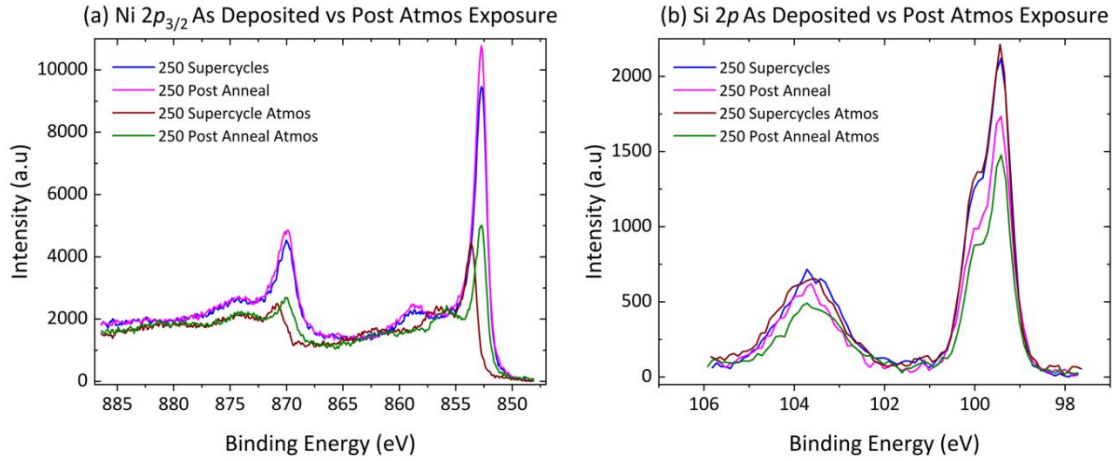
Figure 4.15 XPS high resolution spectra showing the 250 supercycle and post anneal samples in their as deposited states alongside spectra obtained following brief exposures to atmosphere (a) Ni 2p 3/2 (b) Si 2p.

In summary of the results presented within this Chapter, firstly the characterisation of the NiCp$_2$ precursor was performed with optimum deposition parameters of substrate temperature, precursor dose and plasma dose times identified. Nucleation studies were performed with these optimized parameters and a clear reduction of the silicon bulk-oxide binding energy separation as a function of increasing ALD cycles was observed indicative of the formation of nickel silicate over the course of the deposition. These sequential depositions allowed for the determination of film chemical composition as function of growth showing the onset of nickel growth following 3 ALD cycles with carbon incorporation within the film seen to be steady at > 5%. During film characterisation and depth profiling of deposited NiO films the mechanism of preferential sputtering of the NiO film removing oxygen thus converting the film to a more metallic state was observed and developed. Efforts made to deposit metallic nickel a material not often studied within the

field for its PEC protective capabilities with the post deposition annealing treatment being shown to yield more metallic nickel versus mid deposition annealing.

4.3.2 Photoelectrochemical Testing

Time degradation PEC testing allows for the investigation of the stability of films under water oxidation conditions using an electrolyte solution of 50:50 deionized water to phosphate buffer. Figure 4.16 shows the degradation measurements for the Ni based films produced in this work with an applied voltage of 1 V vs Ag/AgCl equivalent to 1.65 V vs RHE and contrasts the application of a post deposition anneal versus the supercycle deposition with shorter plasma annealing stages carried out during the deposition itself. It can be seen that the application of the annealing treatment at the end of the ALD deposition is preferable in terms of gross initial photocurrent output. However, although achieving significant photocurrent output, both post deposition annealed samples show a sharp decline over the course of the PEC test duration.
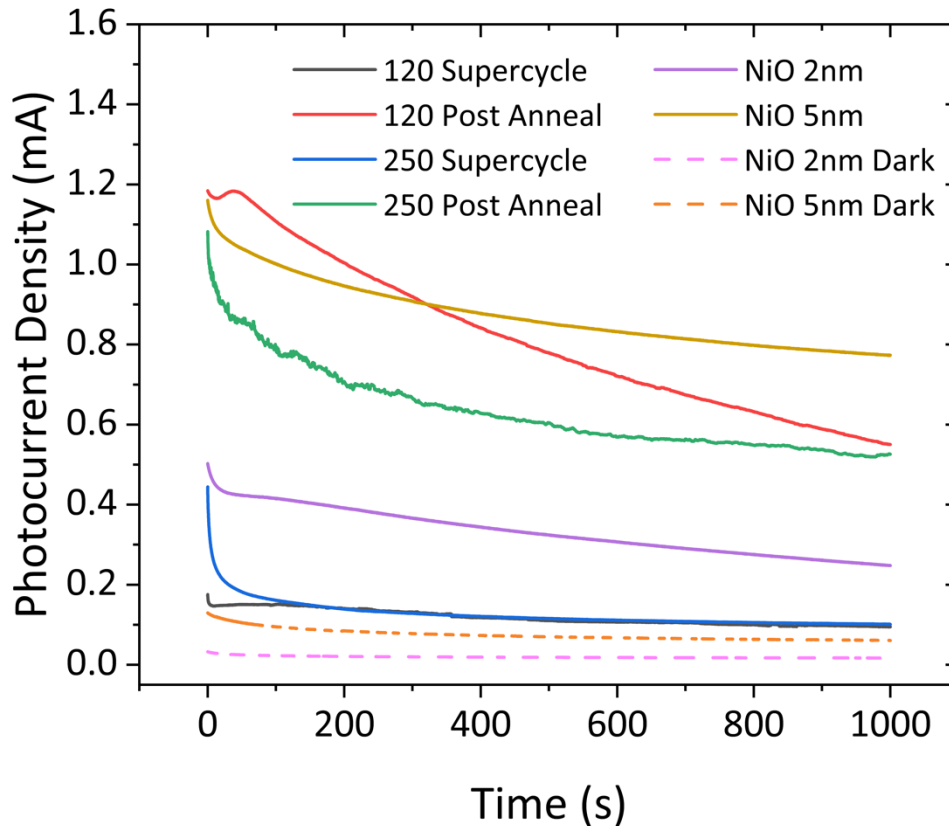
Figure 4.16 Chronoamperometric (time degradation; 1V vs Ag/AgCl applied) photoelectrochemical cell testing of supercycle grown Ni films contrasting continuous (thru) growth followed by plasma annealing with the supercycle method of interspersed plasma annealing stages during deposition. 120 Super: 120 total ALD cycles with interspersed annealing stages. 120 Post Anneal: 120 total ALD cycles with the annealing step performed at the end of the deposition. Dark and light current testing of a 5 nm and 2 nm NiO sample is also illustrated for comparison.

The supercycle samples exhibit drastically reduced photocurrent output compared to the post deposition annealed samples. This result suggests film stability is not improved through the application of the annealing treatments throughout the deposition in the supercycle regime.. For reference and comparison, additional degradation measurements of 2nm and 5nm NiO films are also shown being that the 120 and 250 cycles are in the thickness range of 2nm and 5nm respectively. It is clear that NiO films perform better in terms of gross photocurrent output alongside improved film stability at both thicknesses through beginning and finishing

degradation testing with current output higher than that exhibited by the supercycle, or post anneal samples a result not previously seen within the literature.
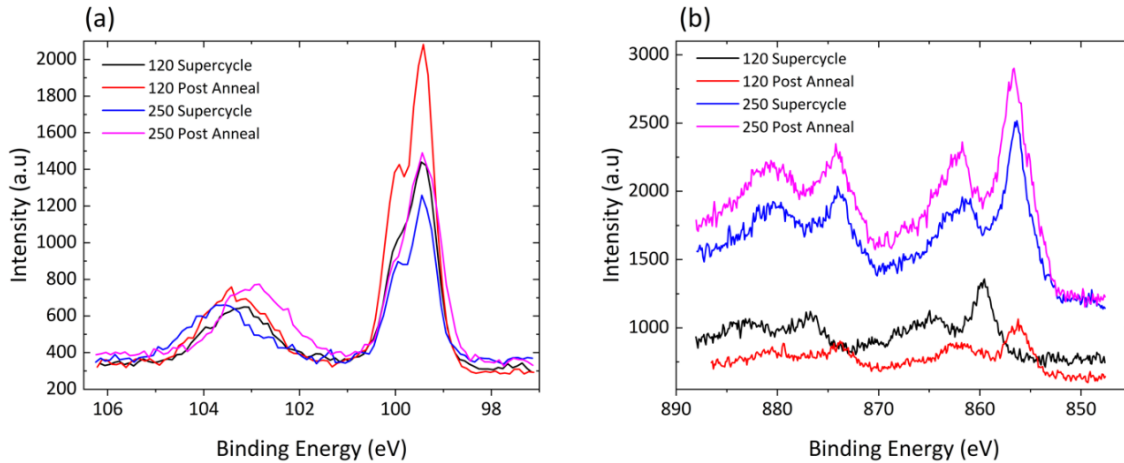
Figure 4.17 XPS high resolution spectra showing the 4 supercycle samples following photoelectrochemical cell testing (a) Si 2p (b) Ni 2p $_{3/2}$

Figure 4.17 shows the XPS high resolution Si $2p$ and Ni $2p_{3/2}$ spectra for the supercycle and post anneal samples following testing in the PEC cell. This testing and results from Figure 4.17 (b) showing conversion from metal to oxide further verifies the inaccuracy of a previous report on the effects of Ar sputtering and the protection offered by a metallic overlayer to underlying NiO [34]. Furthermore, it can be seen from Figure 4.17 (a) that the application of a post deposition H$_2$ anneal yields a reduced Si $2p$ bulk-oxide energy separation through the additional presence of sub oxide states compared to that seen in the supercycle deposited films. From Figure 4.17 (b) it is clear that PEC testing results in the complete oxidation of the Ni films. This result is most clear from the 250 cycle samples which exhibited highly metallic peak profiles in Figure 4.13 when deposited however cell testing converts the film to NiO. Figure 4.15 (a) shows that a highly metallic film even when exposed to atmosphere

begins oxidizing although not entirely. Only upon being tested under the harsh electrolyte environment of the PEC cell does the film entirely convert to NiO oxidizing throughout the film as can be seen clearly in Figure 4.17.

The results shown in Figure 4.16 showing the superior photoelectrochemical performance of samples which were exposed to a post deposition annealing treatment as opposed to the supercycle deposition regime is further verified in Figure 4.18 below which shows the linear sweep voltammetry measurements performed on such supercycle and post deposition anneal samples. It is observed that for both the 120 and 250 cycle depositions, samples which received an annealing treatment after the deposition was complete yielded higher photocurrent density than those subjected to the anneals interspersed throughout the deposition in the supercycle deposition regime.

These results indicate that the application of plasma annealing stages during the ALD deposition process are less effective than carrying out this treatment once the deposition has been completed. This is evident from the enhanced photocurrent of the post deposition annealed sample to those annealed during the deposition shown in Figure 4.16 and Figure 4.16. From Figure 4.17 a lower binding energy separation between the silicon oxide and silicon bulk is observed consistent with the presence of suboxides and silicate which could be providing vacancies within the film which promote the tunneling of holes to the film surface which although being key to maximizing photocurrent could also be facilitating oxygen diffusion causing poor reliability. This formation of suboxides and silicate by means of post deposition annealing is consistent with earlier findings in Chapter 3 which observed a similar effect of titanium silicate acting to enhance the film performance.
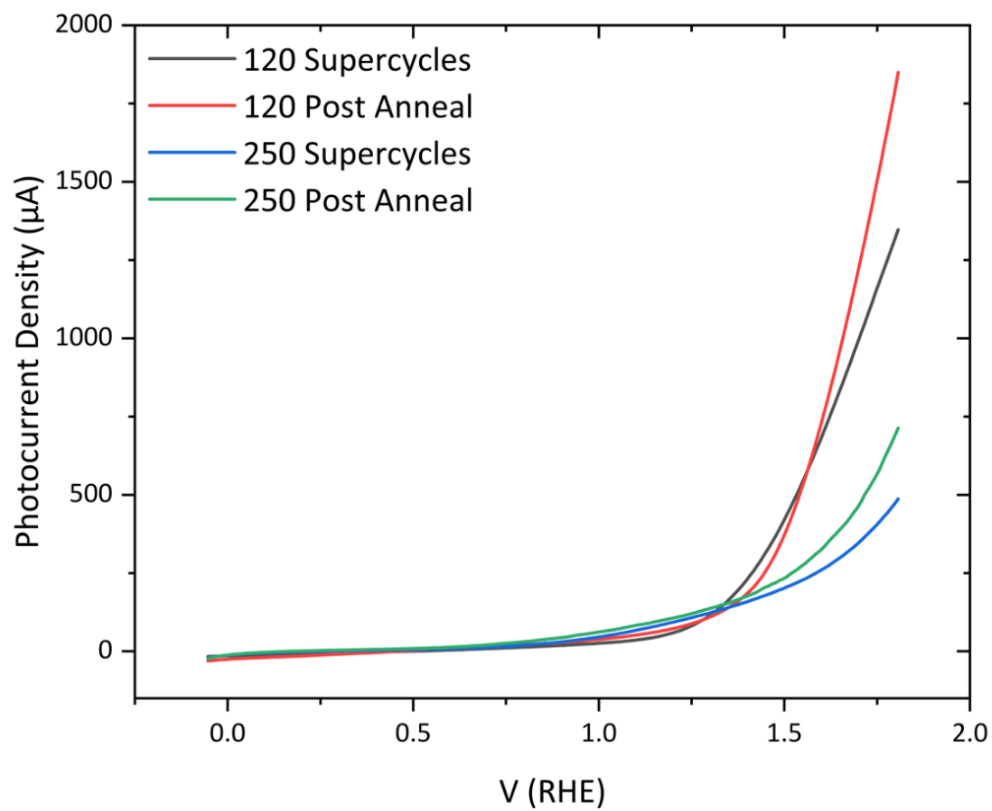
Figure 4.18 PEC linear sweep voltammetry measurements showing the outward voltage sweep for both the post deposition anneal and supercycle samples for 120 and 250 total ALD cycles.

4.4 Conclusions

Results presented within this chapter show an in-situ study of the PEALD of NiO. The *in-situ* XPS characterisation of the deposition process and parameters allows for unique understanding of the film chemistry in their as deposited states without the additional complexity of adventitious atmospheric contamination. The growth and study of films deposited in the sequential regime allowed for detailed understanding of the cycle-by-cycle growth of the films in addition to accurately monitoring film nucleation delay. The PEALD process was optimized for the ALD system used within this study. It was shown to yield the desired NiO films with remnant carbon ligand incorporation observed which was deemed a result of incomplete reactions during the process, a result which without *in-situ* XPS analysis would have previously been labelled as a result of atmospheric contamination.

The application of post deposition plasma annealing on film stoichiometry was studied using H_2 plasma. It showed NiO can be only partially reduced to metallic Ni following an extended 20-minute exposure. Supercycle ALD depositions were employed in an effort to produce pure metallic Ni films from the outset such as to eliminate the requirement for post deposition treatments which were proved ineffective. However, PEC testing shows these supercycle deposited films yield enhanced film stability for water splitting applications compared to films NiO films which had been treated post deposition. Claims of previous reports on the effects of Ar milling on NiO thin films are explored and found to be inaccurate. Ar milling is shown within this work to reduce NiO to Ni metal due to the preferential sputtering of oxygen from the film, this result has previously been mistaken to show the capping and protective capability of a 2nm film against the oxidation of a metallic film upon atmospheric exposure.

4.5 References

(1)   Boyd, C. C.; Shallcross, R. C.; Moot, T.; Kerner, R.; Bertoluzzi, L.; Onno, A.; Kavadiya, S.; Chosy, C.; Wolf, E. J.; Werner, J.; Raiford, J. A.; de Paula, C.; Palmstrom, A. F.; Yu, Z. J.; Berry, J. J.; Bent, S. F.; Holman, Z. C.; Luther, J. M.; Ratcliff, E. L.; Armstrong, N. R.; McGehee, M. D. Overcoming Redox Reactions at Perovskite-Nickel Oxide Interfaces to Boost Voltages in Perovskite Solar Cells. *Joule* **2020**, *4* (8), 1759–1775. https://doi.org/10.1016/j.joule.2020.06.004.

(2)   Yin, X.; Guo, Y.; Xie, H.; Que, W.; Kong, L. B. Nickel Oxide as Efficient Hole Transport Materials for Perovskite Solar Cells. *Sol. RRL* **2019**, *3* (5), 1–27. https://doi.org/10.1002/solr.201900001.

(3)   Chen, K.-T.; Hsu, C.-H.; Ren, F.-B.; Wang, C.; Gao, P.; Wu, W.-Y.; Lien, S.-Y.; Zhu, W.-Z. Influence of Annealing Temperature of Nickel Oxide as Hole Transport Layer Applied for Inverted Perovskite Solar Cells. *J. Vac. Sci. Technol. A* **2021**, *39* (6), 062401. https://doi.org/10.1116/6.0001191.

(4)   Zhang, P. P.; Zhou, Z. J.; Kou, D. X.; Wu, S. X. Perovskite Thin Film Solar Cells Based on Inorganic Hole Conducting Materials. *Int. J. Photoenergy* **2017**, *2017*. https://doi.org/10.1155/2017/6109092.

(5)   Liu, Z.; Chang, J.; Lin, Z.; Zhou, L.; Yang, Z.; Chen, D.; Zhang, C.; Liu, S. (Frank); Hao, Y. High-Performance Planar Perovskite Solar Cells Using Low Temperature, Solution–Combustion-Based Nickel Oxide Hole Transporting Layer with Efficiency Exceeding 20%. *Adv. Energy Mater.* **2018**, *8* (19), 1–9. https://doi.org/10.1002/aenm.201703432.

(6)   He, L.; Zhou, W.; Cai, D.; Mao, S. S.; Sun, K.; Shen, S. Pulsed Laser-Deposited n-Si/NiOx Photoanodes for Stable and Efficient Photoelectrochemical Water Splitting. *Catal. Sci. Technol.* **2017**, *7* (12), 2632–2638. https://doi.org/10.1039/c7cy00114b.

(7)   Sun, K.; McDowell, M. T.; Nielander, A. C.; Hu, S.; Shaner, M. R.; Yang, F.; Brunschwig, B. S.; Lewis, N. S. Stable Solar-Driven Water Oxidation to O2(G) by Ni-Oxide-Coated Silicon Photoanodes. *J. Phys. Chem. Lett.* **2015**, *6* (4), 592–598. https://doi.org/10.1021/jz5026195.

(8)   Kang, J. H.; Kim, S. H.; Ebaid, M.; Lee, J. K.; Ryu, S. W. Efficient

Photoelectrochemical Water Splitting by a Doping-Controlled GaN Photoanode Coated with NiO Cocatalyst. *Acta Mater.* **2014**, *79*, 188–193. https://doi.org/10.1016/j.actamat.2014.07.032.

(9)   Babar, N. U. A.; Joya, K. S. Spray-Coated Thin-Film Ni-Oxide Nanoflakes as Single Electrocatalysts for Oxygen Evolution and Hydrogen Generation from Water Splitting. *ACS Omega* **2020**, *5* (19), 10641–10650. https://doi.org/10.1021/acsomega.9b02960.

(10)   Herrera-Gomez, A.; Bravo-Sanchez, M.; Ceballos-Sanchez, O.; Vazquez-Lepe, M. O. Practical Methods for Background Subtraction in Photoemission Spectra. *Surf. Interface Anal.* **2014**, *46* (10–11), 897–905. https://doi.org/https://doi.org/10.1002/sia.5453.

(11)   Himpsel, F. J.; McFeely, F. R.; Taleb-Ibrahimi, A.; Yarmoff, J. A.; Hollinger, G. Microscopic Structure of the SiO2/Si Interface. *Phys. Rev. B* **1988**, *38* (9), 6084–6096. https://doi.org/10.1103/PhysRevB.38.6084.

(12)   Herrera-Gomez, A.; Sun, Y.; Aguirre-Tostado, F. S.; Hwang, C.; Mani-Gonzalez, P. G.; Flint, E.; Espinosa-Magaña, F.; Wallace, R. M. Structure of Ultra-Thin Diamond-like Carbon Films Grown with Filtered Cathodic Arc on Si(001). *Anal. Sci.* **2010**, *26* (2), 267–272. https://doi.org/10.2116/analsci.26.267.

(13)   Shallenberger, J. R. Determination of Chemistry and Ray Photoelectron Spectroscopy. **2013**, *693* (June 1998).

(14)   Cumpson, P. J.; Zalm, P. C. Thickogram: A Method for Easy Film Thickness Measurement in XPS. *Surf. Interface Anal.* **2000**, *29* (6), 403–406. https://doi.org/10.1002/1096-9918(200006)29:6<403::AID-SIA884>3.0.CO;2-8.

(15)   Wagner, C. D.; Davis, L. E.; Zeller, M. V; Taylor, J. A.; Raymond, R. H.; Gale, L. H. Empirical Atomic Sensitivity Factors for Quantitative Analysis by Electron Spectroscopy for Chemical Analysis. *Surf. Interface Anal.* **1981**, *3* (5), 211–225. https://doi.org/https://doi.org/10.1002/sia.740030506.

(16)   Burgess, C.; Zardetto, V.; Weijtens, C.; Verheijen, M. A.; Kessels, W. M. M.; Creatore, M. Plasma-Assisted Atomic Layer Deposition of Nickel Oxide as Hole Transport Layer for Hybrid Perovskite. **2019**, 12532–12543. https://doi.org/10.1039/c9tc04282b.

(17)   Sci, J. V. Influence of Annealing Temperature of Nickel Oxide as Hole Transport

Layer Applied for Inverted Perovskite Solar Cells Influence of Annealing Temperature of Nickel Oxide as Hole Transport Layer Applied for Inverted Perovskite Solar Cells. **2021**, *062401* (June). https://doi.org/10.1116/6.0001191.

(18)   You, A.; Be, M. A. Y.; In, I. Atomic Layer Deposition of Nickel Oxide Films Using and Water. **2019**, *1238* (October 2004). https://doi.org/10.1116/1.1875172.

(19)   Koshtyal, Y.; Nazarov, D.; Ezhov, I.; Mitrofanov, I.; Kim, A.; Rymyantsev, A.; Lyutakov, O.; Popovich, A.; Maximov, M. Atomic Layer Deposition of Nio to Produce Active Material for Thin-Film Lithium-Ion Batteries. *Coatings* **2019**, *9* (5). https://doi.org/10.3390/coatings9050301.

(20)   Arts, K.; Deijkers, S.; Puurunen, R. L.; Kessels, W. M. M.; Knoops, H. C. M. Oxygen Recombination Probability Data for Plasma-Assisted Atomic Layer Deposition of SiO2and TiO2. *J. Phys. Chem. C* **2021**, *125* (15), 8244–8252. https://doi.org/10.1021/acs.jpcc.1c01505.

(21)   Koushik, D.; Jošt, M.; Dučinskas, A.; Burgess, C.; Zardetto, V.; Weijtens, C.; Verheijen, M. A.; Kessels, W. M. M.; Albrecht, S.; Creatore, M. Plasma-Assisted Atomic Layer Deposition of Nickel Oxide as Hole Transport Layer for Hybrid Perovskite Solar Cells. *J. Mater. Chem. C* **2019**, *7* (40), 12532–12543. https://doi.org/10.1039/c9tc04282b.

(22)   Kim, M.; Nabeya, S.; Nandi, D. K.; Suzuki, K.; Kim, H. M.; Cho, S. Y.; Kim, K. B.; Kim, S. H. Atomic Layer Deposition of Nickel Using a Heteroleptic Ni Precursor with NH3 and Selective Deposition on Defects of Graphene. *ACS Omega* **2019**, *4* (6), 11126–11134. https://doi.org/10.1021/acsomega.9b01003.

(23)   Song, S. J.; Lee, S. W.; Kim, G. H.; Seok, J. Y.; Yoon, K. J.; Yoon, J. H.; Hwang, C. S.; Gatineau, J.; Ko, C. Substrate Dependent Growth Behaviors of Plasma-Enhanced Atomic Layer Deposited Nickel Oxide Films for Resistive Switching Application. *Chem. Mater.* **2012**, *24* (24), 4675–4685. https://doi.org/10.1021/cm302182s.

(24)   Grosvenor, A. P.; Biesinger, M. C.; Smart, R. S. C.; McIntyre, N. S. New Interpretations of XPS Spectra of Nickel Metal and Oxides. *Surf. Sci.* **2006**, *600* (9), 1771–1779. https://doi.org/10.1016/j.susc.2006.01.041.

(25)   Koshtyal, Y.; Nazarov, D.; Ezhov, I.; Mitrofanov, I.; Kim, A.; Rymyantsev, A.; Lyutakov, O.; Popovich, A.; Maximov, M. Atomic Layer Deposition of Nio to

Produce Active Material for Thin-Film Lithium-Ion Batteries. *Coatings* **2019**, *9* (5), 1–16. https://doi.org/10.3390/coatings9050301.

(26) Nardi, K. L.; Yang, N.; Dickens, C. F.; Strickler, A. L.; Bent, S. F. Creating Highly Active Atomic Layer Deposited NiO Electrocatalysts for the Oxygen Evolution Reaction. *Adv. Energy Mater.* **2015**, *5* (17), 1–10. https://doi.org/10.1002/aenm.201500412.

(27) Roberts, M. W.; Smart, R. S. C. The Defect Structure of Nickel Oxide Surfaces as Revealed by Photoelectron Spectroscopy. *J. Chem. Soc. Faraday Trans. 1 Phys. Chem. Condens. Phases* **1984**, *80* (11), 2957–2968. https://doi.org/10.1039/F19848002957.

(28) Naumkin, A. V; Kraut-Vass, A.; Gaarenstroom, S. W.; Powell, C. J. NIST Standard Reference Database 20, Version 4.1. **2012**. https://doi.org/http://dx.doi.org/10.18434/T4T88K.

(29) Biesinger, M. C.; Payne, B. P.; Lau, L. W. M.; Gerson, A.; Smart, R. S. C. X-Ray Photoelectron Spectroscopic Chemical State Quantification of Mixed Nickel Metal, Oxide and Hydroxide Systems. *Surf. Interface Anal.* **2009**, *41* (4), 324–332. https://doi.org/10.1002/sia.3026.

(30) Huang, W.; Ding, S.; Chen, Y.; Hao, W.; Lai, X.; Peng, J.; Tu, J.; Cao, Y.; Li, X. 3D NiO Hollow Sphere/Reduced Graphene Oxide Composite for High-Performance Glucose Biosensor. *Sci. Rep.* **2017**, *7* (1), 1–11. https://doi.org/10.1038/s41598-017-05528-1.

(31) Cheng, M.; Fan, H.; Song, Y.; Cui, Y.; Wang, R. Interconnected Hierarchical NiCo2O4 Microspheres as High-Performance Electrode Materials for Supercapacitors. *Dalt. Trans.* **2017**, *46* (28), 9201–9209. https://doi.org/10.1039/c7dt01289f.

(32) Huang, H.; Zhao, Y.; Bai, Y.; Li, F.; Zhang, Y.; Chen, Y. Conductive Metal–Organic Frameworks with Extra Metallic Sites as an Efficient Electrocatalyst for the Hydrogen Evolution Reaction. *Adv. Sci.* **2020**, *7* (9), 1–9. https://doi.org/10.1002/advs.202000012.

(33) Biesinger, M. C.; Payne, B. P.; Grosvenor, A. P.; Lau, L. W. M.; Gerson, A. R.; Smart, R. S. C. Resolving Surface Chemical States in XPS Analysis of First Row Transition Metals, Oxides and Hydroxides: Cr, Mn, Fe, Co and Ni. *Appl. Surf. Sci.* **2011**, *257* (7),

2717–2730. https://doi.org/10.1016/j.apsusc.2010.10.051.

(34)   Kenney, M. J.; Gong, M.; Li, Y.; Wu, J. Z.; Feng, J.; Lanza, M.; Dai, H. High-Performance Silicon Photoanodes Passivated with Ultrathin Nickel Films for Water Oxidation. *Science (80-.).* **2013**, *342* (6160), 836–840. https://doi.org/10.1126/science.1241327.

(35)   González-Elipe, A. R.; Holgado, J. P.; Alvarez, R.; Munuera, G. Use of Factor Analysis and XPS to Study Defective Nickel Oxide. *J. Phys. Chem.* **1992**, *96* (7), 3080–3086. https://doi.org/10.1021/j100186a056.

(36)   Kim, K. S.; Winograd, N. X-Ray Photoelectron Spectroscopic Studies of Nickel-Oxygen Surfaces Using Oxygen and Argon Ion-Bombardment. *Surf. Sci.* **1974**, *43* (2), 625–643. https://doi.org/10.1016/0039-6028(74)90281-7.

(37)   Yin, L. I.; Ghose, S.; Adler, I. X-Ray Photoelectron Spectroscopic Studies of Valence States Produced By Ion-Sputtering Reduction. *Appl. Spectrosc.* **1972**, *26* (3), 355–357. https://doi.org/10.1366/000370272774352092.

(38)   Langell, M. A. Preferential Sputtering in the 3d Transition Metal Monoxides. *Surf. Sci.* **1987**, *186* (1–2), 323–338. https://doi.org/10.1016/S0039-6028(87)80052-3.

(39)   Kelly, R. Theory of Thermal Sputtering. *http://dx.doi.org/10.1080/00337577708237462* **2006**, *32* (1–2), 91–100. https://doi.org/10.1080/00337577708237462.

(40)   Chen, Y. S.; Kang, J. F.; Chen, B.; Gao, B.; Liu, L. F.; Liu, X. Y.; Wang, Y. Y.; Wu, L.; Yu, H. Y.; Wang, J. Y.; Chen, Q.; Wang, E. G. Microscopic Mechanism for Unipolar Resistive Switching Behaviour of Nickel Oxides. *J. Phys. D. Appl. Phys.* **2012**, *45* (6). https://doi.org/10.1088/0022-3727/45/6/065303.

(41)   Malherbe, J. B.; Hofmann, S.; Sanz, J. M. Preferential Sputtering of Oxides: A Comparison of Model Predictions with Experimental Data. *Appl. Surf. Sci.* **1986**, *27* (3), 355–365. https://doi.org/10.1016/0169-4332(86)90139-X.

(42)   Sigmund, P. 2 . Sputtering by Ion Bombardment : Theoretical Concepts 2 . 1 Introductory and Historical Survey.

(43)   Mende, M.; Carstens, F.; Ehlers, H.; Ristau, D. Preferential Sputtering of Metal Oxide Mixture Thin Films. *J. Vac. Sci. Technol. A* **2021**, *39* (2), 023406. https://doi.org/10.1116/6.0000799/397389.

(44)   Scherzer, B. M. U. *Sputtering by Particle Bombardment II*; 1983; Vol. 52.

(45)   James Ziegler - SRIM & TRIM http://www.srim.org/ (accessed Aug 13, 2023).

(46)   Jiang, C.; Moniz, S. J. A.; Wang, A.; Zhang, T.; Tang, J. Photoelectrochemical Devices for Solar Water Splitting-Materials and Challenges. *Chem. Soc. Rev.* **2017**, *46* (15), 4645–4660. https://doi.org/10.1039/c6cs00306k.

(47)   S.C. Bulakhe; P. V. Patil; R. J. Deokate. Electrodeposited Nickel Oxide Thin Film for Electrochemical Water Splitting. *Int. J. Adv. Res. Sci. Commun. Technol.* **2022**, *2* (4), 38–42. https://doi.org/10.48175/ijarsct-3445.

(48)   Hu, C.; Chu, K.; Zhao, Y.; Teoh, W. Y. Efficient Photoelectrochemical Water Splitting over Anodized P-Type NiO Porous Films. *ACS Appl. Mater. Interfaces* **2014**, *6* (21), 18558–18568. https://doi.org/10.1021/am507138b.

(49)   Santos, H. L. S.; Corradini, P. G.; Andrade, M. A. S.; Mascaro, L. H. CuO/NiOx Thin Film–Based Photocathodes for Photoelectrochemical Water Splitting. *J. Solid State Electrochem.* **2020**, *24* (8), 1899–1908. https://doi.org/10.1007/s10008-020-04513-5.

(50)   Guo, Z.; Wang, X.; Gao, Y.; Liu, Z. Co/Cu-Modified NiO Film Grown on Nickel Foam as a Highly Active and Stable Electrocatalyst for Overall Water Splitting. *Dalt. Trans.* **2020**, *49* (6), 1776–1784. https://doi.org/10.1039/c9dt04771a.

5 Investigating the Passivating Performance of Nitrides for Photoelectrodes through the deposition of CoN

5.1 Introduction

This chapter examines the growth of cobalt nitride (CoN) via atomic layer deposition (ALD). CoN is a material which has been investigated for a wide range of applications from adhesion promotion for copper interconnects in the backend of complementary metal oxide semiconductors (CMOS) processes to the study of inexpensive and non-rare earth materials for magnetic applications [1,2].

With oxides having been typically the go-to as photoelectrode candidate materials for some time, nitrides and carbides have begun to gain growing interest for their potential application in water splitting [3,4]. This is due to transition metal nitrides (TMNs) exhibiting desirable characteristics such as high conductivity, resistance to corrosion, and stability over a range broad pH range [5–7]. CoN is recognised as a material of interest in water splitting which is capable of catalysing the oxygen evolution reaction (OER) as part of the water splitting process having shown impressive performance when compared against current benchmarks within the field [8–17]. However, as has been discussed throughout this work, it is the corrosion of the photoelectrodes in either the HER or OER processes which acts to severely hinder PEC water splitting performance and as such, protective films must be implemented.

PEC water splitting is long since highlighted within the literature as a promising route to producing green hydrogen with Pt and Pt-based electrocatalysts being among the best performing materials to this end. However, Pt is a costly material to used especially when considering large scale adoption of water splitting and as such the screening and development

of low-cost HER catalyst materials such as transition metal compounds (TMCs) and transition metal nitrides (TMNs) [18–21]. TMCs such as phosphides, sulfides and nitrides have been the subject of a growing amount of research to replace the more costly counterparts such as Pt helped by their earth abundant, comparably lower cost environmental benignity [22]. Among the TMCs, TMNs have gained increased awareness due to their 3 d electron numbers [23–27]. Cobalt nitrides have been shown to exhibit excellent electrical conductivity in addition to being highly resistant to corrosion [22,27,28].

Various forms of cobalt nitrides in their binary states such as CoN and Co_xN have been highlighted theoretically as well as experimentally to show impressive performance in OER applications with their application as HER catalysts scarcely reported. This being said, Wang et al reported on the enhancement of the HER performance of Co_4N nanosheets via doping using V, W and Mo [24,29].

Due to the potential highlighted within the literature for nitrides to be applied on photoelectrodes and with the lack of reports detailing the performance of CoN specifically focusing on detailed analysis of undoped planar ALD grown films [30–33]. To this end, it was deemed worthwhile to perform a systematic investigation of this material's growth characteristics through to testing its PEC performance as a protective layer for the p-Si cathode responsible for the HER. The application of in-situ characterisation by the coupled XPS system allows for unique insights into the ALD deposition of cobalt nitride with XPS more specifically HAXPES findings rarely reported on this material for application in PEC water splitting.

Regardless of application from CMOS processors to PEC water splitting thin films, each requires a high degree of control over material properties such as stoichiometry and thickness,

and growth techniques such as ALD are particularly suitable, offering a pathway to control the films properties such that they can be tailored to individual applications.

Growing cobalt nitride through ALD processing is an interesting field of study. As illustrated by van Straaten et al.[34] in earlier work, the electrochemical potential of cobalt nitride is close to 0 kJ/mol suggesting the metal should be more stable than the nitride. Using cobaltocene ($CoCp_2$) as the cobalt precursor and NH_3 plasma as a co-reactant, their work showed that the formation of nitride or metal was dictated by the processing temperature, with chiefly Co_2N formed at temperatures below 260°C and metal above 350°C and a mixed phase material at intermediate temperatures. Argon sputtering of the films and subsequent x-ray photoelectron spectroscopy (XPS) showed bulk nitrogen concentrations of approximately 20% at low temperatures and little to no carbon incorporation. Reif et al.[35] also studied cobalt thin film growth by PEALD, employing cyclopentadienylcobalt dicarbonyl [$CpCo(CO)_2$] as the cobalt precursor, investigating H_2, N_2, NH_3 and argon plasma doses. Their work shows that an optimised H_2/N_2 plasma yielded films with approximately 20% nitrogen and very little carbon incorporation from the precursor ligands, while the use of an NH_3 plasma yielded films with 30% nitrogen but also 30% carbon. Their work however, does not discuss optimisation of the NH_3 plasma process to reduce carbon incorporation, with all experiments are performed at relatively low temperature (<250°C). From comparison of these two studies, it appears that a $CpCo(CO)_2$ – NH_3 combination results in films that are carbon rich while $CoCP_2$-NH_3 yields cleaner films.

In this chapter the growth of cobalt nitride using $CoCp_2$ as the cobalt precursor and NH_3 plasma as the co-reactant is investigated. An in-situ XPS study of the $CoCP_2$-NH_3 PEALD growth process is presented at temperatures from 200°C - 400°C. Films are grown in the

ALD-XPS system and transferred by a robotic handler to an XPS chamber to allow for a cycle-by-cycle analysis of the growth chemistry without atmospheric exposure. As previously stated, this in-situ approach offers a clear understanding of the ALD process which is not complicated by the effects of contamination from atmospheric carbon and oxygen. Combining this analysis with synchrotron-based hard X-ray photoelectron spectroscopy (HAXPES) studies of the resulting films gives an understanding of the bulk properties without the need for physical removal of material by sputtering. The impact of the temperature and plasma pulse duration on the film composition is examined, with adaptations shown to have several effects on the stoichiometry of the resulting cobalt nitride film. It is shown that rather than displaying saturation, longer plasma pulses severely inhibit the growth rate at all temperatures. The optimum plasma pulse duration for maximum growth per cycle is shown to reduce with increasing temperature. Furthermore, the results are similar to those of Reif and colleagues whereby carbon concentrations of up to approximately 40% are observed [35]. The investigation shows that the only set of process parameters which allow for reduced carbon incorporation are a combination of high temperature and long plasma pulse time which are accompanied by an exceptionally low growth rate and yield cobalt rich films. The ability to form cobalt nitride films that have a homogenous chemical composition is shown, however these films contain high amounts of carbon-nitrogen bonding throughout the film.

5.2 Experimental Details

ALD and XPS analysis was performed in the Oxford Instruments FlexAl ALD system (base pressure 5×10^{-5} Pa) equipped with an inductively coupled plasma source coupled in-vacuum by a fast-transfer robotic handler to the Scienta Omicron XPS (monochromatic Al Ka X-ray source, base pressure 6×10^{-7} Pa) with a 128 channel Argus CU detector. The XPS pass energy applied was 100 eV and 50 eV for survey and high-resolution spectra, respectively.

All ALD films were grown on silicon samples of approximately 2 cm^2. Prior to entering the deposition chamber, the silicon was ultrasonicated in isopropyl alcohol for 15 minutes, before being blown dry with compressed N_2. Upon entering the ALD chamber, samples were heated to the desired process temperature for 20 minutes, before being exposed to a 5.3 Pa (40 mTorr), 300 W plasma process that consisted of 3 minutes of O_2 flowed at 100 sccm followed by 3 minutes of NH_3 flowed at 50 sccm.[34] By considering the intensities of the Si^0 and $Si^{1+/2+/3+/4+}$ in the Si $2p$ XPS spectra, the residual silicon oxide thickness after this cleaning process was estimated at 0.8 nm.[36]

The ALD process began immediately after the cleaning step, using $CoCp_2$ (Bis(cyclopentadienyl)cobalt(II), purchased from Merck and heated to 80 °C) as the precursor and NH_3 as the PEALD co-reactant. An ALD cycle consisted of a dose of $CoCp_2$, followed by a purge of Ar gas. The chamber was pumped for 6 s before a 4 Pa (30 mTorr), 100 W and 50 sccm NH_3 plasma step. The plasma was followed by a purge of Ar and 3 s of pumping before the next cycle began. Aside from temperature, the other variables investigated were the time duration of the $CoCp_2$ and NH_3 plasma steps, which is discussed in the results section. An example of a typical process is shown in the supporting information

Table 5.1 with the variables highlighted in yellow indicating those altered for precursor characterisation purposes.

Table 5.1 ALD process parameters used for the deposition in this study.

Description	Step Time (s)	Pressure (mTorr)	Rf Power (W)	Ar Purge (sccm)	Ar (sccm)	NH₃ (sccm)	Table Heater (°C)
CoCp₂ Dose	3	15	0	20.0	100.0	0.0	200
CoCp₂ purge	3	15	0	200.0	100.0	0.0	200
Pump	6	0	0	0.0	0.0	0.0	200
NH₃ Plasma Setup	3	30	0	20.0	0.0	50.0	200
NH₃ Plasma	10	30	100	20.0	0.0	50.0	200
Plasma Purge	5	15	0	200.0	100.0	0.0	200
Pump	3	0	0	0.0	0.0	0.0	200

Ellipsometry measurements were performed using the Woollam XLS-100 and analysed using a Cauchy model. HAXPES measurements were performed at the National Institute of Standards and Technology beamline 7-ID-2, located at the National Synchrotron Light Source II, Brookhaven, New York (NSLS-II). To depth profile the samples, photon energies of 2, 4 and 6 keV were implemented, with a pass energy of 100 eV applied for the 2 keV and 200 eV for the 4 and 6 keV photon energies.

All XPS/HAXPES spectra analysis was performed using the software AAnalyzer.[37] All fitted spectra used a Shirley Sherwood type background and a Voigt type curve profile. Where possible, all spectra were shifted so that the Si 2p (bulk) peak for the relevant dataset was located at 99.4 eV,[38] with care taken due to the overlap of the Si 2p and Co 3s binding energy positions.

5.3 Results

5.3.1 ALD Process Characterisation

Prior to ALD characterisation, an investigation into obtaining an optimal $CoCp_2$ dose time for the FlexAl system was carried out. Saturation was determined by monitoring the ratio of the Co $2p_{3/2}$ XPS peak intensity to the Si $2s$ in-situ. The ratio of peak intensity of Co $2p_{3/2}$ to the Si $2s$ was performed due to the Co $3s$ photoemission peak overlapping Si $2p$ making determining the Si $2p$ peak intensity inaccurate. A saturation point is established through analysing the rate of Si $2s$ peak suppression as a function of Co deposition cycles. It was found that $CoCp_2$ saturation occurred between $0.5 - 3$ s Figure 5.1 for a 270 °C – chuck temperature that received a 10 s NH_3 plasma dose. All further investigations implemented a 3 s $CoCp_2$ dose time.
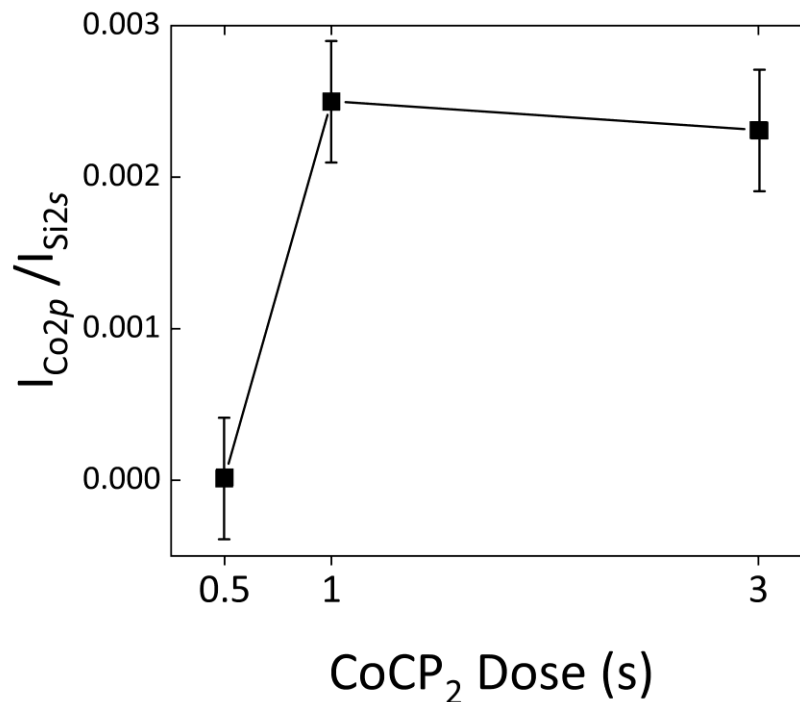
Figure 5.1 CoCP$_2$ dose saturation curve for a 120 cycle, 270°C process with a 10s NH$_3$ plasma dose time.

The same principle of monitoring the Co $2p_{3/2}$ / Si $2s$ intensity was performed for the determination of the optimal NH_3 plasma dose time. The XPS intensity graphs of the I_{Co2p}/I_{Si2s} versus plasma dose time at three different temperatures, normalised to the maximum signal for that temperature, is shown in Figure 5.2. Unlike typical ALD processes, saturation in growth rate with increasing plasma exposure time was not observed.
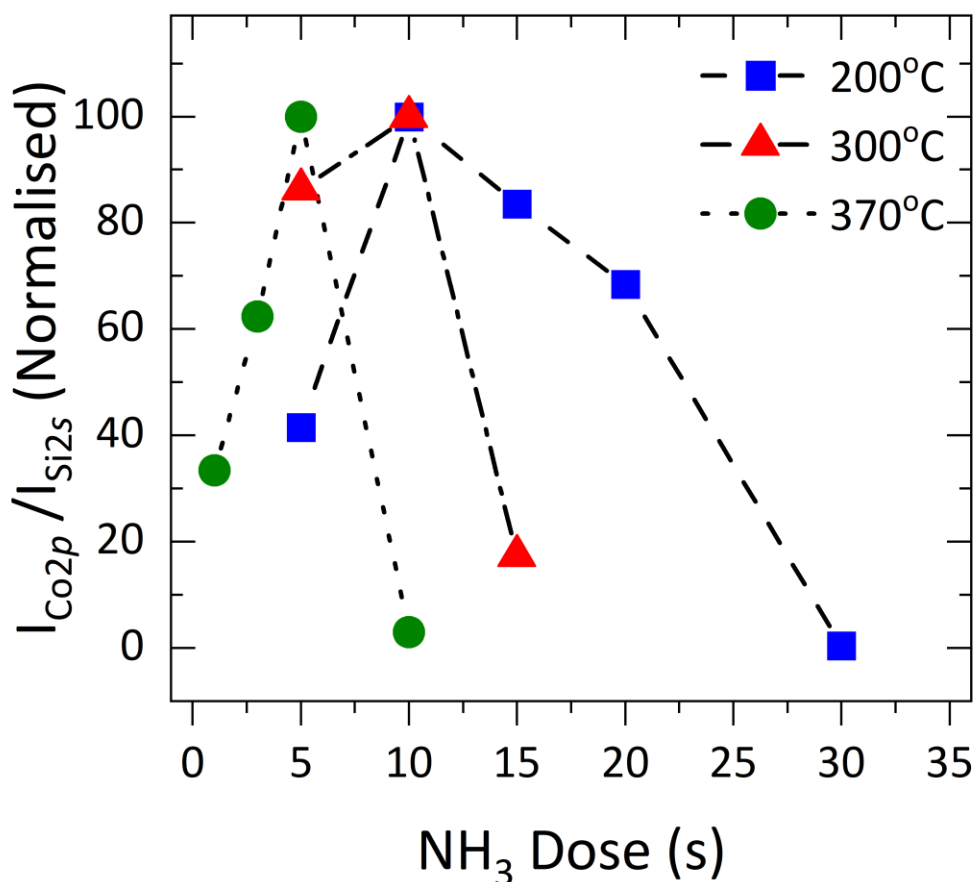
Figure 5.2 NH_3 plasma dose time saturation curves for 150 cycle processes at three temperatures with a 3 s Co dose time. The data was obtained through monitoring the ratio of the XPS intensity of the Co $2p_{3/2}$ peak to the intensity of the Si $2s$ peak. An ALD window for achieving optimal cobalt nitride growth was observed, which narrowed with increasing temperature.

As expected, an increasing growth rate is observed initially where longer plasma exposure times allow for precursor ligand removal and activation of the surface for the next ALD cycle. However, as exposure time was further increased, it was observed that cobalt nitride growth was severely inhibited at high plasma dose times, thereby creating a window for NH_3 plasma dosing to achieve the highest growth rates. The drop off in growth rate was more severe at higher temperature. Following the acquisition of the saturation curves, XPS analysis of the growth of the cobalt nitride at different stages of the ALD process was performed in order to understand the growth chemistry. Films were processed at 200°C, 300°C, 350°C and 400°C, and XPS analysis was carried out immediately after 50, 100, 200, 500 and 1000 cycles in each case.

To enable easy cross analysis, the four ALD recipes used identical process parameters. As Figure 5.2 shows, high plasma times resulted in very slow growth for high temperature processes, resulting in a NH_3 time of 5 s being chosen for all temperatures. Estimations of the growth rate for each ALD process temperature were obtained through ellipsometry, with films analysed ex-situ after 1000 cycles. Figure 5.3 shows the thickness and the calculated growth per cycle (GPC, in nm/cyc) for the four process temperatures. Despite decreasing the NH_3 plasma dose time to encourage reasonable growth at high temperatures, the GPC clearly scales inversely with temperature.
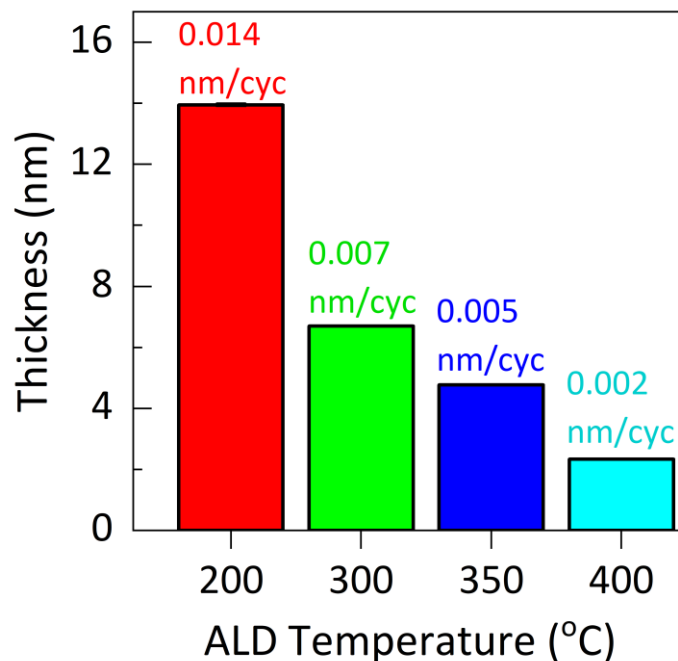
Figure 5.3 Ellipsometry thickness measurements of a 1000 cycle ALD recipe for 4 different process temperatures. Their growth rate in nm/cyc is also shown.

The XPS spectra of the Co 2p for the four ALD process temperatures are shown in Figure 5.4. Both the 200°C (a) and 300°C (b) depositions have peak maxima located at approximately 781 eV at all stages of the process, which is associated with cobalt nitride. The Co 2p spectra for the 350°C process (c) has a peak maximum at approximately 781 eV, attributed to cobalt nitride, and a lower binding energy component at 779 eV, which is associated with metallic cobalt [39,40]. This result supports previous work which showed that a blend of cobalt nitride and Co^0 is formed during ALD processes at 350°C.[34] Our results show however that only Co^0 is present for the first 200 cycles, with cobalt nitride forming at 500+ cycles. At 400°C, the growth of Co^0 is observed with no other Co oxidations state observable

in the chosen cycle range. The position of the main Co $2p_{3/2}$ peak at approximately 778.5 eV, in addition to the asymmetry of the spectra, confirms the growth of metallic Co.[41]
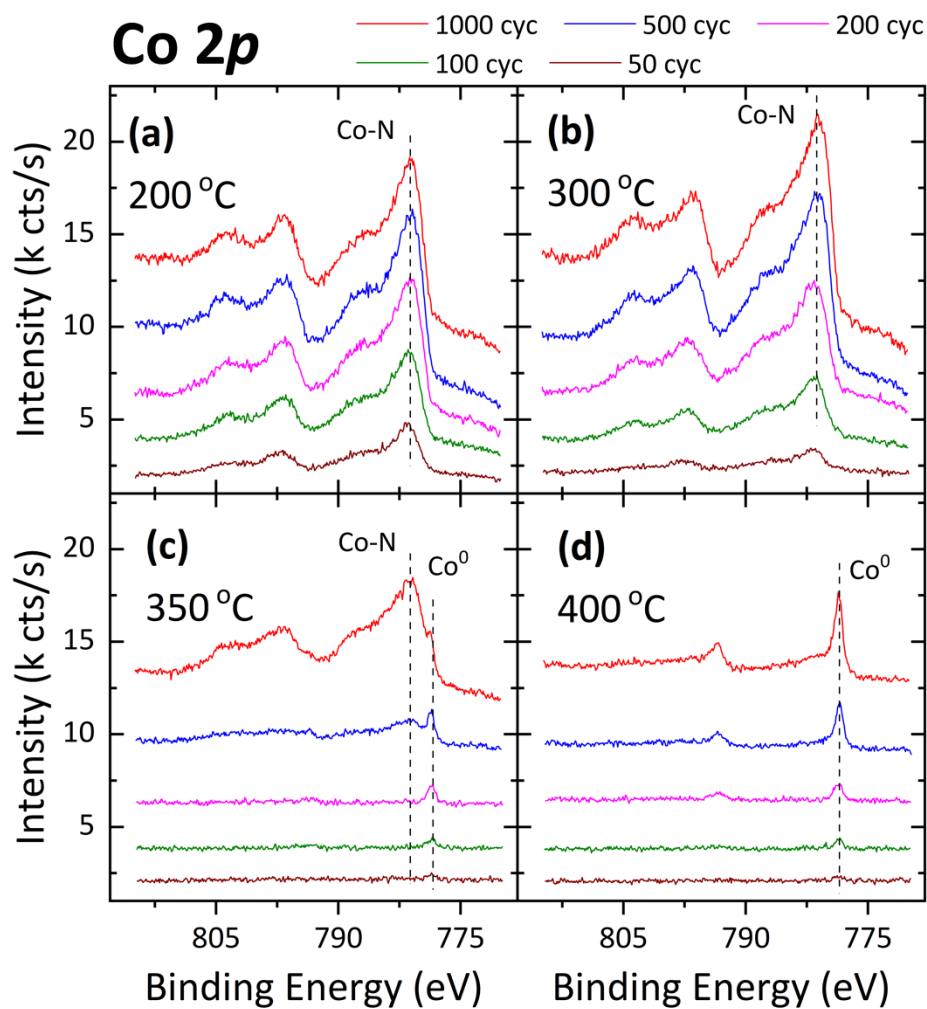
Figure 5.4 XPS Co 2p spectra for the four ALD process temperatures at different stages of a 1000 cycle process, (a) 200°C, (b) 300°C, (c) 350°C and (d) 400°C. CoN$_x$ is visible for the 200°C and 300°C process. The 350°C process consists of Co^0 only until approximately 500 cycles, where a CoN$_x$ and Co^0 blend is formed. The 400°C yields Co^0 only.

Clear N $1s$ signals are observed in Figure 5.5 for all processing temperatures, despite only Co^0 being visible for the 400°C process in as seen in Figure 5.6 (d). The maxima for each

process are located at approximately 399 eV, however the broad and asymmetric peak profile, suggests that more than one chemical state of nitrogen is present in the film.
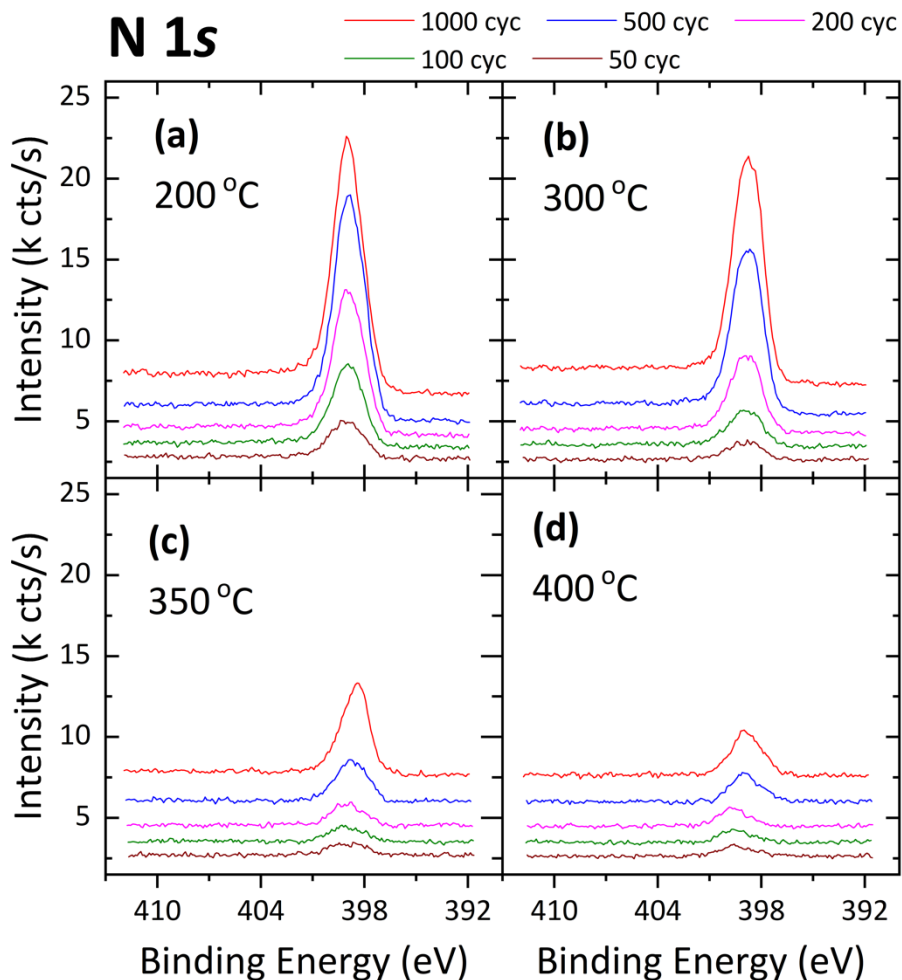
Figure 5.5 XPS N 1s spectra for the four ALD process temperatures at different stages of a 1000 cycle process, (a) 200°C, (b) 300°C, (c) 350°C and (d) 400°C.A broad nitrogen peak is visible across all four deposition temperatures.

ALD grown films of cobalt nitride have typically exhibited a high concentration of carbon impurities [35,42]. These results show similar behaviour, with XPS spectra of the C 1s region revealing significant carbon incorporation after 1000 cycles in the temperature range of 200

– 350 °C. Figure 5.6 (a), (b) and (c) for the 200°C, 300°C and 350°C ALD process respectively show that the carbon exists in two main states, a lower binding energy component associated to C-C type bonding, and a higher binding energy component which is attributed to C-N bonds (all oxygen in the spectra is associated with the SiO_2 interlayer). Notably there is no evidence of carbidic carbon in the films.
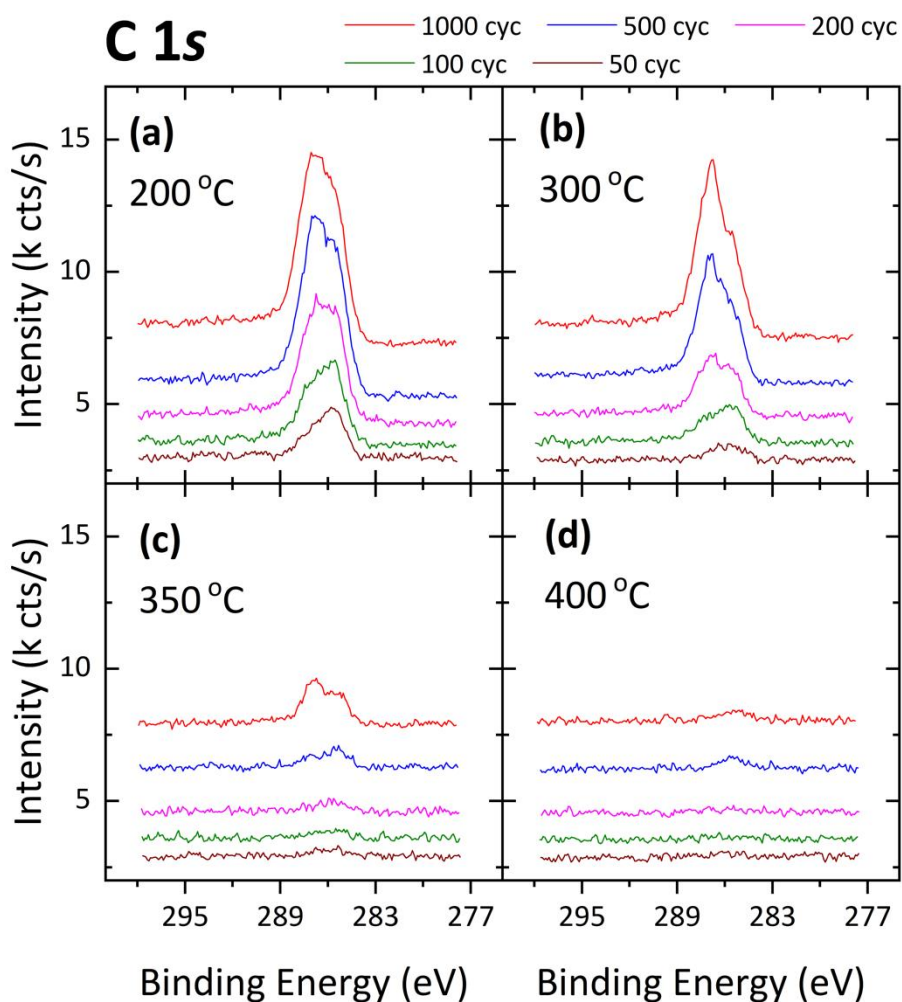
Figure 5.6 XPS C 1s spectra for the four ALD process temperatures at different stages of a 1000 cycle process, (a) 200°C, (b) 300°C, (c) 350°C and (d) 400°C. Two major components are visible in the spectra for the 200°C, 300°C and 350°C processes, the low and high binding energy components are associated with C-C and C-N bonds respectively.

The ratio of C-C to C-N type bonding favours C-C in the early stage of the ALD process, however C-N becomes dominant with increasing cycles. Due to the in-situ nature of the analysis we can confidently identify that the C-C component of the peak is associated with the carbon from the precursor that has not been effectively removed by the co-reactant plasma (and not adventitious carbon), with a gradual growth in C-N in the film being obtained through continued exposure to NH_3 plasma. This correlates with the broad spectra of the N $1s$ as seen in Figure 5.5, and is discussed in more detail with the HAXPES analysis. The XPS chemical compositions of each ALD process for increasing cycle numbers are shown in Figure 5.7. Carbon, nitrogen, and cobalt were the only signals considered, with the oxygen and silicon signals attributed to the substrate only. The compositions were calculated by applying the relevant atomic sensitivity factors[43] to the C $1s$, N $1s$ and Co $2p_{3/2}$ spectra.
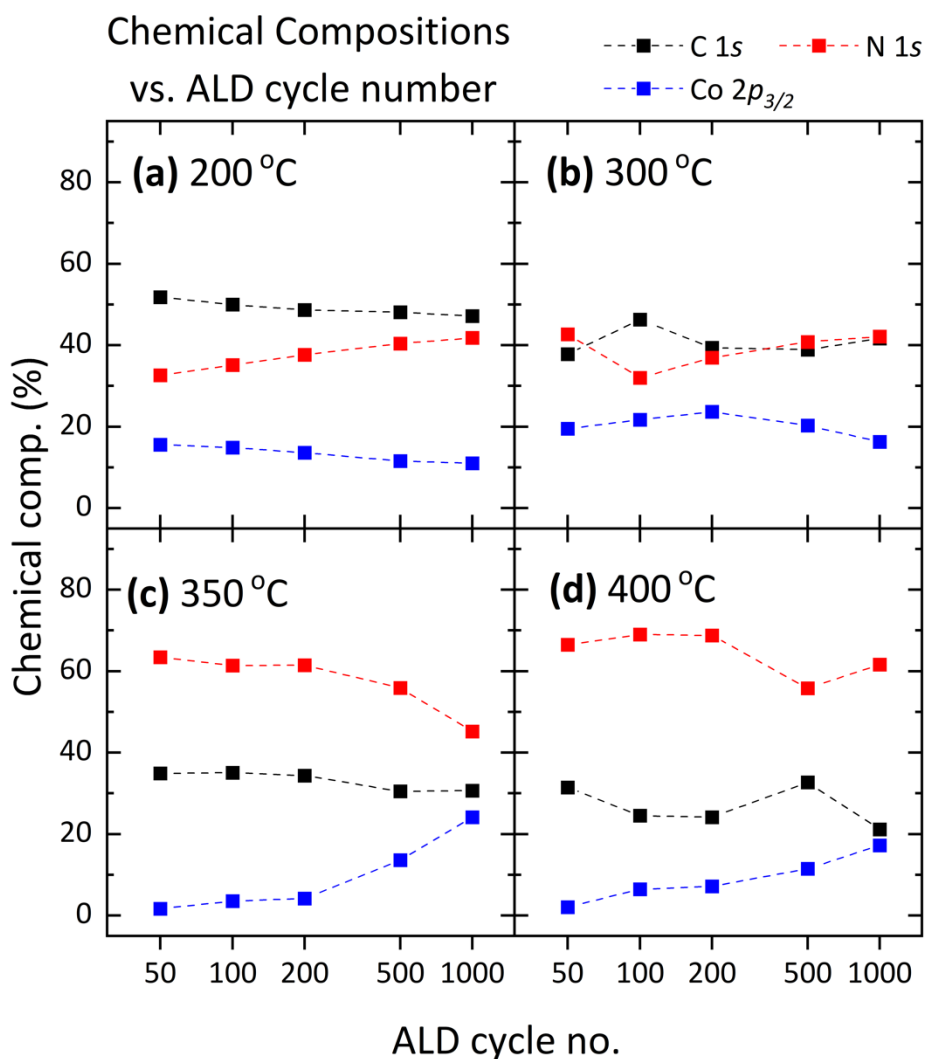
Figure 5.7 XPS chemical compositions of the (a) 200°C, (b) 300°C, (c) 350°C and (d) 400°C ALD process for cycles 50 - 1000.

The carbon concentration in the film is seen to be relatively steady throughout the ALD process at all temperatures, with the sample processed at 200°C Figure 5.7 (a) containing the highest amount of incorporation. This decreases with increasing temperature, with carbon incorporation at 1000 cycles being 47%, 42%, 31% and 21 % for the 200°C, 300°C (b), 350°C (c) and 400°C (d) respectively. In contrast to this behaviour, cobalt in the film tends

to increase with increasing temperature – at 1000 cycles, the concentration of cobalt is 11%, 16%, 24% and 17% for the 200°C 300°C, 350°C and 400°C (d) respectively, although it should be noted that this coincides with dramatic decrease in growth rate as shown in Figure 5.3. The cobalt concentration appears to act oppositely to the nitrogen concentration – there is a slight increase of nitrogen at the expense of cobalt with increasing ALD cycles at 200°C and 300°C, while decreasing amounts of nitrogen can be linked with increasing amounts of cobalt concentration at 350°C and 400°C.

5.3.2 Characterising Optimised Films

Further analysis is now focused on the characterisation of cobalt nitride films grown at 200°C and 300°C, as it was observed from Figure 5.4 that higher temperatures yielded films with increasing amounts of Co^0. Thick (10+ nm) cobalt nitride films were fabricated in order to assess the bulk and surface of the ALD films, with 1000 and 2000 cycles used for the 200°C and 300°C process, respectively. Based on the learnings from Figure 5.2, the optimal parameters for both processes consisted of a 3s and 10s dose time for the $CoCp_2$ and NH_3 plasma, respectively.

XPS measurements were performed on the cobalt nitride samples immediately after the ALD process before being removed and exposed to atmosphere to allow for ellipsometry thickness measurements. These samples were then loaded back into the XPS vacuum chamber to reveal the effect of atmospheric exposure before being treated with a 2 hour NH_3 plasma (5.3 Pa / 40 mTorr, 50 sccm, 300 W) at the same temperature as the corresponding ALD process, to assess whether carbon removal to yield cleaner more stoichiometric cobalt nitride films using such a treatment is achievable.

The ellipsometry results and XPS chemical compositions for each stage of the process is shown in Table 5.2. The XPS compositions were calculated from the survey scans shown in Figure 5.8, for each sample. Each column represents the film at different stages of the process 200/300°C *ALD* – post ALD, *200/300°C* + post atmosphere exposure (*atm*), *200/300°C* + *NH₃* – post 2 hour NH₃ plasma).
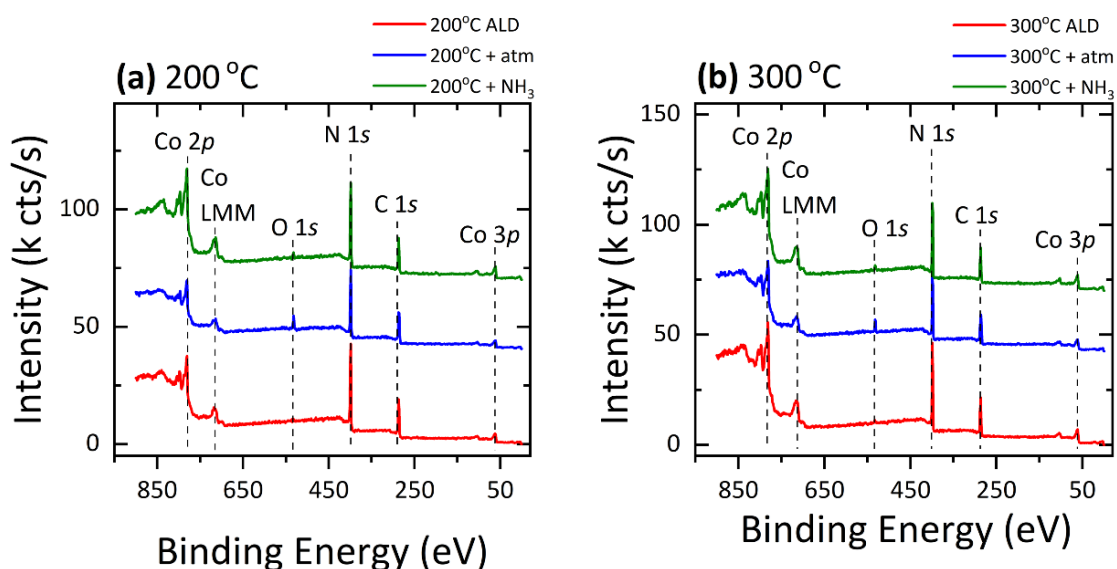
Figure 5.8 XPS survey scans (not shifted for charging) for a 200°C (a) and 300°C (b) ALD process. Limited oxygen growth is observed once the sample is exposed to atmosphere.

Table 5.2: Ellipsometry and XPS chemical compositions for a 200°C and 300°C ALD process (1000 and 2000 cycles respectively). Multiple samples were measured via ellipsometry to obtain a standard deviation.

	200°C ALD	200°C + atm	200°C + NH₃	300°C ALD	300°C + atm	300°C + NH₃
Thickness (nm)	---	18.3 ± 0.32	---	---	13.6 ± 0.51	---
Co %	12	10	15	17	14	19
N %	44	37	46	45	39	45
C %	43	47	37	37	42	34
O %	1	6	2	0	5	2

The ellipsometry revealed a GPC of 0.018 nm/cyc and 0.007 nm/cyc for the 200°C and 300°C process respectively. Post ALD, the XPS compositions reveal films that are dominated by nitrogen and carbon, with negligible oxygen seen in the film. Pre- atmospheric exposure, the 200°C and 300°C compositions show consistent correlation with Figure 5.7 – a slightly higher carbon incorporation is observed for the lower temperature process. The oxygen contribution increases slightly after atmospheric exposure but remains extremely minor to the overall makeup of the film. The carbon concentration also increases, due to the adsorption of adventitious carbon, which results in the attenuation of the cobalt and nitrogen signals. After prolonged NH_3 plasma exposure, carbon removal is noted but in a limited capacity. These results are corroborated by the high resolution XPS spectra of the C 1s, N 1s, O 1s and Co 2p spectra for the 200°C and 300°C processes, shown in Figure 5.9 and Figure 5.10 respectively from the supporting information.

Looking to Figure 5.9 (a) showing the C 1s high resolution spectra it is clear that there is a significant increase in a low binding energy component in the post atmospheric exposure stage which is attributed to adventitious carbon contamination on the sample. From Figure 5.9 (c) a growth in the O 1s component is also observed and attributed to absorbed water from the atmospheric exposure. The N 1s and the Co 2p spectra in Figure 5.9 (b) and (d) respectively are seen to remain unchanged following the atmospheric exposure which shows the stability of the film. Furthermore, the presence of a strong satellite feature is always observed within the Co 2p spectra irrespective of whether there is oxygen present. The exposure to extended NH_3 plasma treatments is seen to remove the C-C bonding at approximately 284 eV which corresponds to the adventitious carbon content however it has

no significant effect in removing the higher binding energy component of the C 1s spectra which is consistent with the presence of C-N bonding [44].
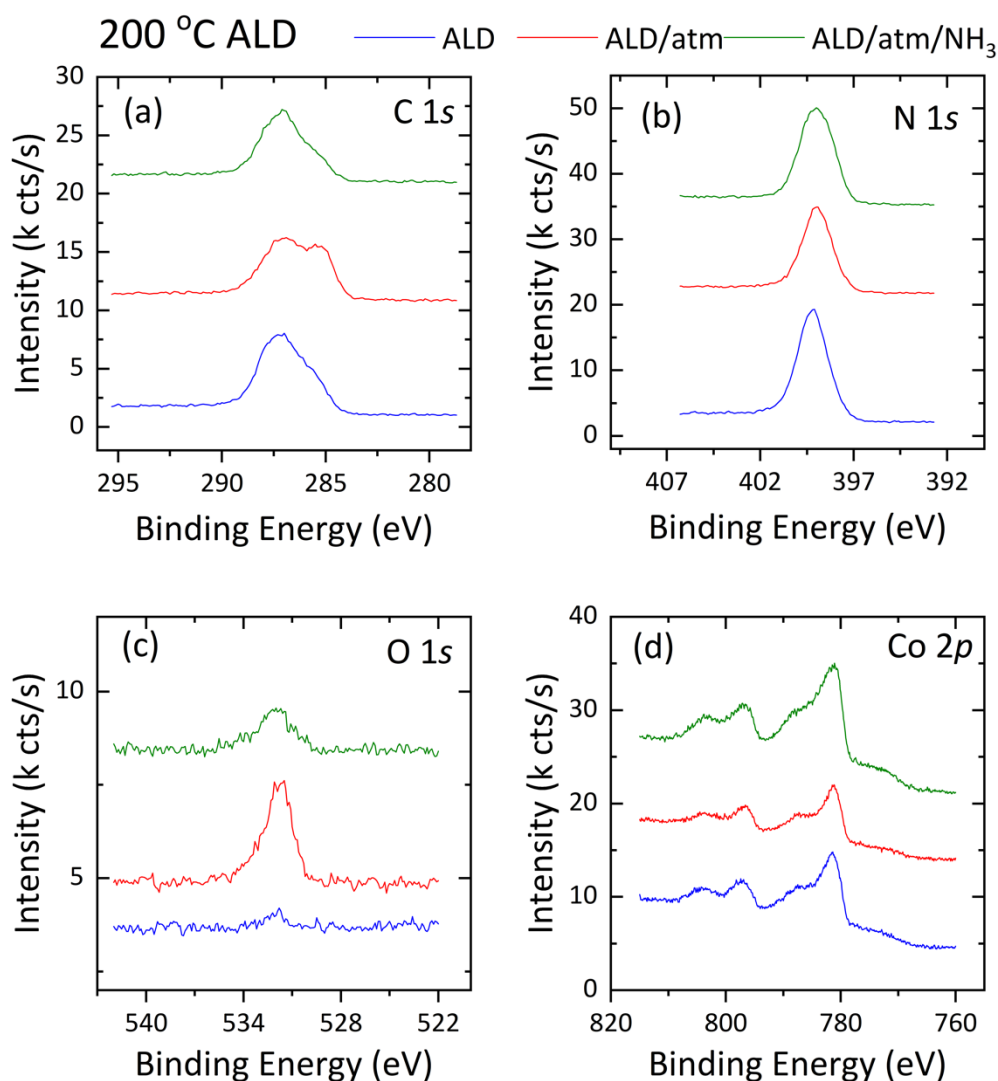
Figure 5.9 High resolution XPS scans (not shifted for charging) of a 200°C ALD process. C 1s (a), N 1s (b), O 1s (c) and Co 2p (d) are shown.

It is noted that the peak shape of the N 1s and Co 2p spectra remain consistent throughout each stage of the process, showing that the Co-N and C-N aspects of the film are constant regardless of exposure to atmosphere and additional NH_3 plasma. This is not the case for the

C-C associated components of the C 1*s*, which increase after atmospheric exposure before decreasing after the additional NH$_3$ plasma treatment.
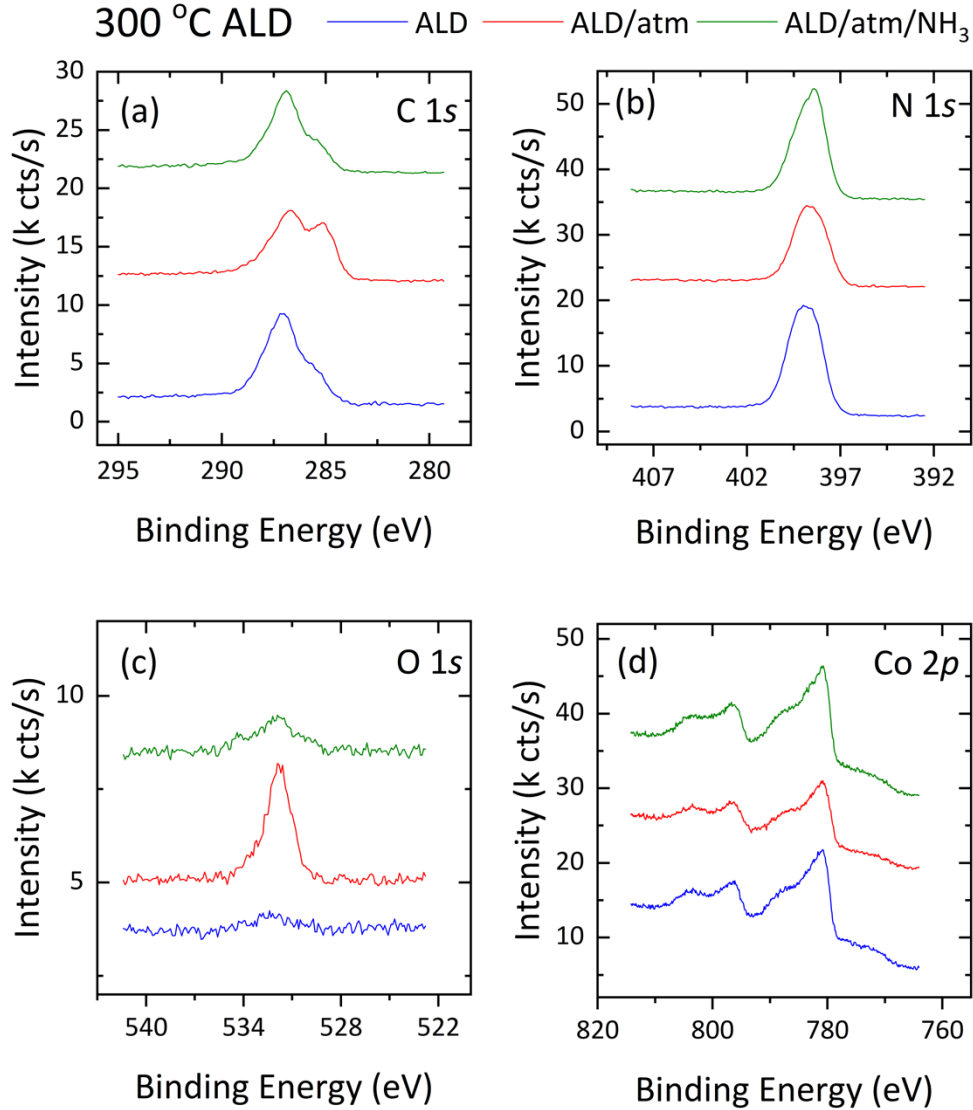
Figure 5.10 High resolution XPS scans (not shifted for charging) of a 300°C ALD process. C 1s (a), N 1s (b), O 1s (c) and Co 2p (d) are shown. The behaviour of the spectra mirrors that of the 200°C ALD process shown in Figure 5.9.

Both the 200°C and 300°C samples were analysed ex-situ with HAXPES. The Co 2*p* and N 1*s* spectra for the different processing temperatures are shown in Figure 5.11. Photon energies of 2 keV, 4 keV and 6 keV were used, with higher values providing more

information about the cobalt nitride bulk chemical composition. Varying the photon energy allows for an unobtrusive method of obtaining depth profile information of the films. Additionally, using a different photon energy from Al kα simplified the fitting process of the Co 2p spectra, shown in Figure 5.11 (a-b), due to the removal of the overlap between the Co 2p and the Co LMM Auger line.[45]

The curve fit for the Co 2p was applied with caution, due to the presence of strong satellite features. These satellite peaks, associated with multiplet splitting or shakeup features, are usually attributed with cobalt oxides,[46,47] with strong satellites indicating the presence of Co^{2+}.[41] The Co 2p spectra profiles remained unchanged following the atmospheric exposure as seen in Figure 5.9 and Figure 5.10, and therefore these satellites are attributed to the Co-N bonding that is occurring in the film.

For the 200°C process in Figure 5.11 (a) the Co 2p profile was fitted with 5 peaks. The non-satellite components had a Lorentzian and Gaussian width of 0.1 and 2.5 eV respectively. Two satellite peaks were fitted in the spectra, located at approximately 786 and 788 eV. The peak positions, and the Gaussian value of 5.8 eV (correlated to be 2.4 times larger than the non-satellite peaks) were chosen after fitting and comparison to previous work by Biesinger et al.[41] A minor peak at 784.0 eV was associated with nitrogen-rich cobalt nitride (Co_zN_ω, where z < ω) such as Co_2N_3. A peak at 782.6 eV was associated with CoN. The most predominant and lowest binding energy peak was associated with the most cobalt-rich component (Co_xN_y, where x > y). The position of this peak (highlighted in the figure) was found to increase slightly with decreasing photon energy, being located at 780.6, 780.7 and 781.0 eV for $hv = 6$, 4 and 2 keV, respectively. The same peak parameters and positions were applied to the 300°C process in Figure 5.11 (b), with the notable exception of the Co_xN_y peak.

The position of this component also increased with decreasing photon energy, however it occurred at a slightly lower binding energy of 780.4, 780.5 and 780.6 eV for hv = 6, 4 and 2 keV, respectively.
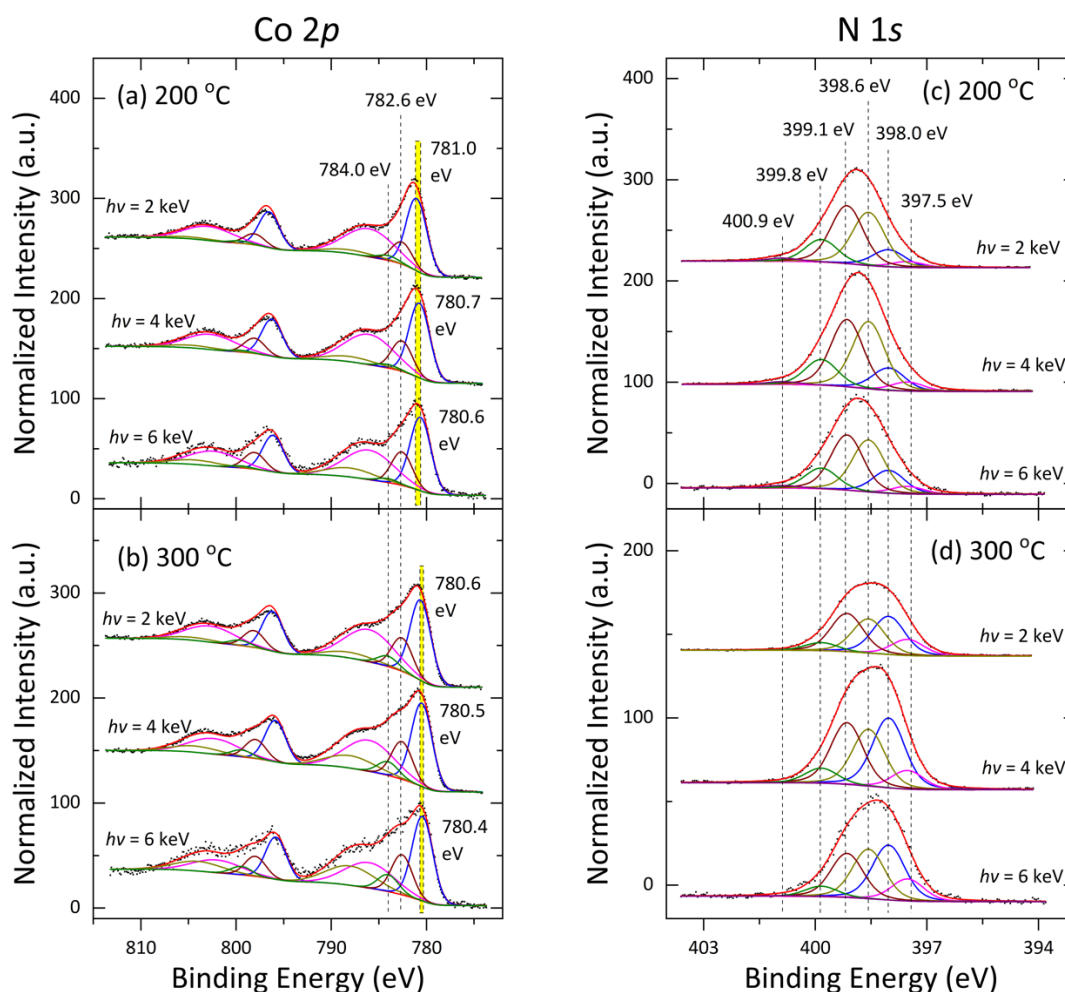
Figure 5.11 HAXPES Co 2p spectra at different photon energies of a 200°C (a) and 300°C (b) process. The $2p_{3/2}$ peaks associated with chemical bonds are labelled. N 1s peaks for the 200°C (c) and 300°C (d) process are also shown. All peaks have been normalized to the Co 2p spectra.

It can therefore be concluded that both ALD processing temperatures produce cobalt nitride films dominated by a cobalt rich component, Co_xN_y. The higher binding energy position of this peak in the 200°C compared to the 300°C process suggests that lower temperature

processes contain more nitrogen in this component as verified in Figure 5.11 (a,b) showing a small 4eV shift to higher binding energy. Furthermore, from Figure 5.12 the C-N bond peak is seen to be more prominent in the 300°C film compared to that seen in the 200°C. These findings are consistent with previous reports however, conclusions are speculative based on data obtained and as such remain open to interpretation [34]. For both temperatures, the binding energy of this peak gradually shifts to higher binding energy with decreasing photon energy, suggesting that both films are slightly more nitrogen rich closer to the surface. Additionally, it is observed that the 300°C process contains significantly more nitrogen-rich cobalt nitride, Co_zN_ω.

The N $1s$ peaks for the 200°C and 300°C processes are shown in *Figure 5.11* (c) and (d), respectively. The spectra were fitted with a Lorentzian width fixed at 0.28 eV,[48] and a Gaussian value of 0.86 eV. The low binding energy components at 397.5, 398.0 and 398.6 eV are associated with Co_zN_ω, CoN and Co_xN_y respectively. The 300°C process results in a significantly broader peak profile containing larger amounts of Co_zN_ω and CoN, consistent with the Co $2p$ fit. For the 200°C process, the Co_xN_y related peak at 386.6 eV is significantly higher than the other cobalt containing peaks, which is expected as the Co_xN_y is more nitrogen rich than the 300°C process.

Three additional peaks are associated with the N $1s$ fit, occurring at higher binding energies, are associated with nitrogen – carbon bonding. The component at 399.1 eV lies within the agreed 'pyridinic nitrogen' range,[49] while the peaks at 399.8 is associated with pyrrolic nitrogen.[50] The high binding energy peak at 400.9 eV may represent protonated or graphitic nitrogen, however it is a minor peak in the fit.[49–51] For both ALD processes, the peak shape remains consistent regardless of photon energy used, suggesting a film that is chemically

homogenous within the analysis depth of HAXPES measurements, aside from the slight increase in nitrogen towards the surface of the film noted in the slight shifting as described in the Co 2*p* spectra in Figure 5.11 (a-b).

Figure 5.12 shows the HAXPES C 1*s* spectra for the 200°C (a) and 300°C (b) processes. While assignment of the different components in the C 1*s* is complex, it is clear that two main components are present at approximately 285 and 287 eV. Due to the exposure to atmosphere, the lower binding energy region can be attributed to adsorbed hydrocarbons,[52,53] as well as precursor that has not been effectively removed by the co-reactant plasma, while the higher binding energy region is attributed to the various forms of C-N bonding observed in the N 1*s* spectra.[49,51] Unlike the Co 2*p* and N 1*s* spectra, which display broadly consistent peak profiles at a range of photon energies, the peak profile of the C 1*s* changes significantly.
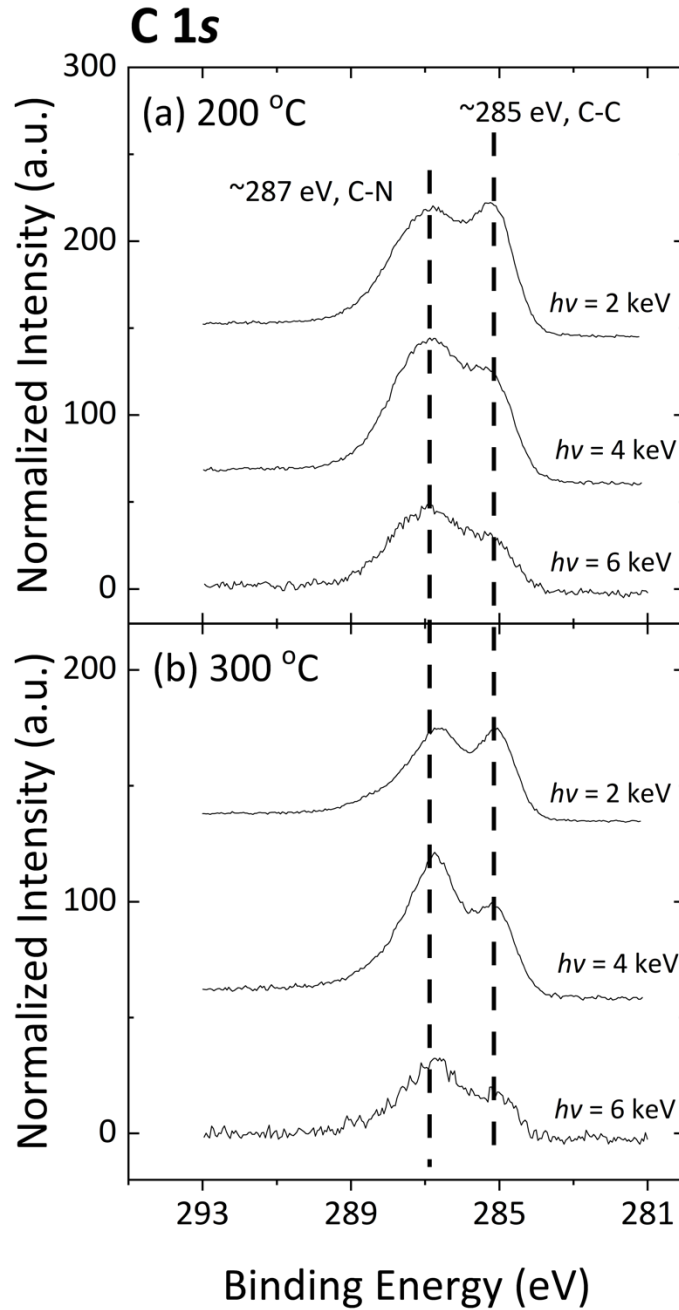
Figure 5.12 HAXPES C1s spectra of a 200°C (a) and 300°C (b) process. All peaks have been normalised to the Co 2p spectra.

As the C 1*s* is the only spectrum to show change with photon energy, it is hypothesized that

the only variation in the film is with the C-C/hydrocarbons contained within the film, which

are found at greater concentration towards the surface of the film due to exposure to

240

atmosphere. This correlates well with the data presented in Table 5.2, which showed increases in carbon upon exposure to atmosphere for both samples. Additionally, by comparing the intensity of the C-C and C-N associated regions, the 200°C ALD process yields films with a slightly higher C-C contribution, correlating with the data presented in Table 5.2, which shows the 200°C process contains more carbon in the entire film.

The Co $2p$ and N $1s$ spectra in Figure 5.11 show good correlation with the X-ray diffraction results in the work by Van Straaten et al.,[34] whom demonstrated that $CoCP_2$-NH_3 ALD processes at 260°C and 230°C yield Co_2N while a 300°C process yields Co_3N. However, by depth profiling the films via Ar ion sputtering, the authors noted that minimal carbon is visible in the film, contradicting the results presented here in Figure 5.12. It is possible that this difference arises from the destructive aspect of the argon sputtering depth profiling. Argon ion sputtering is known to reduce cobalt oxides,[54,55] and the resulting Co $2p$ XPS spectra presented after sputtering does not represent cobalt nitride. The depth profiling technique applied in the current work is non-destructive and may indicate that the argon ion sputtering resulted in the preferential removal of carbon from the film. We conclude that, like $CpCo(CO)_2$ – NH_3 ALD processes, $CoCP_2$-NH_3 ALD processes are impacted by large amounts of carbon impurities that post treatments have limited effects in resolving.

5.3.3 PEC Testing

Figure 5.13 shows the chronoamperometry measurements comparing the stability of a bare p-Si reference sample versus that of a CoN protected photocathode. The bare Si sample is seen to begin at very low photocurrent density before gradually falling off over the course of the measurements. The CoN sample shows enhanced photocurrent from the outset reaching almost 0.7 mA/cm^2 before rapidly decreasing in as little as 40 seconds into the measurement

so although increasing the overall photoelectrochemical performance, the stability of the coating remains low and therefore unsuitable for extended use in a real-world application. This observation of poor stability performance is likely resultant from cathodic photocorrosion which is the degradation of a material in contact with an electrolyte solution in the presence of light. The role of the PEC photocathode is the generation of charge carriers for use in the evolution of hydrogen, however in some instances these charge carriers may interact with the material itself or even impurities within the electrolyte rather than being used at the HER site, this leads to cathodic photocorrosion which is an undesirable effect for water splitting [56]. Cathodic photocorrosion has a range of detrimental effects on the performance of a PEC photoelectrode [57]. One such effect is the loss of active surface area due to the dissolution of the material itself leaving behind a reduced area for reaction to occur and facilitate the HER reaction. As the material continues to corrode the charge carriers themselves are impacted with an insulating layer forming on the photoelectrode which negatively impacts the collection and transport of charge carriers to and from the electrode-electrolyte interface. The specific mechanisms of this cathodic photocorrosion will vary depending on the material as well as the experimental conditions and is to be mitigated where possible to enhance the PEC performance [58].

This insufficient stability performance is further developed in Figure 5.14. It is to be noted that the Ni films from chapter 4 and Co films within this chapter exhibit notable catalytic properties in line with reports within the literature [59–62]. This is in comparison to bare Si photoanodes and photocathodes which generally offer poor charge transfer with the incorporation of these Ni and Co layers appearing to enhance the process as evident from Figure 5.13.
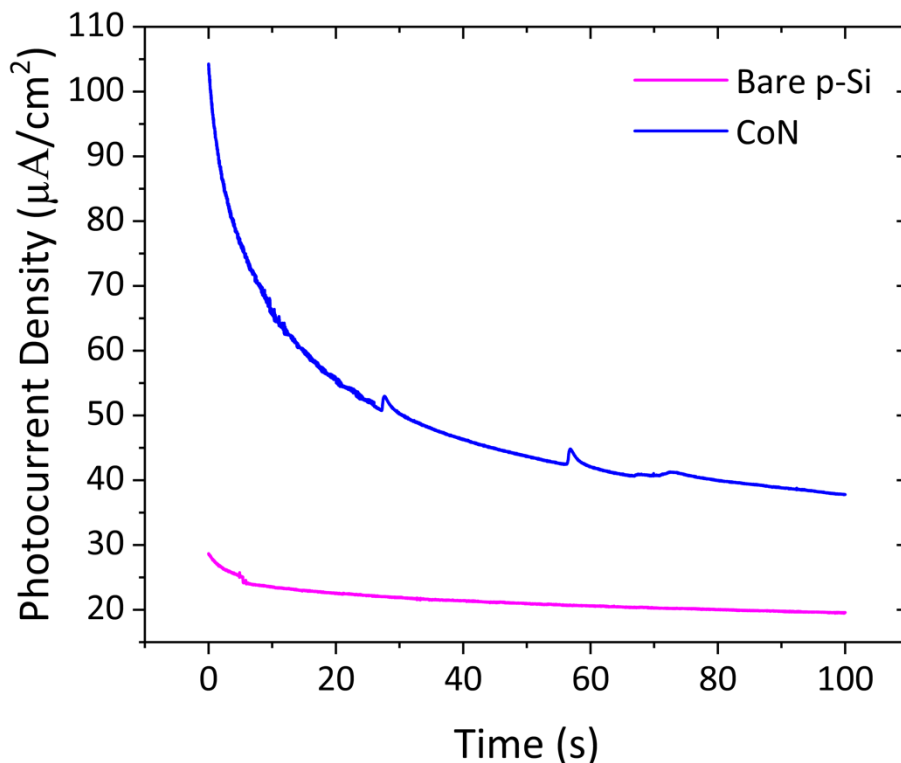
Figure 5.13 PEC chronoamperometric testing comparing a bare p-Si reference sample with a CoN coated sample.

The finding shown in Figure 5.13 of insufficient stability performance of the CoN protective layers is confirmed in Figure 5.14 which shows a series of consecutive chronoamperometric measurements performed on a new CoN coated samples. Run 1 is seen exhibit the highest photocurrent density as would be anticipated as the sample is in its most fresh state during this measurement before performing Run 2 & 3 which allowed for the purging of bubbles from the system to prevent them influencing the measurement. Though initially relatively high, this current is seen to very rapidly fall off showing the instability of the film. This is verified looking to Run 2 & 3 which show less than half of the initial photocurrent density observed in Run 1 showing that the film has been broken down by this stage with the current

not all that dissimilar to what is observed for a bare Si sample as was shown in Figure 5.13. This illustrates the poor stability of the protective films and suggests their unsuitability for use as protective layers for photocathodes in PEC water splitting applications.
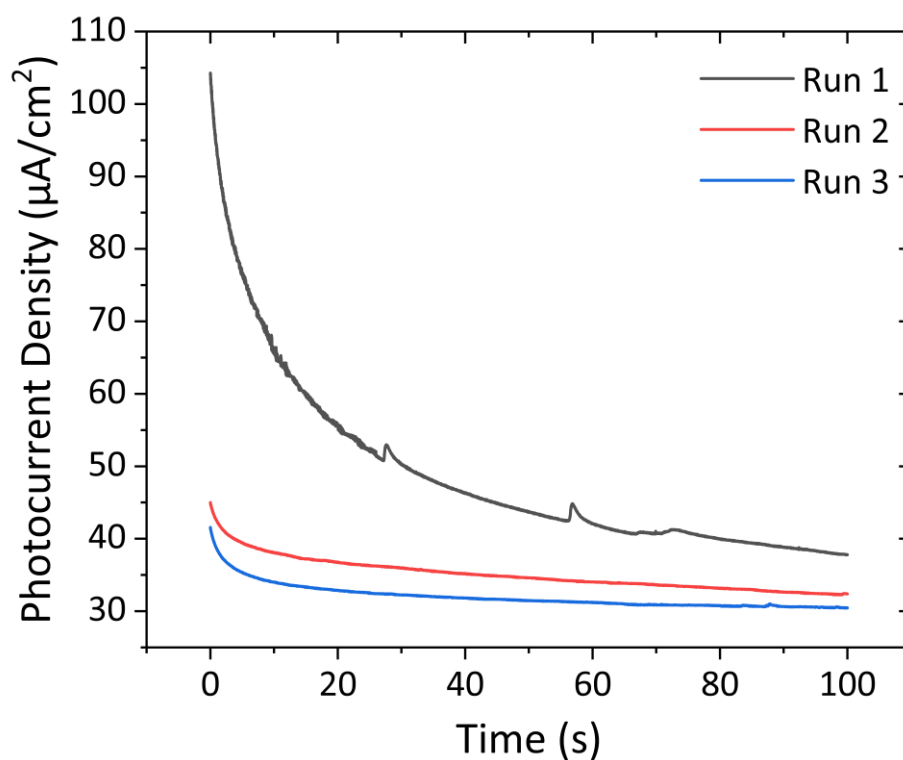
Figure 5.14 PEC chronoamperometric testing showing the degradation in the protective ability of a CoN film as a function of additional test cycles.

Figure 5.15 shows cyclic voltammetry plots which have been plotted on the outward sweep and contains IV curves for both a reference p-Si bare reference sample in addition to a CoN coated sample with measurements taken in the dark and under illumination. From the light current sweep of the CoN an onset potential of 0.42 V vs. RHE is observed along with an increase in photocurrent density as a function of increasing bias potential.
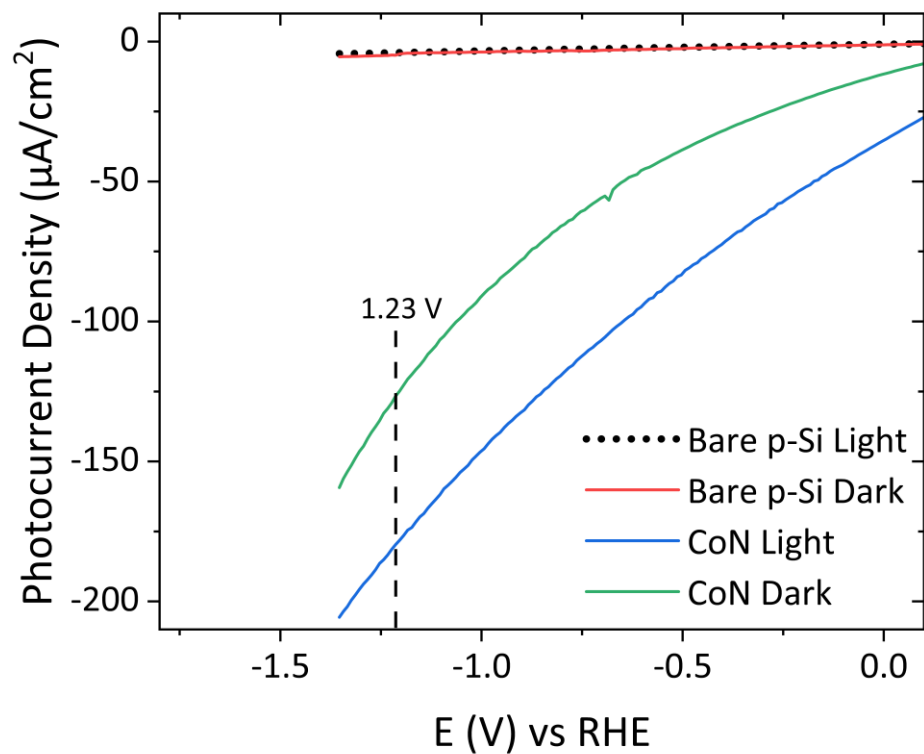
Figure 5.15 PEC cyclic voltammetry testing plotting photocurrent density as a function of increasing Voltage vs RHE detailing the performance of a bare p-Si sample in the light and dark and same for a CoN film with a line highlighting 1.23 V vs RHE.

5.4 Conclusions

To achieve cobalt nitride growth, an ALD window for NH_3 plasma dose time was observed, with plasma doses above a certain time duration severely inhibiting growth. This window decreased with increasing process temperature. Optimal growth rates for a range of temperatures were determined, and it was found that the growth rate decreased rapidly with increasing temperature. The in situ XPS measurements revealed that films processed at 300°C and under yielded cobalt nitride films though still retaining significant contributions of remnant unreacted carbon, while a process temperature of 350°C resulted in a cobalt nitride and metallic cobalt blend. A 400°C process resulted in the acquisition of metallic cobalt only, albeit at a low growth rate with large amounts of nitrogen still contained in the film.

The cobalt nitride films contained high levels of carbon, associated with precursor not removed during the plasma dosing and also carbon nitrogen bonding. A lower ALD temperature results in higher amounts of remnant precursor ligands in the film. This was an unexpected result, as previous reports concerning argon ion sputtering of $CoCP_2$-NH_3 ALD processes had suggested minimal amounts of carbon were incorporated into the film. Upon exposure to atmosphere, increases in the C $1s$ XPS signal was attributed to adventitious carbon. The rest of the film Co-N and N-C bonding was unchanged.

HAXPES allowed for a depth profiling technique that was non-destructive, with no concern over the reduction of the cobalt in the film or the preferential removal of carbon and nitrogen species. The large satellite features in the Co $2p$ spectra were attributed to Co-N due to the lack of oxygen in the film. This work shows that a 300°C ALD process contains larger amounts of different cobalt nitride chemical states in the film when compared to a 200°C

process. Both films had a main component associated to cobalt nitride that was cobalt rich (Co_xN_y, $x > y$). From the binding energy positions, it was observed that this Co_xN_y signal for the 300°C film has a higher cobalt concentration than the 200°C film. The HAXPES measurements also reveal that the Co-N and C-N aspects of the film are consistent with depth, with the only change in the films associated to adventitious carbon at the top of the film due to atmosphere exposure. This work highlights the current challenges in the growth of cobalt nitride films using a state-of-the-art in situ characterisation approach and provides insight into the effect of changing fundamental ALD parameters for the novel $CoCP_2$-NH_3 ALD process.

5.5 References

(1)   Bhandari, H. B.; Yang, J.; Kim, H.; Lin, Y.; Gordon, R. G.; Wang, Q. M.; Lehn, J.-S. M.; Li, H.; Shenai, D. Chemical Vapor Deposition of Cobalt Nitride and Its Application as an Adhesion-Enhancing Layer for Advanced Copper Interconnects. *ECS J. Solid State Sci. Technol.* **2012**, *1* (5), N79–N84. https://doi.org/10.1149/2.005205jss.

(2)   Balasubramanian, B.; Zhao, X.; Valloppilly, S. R.; Beniwal, S.; Skomski, R.; Sarella, A.; Jin, Y.; Li, X.; Xu, X.; Cao, H.; Wang, H.; Enders, A.; Wang, C. Z.; Ho, K. M.; Sellmyer, D. J. Magnetism of New Metastable Cobalt-Nitride Compounds. *Nanoscale* **2018**, *10* (27), 13011–13021. https://doi.org/10.1039/c8nr02105h.

(3)   Chen, P.; Ye, J.; Wang, H.; Ouyang, L.; Zhu, M. Recent Progress of Transition Metal Carbides/Nitrides for Electrocatalytic Water Splitting. *J. Alloys Compd.* **2021**, *883*, 160833. https://doi.org/10.1016/j.jallcom.2021.160833.

(4)   Bae, H.; Rho, H.; Min, J. W.; Lee, Y. T.; Lee, S. H.; Fujii, K.; Lee, H. J.; Ha, J. S. Improvement of Efficiency in Graphene/Gallium Nitride Nanowire on Silicon Photoelectrode for Overall Water Splitting. *Appl. Surf. Sci.* **2017**, *422*, 354–358. https://doi.org/10.1016/j.apsusc.2017.05.215.

(5)   Chu, S.; Li, W.; Yan, Y.; Hamann, T.; Shih, I.; Wang, D.; Mi, Z. Roadmap on Solar Water Splitting: Current Status and Future Prospects. *Nano Futur.* **2017**, *1* (2). https://doi.org/10.1088/2399-1984/aa88a1.

(6)   Jung, H. S.; Hong, Y. J.; Li, Y.; Cho, J.; Kim, Y. J.; Yi, G. C. Photocatalysis Using GaN Nanowires. *ACS Nano* **2008**, *2* (4), 637–642. https://doi.org/10.1021/nn700320y.

(7)   Moustakas, T. D. The Role of Extended Defects on the Performance of Optoelectronic Devices in Nitride Semiconductors. *Phys. Status Solidi Appl. Mater. Sci.* **2013**, *210* (1), 169–174. https://doi.org/10.1002/pssa.201200561.

(8)   Zhang, X.; Yang, Z.; Lu, Z.; Wang, W. Bifunctional CoNx Embedded Graphene Electrocatalysts for OER and ORR: A Theoretical Evaluation. *Carbon N. Y.* **2018**, *130*, 112–119. https://doi.org/10.1016/j.carbon.2017.12.121.

(9)   Liu, C.; Bai, G.; Tong, X.; Wang, Y.; Lv, B.; Yang, N.; Guo, X. Y. Mesoporous and Ultrathin Arrays of Cobalt Nitride Nanosheets for Electrocatalytic Oxygen Evolution.

Electrochem.   commun.   **2019**,   *98*,   87–91.
https://doi.org/10.1016/j.elecom.2018.11.022.

(10)   Chen, P.; Xu, K.; Tong, Y.; Li, X.; Tao, S.; Fang, Z.; Chu, W.; Wu, X.; Wu, C. Cobalt
Nitrides as a Class of Metallic Electrocatalysts for the Oxygen Evolution Reaction.
Inorg. Chem. Front. **2016**, *3* (2), 236–242. https://doi.org/10.1039/c5qi00197h.

(11)   Chen, Z.; Ha, Y.; Liu, Y.; Wang, H.; Yang, H.; Xu, H.; Li, Y.; Wu, R. In Situ
Formation of Cobalt Nitrides/Graphitic Carbon Composites as Efficient Bifunctional
Electrocatalysts for Overall Water Splitting. *ACS Appl. Mater. Interfaces* **2018**, *10* (8),
7134–7144. https://doi.org/10.1021/acsami.7b18858.

(12)   Zhang, Y.; Ouyang, B.; Xu, J.; Jia, G.; Chen, S.; Rawat, R. S.; Fan, H. J. Rapid
Synthesis of Cobalt Nitride Nanowires: Highly Efficient and Low-Cost Catalysts for
Oxygen Evolution. *Angew. Chemie Int. Ed.* **2016**, *55* (30), 8670–8674.
https://doi.org/10.1002/anie.201604372.

(13)   Song, F.; Li, W.; Yang, J.; Han, G.; Yan, T.; Liu, X.; Rao, Y.; Liao, P.; Cao, Z.; Sun,
Y. Interfacial Sites between Cobalt Nitride and Cobalt Act as Bifunctional Catalysts
for Hydrogen Electrochemistry. *ACS Energy Lett.* **2019**, *4* (7), 1594–1601.
https://doi.org/10.1021/acsenergylett.9b00738.

(14)   Jiang, H.; Li, X.; Zang, S.; Zhang, W. Mixed Cobalt-Nitrides CoxN and Ta2N
Bifunction-Modified Ta3N5 Nanosheets for Enhanced Photocatalytic Water-Splitting
into   Hydrogen.   *J.   Alloys   Compd.*   **2021**,   *854*,   155328.
https://doi.org/10.1016/j.jallcom.2020.155328.

(15)   Yuan, W.; Wang, S.; Ma, Y.; Qiu, Y.; An, Y.; Cheng, L. Interfacial Engineering of
Cobalt Nitrides and Mesoporous Nitrogen-Doped Carbon: Toward Efficient Overall
Water-Splitting Activity with Enhanced Charge-Transfer Efficiency. *ACS Energy Lett.*
2020, *5* (3), 692–700. https://doi.org/10.1021/acsenergylett.0c00116.

(16)   Ejeta, S. Y.; Imae, T. Cobalt Incorporated Graphitic Carbon Nitride as a Bifunctional
Catalyst for Electrochemical Water-Splitting Reactions in Acidic Media. *Molecules*
2022, *27* (19). https://doi.org/10.3390/molecules27196445.

(17)   Jamil, R.; Ali, R.; Loomba, S.; Xian, J.; Yousaf, M.; Khan, K.; Shabbir, B.;
McConville, C. F.; Mahmood, A.; Mahmood, N. The Role of Nitrogen in Transition-
Metal Nitrides in Electrochemical Water Splitting. *Chem Catal.* **2021**, *1* (4), 802–854.

https://doi.org/10.1016/j.checat.2021.06.014.

(18)   Ouyang, B.; Zhang, Y.; Zhang, Z.; Fan, H. J.; Rawat, R. S. Nitrogen-Plasma-Activated Hierachical Nickel Nitride Nanocorals for Energy Applications. *Small* **2017**, *13* (34), 1–10. https://doi.org/10.1002/smll.201604265.

(19)   Wang, J. Y.; Ouyang, T.; Li, N.; Ma, T.; Liu, Z. Q. S, N Co-Doped Carbon Nanotube-Encapsulated Core-Shelled CoS2@Co Nanoparticles: Efficient and Stable Bifunctional Catalysts for Overall Water Splitting. *Sci. Bull.* **2018**, *63* (17), 1130–1140. https://doi.org/10.1016/j.scib.2018.07.008.

(20)   Yu, M.; Zhao, S.; Feng, H.; Hu, L.; Zhang, X.; Zeng, Y.; Tong, Y.; Lu, X. Engineering Thin MoS2 Nanosheets on TiN Nanorods: Advanced Electrochemical Capacitor Electrode and Hydrogen Evolution Electrocatalyst. *ACS Energy Lett.* **2017**, *2* (8), 1862–1868. https://doi.org/10.1021/acsenergylett.7b00602.

(21)   Huang, Y.; Xu, H.; Yang, H.; Lin, Y.; Liu, H.; Tong, Y. Efficient Charges Separation Using Advanced BiOI-Based Hollow Spheres Decorated with Palladium and Manganese Dioxide Nanoparticles. *ACS Sustain. Chem. Eng.* **2018**, *6* (2), 2751–2757. https://doi.org/10.1021/acssuschemeng.7b04435.

(22)   Hu, Y.; Yang, H.; Chen, J.; Xiong, T.; Balogun, M. S. J. T.; Tong, Y. Efficient Hydrogen Evolution Activity and Overall Water Splitting of Metallic Co 4 N Nanowires through Tunable D-Orbitals with Ultrafast Incorporation of FeOOH. *ACS Appl. Mater. Interfaces* **2019**, *11* (5), 5152–5158. https://doi.org/10.1021/acsami.8b20717.

(23)   Liu, T.; Cai, S.; Mei, Z.; Zhao, G.; Xu, L.; An, Q.; Fu, Y.; Wang, H.; Li, M.; Guo, H. Boosting the Water Splitting Activity of Cobalt Nitride through Morphological Design: A Comparison of the Influence of Structure on the Hydrogen and Oxygen Evolution Reactions. *Sustain. Energy Fuels* **2021**, *5* (14), 3632–3639. https://doi.org/10.1039/D1SE00616A.

(24)   Yang, H.; Hu, Y.; Huang, D.; Xiong, T.; Li, M.; Balogun, M. S.; Tong, Y. Efficient Hydrogen and Oxygen Evolution Electrocatalysis by Cobalt and Phosphorus Dual-Doped Vanadium Nitride Nanowires. *Mater. Today Chem.* **2019**, *11*, 1–7. https://doi.org/10.1016/j.mtchem.2018.10.004.

(25)   Balogun, M. S.; Huang, Y.; Qiu, W.; Yang, H.; Ji, H.; Tong, Y. Updates on the

Development of Nanostructured Transition Metal Nitrides for Electrochemical Energy Storage and Water Splitting. *Mater. Today* **2017**, *20* (8), 425–451. https://doi.org/10.1016/j.mattod.2017.03.019.

(26) Fan, X.; Kong, F.; Kong, A.; Chen, A.; Zhou, Z.; Shan, Y. Covalent Porphyrin Framework-Derived Fe2P@Fe4N-Coupled Nanoparticles Embedded in N-Doped Carbons as Efficient Trifunctional Electrocatalysts. *ACS Appl. Mater. Interfaces* **2017**, *9* (38), 32840–32850. https://doi.org/10.1021/acsami.7b11229.

(27) Xu, K.; Chen, P.; Li, X.; Tong, Y.; Ding, H.; Wu, X.; Chu, W.; Peng, Z.; Wu, C.; Xie, Y. Metallic Nickel Nitride Nanosheets Realizing Enhanced Electrochemical Water Oxidation. *J. Am. Chem. Soc.* **2015**, *137* (12), 4119–4125. https://doi.org/10.1021/ja5119495.

(28) Zhang, Y.; Ouyang, B.; Xu, J.; Jia, G.; Chen, S.; Rawat, R. S.; Fan, H. J. Rapid Synthesis of Cobalt Nitride Nanowires: Highly Efficient and Low-Cost Catalysts for Oxygen Evolution. *Angew. Chemie* **2016**, *128* (30), 8812–8816. https://doi.org/10.1002/ange.201604372.

(29) Wang, J.; Li, K.; Zhong, H.; Xu, D.; Wang, Z.; Jiang, Z.; Wu, Z.; Zhang, X. Synergistic Effect between Metal-Nitrogen-Carbon Sheets and NiO Nanoparticles for Enhanced Electrochemical Water-Oxidation Performance. *Angew. Chemie* **2015**, *127* (36), 10676–10680. https://doi.org/10.1002/ange.201504358.

(30) Kibria, M. G.; Qiao, R.; Yang, W.; Boukahil, I.; Kong, X.; Chowdhury, F. A.; Trudeau, M. L.; Ji, W.; Guo, H.; Himpsel, F. J.; Vayssieres, L.; Mi, Z. Atomic-Scale Origin of Long-Term Stability and High Performance of p-GaN Nanowire Arrays for Photocatalytic Overall Pure Water Splitting. *Adv. Mater.* **2016**, *28* (38), 8388–8397. https://doi.org/10.1002/adma.201602274.

(31) Vanka, S.; Arca, E.; Cheng, S.; Sun, K.; Botton, G. A.; Teeter, G.; Mi, Z. High Efficiency Si Photocathode Protected by Multifunctional GaN Nanostructures. *Nano Lett.* **2018**, *18* (10), 6530–6537. https://doi.org/10.1021/acs.nanolett.8b03087.

(32) Alotaibi, B.; Nguyen, H. P. T.; Zhao, S.; Kibria, M. G.; Fan, S.; Mi, Z. Highly Stable Photoelectrochemical Water Splitting and Hydrogen Generation Using a Double-Band InGaN/GaN Core/Shell Nanowire Photoanode. *Nano Lett.* **2013**, *13* (9), 4356–4361. https://doi.org/10.1021/nl402156e.

(33) Varadhan, P.; Fu, H. C.; Priante, D.; Retamal, J. R. D.; Zhao, C.; Ebaid, M.; Ng, T. K.; Ajia, I.; Mitra, S.; Roqan, I. S.; Ooi, B. S.; He, J. H. Surface Passivation of GaN Nanowires for Enhanced Photoelectrochemical Water-Splitting. *Nano Lett.* **2017**, *17* (3), 1520–1528. https://doi.org/10.1021/acs.nanolett.6b04559.

(34) Van Straaten, G.; Deckers, R.; Vos, M. F. J.; Kessels, W. M. M.; Creatore, M. Plasma-Enhanced Atomic Layer Deposition of Cobalt and Cobalt Nitride: What Controls the Incorporation of Nitrogen? *J. Phys. Chem. C* **2020**, *124* (40), 22046–22054. https://doi.org/10.1021/acs.jpcc.0c04223.

(35) Reif, J.; Knaut, M.; Killge, S.; Winkler, F.; Albert, M.; Bartha, J. W. In Vacuo Studies on Plasma-Enhanced Atomic Layer Deposition of Cobalt Thin Films. *J. Vac. Sci. Technol. A* **2020**, *38* (1), 012405. https://doi.org/10.1116/1.5132891.

(36) Jensen, D. S.; Kanyal, S. S.; Madaan, N.; Vail, M. A.; Dadson, A. E.; Engelhard, M. H.; Linford, M. R. Silicon (100)/SiO 2 by XPS. *Surf. Sci. Spectra* **2013**, *20* (1), 36–42. https://doi.org/10.1116/11.20121101.

(37) Herrera-Gomez, A.; Bravo-Sanchez, M.; Ceballos-Sanchez, O.; Vazquez-Lepe, M. O. Practical Methods for Background Subtraction in Photoemission Spectra. *Surf. Interface Anal.* **2014**, *46* (10–11), 897–905. https://doi.org/10.1002/sia.5453.

(38) Herrera-Gomez, A.; Sun, Y.; Aguirre-Tostado, F.-S.; Hwang, C.; Mani-Gonzalez, P.-G.; Flint, E.; Espinosa-Magaña, F.; Wallace, R. M. Structure of Ultra-Thin Diamond-like Carbon Films Grown with Filtered Cathodic Arc on Si(001). *Anal. Sci.* **2010**, *26* (2), 267–272.

(39) Zhong, X.; Jiang, Y.; Chen, X.; Wang, L.; Zhuang, G.; Li, X.; Wang, J. G. Integrating Cobalt Phosphide and Cobalt Nitride-Embedded Nitrogen-Rich Nanocarbons: High-Performance Bifunctional Electrocatalysts for Oxygen Reduction and Evolution. *J. Mater. Chem. A* **2016**, *4* (27), 10575–10584. https://doi.org/10.1039/c6ta03820d.

(40) Wu, W.; Zhang, Q.; Wang, X.; Han, C.; Shao, X.; Wang, Y.; Liu, J.; Li, Z.; Lu, X.; Wu, M. Enhancing Selective Photooxidation through Co−Nx-Doped Carbon Materials as Singlet Oxygen Photosensitizers. *ACS Catal.* **2017**, *7* (10), 7267–7273. https://doi.org/10.1021/acscatal.7b01671.

(41) Biesinger, M. C.; Payne, B. P.; Grosvenor, A. P.; Lau, L. W. M.; Gerson, A. R.; Smart, R. S. C. Resolving Surface Chemical States in XPS Analysis of First Row Transition

Metals, Oxides and Hydroxides: Cr, Mn, Fe, Co and Ni. *Appl. Surf. Sci.* **2011**, *257* (7), 2717–2730. https://doi.org/10.1016/j.apsusc.2010.10.051.

(42) Lee, H. B. R.; Kim, H. High-Quality Cobalt Thin Films by Plasma-Enhanced Atomic Layer Deposition. *Electrochem. Solid-State Lett.* **2006**, *9* (11), G323. https://doi.org/10.1149/1.2338777.

(43) Wagner, C. D.; Davis, L. E.; Zeller, M. V; Taylor, J. A.; Raymond, R. H.; Gale, L. H. Empirical Atomic Sensitivity Factors for Quantitative Analysis by Electron Spectroscopy for Chemical Analysis. *Surf. Interface Anal.* **1981**, *3* (5), 211–225. https://doi.org/https://doi.org/10.1002/sia.740030506.

(44) Majumdar, A.; Das, S. C.; Shripathi, T.; Hippler, R. Chemical Synthesis and Surface Morphology of Amorphous Hydrogenated Carbon Nitride Film Deposited by N2/CH4 Dielectric Barrier Discharge Plasma. *Compos. Interfaces* **2012**, *19* (3–4), 161–170. https://doi.org/10.1080/15685543.2012.699751.

(45) Moulder, J. F.; Stickle, W. F.; Sobol, P. E.; Bomben, K. D. *Handbook of X-Ray Photoelectron Spectroscopy*; Chastain, J., Ed.; Perkin-Elmer Corporation: eden prairie, 1992.

(46) Mcintyre, N. S.; Cook, M. G. X-Ray Photoelectron Studies on Some Oxides and Hydroxides of Cobalt, Nickel, and Copper. *Anal. Chem.* **1975**, *47* (13), 2208–2213. https://doi.org/10.1021/ac60363a034.

(47) Grosvenor, A. P.; Wik, S. D.; Cavell, R. G.; Mar, A. Examination of the Bonding in Binary Transition-Metal Monophosphides MP (M) Cr, Mn, Fe, Co) by X-Ray Photoelectron Spectroscopy. **2005**. https://doi.org/10.1021/ic051004d.

(48) Johansson, L. I.; Johansson, H. I. P. Core Level Study of NbC(100) and NbN(100). *J. Electron Spectros. Relat. Phenomena* **1996**, *80*, 237–240. https://doi.org/10.1016/0368-2048(96)02965-9.

(49) Artyushkova, K. Misconceptions in Interpretation of Nitrogen Chemistry from X-Ray Photoelectron Spectra. *J. Vac. Sci. Technol. A* **2020**, *38* (3), 031002. https://doi.org/10.1116/1.5135923.

(50) Fei, H.; Dong, J.; Arellano-Jiménez, M. J.; Ye, G.; Dong Kim, N.; Samuel, E. L. G.; Peng, Z.; Zhu, Z.; Qin, F.; Bao, J.; Yacaman, M. J.; Ajayan, P. M.; Chen, D.; Tour, J. M. Atomic Cobalt on Nitrogen-Doped Graphene for Hydrogen Generation. *Nat.*

Commun. **2015**, *6*. https://doi.org/10.1038/ncomms9668.

(51)   Hellgren, N.; Haasch, R. T.; Schmidt, S.; Hultman, L.; Petrov, I. Interpretation of X-Ray Photoelectron Spectra of Carbon-Nitride Thin Films: New Insights from in Situ XPS. *Carbon N. Y.* **2016**, *108*, 242–252. https://doi.org/10.1016/j.carbon.2016.07.017.

(52)   Gelius, U.; Hedén, P. F.; Hedman, J.; Lindberg, B. J.; Manne, R.; Nordberg, R.; Nordling, C.; Siegbahn, K. Molecular Spectroscopy by Means of ESCA: III Carbon Compounds. *Phys. Scr.* **1970**, *2* (1–2), 70–80. https://doi.org/10.1088/0031-8949/2/1-2/014.

(53)   Miller, D. J.; Biesinger, M. C.; McIntyre, N. S. Interactions of CO2 and CO at Fractional Atmosphere Pressures with Iron and Iron Oxide Surfaces: One Possible Mechanism for Surface Contamination? *Surf. Interface Anal.* **2002**, *33* (4), 299–305. https://doi.org/10.1002/sia.1188.

(54)   Greczynski, G.; Hultman, L. Towards Reliable X-Ray Photoelectron Spectroscopy: Sputter-Damage Effects in Transition Metal Borides, Carbides, Nitrides, and Oxides. *Appl. Surf. Sci.* **2021**, *542*. https://doi.org/10.1016/j.apsusc.2020.148599.

(55)   Patrinoiu, G.; Rodriguez, J. R.; Wang, Y.; Birjega, R.; Osiceanu, P.; Musuc, A. M.; Qi, Z.; Wang, H.; Pol, V. G.; Calderon-Moreno, J. M.; Carp, O. Versatile by Design: Hollow Co3O4 Architectures for Superior Lithium Storage Prepared by Alternative Green Pechini Method. *Appl. Surf. Sci.* **2020**, *510* (January), 145431. https://doi.org/10.1016/j.apsusc.2020.145431.

(56)   Paracchino, A.; Mathews, N.; Hisatomi, T.; Stefik, M.; Tilley, S. D.; Grätzel, M. Ultrathin Films on Copper(i) Oxide Water Splitting Photocathodes: A Study on Performance and Stability. *Energy Environ. Sci.* **2012**, *5* (9), 8673–8681. https://doi.org/10.1039/c2ee22063f.

(57)   Jiang, C.; Moniz, S. J. A.; Wang, A.; Zhang, T.; Tang, J. Photoelectrochemical Devices for Solar Water Splitting-Materials and Challenges. *Chem. Soc. Rev.* **2017**, *46* (15), 4645–4660. https://doi.org/10.1039/c6cs00306k.

(58)   Sun, K.; Shen, S.; Liang, Y.; Burrows, P. E.; Mao, S. S.; Wang, D. Enabling Silicon for Solar-Fuel Production. *Chem. Rev.* **2014**, *114* (17), 8662–8719. https://doi.org/10.1021/cr300459q.

(59)   Lee, S. A.; Park, I. J.; Yang, J. W.; Park, J.; Lee, T. H.; Kim, C.; Moon, J.; Kim, J. Y.;

Jang, H. W. Electrodeposited Heterogeneous Nickel-Based Catalysts on Silicon for Efficient Sunlight-Assisted Water Splitting. *Cell Reports Phys. Sci.* **2020**, *1* (10), 100219. https://doi.org/10.1016/j.xcrp.2020.100219.

(60) Yi, Y.; Zhang, P.; Qin, Z.; Yu, C.; Li, W.; Qin, Q.; Li, B.; Fan, M.; Liang, X.; Dong, L. Low Temperature CO Oxidation Catalysed by Flower-like Ni-Co-O: How Physicochemical Properties Influence Catalytic Performance. *RSC Adv.* **2018**, *8* (13), 7110–7122. https://doi.org/10.1039/c7ra12635b.

(61) Saraswat, S. K.; Rodene, D. D.; Gupta, R. B. Recent Advancements in Semiconductor Materials for Photoelectrochemical Water Splitting for Hydrogen Production Using Visible Light. *Renew. Sustain. Energy Rev.* **2018**, *89* (April), 228–248. https://doi.org/10.1016/j.rser.2018.03.063.

(62) Li, D.; Shi, J.; Li, C. Transition-Metal-Based Electrocatalysts as Cocatalysts for Photoelectrochemical Water Splitting: A Mini Review. *Small* **2018**, *14* (23), 1–22. https://doi.org/10.1002/smll.201704179.

6 Conclusions and Future Work

6.1 Conclusions

This work has presented a detailed ALD study, with the application of a variety of materials and precursors which have been investigated for the use as thin protective films for photoelectrode performance improvement in PEC water splitting. This involved the fundamental investigation and characterisation of each precursor material deposited via ALD processes to gain insight into their growth kinetics from early-stage nucleation through to bulk film properties. To this end, films underwent photoemission measurements with the use of x-ray photoelectron spectroscopy being the primary analysis technique employed to explore the chemical characteristics of the protective films. A range of other techniques were applied for further analysis before ultimately subjecting them to simulated PEC solar conditions to test the effectiveness of the applied thin protective films in protecting the underlying photoelectrode substrate.

Due to the experimental variability of photoelectrochemical testing set ups utilising a range of electrolyte solutions of various pH levels among other factors, side by side comparison of literature reported data is highly complex and inaccurate. Therefore, within this study one key advantage of exploring a variety of materials in their as deposited states as well as following post deposition treatments within the same work under identical photoelectrochemical testing conditions allowed for accurate assessment of the best performing surface coating. With this in mind, the highest performing coatings from all three results chapters are presented together within Figure 6.1. From this it is clear that NiO films within this work were the most effective protective layer offering both the highest onset photocurrent along with being the most stable of all layers applied so much so that surface

coatings of Co and Ti become indistinguishable at the lower photocurrent density end of the scale further highlighting the superiority of Ni films.
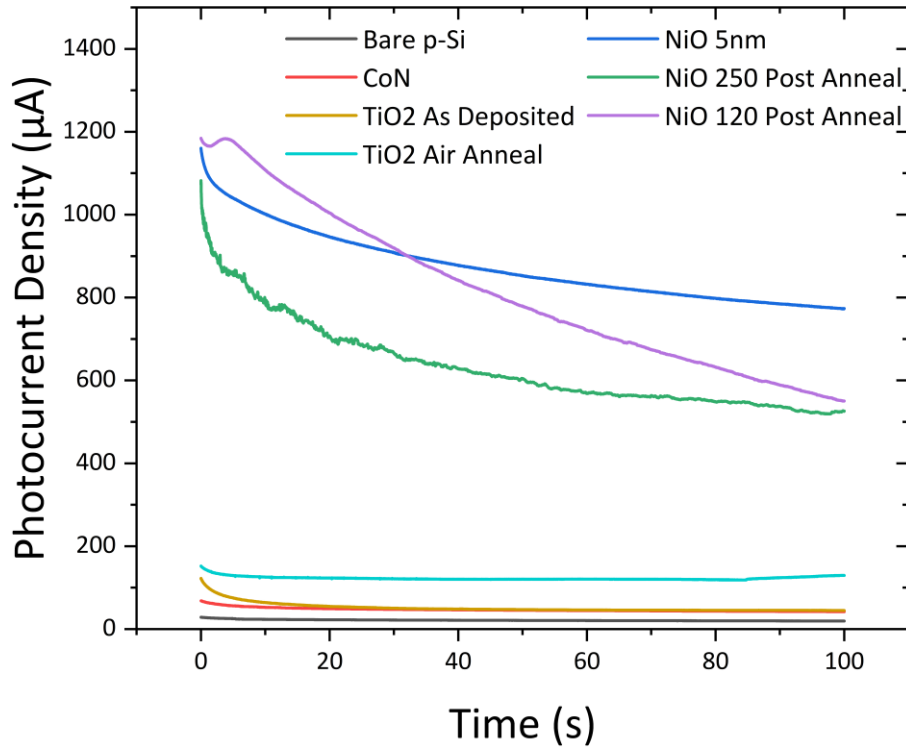
Figure 6.1 Most effective surface coatings from each material compared for their stability during time degradation testing.

6.1.1 TiO2: Simultaneous Characterisation of TDMAT and TTIP

As one of the most widely studied materials in the field of PEC and wider water splitting applications as both the photoelectrode substrate material as well as for its catalytic and protective qualities Chapter 3 goes about the investigation of two of the most common TiO_2 precursors comparing TTIP and TDMAT subjecting them to simultaneous scrutiny under the same conditions to accurately establish the characteristics of these alkoxide and amide precursors, respectively. This served to remove experimental variance from literature source

to literature source given that both were deposited in and identical ALD chamber which is well known to be influential in the deposition of ALD films. The ability to analyse the deposited films from both precursors using *in-situ* XPS allowed for a unique perspective into their stoichiometry which is all too often unavailable within the literature due to few laboratories possessing the capabilities presented by the ALD-XPS system used within this work.

The presented results detail an *in-situ* study on the deposition of these amide and alkoxide based precursors grown via PEALD and TALD processes, in contrast to some previous literature reports which detail only the comparison of two precursors for a single growth process or vice versa. Characterisation of these deposition processes with *in-situ* XPS allows for unique understandings of film chemistry in their as deposited states without the added complexity of film contamination via atmospheric exposure while sequential growth of all processes allowed for precise monitoring of film nucleation.

The primary variations in stoichiometry of deposited films between the plasma and air annealed sampled showed a significant increase in the growth of titanium silicate in samples which received the air annealing treatment. This is highlighted by the reduction in the Si bulk and oxide binding energy separation by approximately 0.2 eV. The relationship between the development of titanium silicate and enhanced photoelectrochemical effectiveness and stability indicates that achieving maximum photocurrent from silicon photoanodes, which are shielded by ultra-thin films, necessitates a high-temperature annealing process that allows for the transformation of the mixed phase material into titanium silicate. After undergoing such a treatment, films produced using both precursors and through both atomic layer deposition (ALD) techniques become chemically indistinguishable.

The application of post deposition annealing treatments were revealed through photoelectrochemical testing to enhance both current output and stability under test conditions. Of the annealing treatments, air annealing at 500°C for 1 hour yielded both the most stable and efficient titania films grown from either precursor material or deposition process with plasma grown films showing only marginally higher current outputs versus thermally grown films.

Through comparing plasma and air annealed samples, it was found that the stoichiometry of deposited films varied significantly. Air annealing treatment resulted in a notable increase in the growth of titanium silicate, as indicated by a reduction in the separation of Si bulk and oxide binding energy by approximately 0.2 eV. The formation of titanium silicate was found to enhance the photoelectrochemical effectiveness and stability, suggesting that achieving maximum photocurrent from silicon photoanodes covered by ultra-thin films requires a high-temperature annealing process. Interestingly, chemically, the films produced using both precursors and ALD techniques became indistinguishable after undergoing this treatment.

This *in-situ* study highlights the importance of analysing films prior to exposure to atmospheric contamination and the influence of annealing treatments and film composition in achieving improved performance and stability of titania films grown via ALD. The findings emphasize the potential of high-temperature air annealing to transform mixed phase materials into titanium silicate, leading to enhanced photoelectrochemical properties. These insights contribute to the advancement of titania film deposition techniques and the development of efficient silicon photoanodes for PEC water splitting and other applications.

6.2 Nickel: Exploring NiO and Ni-Metal

With the field of water splitting be dominated by the application of transition metal oxides for the protection of PEC photoelectrodes, work within Chapter 4 looked to develop first a solid understanding of NiO before moving to explore the performance of metallic nickel, a less explored material within this field. The deposition of nickel metal involved the development of a process of deposition called supercycling with the effects of this variant of ALD explored within. Moreover, through performing further film analysis via depth profiling of deposited films using the slow argon milling method, findings of some previous literature reports were found to be inaccurate demonstrating further advantages to the *in-situ* XPS analysis performed throughout this work. Following on from Chapter 3 investigating titania films, Ni thin films were subjected to the simulated PEC solar water splitting testing to establish their efficacy in preventing the degradation of water splitting photoelectrodes such as to extend and enhance the performance of these vital PEC components.

Following findings from the earlier study on titania films which suggested the benefits of depositing thin films via PEALD rather than the conventional TALD, this chapter presents the results of an *in-situ* study on the plasma-enhanced atomic layer deposition (PEALD) of NiO. XPS characterization of the deposition process provides useful insights into the film chemistry in its original state, free from atmospheric contamination. By depositing and studying films sequentially, the growth behaviour and nucleation delay were accurately monitored, providing a detailed understanding of the cycle-by-cycle growth process of this precursor material. The PEALD process was optimized for the specific ALD system used, resulting in Ni films with some residual carbon ligand incorporation due to incomplete reactions, which was correctly identified through *in-situ* XPS analysis to be by virtue of

incomplete surface reactions of the ALD deposition process rather than misattributed to atmospheric contamination.

The impact of post-deposition plasma annealing on film stoichiometry was also investigated using H_2 plasma for this material. It was found that NiO could only be partially reduced to metallic Ni after an extended 20-minute exposure. Attempts were made to produce pure metallic Ni films from the outset using supercycle ALD depositions, aiming to eliminate the need for post-deposition treatments, which proved to be ineffective. However, photoelectrochemical (PEC) testing demonstrated that these supercycle deposited films exhibited enhanced stability for water splitting applications compared to NiO films that underwent post-deposition treatment.

Furthermore, previous claims regarding the effects of argon (Ar) milling on NiO thin films were found to be inaccurate. This work revealed that Ar milling actually reduces NiO to Ni metal by preferentially sputtering oxygen from the film. This result had previously been mistakenly interpreted as the protective capability of a 2 nm film against the oxidation of a metallic film upon atmospheric exposure whereas this work finds that 2 nm of Ni is insufficient to prevent the oxidation of the bulk film.

Therefore, this in-situ study sheds light on the PEALD deposition of NiO films and their characterization using XPS analysis. By accurately understanding the film chemistry and growth behaviour, valuable insights were gained regarding residual carbon ligand incorporation, the impact of post-deposition plasma annealing, and the effects of Ar milling. These findings contribute to the optimization of Ni oxide and metal film deposition processes and provide crucial knowledge for the development of stable and efficient Ni films for various applications, particularly in the field of water splitting.

6.3 CoN: Investigating the Potential of Nitrides in PEC Water Splitting

In the field of water splitting photoelectrode protection, the majority of existing literature has predominantly focused on exploring various oxide materials. However, Chapter 5 explores the efficacy of cobalt nitride as an alternative material for this purpose. Through exhaustive analysis and in-situ characterization, this study provides valuable insights into the growth and characteristics of cobalt nitride films, offering a fresh perspective and potential avenues for advancing the field of water splitting photoelectrode protection.

This chapter focuses on the growth of cobalt nitride films using PEALD process. It was observed that there is a specific window of NH_3 plasma dose time for optimal cobalt nitride growth, with doses beyond a certain duration inhibiting growth. The optimal growth rates were determined for various temperatures, revealing a rapid decrease in growth rate with increasing temperature. In-situ XPS measurements showed that films processed at 300°C resulted in cobalt nitride films, while 350°C led to a blend of cobalt nitride and metallic cobalt. At 400°C, only metallic cobalt was obtained, albeit at a low growth rate with residual nitrogen in the film.

Surprisingly, the cobalt nitride films contained high levels of carbon, associated with residual precursor and carbon-nitrogen bonding. Lower ALD temperatures resulted in higher levels of leftover precursor in the film, contrary to previous reports suggesting minimal carbon incorporation. Upon exposure to atmosphere, an increase in the C 1s XPS signal was attributed to adventitious carbon as expected, while the Co-N and N-C bonding remained unchanged.

HAXPES (hard X-ray photoelectron spectroscopy) provided a non-destructive depth profiling technique for this chapter, allowing for further extensive analysis of deposited films. The Co 2p spectra revealed large satellite features attributed to Co-N bonding. The study demonstrated that a 300°C ALD process yielded cobalt nitride films with varying cobalt concentrations compared to a 200°C process. The depth profiling analysis also confirmed consistent Co-N and C-N signatures throughout the film, with the only change associated with adventitious carbon on the film surface due to atmospheric exposure being that HAXPES is performed *ex-situ*.

Overall, this work highlights the challenges in growing cobalt nitride films using the $CoCP_2$-NH_3 ALD process and provides valuable insights into the impact of changing ALD parameters. The in-situ characterization approach employed in this study enhances our understanding of cobalt nitride film growth and paves the way for further advancements in this field. As was done in the previous Chapters 3 & 4, CoN films were subjected the simulated PEC testing for the determination of their potential as protective layers. CoN films were shown to yield enhanced photoelectrochemical performance initially before failing to remain stable in the harsh PEC electrolyte environment as is crucial to their application a protective layers. This suggests that CoN films in their as deposited state are unsuitable for extending the operable lifetime of PEC photoelectrodes despite showing promising photocurrent density output.

6.4 Future Work

This work focused on exploring various first-row transition metals in their oxide, metallic, and nitride forms for their application as protective layers for PEC water splitting photoelectrodes to extend their usable lifetime in carrying out the HER and OER reactions. It has been observed that these materials do exhibit enhanced stability and improved photocurrent output when compared to bare silicon. However, despite these advancements, their performance still falls short when compared to alternative methods of energy generation making the potential for widespread development and adoption of this technique for green hydrogen generation futile. To overcome this limitation, it could be beneficial to investigate the combination of these and other materials to leverage their unique strengths, thereby creating a more robust and efficient architecture.

By synergistically combining the advantageous properties of different transition metal films, it may be possible to overcome individual limitations and achieve an overall superior performance. For instance, one transition metal film may exhibit exceptional stability, while another demonstrates superior charge transport characteristics. By integrating these complementary traits, it is plausible to develop a system which surpasses the limitations of individual materials and achieves enhanced stability and efficiency.

With this work having focused on examining the nucleation and growth characteristics of these films in detail, it has provided valuable insights into the field of ALD of thin films. The application of in-situ X-ray Photoelectron Spectroscopy (XPS) has proven to be extremely beneficial, as it enables the investigation of the deposited films' chemical signatures without the interference of adventitious carbon contamination. This approach reveals the true,

unobscured chemical composition, facilitating a more accurate understanding of the materials' behaviour and properties.

Looking ahead, it is evident in-situ XPS will continue to play a pivotal role in advancing the field. Its ability to unveil the intrinsic characteristics of deposited films will contribute significantly to the development of more precise and reliable fabrication processes. By eliminating the influence of extraneous factors, researchers can gain a deeper understanding of material behaviour and further optimize their performance.

In terms of the broader direction of research, the findings within this work suggest that semiconductor-based photoelectrochemical (PEC) water splitting might not be the most promising path forward. PEC water splitting imposes numerous demands on photoelectrode materials, requiring them to fulfil multiple requirements simultaneously such as including stability, charge transport, charge transport, suitable band gaps and more. Considering these challenges, an alternative approach involving electrolysis, utilizing externally acquired renewable energy such as solar or wind energy, appears to be a more realistic and feasible solution for the large-scale production of green hydrogen.

By leveraging renewable energy sources such as solar or wind power for electrolysis, it may be possible to overcome the limitations posed by photoelectrode materials and achieve significant quantities of green hydrogen to meet the escalating demand. This approach allows for a more focused optimization of materials and systems dedicated to electrolysis, ultimately resulting in a more economically and environmentally viable method for hydrogen production.

That being said, the results within this work are based on thin films deposited via ALD and as such cannot speak for the overall outlook entirely but rather when considering the stringent

material characteristic requirements, it may be the case that films at least grown via ALD may not be optimal. There could be potentially greater enhancements achieved through the application of other thin film deposition techniques such as sputtering or perhaps the application of PEALD with an applied DC bias such as to produce denser films which may be more stable in the PEC environment.

In summary, the combination of transition metal films to harness their unique strengths, the continued utilization of in-situ XPS for accurate characterization, and a shift towards electrolysis using externally acquired renewable energy sources present potential avenues for future research in this field. By pursuing these directions, developing more stable, efficient, and sustainable means of green hydrogen generation could be made possible.